Particle-Based Geometric and Mechanical Modelling of Woven Technical Textiles and Reinforcements for Composites

by

Reza Samadi

Thesis submitted to the
Faculty of Graduate and Postdoctoral Studies
In partial fulfilment of the requirements
for the Ph.D. degree in
Mechanical Engineering

Ottawa-Carleton Institute for Mechanical and Aerospace Engineering
Faculty of Engineering
University of Ottawa

To my parents

Abstract

Technical textiles are increasingly being engineered and used in challenging applications, in areas such as safety, biomedical devices, architecture and others, where they must meet stringent demands including excellent and predictable load bearing capabilities. They also form the bases for one of the most widespread group of composite materials, fibre reinforced polymer-matrix composites (PMCs), which comprise materials made of stiff and strong fibres generally available in textile form and selected for their structural potential, combined with a polymer matrix that gives parts their shape. Manufacturing processes for PMCs and technical textiles, as well as parts and advanced textile structures must be engineered, ideally through simulation, and therefore diverse properties of the textiles, textile reinforcements and PMC materials must be available for predictive simulation. Knowing the detailed geometry of technical textiles is essential to predicting accurately the processing and performance properties of textiles and PMC parts. In turn, the geometry taken by a textile or a reinforcement textile is linked in an intricate manner to its constitutive behaviour.

This thesis proposes, investigates and validates a general numerical tool for the integrated and comprehensive analysis of textile geometry and constitutive behaviour as required toward engineering applications featuring technical textiles and textile reinforcements. The tool shall be general with regards to the textiles modelled and the loading cases applied. Specifically, the work aims at fulfilling the following objectives: 1) developing and implementing dedicated simulation software for modelling textiles subjected to various load cases; 2) providing, through simulation, geometric descriptions for different textiles subjected to different load cases namely compaction, relaxation and shear; 3) predicting the constitutive behaviour of the textiles undergoing said load cases; 4)

identifying parameters affecting the textile geometry and constitutive behaviour under evolving loading; 5) validating simulation results with experimental trials; and 6) demonstrating the applicability of the simulation procedure to textile reinforcements featuring large numbers of small fibres as used in PMCs.

As a starting point, the effects of reinforcement configuration on the in-plane permeability of textile reinforcements, through-thickness thermal conductivity of PMCs and in-plane stiffness of unidirectional and bidirectional PMCs were quantified systematically and correlated with specific geometric parameters. Variability was quantified for each property at a constant fibre volume fraction. It was observed that variability differed strongly between properties; as such, the simulated behaviour can be related to variability levels seen in experimental measurements. The effects of the geometry of textile reinforcements on the aforementioned processing and performance properties of the textiles and PMCs made from these textiles was demonstrated and validated, but only for simple cases as thorough and credible geometric models were not available at the onset of this work. Outcomes of this work were published in a peer-reviewed journal [101].

Through this thesis it was demonstrated that predicting changes in textile geometry prior and during loading is feasible using the proposed particle-based modelling method. The particle-based modelling method relies on discrete mechanics and offers an alternative to more traditional methods based on continuum mechanics. Specifically it alleviates issues caused by large strains and management of intricate, evolving contact present in finite element simulations. The particle-based modelling method enables credible, intricate modelling of the geometry of textiles at the mesoscopic scale as well as faithful mechanical modelling under load. Changes to textile geometry and configuration due to the normal compaction pressure, stress relaxation, in-plane shear and other types of loads were successfully predicted.

During simulation, particles were moved randomly until a stable state of minimum strain energy in the system was reached; as particles moved upon iteration, the configuration of fibres in the textile changed under constant boundary conditions. Then boundary conditions were altered corresponding to strains imposed on the textile, and the system was iterated again towards a new state of minimum strain energy. The Metropolis algorithm of the Monte Carlo method was adopted in this specific implementation. The method relies on a statistical approach implemented in computational algorithms. In addition to geometrical modelling, the proposed particle-based modelling method enables the prediction of major elements of the constitutive behaviour of textiles and textile reinforcements. In fact, prediction of the constitutive behaviour is integral to the prediction of the meso-scale geometry.

Simulation results obtained from the proposed particle-based modelling method were validated experimentally for yarns, single-layer textiles and multi-layer textiles undergoing compaction. Validation work showed that the particle-based modelling method replicates reality very faithfully, and it also showed the suitability of including Gutowski's function along with Hertz' function for representing lateral compaction of yarns. The procedure and results were accepted in final form for publication in a peer reviewed journal [104].

The capability of the proposed particle-based modelling method towards replicating the time-dependent relaxation and reconfiguration of woven textiles subjected to compaction loading was investigated. The capability, which was demonstrated for single and double-layers of plain woven textiles, is intrinsic to the modelling method. The method is unique in the fact that in contrary to work previously reported in the literature, it models the compaction and the relaxation seamlessly in the same simulations and environment. This work is being finalised towards submission for publication in a peer reviewed journal [103].

The proposed particle-based modelling method was also used for modelling in-plane shear in woven textiles. Simulation results were validated experimentally for a single-layer plain woven textile. Validation work showed that the particle-based modelling method reproduces experimental data and published trends very well. A novel algorithm for modelling friction was introduced, leading to results being obtained from a significantly less computationally demanding procedure in these simulations. This work was submitted for publication in a peer reviewed journal [102].

Finally the thesis discusses early work towards the application of the method to carbon fibre fabrics through the description of expansion algorithm (EA) to be used in modelling textiles made of yarns featuring very large numbers of fibres. Furthermore, additional modelling work is presented towards further manufacturing process involving technical textiles, namely textile bending and punching. The latter part is presented as early steps towards future work.

Acknowledgements

I would like to thank my supervisor Dr. Robitaille for his incredible guidance, support and friendship. He has been a constant source of inspiration at both the professional and personal levels. He brought a different perspective on my work and guided me to view my work from different angles. His insight and encouragement throughout my days at the University of Ottawa were crucial motivators. I am indebted to him more than he knows.

I wish to extend my gratitude to Dr. Jodoin, Dr. Laliberte, Dr. Pham and Dr. Weck for taking the time to stand on my thesis and defence committee and offer their valuable ideas and suggestions. I would also like to thank the mechanical engineering department's machine shop technicians for their assistance and support.

I am so grateful to my sister Mahnaz, her eyes shined even during challenging times, Nazanin for being a true friend and Bahar for her life-giving smiles. I acknowledge the sweet and supportive memories of Javad. I would like to deeply thank Ali Shahroud for inspiring me to pursue knowledge in my early ages. Also many thanks go out to my in-laws for their support and for providing me with an energetic environment.

Special thanks to my mother, for her continued love, my father, for his endless moral and emotional support and my dear wife, Parisa, for her encouragements. Also many thanks to my beloved daughter Aysa, for her smiles and hugs that offered me continued sweet life. Their dedication and inspiration will never be forgotten.

Contents

1 Introduction **1**

1.1 Composite materials 1

1.2 Geometry of preforms 3

1.3 Geometric and mechanical modelling of textiles and textile reinforcements 6

1.4 Contribution of the thesis 7

1.5 Thesis overview 8

2 Geometric Modelling Methodology **11**

2.1 Introduction 11

2.2 Literature review 12

2.2.1 Basic analytical models of textile unit cells 12

2.2.2 Textile geometric modelling software packages 15

2.2.3 Recent textile geometric models 19

2.3 Modelling method 21

2.3.1 Particle interactions 23

2.3.2 Metropolis algorithm 23

2.3.3 Strain energy terms 25

2.3.4 Uniform random distribution 32

2.3.5 Random walk 33

2.4 Software development 34
2.4.1 Implementation 34
2.4.2 Core 34
2.4.3 Render 35
2.5 Equilibrium verification procedure 36
2.6 Summary for procedure of the representation of textile geometry using particle-based modelling 37

3 Concurrent simulation of permeability, thermal conductivity and modulus for carbon fibre reinforcements and composites 39
3.1 Preamble 39
3.2 Abstract 40
3.3 Introduction 41
3.4 Literature review 43
3.5 Geometry and properties 45
3.6 Simulations 50
3.6.1 Resin flow simulations 52
3.6.2 Heat transfer simulations 55
3.6.3 Static loading simulations 57
3.7 Experiments 59
3.8 Discussion 62
3.9 Conclusion 63

4 Particle-based modelling of the compaction of fibre yarns and woven textiles 65
4.1 Preamble 65

4.2 Abstract 66

4.3 Introduction 67

4.4 Modelling methodology 71

  4.4.1 Modelling method 72

  4.4.2 Strain energy terms 72

4.5 Simulations and validation experiments 78

  4.5.1 Series 1: fibre compaction 81

  4.5.2 Series 2: yarn compaction 83

  4.5.3 Series 3: textile compaction 90

4.6 Conclusion 92

5 Particle-based modelling of relaxation and reconfiguration in woven textiles 99

5.1 Preamble 99

5.2 Abstract 100

5.3 Introduction 101

5.4 Modelling method 112

  5.4.1 Strain energy terms 112

5.5 Simulations and validation experiments 114

  5.5.1 Experimental trails 116

  5.5.2 Simulation trials 127

5.6 Conclusion 139

6 Particle-based modelling of in-plane shear of textiles 140

6.1 Preamble 140

6.2 Abstract 141

6.3 Introduction 142
6.4 Modelling methodology 147
6.4.1 Modelling method 148
6.4.2 Yarn configurations and tension upon in-plane shear of textiles . . 151
6.4.3 Strain energy terms 152
6.5 In-plane shear simulation methodology 154
6.5.1 Shear angle and shear forces 156
6.5.2 Boundary conditions 158
6.6 Articulated frame in-plane shear testing 161
6.7 Simulations of in-plane shear: mechanical behaviour 165
6.7.1 Effect of domain size: simulations 1A and 1B 166
6.7.2 Effect of fibre tension: simulations 2A, 2B and 2C 167
6.7.3 Effect of fibre friction: simulations 3A, 3B and 3C 169
6.7.4 Effect of bending stiffness: simulations 4A, 4B and 4C 170
6.8 Simulation of in-plane shear: evolution of geometry 171
6.9 Conclusion 175

7 Discussion and Conclusion 177

7.1 Introduction 177
7.2 Expansion algorithm 178
7.2.1 Intra-fibre strain energy terms for *EA*-fibres 178
7.2.2 Inter-fibre strain energy terms for *EA*-fibres 181
7.3 Demonstration 184
7.4 Modelling of manufacturing operations 187
7.4.1 Textile bending 187
7.4.2 Textile punching for assembly through stitching 189

7.5 Discussion 191
7.5.1 Geometric modelling 192
7.5.2 Mechanical modelling 192
7.6 Conclusion 193
7.7 Future work 195

A Appendix A: Flowchart **214**

List of Tables

3.1 Reinforcement geometry for cell models 47
3.2 Properties of carbon fibres and epoxy resin 48
3.3 Tow properties for cell models 49
3.4 Significant parameters and contrast values ć 64

4.1 Characteristics of fibres and textiles 80

5.1 Characteristics of fibres and textiles 115

6.1 Characteristics of fibres and textiles 161

7.1 Results of two scenarios 186

List of Figures

1.1 Different scale in textiles: a)macroscopic scale; b)mesoscopic scale; c)microscopic scale . . . 4

1.2 Textile architectures for composite reinforcements: a) non-woven, b) 2D plain weave, c) 3D weave, d) non-crimp stitched, e) braid, f) weft knit [111] 5

2.1 Evolution of unit cell geometry modelling: a) Peirce [82], b) Kemp [52], c) Hofstee [45] d) Ning and Chou [77], e) Hearle [109], f) Searles [108] . . 13

2.2 Plain weave RUC generated by the author using TexGen [111] 16

2.3 Plain weave textile generated by the author using TechText CAD [44] . . 17

2.4 Plain weave textile generated by the author using WiseTex [68] 18

2.5 Digital element simulation: a) fibre representation b) yarn representation with 19 fibres [118] . . . 20

2.6 Geometrical modelling of a textile with digital elements containing different number of fibres within yarns [118] . . . 21

2.7 Intra-fibre strain energy terms . . . 26

2.8 Contact between simulated particles of two fibres . . . 28

2.9 Shape and dimensions of fibres in Gutowski's model . . . 30

2.10 Particle positions in 2D space: a) randomly generated positions, b) uniformly distributed random positions . . . 33

2.11 Random walk in: a)2D and b)3D 34
2.12 Implementation of computational modules 35
2.13 Selection of individual fibre from textile 36
2.14 Equilibrium verification within a fibre assembly 37

3.1 Geometric parameters 43
3.2 Geometric parameters $th + gv$ (models 1A-1P, 1Z) or 2 $(th + gv)$ (models 2A-2P, 2Z) and vf_t 51
3.3 Typical flow domains; a) material 1, flow along x; b) material 1, flow along y; c) material 2 52
3.4 Flow field: velocity vectors collared by amplitude (m/s), cell model 1C, flow along x 53
3.5 Flow simulation results 54
3.6 Typical heat transfer domains: material 1, material 2 55
3.7 Temperature field (K), cell model 2A 56
3.8 Heat transfer simulation results 57
3.9 Von Mises stress field (MPa), cell model 1B, stress along x 58
3.10 Static loading simulation results 59
3.11 Permeability measurement apparatus 60
3.12 Hukseflux THASYS transverse permeability measurement apparatus and samples 61

4.1 Tension/compression axial strain energy between two particles (right) and bending strain energy between three particles (left) 73
4.2 Contact between the curved surfaces of two fibres 75
4.3 Fibre segments and encompassing prisms in Gutowski's model 76
4.4 Compaction rig for single yarn with restrictions on lateral fibre displacement 79

4.5 Manufactured textile with Nylon 6/6 80

4.6 Compaction rig with a single layer textile 81

4.7 Results of the compaction of two superimposed fibres with lateral constrains (series 1) 82

4.8 Single yarn compaction with restrictions on lateral fibre displacement (series 2.1) 83

4.9 Results of single copper yarn compaction with lateral restrictions (series 2.1) 85

4.10 Results of single Nylon 6/6 yarn compaction with lateral restrictions (series 2.1) 86

4.11 Single yarn compaction without restrictions on lateral fibre displacement (series 2.2) 87

4.12 Results of 5 compaction trials for yarn without lateral restrictions (series 2.2) 88

4.13 Values of v_f over different cross-section planes normal to axis x (series 2.2) 89

4.14 v_f variation within a yarn at thickness = 0.63 mm (series 2.2) 90

4.15 Compaction of crossed yarns without restrictions on lateral fibre displacement (series 2.3) 91

4.16 Single unit cell of plain woven textile (series 3.1) 92

4.17 P as a function of v_f in a single unit cell of plain woven textile (series 3.1) 93

4.18 Extreme fibre deformations for both scenarios of: a) with lateral boundaries, b) without lateral boundaries (series 3.1) 94

4.19 Simulations of single-layer with multiple unit cells in plain woven textile: a)3D view, b) 2D view (series 3.2) 95

4.20 P as a function of v_f in a single layer plain woven textile (series 3.2) . . . 96

4.21 Simulations of double-layer plain woven textile with multiple unit cells: a)perfectly aligned yarns, b) perfectly staggered yarns 97
4.22 Fibre volume fraction of double-layer textile: a) perfectly aligned yarns, b) perfectly staggered yarns 98

5.1 Evolution of h_p, v_f and P during 3 phases of textile processing 102
5.2 Simulation of single-layer of plain woven textile featuring multiple unit cells: a) before compaction, b) after compaction, at the onset of relaxation 114
5.3 Compaction/relaxation platens with single layer textile 116
5.4 Compaction and relaxation of single layer plain woven textile samples (series A-1) 117
5.5 P as a function of v_f during compaction and relaxation of a single layer plain woven textile sample (series A-1) 117
5.6 Compaction and relaxation of single layer plain woven textiles at different compaction rates, target pressure P=0.45 MPa (series A-2) 118
5.7 v_f as a function of time for single layer plain woven textiles subjected to different compaction rates with target pressure P=0.45 MPa (series A-2) 119
5.8 Relaxation of single layer plain woven textiles subjected to different compaction rates (series A-2) 120
5.9 Compaction and relaxation of single layer plain woven textiles at different compaction rates, target v_f=0.53 (series A-3) 121
5.10 v_f as a function of time for single layer plain woven textiles subjected to different compaction rates with target v_f=0.53 (series A-3) 121
5.11 Relaxation of single layer plain woven textiles subjected to different compaction rates (series A-3) 122

5.12 Compaction and relaxation of single layer plain woven textiles at one compaction rate for different target P (series A-4) 123
5.13 Relaxation of single layer plain woven textiles subjected to the same compaction rate, for different target P (series A-4) 123
5.14 Compaction and load removal of single layer plain woven textile (series A-5) 124
5.15 Topography of textile surface: a) before compaction, b) after 100 cycles of compaction and load removal 126
5.16 Compaction of a virtual single layer plain woven textile using different iteration numbers, and experimental trial (series B-1 vs. A-1) 128
5.17 Compaction and relaxation of virtual single layer plain woven textile (series B-1.2) 129
5.18 Compaction and relaxation of virtual single layer plain woven textile (series B-2.5) 130
5.19 Relaxation of virtual single layer plain woven textile from various onset pressure P (series B-1.1) 130
5.20 Compaction and relaxation of virtual single layer plain woven textiles subjected to different number of iterations with the same target P=0.5 MPa (series B-3) 131
5.21 Relaxation of virtual single layer plain woven textiles subjected to different numbers of iterations (series B-3) 132
5.22 v_f as a function of the number of iterations for virtual single layer plain woven textiles subjected to different iteration number for target P=0.5 MPa (series B-3) 133
5.23 Compaction and relaxation of virtual single layer plain woven textile subjected to different iteration numbers for target v_f=0.5 (series B-4) 134

5.24 Relaxation of virtual single layer plain woven textiles for various numbers of iterations and target v_f (series B-4) 135

5.25 v_f as a function of number of iterations for virtual single layer plain woven textiles subjected to different iteration number for target v_f (series B-4) . 135

5.26 Compaction and load removal of virtual single layer plain woven textile (series B-5) 136

5.27 P as a function of v_f in a double-layer aligned and staggered plain woven textile in compaction phase 137

5.28 Geometric representation of compaction and relaxation of virtual double-layer plain woven textiles subjected to different layering for target P=0.5 MPa (series B-6) 138

5.29 Compaction and relaxation of virtual double layer plain woven textiles subjected to different stacking for target P=0.5 MPa (series B-6) 139

6.1 Textiles: a) undeformed, b) after in-plane shear 142

6.2 Simulation of 16 crossovers of plane woven textile undergoing in-plane shear in articulated frame configuration 151

6.3 Distance and angle between neighbouring particles within a fibre, enabling calculation of axial and bending strain energy terms 153

6.4 Schematic representation of fibres and their deflection in Gutowski's compaction model 154

6.5 Imposed displacements applied to: a) boundary particles, b) all particles 156

6.6 Shear angle and shear forces 157

6.7 Four different boundary conditions: a) fixed segments, b) fixed pivots, c) pivots unlimited in edge plane, d) pivots limited in edge plane 158

6.8 Simulation of unit cell with fixed pivots boundary condition; top view unit cell on shear, 3D view and problematic zones 159

6.9 Simulation of unit cell with pivots unlimited in edge plane boundary condition; top view unit cell on shear, 3D view and problematic zones . . . 160

6.10 Initial and deformed configurations of articulated frame 162

6.11 Force F as function of shear angle α from experimental trials 163

6.12 Nylon 6/6 textile sample undergoing in-plane shear test in articulated frame 164

6.13 Normalized shear force F_N as a function of shear angle α obtained from experimental trials 164

6.14 Larger and smaller domains used towards virtual in-plane shear simulations 1A and 1B 166

6.15 Normalized shear force F_N as function of shear angle α for simulations 1A and 1B and experimental trials 167

6.16 Effect of initial fibre tension on in-plane shear simulation results for simulations 2A, 2B and 2C, compared with experimental results 168

6.17 Effect of friction parameter FP on in-plane shear simulation results for simulations 3A, 3B and 3C 169

6.18 Effect of bending stiffness parameter BP on in-plane shear simulation results for simulations 4A, 4B and 4C 170

6.19 Parameters quantifying the cross-section of a unit cell in sheared fixture . 172

6.20 Yarn centre spacing as a function of shear angle α, for simulations 1A and 1B 174

6.21 Textile thickness and yarn centre spacing as a function of shear angle α, for simulation 1B 174

6.22 Yarn centre spacing and inter-yarn gaps as a function of shear angle α, for simulation 1B 175
6.23 Yarn centre spacing and yarn gaps of plane AA and BB for simulation 1B 176
6.24 Yarn width and thickness as a function of shear angle α on in-plane shear for simulation 1B 176

7.1 Schematic for two scenarios 185
7.2 Selected deformation states in simulations of bending for: a) a single unit cell, b) plain woven textile 188
7.3 T-section profile undergoing concurrent bending and compaction 189
7.4 Process of punching through a virtual textile 190
7.5 Punching performed for different cases of compacted and sheared single layers, and a double-layer textile 190
7.6 Punching virtual textile at 90° and 60° from its plane 191

A.1 Flow chart of particle-based modelling method 215

Chapter 1

Introduction

1.1 Composite materials

Composites are engineered materials made of two or more constituent materials that, once combined, offer specific advantages when compared with the constituent materials taken separately. Each constituent of a composite material has its own physical properties; once constituent materials are combined these properties can be used towards an intended purpose. One of the most widespread group of composite materials, fibre-reinforced polymer-matrix composite (PMCs), comprises materials made of stiff and strong fibres selected for their structural potential and combined with a polymer matrix that gives parts their shape.

Fibre-reinforced PMCs have found numerous applications because of their superior specific structural properties. They are lightweight and are easily put into shape compared to most conventional structural materials. Fibre-reinforced PMCs are also relatively inexpensive to produce, especially in limited series given generally low equipment costs [17, 120].

PMC parts are made using a number of PMC manufacturing processes. Resin transfer moulding (RTM) and vacuum-assisted resin transfer moulding (VARTM) are two commonly used PMC manufacturing processes, where a curable polymeric resin is injected through a shaped textile reinforcement called preform, itself previously loaded in a mould. In these processes the dry textile preform is generally laid in a rigid lower part mould. Unless this lower part mould is flat, shaping the preform to the mould generally involves imparting large in-plane shear strains to the preform [93]. The upper mould part is rigid in RTM, and it consists of a sealed flexible bag in VARTM. In RTM the resin is pumped into the cavity under positive pressure. In VARTM vacuum is applied to the mould cavity from vent ports so that resin is drawn into the preform. In both cases, mechanical pressure from the mould (RTM) or vacuum (VARTM) drawn on the resin compacts the preform along the normal to its plane. Once the preform is saturated with infused resin the inlets are closed and the resin is allowed to polymerize, or cure.

The shaping operation, compaction pressure and resin pressure inside RTM and VARTM moulds affect the configuration of yarns in the preform. The preforming and composite manufacturing processes result in in-plane shear and compaction of the preform, imparting both elastic and permanent deformations as well as flattening of yarns in textile unit cells; it also results in the nesting and inter-layer packing of textile layers. Therefore, actual preform geometry at the level of the yarns and textile unit cells is complex.

PMC manufacturing processes and PMC part performance need to be engineered, ideally through simulation, and therefore diverse properties of the preforms and PMC material must be available for predictive simulation. Some of these properties are strongly influenced by yarn configuration, hence the latter should be known; knowing the detailed geometry of preforms is essential to predicting the processing and performance of preforms and PMC parts. Preform and PMC material properties should be derived by simulation, and software tools for doing this should be available for the numerous types of textile reinforcements that are available or that could be produced. However, for such tools to be effective the geometry of the textile reinforcements must be defined very well.

The most common PMC reinforcements are made of carbon, glass or aramid fibres, combined into yarns featuring a few hundred to a few thousand fibres, and then into textiles of various types, including randomly oriented short or long fibre mats, 2D and 2.5D weaves, 2D biaxial or triaxial tubular braids, weft knits, warp knits, non-crimp 2D or 2.5D fibre reinforcements assembled by knitting or stitching, 3D braids and 3D weaves. The geometry and arrangement of yarns in a textile preform play a major role during PMC manufacturing and in determining the properties of PMC parts.

Prior to PMC manufacturing, fibres and textiles undergo shaping and forming resulting in a shaped preform. During the manufacturing of PMC parts the geometry of the preform is altered due to normal compaction pressure, in-plane shear and other types of loads applied as part of the PMC manufacturing process. Prediction of these changes to the geometry prior and during the manufacturing of PMC parts is a critical task in terms of predicting the processing and performance properties of the PMC part.

1.2 Geometry of preforms

The characterization of preform geometry can be studied at three different scales: a) the macroscopic scale of a full preform; b) the mesoscopic scale, approximately 1 mm to 1 cm sized, which is the scale of yarn sections and repeating unit cells (RUC); c) the microscopic scale, approximately 10 μm to 100 μm, which is scale of a fibre diameter [113], Figure 1.1.

Textile reinforcements can be grouped into three major categories known as 2D, 2.5D and 3D textiles. 2D textiles are most commonly supplied as rolled stock, with individual

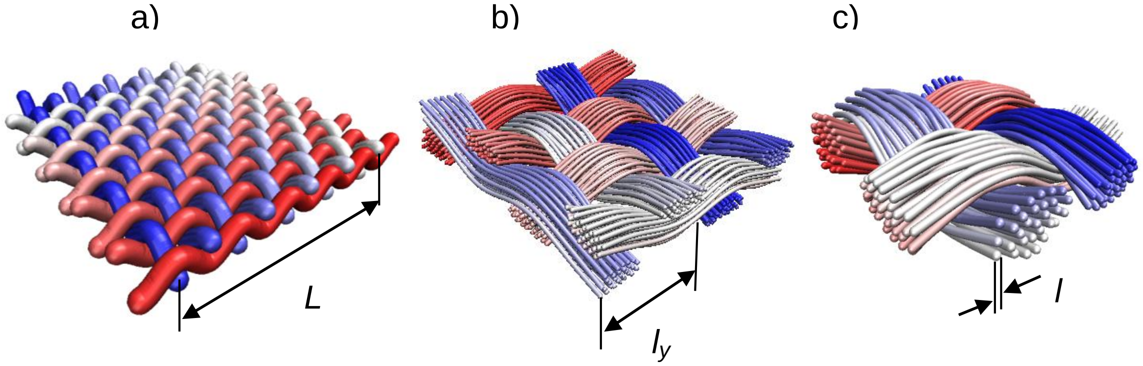

Figure 1.1: Different scale in textiles: a)macroscopic scale; b)mesoscopic scale; c)microscopic scale

layers having low thickness and typical surface densities ranging in the few hundred g/m^2. 2.5D textiles are generally similar to 2D textiles in terms of topology and interlacing, and they feature very few or no yarns extending along the normal z direction; they are essentially thicker, multilayer 2D textiles. 2.5D textiles might contain short fibres in the third dimension, which act as a toughening system in the inter-laminar zones of the PMC material. Finally, 3D textiles are thick fabrics that feature extensive yarn interlacing through the thickness.

The arrangement of yarns at the mesoscopic scale is known as the textile architecture. In a context of modelling of the geometry of preforms, at this scale yarns may be represented as homogeneous smooth strands interlocked in different arrangements, Figure 1.2.

2D woven fabrics are amongst the most broadly used textiles in PMC production. Yarns are typically laid along the warp (0°) and weft (90°) directions and interlace following different patterns. On the other hand, non-woven fabrics are typically made of light yarns that extend randomly in all in-plane orientations and are kept together by small amounts of adhesives called binders. 2D and 3D braiding are suitable ways of producing preforms for rods, cylinders and beams. Basic braided preforms are produced by intertwining three or more yarns in a diagonally overlapping pattern around a mandrel [86]. Stitching is a fast preform preparation process in which yarns are laid along selected in-plane directions and a stitching needle is penetrated between them to attach the yarns together along predefined patterns. Warp and weft knitting are processes where sets of yarns are arranged with predetermined spacing on a base plate, then a line of yarn is looped back and forth along the machine direction or width-wise through the yarn arrays [94]. In the scope of this thesis, plain woven 2D textiles will be explored.

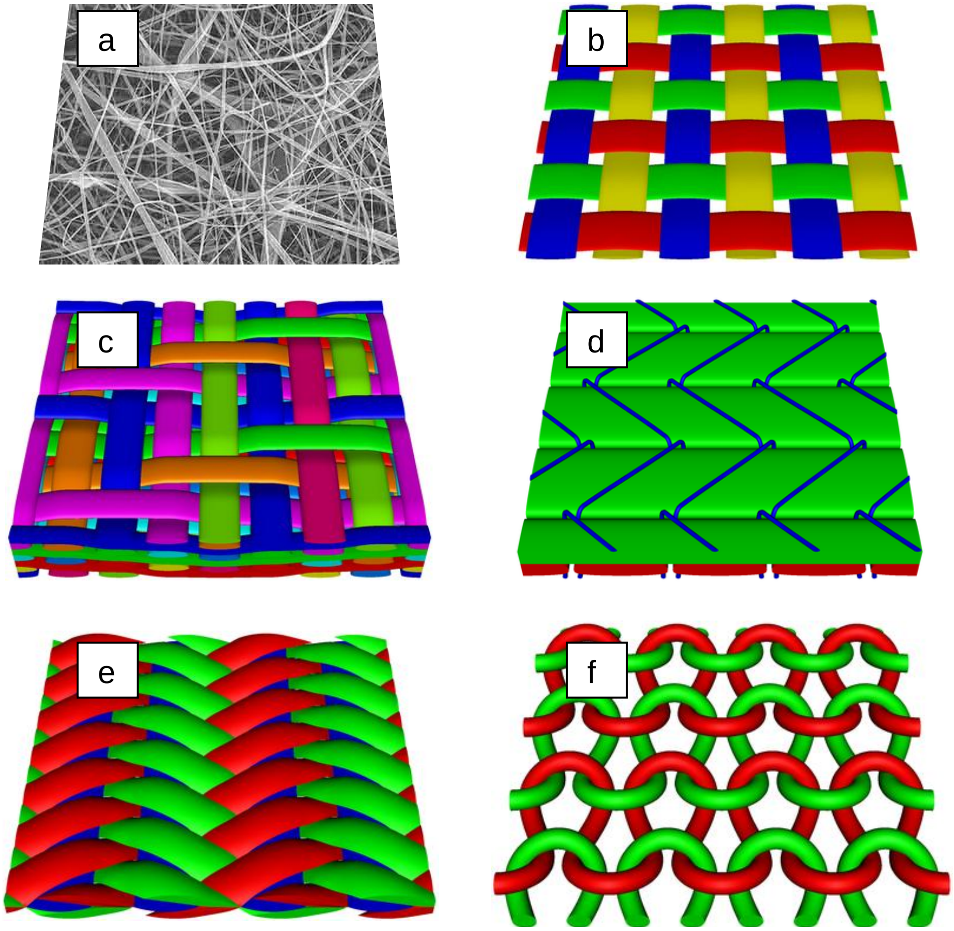

Figure 1.2: Textile architectures for composite reinforcements: a) non-woven, b) 2D plain weave, c) 3D weave, d) non-crimp stitched, e) braid, f) weft knit [111]

1.3 Geometric and mechanical modelling of textiles and textile reinforcements

Different mathematical and software models were created for modelling, simulating and predicting various aspects of the geometry of specific textile reinforcements during PMC manufacturing, with a given method typically applying at a given scale. Geometric models are needed if one is to obtain engineering properties for a textile reinforcement, leading to reliable and repeatable PMC processes. However, the complexity of textile architectures makes it difficult to predict the geometry of textile reinforcements at the mesoscopic scale accurately. Microscopic and mesoscopic scale geometries are important for PMC manufacturing processes because of their effect on compaction, permeability and void formation, for example. All this makes productive engineering of manufacturing processes for textiles and PMCs a significant challenge given the large array of textile reinforcements that are available and/or possible. This challenge is addressed in this thesis.

To model the constitutive behaviour of textile reinforcements, geometric models are essential; while these two aspects are mostly discussed and demonstrated separately in the literature they are closely intertwined, and any change in one will affect the other. Therefore, in the study of complex textiles both aspects should be considered indistinguishable. Any geometric modeller distinct from analytical methods enabling the analysis of the constitutive behaviour, will produce simplified or generic shapes for forwarding towards other software for downstream investigations and prediction of processing and performance properties. In recent years some researchers [6, 13, 14, 22, 42, 64, 66, 67] have tried to bring these two aspects of geometric modelling and mechanical modelling in the same context, either by feeding geometric models to FEA software in a loop or through simple cases of parallel geometric and mechanical modelling procedures. Due to the complexity of textile and reinforcement geometry and mechanical behaviour, there is a need for a better modelling approach that considers the geometric problem and the mechanical behaviour of textile and reinforcements in a unified approach. This may be achieved by using particle-based modelling methods for obtaining the geometry and the constitutive behaviour of textiles and textile reinforcements used in composites, concurrently.

1.4 Contribution of the thesis

In academia as well as in industry there is a need for a realistic, unified geometric and mechanical modelling method for technical textiles and textile reinforcement used in PMC parts and structures. The particle-based modelling method was developed and validated for representing the geometry of technical textiles at the microscopic and mesoscopic scales undergoing different loading conditions. By using the Metropolis, fibre configurations and their constitutive behaviour within a fibre network could be presented algorithm from first principles.

A multi-module software based on the proposed particle-based modelling method was developed for the simulation of compaction, relaxation and in-plane shear of textiles. Results were validated experimentally throughout the thesis for all loading cases. An extension algorithm was introduced for enabling the particle based modelling method to be used for technical textiles containing yarns featuring high numbers of fibres. Initial work towards the modelling of manufacturing processes for technical textiles was introduced pointing at future developments.

1.5 Thesis overview

Each chapter investigates different issues pertaining to textile reinforcements modelled using the proposed particle-based modelling method. Literature reviews relevant to each subject were included in each chapter.

Chapter 2 provides a comprehensive literature review covering various geometric modelling methods. It describes some software packages used for modelling the geometry of textiles, applicable to the manufacturing of technical textiles. Later in this chapter the algorithm developed herein for modelling the geometry of textile reinforcements subjected to loading using particle-based modelling is described. Details of the method and energy terms defined at the microscopic scale are explained. Fibres are modelled as a series of conjoined particles, and their configurations are determined mechanistically using a modified Metropolis algorithm and inter-particle strain energy terms. Energy terms within a fibre and among different fibres in a yarn are described. Modules utilized in software development are explored and a procedure for reaching equilibrium in the system is discussed. The method enables intricate geometric modelling of textiles at the microscopic, mesoscopic and macroscopic scales.

Chapter 3 features a literature survey on relations between the geometric configuration of textile reinforcements and their properties. This chapter presents predictive simulations of the in-plane permeability of dry reinforcements, through-thickness thermal conductivity of composite and in-plane moduli of composites made from unidirectional and bidirectional warp-knitted carbon fibre textile reinforcements. The large array of simulation results obtained for different reinforcement configurations is validated by experimental results. The chapter demonstrates that processing and performance properties are affected by reinforcement configuration; the effects are identified and quantified through systematic variation of the geometric parameters that define the textile configurations. This chapter highlights the different amplitudes of the effects of geometry on processing and performance properties of both the dry textiles and the composites.

Chapter 4 introduces particle-based modelling for the constitutive behaviour of fibre yarns and woven textiles subjected to compaction loading. In a preamble to this chapter, a literature review on known compaction models is presented. Following this, the chapter describes the method where discrete particle mechanics is used as an alternative to traditional continuum mechanics. The method enables extensive modelling of the textiles from first principles, as they are loaded in compaction upon manufacturing. Different simulation cases for the compaction behaviour are presented. Results are validated by experiments, which showed excellent agreement.

Chapter 5 features a study of the relaxation of textile reinforcements during and after compaction. Different scenarios are examined and presented. Simulation results are compared with experimental results, with trends presented in the literature. This chapter demonstrates the capability of the particle-based approach towards replicating the time-dependent relaxation and reconfiguration of woven textiles subjected to compaction loading. The capability, which is demonstrated for single and double layers of plain woven textiles, models the compaction and the relaxation seamlessly in the same simulations. The relaxation behaviour of textiles is characterized through a series of simulations characterized by different compaction rates to set target fibre volume fractions (v_f) and pressures (P). A relation between the number of iterations, compaction rate and lapsing time is drawn. The particle-based modelling method and the simulation results presented in this chapter predict the actual behaviour of a single layer of textile undergoing stress relaxation after different compaction rates. The 3D surface geometry of a plain weave textile was constructed and compared before and after compaction for evidence of reorganization of fibres and occurrence of relaxation in the textile.

Chapter 6 investigates the geometry and constitutive behaviour of textiles subjected to in-plane shear loading using the same particle-based modelling method. In this chapter, the in-plane shear behaviour of textile reinforcements is discussed with respect to shear angle and locking. In order to characterize the in-plane shear behaviour of woven textiles, a series of simulations replicating articulated frame in-plane shear tests was performed. The effects of different boundary conditions at fibre ends upon application of a displacement field to the particles, and iterations of the positions towards lower strain energy levels, are reported. From these simulations, load-displacement curves were constructed; furthermore displacement fields, locking angles and shear stresses are identified. Results were validated using experimental data; results of simulations and experiments show good agreement as an well as improvement in simulation accuracy over other modelling techniques.

Chapter 7 discusses applications of the particle-based modelling method to carbon fibre fabrics through the description of an expansion algorithm (EA) used in modelling textiles made of yarns featuring very large numbers of fibres. Furthermore, ongoing modelling developments are presented towards more advanced manufacturing processes involving technical textiles, namely textile bending, punching and stitching. The chapter concludes with a discussion, conclusions and recommendations for future work.

Chapter 2

Geometric Modelling Methodology

2.1 Introduction

Geometric models of technical textiles and reinforcements are required as a starting point for the thorough understanding and modelling of their mechanical behaviour during PMC manufacturing, either in their initial dry state or as impregnated materials. Such geometric models would ultimately be used for modelling all steps of manufacturing processes for composites or other materials based on technical textiles.

This chapter discusses existing geometric models and computational software programs that are well recognized in the field. Most of these models feature or lead to generic geometries, and so are restricted in terms of modelling accurately the constitutive behaviour and/or features such as the nesting of textiles layers, for example. In this thesis, such restrictions are lifted through the proposed new particle-based modelling approach. Therefore this chapter also provides an extensive presentation of geometric modelling of textiles using particle-based methods. The algorithm developed in the context of this thesis is explained in depth, and it also covers all modules used towards particle-based modelling of the geometry and mechanical properties of technical textiles.

2.2 Literature review

2.2.1 Basic analytical models of textile unit cells

Predictive engineering of textile-based PMC manufacturing processes and part performance requires that a large array of diverse physical properties of preforms and parts be identified. Different technical textiles undergoing mechanical loading during manufacturing process, say either of preforms or PMC parts, perform differently. Different properties pertaining to constitutive behaviour, heat transfer, permeability to gases and fluids, and other physical phenomena depend on the geometry and architecture of the textile, and therefore the geometry and yarn configurations in textiles and preforms must be known with sufficient accuracy [18]. In discussing the constitutive behaviour, performance and other properties of technical textiles, one should be aware that engineering PMCs involves the selection and/or the design of textile reinforcements, from a very wide array of possible fibres, yarns, textile structures, and so forth.

One of the first highly idealized geometric models of a unit cell of plain weave fabric was presented by Peirce [82]. His study aimed at facilitating general comparisons between the geometry of various fabrics, and at expressing experimental results through specifically adapted geometrical models. Peirce's model features yarns with circular and incompressible cross-sections. Yarn paths are represented as circular arcs at crossover points connected by straight line segments as shown in Figure 2.1-a. Peirce successfully represented very basic compaction behaviour of textile using this proposed geometric model.

Kemp [52] modified Peirce's model, describing yarns with either elliptical or racetrack cross-sections, and modified the yarn paths accordingly. In doing this, Kemp achieved somewhat more realistic representations of the geometry than Peirce for the woven textile that he had selected, Figure 2.1-b. Lin and Newton [63] used a method where yarn paths were generated using cubic B-splines, with the same cross-section as used in Peirce's work. Control points were inserted at crossover and midpoint positions for changing the yarn paths. A drawback of this method is the need for manual modification of control point positions.

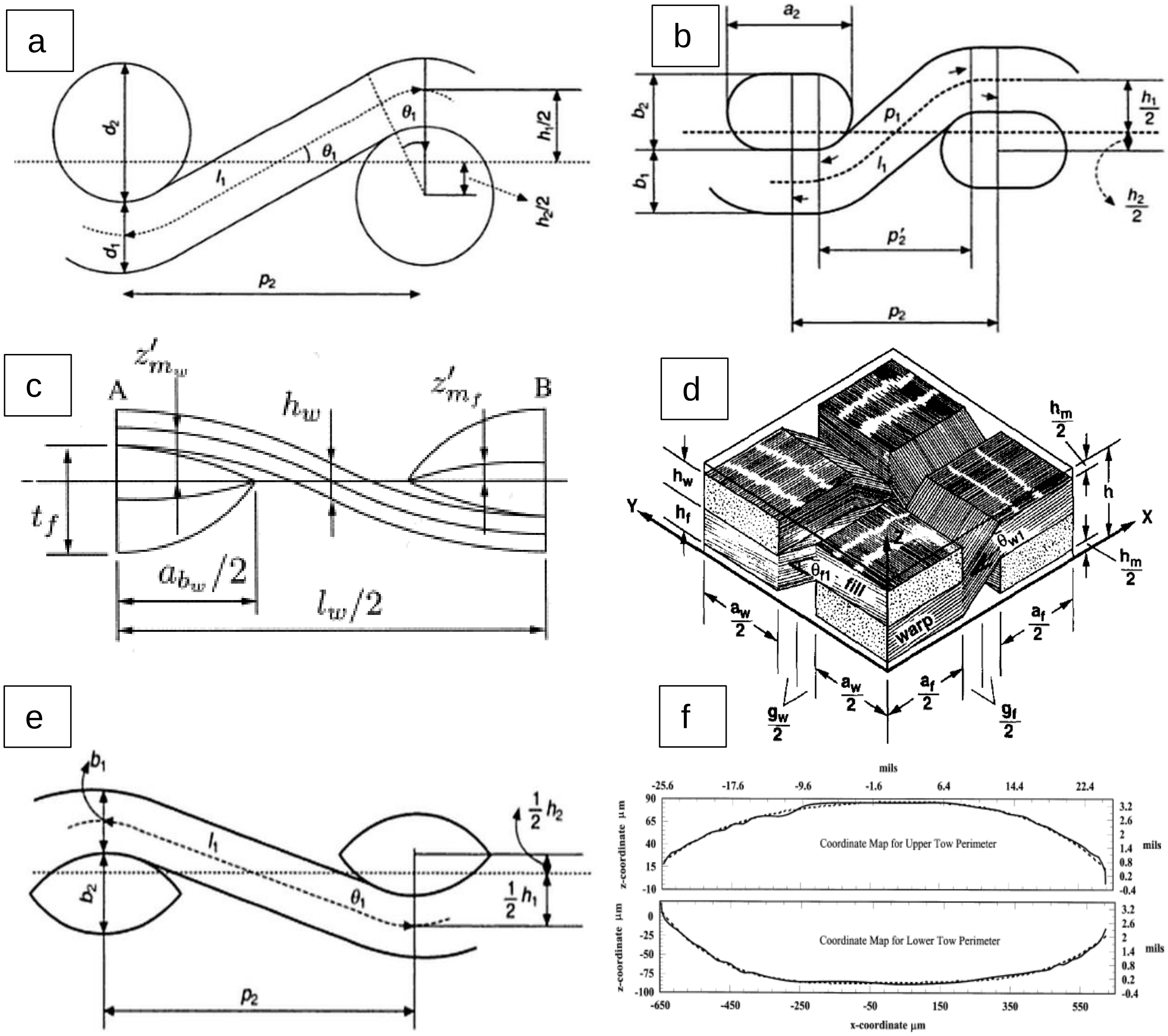

Figure 2.1: Evolution of unit cell geometry modelling: a) Peirce [82], b) Kemp [52], c) Hofstee [45] d) Ning and Chou [77], e) Hearle [109], f) Searles [108]

Hofstee [45] presented a geometric model of woven unit cells featuring yarns of variable cross-sections. Every yarn is described by three sets of parameters: in-plane centreline path, doubly curved horizontal mid-plane and thickness distribution of the cross-sections. This method enables straightforward determination of individual fibre paths, yarn shape and unit cell shape. Largely deformed yarns cannot be modelled by this method because of the assumptions considered. It has been assumed that fibre packing within yarns is constant.

Ning and Chou [77] developed a highly idealized unit cell model for predicting the in-plane effective thermal conductivity of plain weave textile as seen in Figure 2.1-d. Despite the relative crudeness of the model in terms of geometry, good agreement between predictions of thermal conductivity based on it and experimental results were obtained. It is known that the thermal conductivity is relatively insensitive to the geometry of the unit cell [77] and as discussed in this thesis. Therefore, in this case an accurate representation of the geometry is not as critical as it may be to predict say the permeability, for example.

Shanahan and Hearle [109] presented a geometric model for woven textile unit cells using lenticular yarn cross-section shape, and they introduced calculation of the constitutive behaviour of fabrics using energy methods, Figure 2.1-e. This geometric model attempted to avoid short-comings of the racetrack geometric model. The geometry is a modification from that used in Peirce's model [82]. Yarn cross-sections are flattened resulting in a more credible behaviour due to interactions between yarn bending and yarn flattening.

Another representation of yarn cross-sections and paths was proposed by Searles [108]. Functions representing the upper and lower halves of yarn cross-sections relatively to centroid line position were introduced; B-splines and polynomial functions were used, determined by adjusting the models to SEM micrograph of 8 harness satin woven samples,

Figure 2.1-f. However, the horizontal edges of the cross-sections did not correspond well with the geometry, when compared with microscopic observations.

Even though these models were meant to approximate real reinforcements, the geometries are overly simplified for any detailed representation of yarns and textiles at the mesoscopic and microscopic scales. These geometric models are generic; they can only ever represent woven textiles, and in most cases only a single layer with yarns at 90° from one another; yarn sections are mostly constant and yarn paths are over-simplified; even with a high v_f in yarns, large void pockets are seen between the yarns and layers. Due to the generic nature of these geometric models, low v_f is expected in the textiles represented, whether it is single layers and/or stacks of textile layers. The models have no ability to deform say during preforming, no ability for nesting or yarn spreading, so it is doubtful that meaningful prediction of physical properties of technical textiles or PMCs based on these models can be satisfactory.

2.2.2 Textile geometric modelling software packages

More recently, different commercial and open source software packages were developed for modelling the geometry of textile reinforcements at the mesoscopic scale. The main goal of these software packages is to enable the modelling of different textile architectures using the same tools and formalism, hence to lift the restriction to weaves associated with the simple models described above. These software packages were aimed either at providing a visual representation of unit cells, or as preprocessors whereby the unit cell models may be used downstream for calculating textile and/or PMC processing and performance properties linked with textile mechanics, permeability and PMC mechanical behaviour, for example. The software packages discussed here are TexGen [112], TechText CAD [44], Technical Weaver [61] and WiseTex [68].

TexGen [112] was developed at the University of Nottingham, aiming at modelling the geometry of virtually any textile structure. It is distributed freely under a general public license (GPL). TexGen acts as a generic geometric modeller and as a pre-processor towards physical models for textile mechanics, permeability, mechanics of composite and others. TexGen includes some key features such as interference detection and correction, export under several graphic data formats and automated specification of yarn orientations. After a model is created it can be exported and meshed using third party software. Virtually any textile can be represented and libraries are available for common textile types. Figure 2.2 shows a plain weave unit cell generated by the author using TexGen. In TexGen, yarn paths are represented using either Bezier or cubic interpolations. Different variable yarn cross-sections can be specified manually. Yarns are treated as solid volumes; therefore no specific modelling at the microscopic scale is featured. Again, TexGen is strictly a geometric modeller; the models can be made realistic through dedicated manual work, but their configurations are purely arbitrary.

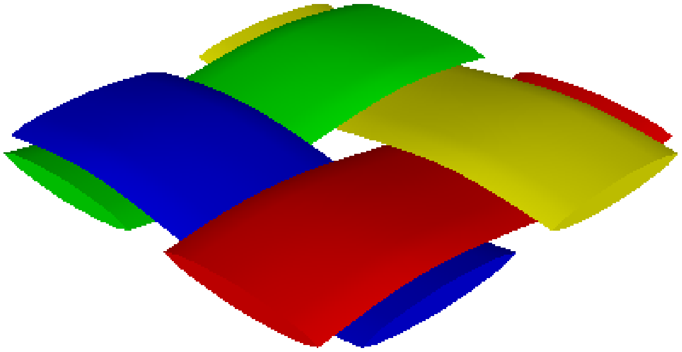

Figure 2.2: Plain weave RUC generated by the author using TexGen [111]

TechText-CAD [44] is used for defining the geometry of weaves and simple weft-knit textiles. Starting from input weave and knit parameters and yarn specification, the geometry of textiles in 3D can be visualized and stress-strain curves of textile reinforcements can be predicted. Yarn break loads, break extensions, polynomial fits for the yarn stress-strain curves, and values for bending stiffness and resistance to flattening are stored in a yarn database. A geometric model of a plain weave textile made by the author using TechText-CAD is shown in Figure 2.3.

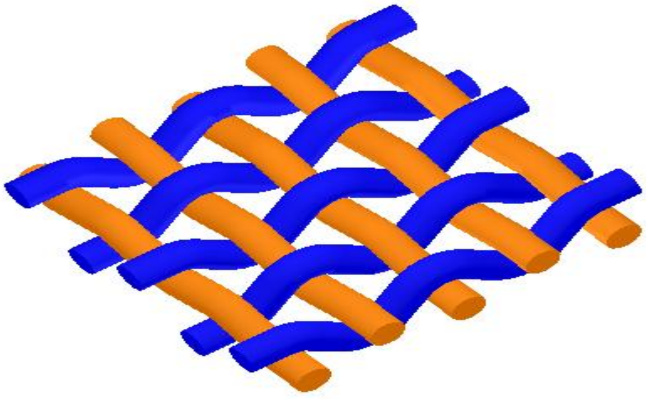

Figure 2.3: Plain weave textile generated by the author using TechText CAD [44]

Another modelling tool for technical textile designers is Technical Weaver by Scot-Weave [61]. The software models the geometry of different woven fabrics at the mesoscopic scale, assisting the production of fabrics for industrial and commercial uses. Yarns can be given different colours to create various visual effects for use in furniture, car interiors, etc. With Technical Weaver, any number of warps and wefts are allowed. Different yarn cross-section shapes can be created and individual yarn parameters, including weight and density, can be stored. The software allows fast checking of the overall structure of a 3D woven textile and of individual areas of interest. Again, textile models created in this software packages are generic; the geometric models can be made close to the geometry of real reinforcements with a fair amount of dedicated effort, but geometries are not determined from first principles.

WiseTex [68] was developed under the leadership of S. Lomov at Katholieke Universiteit Leuven. Contrary to the other software packages discussed above, unit cell models created in WiseTex can be generic but they can be also approximated from first principle in some cases. In the latter case the simulation algorithm uses a finite element formulation of the minimum energy principle, calculating equilibrium in zones of yarn interactions. The mechanical properties of yarns are compared with measurements made using the Kawabata KES-F system [50]. Feasible models cover a wide range of textile structures, either in their relaxed state or after having undergone compaction, in-plain shear or tensile deformations. However, not all structures can be simulated using the FE formulation. Figure 2.4 shows a geometric model made by the author using WiseTex.

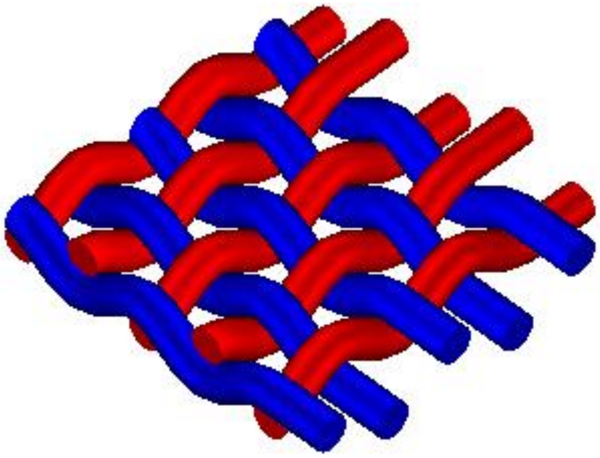

Figure 2.4: Plain weave textile generated by the author using WiseTex [68]

WiseTex supports computations for complex textile structures within a relatively short time for providing the behaviour of these textiles in compression and bending. This textile geometrical modeller also serves as a base for mesoscale mechanical and permeability models for PMC processing and performance prediction: geometrical models can be fed into third party modelling software to enable computation of local permeability and mechanical properties of the deformed reinforcement, for example. WiseTex offers significant advances over the software packages mentioned above, as it does predict deformed textile geometry from first principles in some cases. However, the FE formulation is only applicable to textiles of simple geometry, and it does not handle large strains perfectly well. It also involves some limitations in the management of contact between yarns.

2.2.3 Recent textile geometric models

The above models can not generate descriptions of deformed textile reinforcement structures subjected to general loading cases, nor can they represent the more complex or realistic cases, such as higher numbers of layers for example, adequately; they can not model nesting or other such phenomena associated with such complex textile structures. Hence they can not be used readily in describing and investigating localized phenomena related to compaction or other aspects of forming. Also, whilst some of these models offer interesting insight into the behaviour of fibre contacts in homogeneous assemblies of fibres subjected to loading scenarios such as compaction or in-plane shear, they are not yet sufficiently advanced to model the constitutive behaviour of complex, industrial reinforcements and preforms. Furthermore, the mathematical complexity of the tools used for specifying the geometry makes them largely unsuitable for simple usage. No published compaction, relaxation or in-plane shear models can describe the observed behaviour of the textile reinforcements fully.

To better resolve the geometry and constitutive behaviour of textile reinforcements, Wang and Sun [127] recently proposed the digital element concept to simulate the evolution of yarn geometry during preform or PMC manufacturing processes, Figure 2.5. Rigid rod elements connected with frictionless joints represent yarns in a unit cell. Yarn paths in simple twists and in a 3D braided fabric were simulated by the authors. Zhou et al. [134] adopted a procedure comparable to finite element analysis in their digital elements concept. This concept was labelled as multi-chain digital element analysis, and two numerical examples were presented in their work. The displacements of fibres inside a fabric are derived from a global stiffness matrix and boundary conditions. Yarn paths are defined by the positions of joints. This approach is limited by the amount of fibres that can be simulated due to computational limitations. Some examples presented in the author's work used 19 fibres for each yarn. Sun and Sun [118] also used a digital element approach for investigating the micro-structure of a 3D braided rectangular preform. In the author's work topological models for yarn interactions and cross-section deformations were compared with the digital element approach.

Figure 2.5: Digital element simulation: a) fibre representation b) yarn representation with 19 fibres [118]

Miao et al. [74] stated that full scale geometrical modelling of a textile structure based on digital element analysis would consume huge computational resources. Two algorithms were presented to overcome the problem of computational limitations. A new formulation for contact between elements was developed, which is similar to the contact elements used in ANSYS®. Also, in modelling fibre-to-fibre contact the authors used node-to-element lengths instead of node-to-node distances, multiplying computational times by 10 times. Due to this the authors were forced to use smaller numbers of digital chains in analysing yarn cross-sections, Figure 2.6.

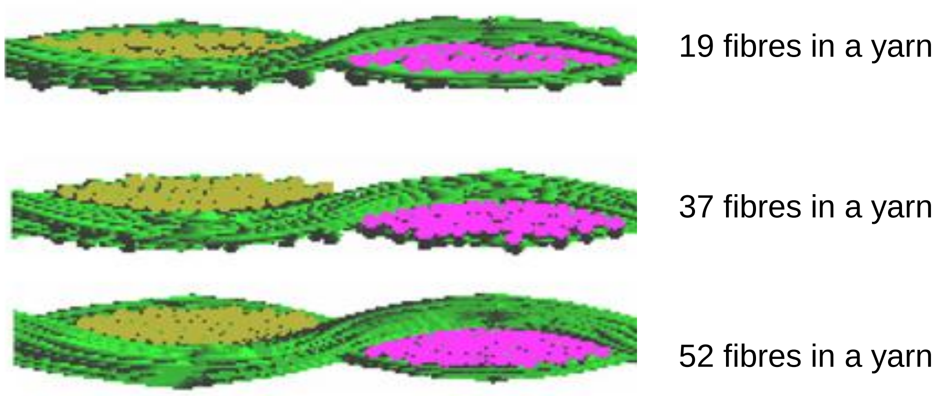

19 fibres in a yarn

37 fibres in a yarn

52 fibres in a yarn

Figure 2.6: Geometrical modelling of a textile with digital elements containing different number of fibres within yarns [118]

2.3 Modelling method

The particle-based modelling method presented in this thesis is used for predicting the geometry and large strain constitutive behaviour of textile reinforcements, say during preform and PMC manufacturing, at the microscopic and mesoscopic scales. This modelling method aims at presenting a different approach from traditional techniques such as the finite elements method, analytical methods or empirical methods, offering more extensive, intricate and accurate representations especially under large strains, as well as the ability to model the response to various load cases and represent time-dependent behaviour such as relaxation. Most tools implemented in existing software packages are used for geometrical modelling of unit cells at the mesoscopic and macroscopic scales; geometries are primarily generic, or defined from first principles in very few cases. Some attempts at modelling at the microscopic scale were also made, primarily for visualization purposes [25].

The particle-based modelling method proposed here is used for modelling fibres at the microscopic scale, leading to unit cell modelling at the mesoscopic scale. A series of particles is used for representing fibres within a fibre assembly; fibre assemblies can be yarns and/or unit cells. These particles are interconnected through various functions that represent elements of the physical behaviour of the fibres. Specifically, these functions represent diverse strain energy terms as well as other fibre-to-fibre interactions in the assembly. During simulation, particles are moved randomly until a stable state of minimum strain energy in the system is reached; as particles move, the configuration of fibres in the assembly changes. Then, once iterations are completed, boundary conditions are altered corresponding to strain imposed on the RUC, and the system is iterated again towards a new state of minimum strain energy.

The Metropolis algorithm of the Monte Carlo method was adopted for use in this specific implementation of the particle-based modelling method [73]. The particle-based modelling method relies on a statistical approach implemented in computational algorithms. The particle-based modelling method was written in C++ programming language, with different modules wrapped onto one core program. The particle-based modelling method implementation structure was designed so that different software modules may be modified and developed separately. Various algorithms were developed by the author to reduce computational time and increase correspondence with realistic geometries.

In addition to geometric modelling, the particle-based modelling method enables the prediction of major elements of the constitutive behaviour of textile reinforcements. In fact, prediction of the constitutive behaviour is integral to the prediction of the mesoscale geometry. In the method implemented, the strain energy is reduced towards a state of equilibrium, within an assigned computational time through a number of iterations. Then, the boundary conditions are changed in accordance with a given deformation and the system is left to re-equilibrate. Compaction, relaxation and shear of textile reinforcements are some elements of the constitutive behaviour that can be predicted using the particle-based modelling method, and so this is done as part of this thesis work.

2.3.1 Particle interactions

The foundation of the particle-based modelling method lies in the reduction of strain energy in fibres, defined from particle positions over for the whole textile reinforcement. The different terms used for calculating interactions between the particles are split in two groups; intra-fibre terms and inter-fibre terms. Some of these terms are conservative strain energies, and other terms include non-conservative friction work spent as the assembly evolves from one configuration to another.

Intra-fibre energy terms include strain energy resulting from tension and compression of fibres along their axial direction, and bending energy stored in fibres. In this work it is reasonably assumed that tension and compression of fibres happen in the linear elastic region, hence the terms are linear elastic strain energies. Inter-fibre energy terms include elastic energy associated with the lateral contact and compaction of yarns and energy lost to fibre-to-fibre friction.

2.3.2 Metropolis algorithm

The Metropolis algorithm is a fundamental scientific computing method which has extensive applications in computational sciences [73]. The algorithm can be applied to discrete data such as the coordinates of particles. In the current application, using the Metropolis algorithm allows textiles to undergo large strains, which are difficult to model using traditional continuum mechanics but can be modelled in a relatively straightforward manner using particles. Therefore, the Metropolis algorithm constitutes a solid foundation for the development of textile geometry modelling based on first principles.

Sampling plays an essential role in Metropolis algorithm. Sampling is defined as selecting units from a population of interest, so that by studying the sample one may generalize results back to the population from which it was chosen [30]. In the particle-based modelling method sampling is done from probability distributions of fibre positions in the 3-dimensional space.

In this implementation, the Metropolis algorithm involves iterations of particle positions summarised into a configuration, which configuration defines the preform geometry at a given stage. Iterations of particles position is done over physical subspace [a, a] with a set limitation on the step size, using a uniformly distributed random walk. The notions and parameters of uniform distribution, step size and random walk are explained below. A major challenge with this computational method is the time required for iterating enough particle positions, in models that feature sufficient numbers of particles to make them appropriately detailed and useful, leading to a configuration of minimum strain energy stored in the system.

Most Metropolis simulation techniques rely on a random number generator which generates values over the range (0, 1) that are statically independent, with a distribution that is uniform over a large period of time. At each step or iteration, the configuration is changed by adding a small random number to the x, y or z coordinate of a randomly chosen particle. This results in a change in strain energy between two given configurations before and after the step. The strain energy for each configuration defines the strength with which it will tend towards equilibrium. After computing the change of energy resulting from the displacement of a single particle, the result is assessed: if the energy of the whole system was reduced by the change in configuration, then this new configuration is accepted and used as a starting state for the next step. If the energy was not reduced, acceptance may still result from statistical arguments based on a predefined probability [74], or alternatively the change is rejected; in the current version of the particle-based modelling method acceptance is based on a Boolean function.

To decrease the computation time needed for assessing changes in system energy a procedure was added to the algorithm. When a random particle is chosen and the position of that particle is changed, only the energy terms that involve that specific particle before and after the change are calculated and compared. During the calculation the energy terms involving other particles are unchanged, hence ignored. This conceptually simple procedure has accelerated the algorithm tremendously. The time required for the system to reach a stable energy level depends on several factors; this time is usually estimated empirically, Appendix A.

2.3.3 Strain energy terms

Interaction forces between particles which produce stresses and strains within the fibres making up a textile, were assessed based on strain energy terms. Strain energy terms defined from particles within a single fibre and labelled as intra-fibre strain energy, as well as and strain energy terms defined from particles belonging to neighbouring fibres within a yarn and labelled as inter-fibre strain energy, are explained in the following sections.

Intra-fibre energy terms

As the fabric is loaded different forces are applied on a single fibre which cause changes in the strain energy stored in this fibre. Two major components of strain energy arise from tension/compression in a fibre, and bending of a fibre. The tensile/compressive axial elastic strain energy is stored as the fibre resists being stretched or compressed axially. In Equation 2.1, L_0 is the distance between 2 particles when no load is applied,

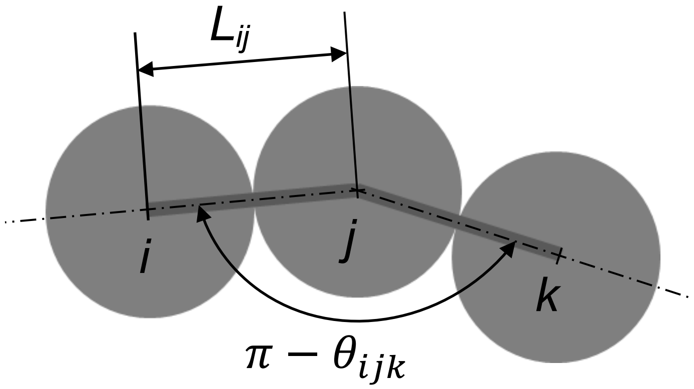

Figure 2.7: Intra-fibre strain energy terms

K_{ij} is the fibre stiffness constant, and L_{ij} the distance between particles i and j under loading, Figure 2.7. The force acting on particle j is equal in magnitude but opposite in direction to the force acting on particle i, and so the strain energy stored in the fibre during tension/compression can be expressed by Equation 2.2:

$$F_{ij} = -K_{ij} \cdot (L_{ij} - L_0) \tag{2.1}$$

$$U_{ij} = -0.5K_{ij} \cdot (L_{ij} - L_0)^2 \tag{2.2}$$

In a fibre, strain energy in tension/compression is related to the fibres Young's modulus E and cross-section area A. Strain energy in a fibre is defined as a function of these parameters in Equation 2.3, where $\mathit{\Delta}$ is the elongation and equal to $L_{ij} - L_0$:

$$U_{ij} = \frac{AE}{2L} \cdot \mathit{\Delta}^2 \tag{2.3}$$

An angle can be defined between two elements sharing a common particle. Such an angle θ_{ijk} is shown in Figure 2.7 for a set of three consecutive particles i, j and k.

Based on the position vectors of the particles $\overrightarrow{r_i}$,$\overrightarrow{r_j}$ and $\overrightarrow{r_k}$, element vectors for the two elements can be defined as $\overrightarrow{r_{ij}} = \overrightarrow{r_i} - \overrightarrow{r_j}$ and $\overrightarrow{r_{kj}} = \overrightarrow{r_k} - \overrightarrow{r_j}$. The strain energy stored in a fibre subjected to pure bending, characterized by Young's modulus E, second moment of inertia I and length L, is defined as follows:

$$U_{ijk} = \frac{EI}{2L} \cdot {\theta_{ijk}}^2 \tag{2.4}$$

where $L = 2 \cdot r_{ij}$ equal to diameter of fibres.

If the fibre is initially defined as wavy as for example in the work of Gutowski [47] a value may be assigned to the initial angle, where the bending energy is zero or minimum.

$$U_{ijk} = \frac{EI}{2L} \cdot (\theta_{ijk} - \theta_0)^2 \tag{2.5}$$

where θ_0 is the initial angle in radian.

Inter-fibre energy terms

Contact forces between fibres within a yarn may be calculated using Hertz' contact model [83], Gutowski's compaction model [99], or a combination of both.

The stresses and strains arising from the contact of two elastic bodies are related to the radii of the curved surfaces and to loads applied, along with the material properties of the contacting bodies. They may be calculated using the Hertzian theory [100]. Figure 2.8 shows two fibres in contact as assemblies of particles. In the most simplified form of Hertz' equation where both bodies are made of the same materials, E^* is the representative modulus of the two contacting bodies with modulus E and Poisson's ratio υ:

$$E^* = \frac{E}{2 \times (1 - \upsilon)^2} \tag{2.6}$$

In the case where fibre radius R is the same for both bodies, R^* is half of R and h_p is penetration distance of the two fibres, then F_H is the force generated between the two contacting fibres required for obtaining penetration distance h_p.

$$F_H = \frac{4}{3} \cdot E^* R^{*0.5} {h_p}^{1.5} \tag{2.7}$$

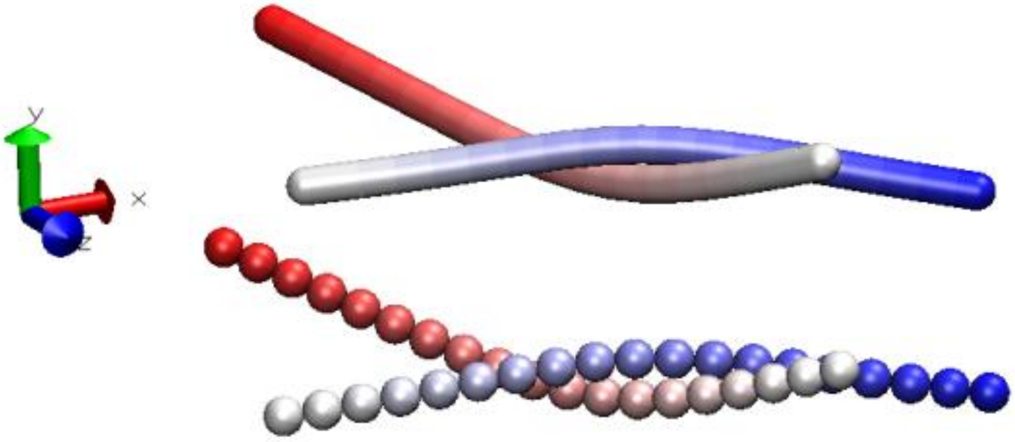

Figure 2.8: Contact between simulated particles of two fibres

Strain energy for the elastic deformation resulting from Hertzian contact can be determined as follow:

$$U_H = \int_0^{h_p} \frac{4}{3} E^* R^{*0.5} {h_p}^{1.5} \cdot dh_p = \frac{8}{15} E^* R^{*0.5} {h_p}^{2.5} \tag{2.8}$$

Gutowski et al. [47] proposed different versions of the equations defining the contact behaviour of fibres within a fibre assembly of textiles. In Gutowski's model the fibres are assumed to show periodic crimp under no force, Figure 2.9; the distance between contacts is proportional to the compacted volume. The equation for beam bending is applied; fibre segments are initially curved and straighten under contact forces, as opposed to localized deformations of the fibre diameter in Hertz' model. Gutowski's model is explained in length in the author's other work [98].

Parameters shown in Figure 2.9 include L, the projected length of a fibre segment; d the fibre diameter, δ the deflection at the centre of the fibre, modulus E, second moment of inertia I and finally C as the vertical distance between the lower and upper points on the fibre centreline. Inter-fibre contact force F is illustrated in the different contact points.

The relation between the vertical deflection δ and the contact force F at the centre of the fibre is:

$$F = \frac{192EI \cdot \delta}{L^3} \tag{2.9}$$

In this version of the model, length L and deflection δ are related to l, l_{min} and l_o which are the actual, minimal and initial heights of a rectangular cuboid encompassing the fibre, with β being a parameter either evaluated by microscopy or fitted to experimental results:

$$\begin{gathered} L = \beta(l - l_{min}) \\ \delta = (l_o - l) \end{gathered} \tag{2.10}$$

The resulting model relating the compaction pressure P_G to v_f is:

$$P_G = \frac{F}{LD} = \frac{3E\pi}{\beta^4} \cdot \frac{[\sqrt{(v_f - v_o)} - 1]}{[\sqrt{(v_a - v_f)} - 1]^4} \tag{2.11}$$

where v_a and v_o represent the initial and maximum values of v_f. From Gutowski's

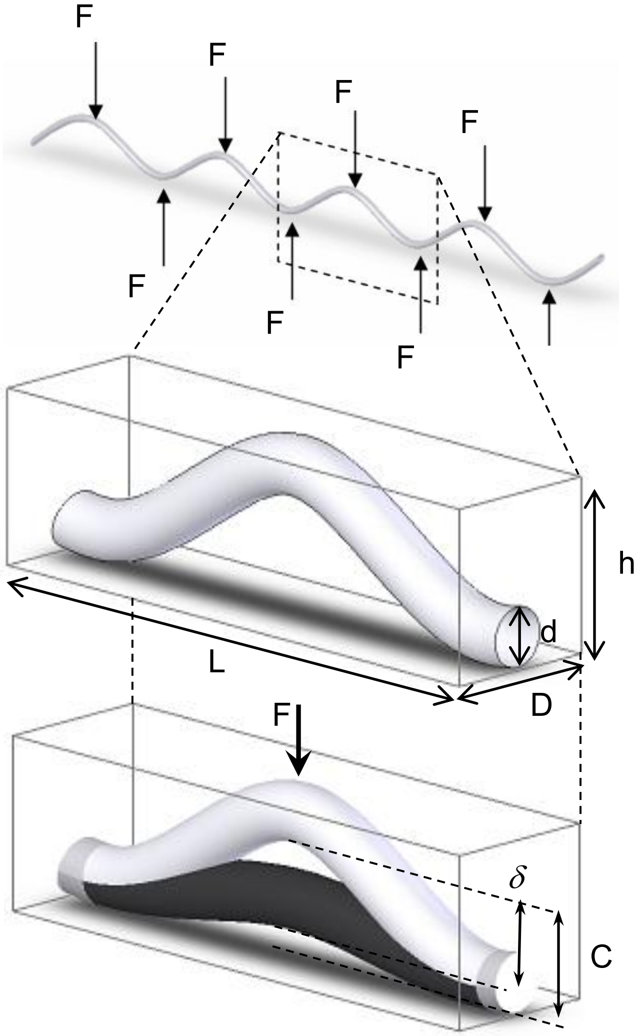

Figure 2.9: Shape and dimensions of fibres in Gutowski's model

model the strain energy is calculated by integrating force over distance for the displaced particle interacting with surrounding fibres:

$$U_G = \int_{l_{min}}^{l_o} F_{ij} \cdot dx = \int_{l_{min}}^{l_o} \frac{192EI}{\beta^3} \cdot \frac{(l_o - l_{ij})}{(l_{ij} - l_{min})^3} \cdot dl_{ij} \tag{2.12}$$

where l_{min} is equal to the fibre diameter. The suitability of jointly using both Hertz' contact model and Gutowski's compaction model for fibre assemblies is validated in Chapter 4.

Friction energy

Other energy terms are present in the system, which must be considered. The presence of friction may keep fibres from slipping relatively to each other; different resins and sizing may affect the slippage of fibres relatively to each other. However, whilst elastic strain energy terms may be calculated for a given static configuration, friction losses only occur as the fibre assembly goes from one configuration to another. Furthermore, friction terms are not conservative. Friction contributes to hysteretic losses observed experimentally in deformed textiles.

In particle-based modelling two methods may be used for managing friction between fibres in a fibre assembly subjected to loads. In a direct method where two fibres are in contact and the coefficient of friction is known, all normal forces are calculated using Hertz' or Gutowski's models. Displacements at contact points after an iteration are also calculated. The total energy loss associated with fibre friction between two configurations is obtained. This energy loss term is added to appropriate strain energy terms defined from the elastic strains previously mentioned. In this approach, the numerous fibre-to-fibre contacts within a textile assembly and the storage of their coordinates and all associated forces require much computationally intensive work. Besides, obtaining a proper value of the coefficient of friction from trials, assuming that use of a single value is acceptable, is not trivial.

Alternatively, an indirect method which was featured here proceeds as follows. Fibre slippage is restricted due to friction, and so additional energy must be expended to obtain configurations corresponding to lower levels of stored strain energy compared to a system devoid of friction. In the absence of friction, a configuration that reduces the elastic strain energy stored in the textile will be accepted as the new configuration on an ongoing basis as contacting fibres slip freely relative to each other. In presence of friction, the same evolution from one configuration to another which corresponds to the same change in elastic strain energy must be combined with a threshold limit due to friction. In this work, the indirect approach was used through a percentage applied on the strain energy in the initial state. As a result, at lower fibre volume fractions when fewer fibre-to-fibre contacts are present, friction generally does not have a major effect. However, with increases in fibre volume fraction and number of contacts, strain energy differences resulting from small displacement have a significant effect as expected for friction.

2.3.4 Uniform random distribution

As mentioned for the Metropolis algorithm in section 2.3.2, random numbers and random generators play a major role in Monte Carlo methods. Three basic types of distributed populations within an area can be identified: uniform, random and clumped distributions [95]. Simulation results in particle-based modelling method critically depend on a good uniform random number generator (RNG). A RNG produces a totally indeterministic and periodic sequence of numbers, once its initial state (or seed) is chosen. The two main assumptions of a sequence being independent and also made of identically distributed random variables are in a disagreement. There is no easy way to completely settle these two opposite aspects [54].

A RNG from its initial state S and in n steps, generates output numbers (0,1). The output space could be more general but in the current implementation it is a population of real numbers between 0 and 1, which can be scaled linearly to any other required domain. As shown in Figure 2.10, randomly generated positions and uniform positions generated using the Bays-Durham shuffling method (ran2) generator with a long periodic time ($> 2 \times 10^8$) actually differ [34].

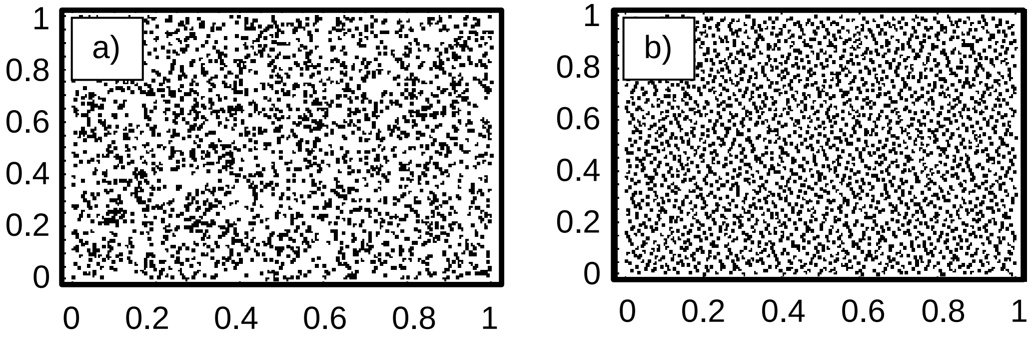

Figure 2.10: Particle positions in 2D space: a) randomly generated positions, b) uniformly distributed random positions

2.3.5 Random walk

The random walk is defined as a sequence of discrete steps of fixed length in space. In particle mechanics, as envisaged here, it is the history of positions for a specific particle during iterations. Each step is defined in all 3 directions x, y and z in a given number of N as total steps. So the probabilities of having steps along x, y and z can be defined; and also the probable leaning of a particle toward any direction after a specific number of steps can be calculated. These probabilities can be calculated in the space for all particles. If there is no force present and acting on the particles in the walk space, probability of positions within uniform random generator will be consistent. Figure 2.11 represents a random walk for particles in (a) 2D and (b) 3D space [129].

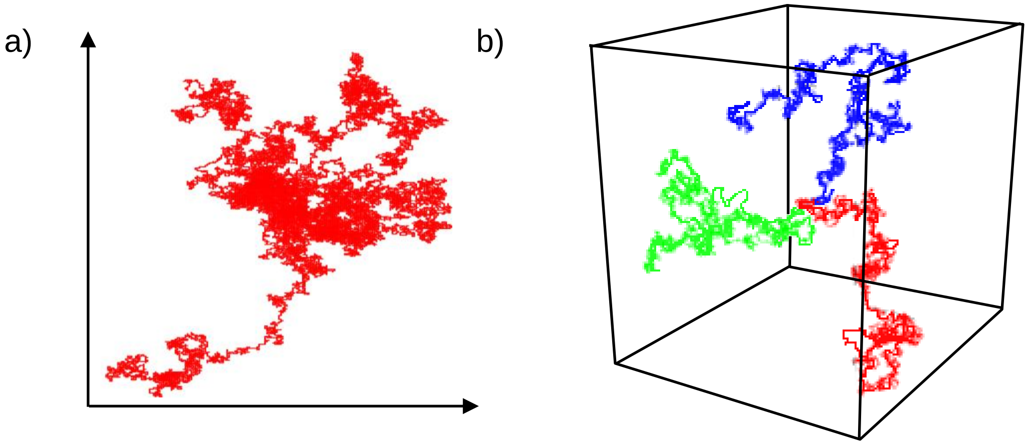

Figure 2.11: Random walk in: a)2D and b)3D

2.4 Software development

2.4.1 Implementation

The particle-based modelling method implemented herein uses an object-oriented software design and is implemented in the C++ programming language. It consists of C++ class libraries and several interpreted modules, listed as core, render and GUI. Each module is explained in the following sections.

2.4.2 Core

The core module contains basic calculations and decisions related to the Metropolis algorithm. It allows executing and communicating with different modules concurrently, enabling integration with other coded programs, wrappers for visualization and user input modules. With object-oriented programming, data generated at each stage of imposed compaction, in-plane shear, etc. can be stored for later use. Core uses cross-platform extensions which facilitate interaction with other modules programmed in environments such as Python or Tcl programming languages, for example.

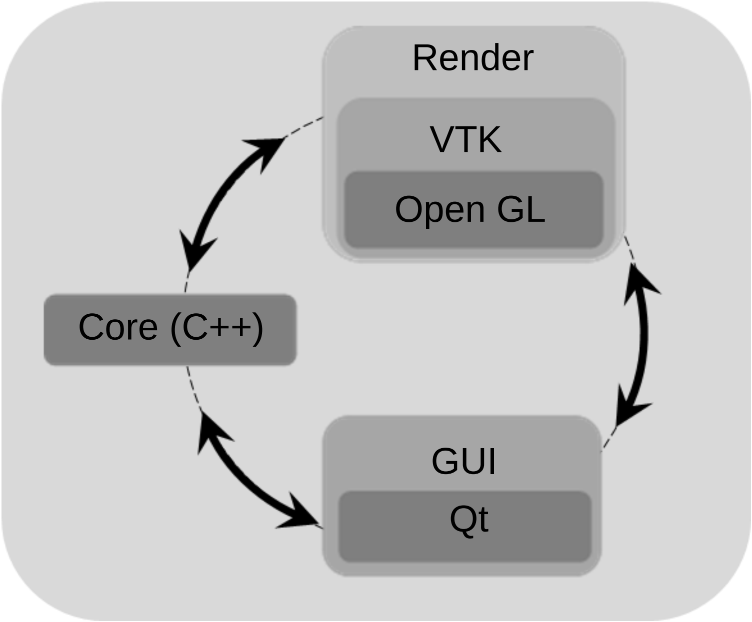

Figure 2.12: Implementation of computational modules

2.4.3 Render

Most implementations of renders have a similar order of operations. Here, a series of processing scripts is used for wrapping C++ core for rendering, sing the Visualization Toolkit (VTK). The VTK is an open-source, freely available software system for 3D computer graphics, image processing and visualization. VTK consists of a C++ class library and several interpreted interface layers that use the OpenGL [132] rendering pipeline. OpenGL provides a powerful but primitive set of rendering commands, which are then used in object oriented programming. Also, a number of libraries such as GLUT and GLU exist to simplify programming tasks, which are used occasionally in the particle-based modelling method. Currently a molecular visualization program, VMD is used to do the rendering, as a home-grown render remains under development.

2.5 Equilibrium verification procedure

Through the procedure described in the above sections, strain energy terms for each particle and selected fibre within an assembly undergoing mechanical loading is quantified. Also, strain energy terms resulting from fibre-to-fibre contact forces are calculated. Figure 2.13 represents one fibre inside of a yarn within a textile undergoing compaction.

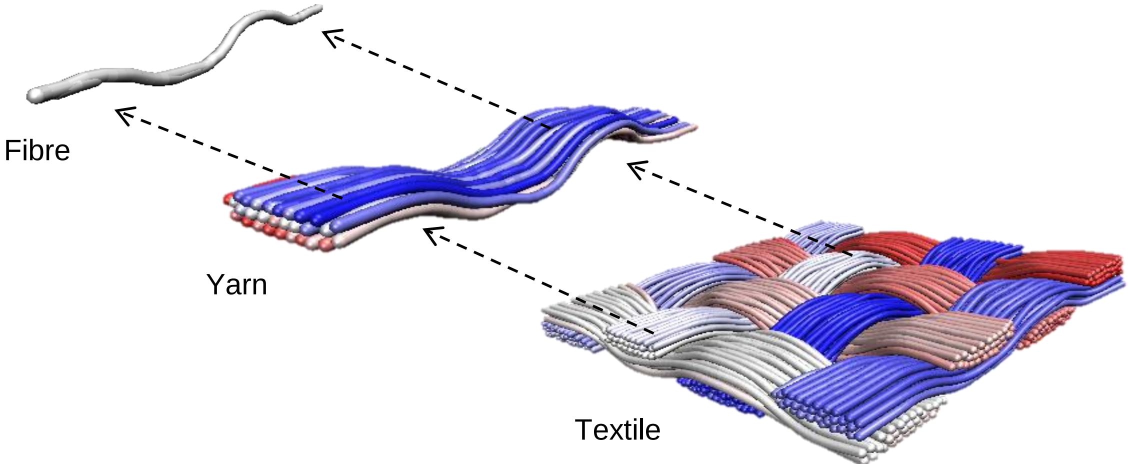

Figure 2.13: Selection of individual fibre from textile

The plain woven textile in the figure is compacted through a reduction of distance between upper and lower boundaries. Contact forces acting on particles associated with a chosen fibre contact point are recorded. Iterations are performed and once again contact forces acting on the same particles are recorded. As shown in Figure 2.14 all contact forces which are represented graphically by vectors are minimized along with changes in the shape of the fibre.

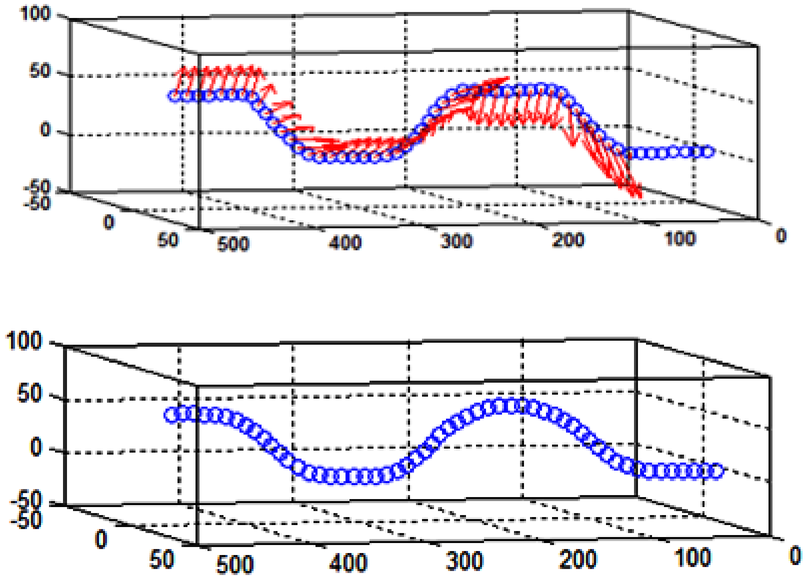

Figure 2.14: Equilibrium verification within a fibre assembly

2.6 Summary for procedure of the representation of textile geometry using particle-based modelling

The particle-based modelling method reported here was used for locating fibre positions which minimize the total strain energy stored in textile assemblies during PMC manufacturing processes. Compaction, shear and other loading cases applied on the reinforcements lead to a shift in position of particles and fibres, from their original positions to new ones. Iterations based on the Metropolis algorithm using interaction functions defined previously provide possible new fibre configurations. In the method, each fibre is free to find a new configuration in its surrounding space. The goal is to bring the fibre assembly from an arbitrary initial state, to a state of minimum strain energy in the system. Then, when strains are applied on the boundaries of the textile domain, the iterative process is repeated. It will take time for the system to reach a state of minimum energy. Applying smaller strains will lead to a stable state within a much shorter time, similarly to what is seen in real textiles in terms of time dependence.

Different cases of compaction, relaxation and in-plane shear were investigated using the particle-based modelling method implemented. Results were validated by comparing with experimental trials as explained further in the following chapters.

Chapter 3

Concurrent simulation of permeability, thermal conductivity and modulus for carbon fibre reinforcements and composites

3.1 Preamble

Chapter 3 features simulations and experimental trials of resin flow through dry carbon fibre textile reinforcements, as well as simulation and experimental trials of heat transfer and static loading of unidirectional and bidirectional carbon fibre reinforced composites. Prior to this study, no systematic investigation of the relation between reinforcement geometry and these different properties was reported for same geometric models of textile reinforcements and their composite. The study aims at showing the effect of geometric models on selected processing and performance properties of reinforcements and composites. These effects are quantified using a series of simple geometric parameters as input, defined in the chapter and selected to show the sensitivity of the selected properties with regards to these geometric parameters. The conclusions drawn in this chapter were obtained from performing 136 simulations. Considering the number of parameters used in this study, a systematic parameter selection procedure was implemented in simulation trials. The geometric parameters having the most effect on the selected responses were identified. Permeability, conductivity and modulus were affected by different combinations of geometric parameters, as highlighted in this chapter. It is shown through this preliminary work that changes in reinforcement geometry can have a very strong effect on some properties such as the permeability, a moderate effect as seen with the thermal conductivity, or virtually no effect as observed with the modulus. Results presented in this chapter were published in a peer-reviewed journal paper [101].

3.2 Abstract

The selection of textile reinforcement for manufacturing structural polymer composite parts requires good knowledge of numerous material properties at the design stage, for both the various textile reinforcements that may be selected and the composite parts to be made from these reinforcements. This chapter presents predictive meso-scale simulations of i) in-plane permeabilities of unidirectional and bidirectional non-woven carbon fibre textile reinforcements, ii) through-thickness thermal conductivity of composites made from these reinforcements, and iii) in-plane moduli of composites made from these reinforcements. Experimental validation results are presented for all simulated properties. The effect of the reinforcement configuration on these processing (i) and performance (ii, iii) properties is quantified through systematic variation of the geometric parameters that define the configuration, for constant reinforcement surface density *(*ρ_s*)* and composite

fibre volume fraction (v_{fc}). Results are presented for 136 simulations performed using 34 geometric models of reinforcements. The geometric parameters that have the strongest effects on the permeability, conductivity and modulus are identified. Differences in the amplitude of these effects observed from simulation correlate well with the different levels of variability observed experimentally for each property.

3.3 Introduction

The material properties of textile composites that govern their manufacturing and their performance are strongly influenced by the configuration of the textile carbon fibre reinforcement used in manufacturing these composites. Therefore, data quantifying these processing and performance properties are required at the design stage, so that a textile reinforcement which is best suited to a specific part and load case may be selected.

Quantifying these data through physical testing for commercially available for commercially available carbon fibre is long and costly. As an alternative, much attention was devoted to the development of meso-scale simulation tools for textile composite unit cells, used for predicting such properties from the reinforcement configuration. Meso-scale predictions were successfully used for mapping trends between a selected processing property of reinforcements or performance property of composites, and configuration-related parameters such as the fibre volume fraction vf_c, in-plane shear angle or reinforcement type [27, 92, 126]. However, the accuracy of geometric models remains an open issue; hence published work is mostly limited to predicting trends and usually aims at reducing physical testing through such trend identification, as opposed to superseding it. The literature focuses mostly on the development of meso-scale simulation methods, with few examples presented.

In this chapter the in-plane permeabilities of reinforcements to resin Kr_x and Kr_y, the through-thickness thermal conductivity of composites kc_z, and the in-plane Young's moduli of composites Ec_x and Ec_y are predicted for unit cells of unidirectional and bidirectional non-woven textiles. The work aims at quantifying the effect of reinforcement configuration on these properties, using established methods appropriate for actual reinforcement selection in an industrial context. Therefore, mature prediction methods based on validated software are used on geometric models of existing reinforcements.

Geometric parameters defining the configuration of these reinforcements were varied. However, all simulations and measurements were performed on models and materials with a fibre volume fraction vf_c held constant at 55%, ensuring that comparisons are meaningful and relevant to industrial practice: the fibre volume fraction was kept constant in all cases as the aim of the work is to quantify the effect of the configuration as opposed to the effect of vf_c . The reinforcement surface density (ρ_s) also stayed constant at 530 g/m^2 in all simulations, for the same reason.

The tow width tw, vertical inter-tow gap gv, horizontal inter-tow gap gh and tow cross-section shape were varied using a Taguchi full-factorial simulation plan, Figure 3.1, and the effects of these parameters on the above processing and performance properties were quantified through 136 simulations performed on 34 geometric models. The tow fibre volume fraction vf_t, which is the fibre volume fraction defined within the cross-section of a tow, fluctuated as a dependent variable allowing vf_c to remain constant. Experimental validation results are presented for all properties.

The same geometric models were used in predicting flow, heat transfer and structural properties. The amplitude of the effects of these geometric parameters on the properties varied from one property to another. These different amplitudes correlate well with the different levels of variability observed in measurements of the permeability, conductivity and stiffness. The geometric parameters most affecting each property at a constant vf_c

were identified.

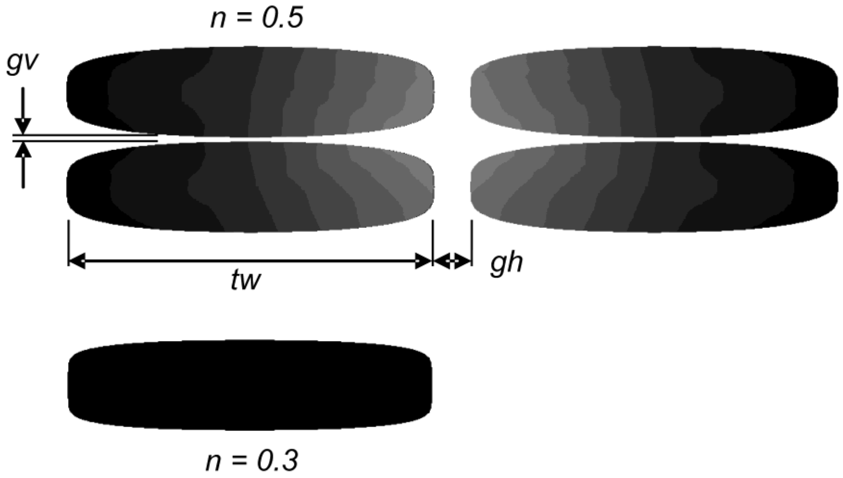

Figure 3.1: Geometric parameters

From a practical perspective, achieving reproducible manufacturing of textile reinforced composite parts which translates into reliable and consistent performance of these parts, only requires that the geometric parameters of reinforcements that have a strong effect on the physical properties of the reinforcements and composites be well controlled during reinforcement manufacturing. The relation between machine settings used in a textile manufacturing operation and the variability of the carbon fibre reinforcements produced can be observed directly during their production. However, currently only meso-scale simulations can identify which geometric parameters of the textile reinforcements must be controlled accurately for achieving reproducible composite processing and performance.

3.4 Literature review

Analytical work investigating relations between the geometric configuration of textiles and their properties predates high-performance textile composites. However, the increased use of these materials in load-bearing structures, notably in aerospace engineering, as well as the resulting need for property quantification has lead to the accelerated development of textile unit cell geometric modellers [92, 126]. In parallel, work aiming at measuring intricate geometry of reinforcement unit cells and predicting it from first principles is ongoing [27, 74, 107].

These textile unit cell modellers have been used for predicting the in-plane permeability of carbon fibre reinforcements to resin. Diverse computational methods were proposed towards this end, featuring varying levels of detail in flow field description [9, 131]. The methods are well described and simulations leading to the identification of trends are presented in the literature. Investigations of variability were also conducted. However, few validation results are available [124, 125].

Unit cell models were also used for predicting the through-thickness thermal conductivity of textile composites. Ning et al. [76] applied a straightforward calculation to simple geometric models. Dasgupta et al. [26] proposed more extensive homogenization method and models for the same purpose. Both groups succeeded at predicting the effects of vf_c and weave style. Gowayed et al. [35] and Bigaud et al. [11] introduced computational methods and presented trends for kc_z as a function of vf_c for different textile reinforcements. Gowayed et al. [35] validated their predictions with an array of experimental results.

Predictive modelling of structural properties has been presented for different textile reinforcement types [12, 23, 75]. Recent published work aims at predicting stiffness and failure, and focuses heavily on the development of numerical methods for the latter. Significant progress was achieved in recent years. However, validation data based on experimental trials remains sparse.

Limited information on the concurrent simulation of different processing and/or performance properties is available in the literature [126]. No concurrent validated permeability, conductivity and stiffness data, nor data where geometric reinforcement parameters affecting all properties are identified systematically, are available. Limited variability information generated from simulation at constant vf_c is available [131], hence conclusions about the effect of the meso-scale geometric parameters are generally not made.

3.5 Geometry and properties

Two carbon fibre reinforcements were modelled in this work. Both materials are made of identical unidirectional textile layers of parallel carbon tows. Material 1 is a unidirectional laminate with sequence $[0°]_m$ where m is the numbers of layers. Material 2 is a balanced bidirectional laminate with sequence $[0°/90°]_m$. Multiple models were created for each material based on different geometric parameters; each model was used in simulating flow, heat transfer and structural behaviour. In flow simulations, a material model effectively represents a textile reinforcement saturated with liquid resin. In simulations of heat transfer and structural loading a material model represents a composite with solid resin.

Unit cells of unidirectional material 1 $[0°]_m$ and balanced bidirectional material 2 $[0°/90°]_m$ featuring $m = 1$ and $m = 2$ layers of reinforcement were modelled. While the geometry of models was unchanged in simulations of the different properties, appropriate unit cell boundaries were selected in view of each case. All reinforcement layers had a surface density (ρ_s) of 530 g/m^2 and all unit cells had a fibre volume fraction vf_c of 55%. The effects of reinforcement configuration on flow, heat transfer and static loading properties were quantified by varying the tow width tw (2 and 4 mm), horizontal inter-tow gap gh (0.2 and 0.4 mm), vertical inter-tow gap gv (0.02 and 0.04 mm) and tow section shape. Tow height th was kept constant at 0.5 mm in all cell models. All above quantities were defined from observations made on actual carbon fibre reinforcements as described below.

Tow sections were modelled as hyperellipses of power n in the local xs, ys plane as described in Equation 3.1. The ratio tr of tow width to height varied with tw. The tow cross-section area ta varied with tw and n. The tow fibre volume fraction vf_t varied with the above parameters to ensure that the fibre volume fraction in a unit cell vf_c stayed constant at 55%. Geometrical parameters are illustrated in Figure 3.3; values appear in Table 3.1 for the 34 unit cell models created for this work.

17 cell models were created for unidirectional material 1 (labelled 1A-1P, 1Z) and 17 for balanced bidirectional material 2 (labelled 2A-2P, 2Z) corresponding to 2 full-factorial 4-parameter simulation plans with additional models in the centre of the simulation space (labelled 1Z, 2Z). The 2 simulation plans evaluate the effect of all geometric parameters and all their interactions on flow, heat transfer and static loading properties. The vertical inter-tow gaps correspond to 3 to 5 carbon fibre diameters and the horizontal inter-tow gaps are representative of reinforcements used in the experiments; hence the models are credible in representing actual reinforcement geometry. The maximum value of vf_t= 0.906 (cases 1G, 2G) corresponds to perfect hexagonal packing of the fibres in the tows.

$$y_s = \pm\frac{th}{2} \cdot \left[1 - \frac{x_s^2}{(th \cdot tr)^2}\right]^n \tag{3.1}$$

Tow properties were calculated from available properties of Hexcel T300 PAN-based carbon fibres and representative epoxy resins listed in Table 3.2 [7,35,88,96]. Axial and transverse tow permeabilities Kt_a and Kt_t were calculated for each cell model from fibre diameter d and tow fibre volume fraction vf_t using Gebart's models [33] stated in Equation 3.2, Equation 3.3. Gebart used adjusted factors to account for differences between calculated values of permeability and those measured on reinforcements featuring hori-

Table 3.1: Reinforcement geometry for cell models

cell model	th	tw(mm)	gv(mm)	gh(mm)	fh(mm)	sn	ta(mm^2)	vf_t
1A,2A	0.5	2	0.02	0.2	0.52	0.5	0.785	0.8
1B,2B	0.5	4	0.02	0.2	0.52	0.5	1.57	0.763
1C,2C	0.5	2	0.04	0.2	0.54	0.5	0.785	0.831
1D,2D	0.5	4	0.04	0.2	0.54	0.5	1.57	0.793
1E,2E	0.5	2	0.02	0.4	0.52	0.5	0.785	0.872
1F,2F	0.5	4	0.02	0.4	0.52	0.5	1.57	0.8
1G,2G	0.5	2	0.04	0.4	0.54	0.5	0.785	0.906
1H,2H	0.5	4	0.04	0.4	0.54	0.5	1.57	0.831
1I,2I	0.5	2	0.02	0.2	0.52	0.3	0.918	0.684
1J,2J	0.5	4	0.02	0.2	0.52	0.3	1.835	0.653
1K,2K	0.5	2	0.04	0.2	0.54	0.3	0.918	0.71
1L,2L	0.5	4	0.04	0.2	0.54	0.3	1.835	0.678
1M,2M	0.5	2	0.02	0.4	0.52	0.3	0.918	0.746
1N,2N	0.5	4	0.02	0.4	0.52	0.3	1.835	0.684
1O,2O	0.5	2	0.04	0.4	0.54	0.3	0.918	0.775
1P,2P	0.5	4	0.04	0.4	0.54	0.3	1.835	0.71
1Z,2Z	0.5	3	0.03	0.3	0.53	0.4	1.342	0.715

th = tow height
tw = tow width
gv = vertical gap
gh = horizontal gap
fh = model full (1) / half height (2)
sn = tow section power n
ta = tow section area
vf_t = tow fibre volume fraction

zontal inter-tow gaps. Such factors do not apply to tows themselves, hence they were not used here. Values of $c = 53$ and $C_1 = 11.54$ corresponding to hexagonal fibre packing were used with maximum tow fibre volume fraction $vf_{max} = 0.906$. Values of Kt_a and Kt_t are presented in Table 3.3.

$$Kt_a = \frac{8}{c} \cdot \left(\frac{d}{2}\right)^2 \cdot \frac{(1 - vf_t)^3}{vf_t^2} \tag{3.2}$$

Table 3.2: Properties of carbon fibres and epoxy resin

Property	Units	Resin	Fibre	Ref
Diameter	μ m	-	8	[7]
Density	g/cm^3	1.2	1.8	[7,88]
Viscosity	Pa.s	1	-	[88]
Conductivity	W/mK	0.2	Axial: 8.4 Transverse: 0.84	[35,96]
Modulus	GPa	5.0	250	[7,88]

$$Kt_t = C_1 \left[\sqrt{\frac{vf_{max}}{vf_t}} - 1 \right]^{5/2} \cdot \left(\frac{d}{2} \right) \tag{3.3}$$

Tow axial and transverse thermal conductivities kt_a and kt_t were calculated for each unit cell from fibre axial and transverse thermal conductivity kf_a and kf_t and resin thermal conductivity kr using the rule of mixture by volume shown in Equation 3.4 and Nielsen's model [88] for aligned cylinders, shown in Equation 3.5 and Equation 3.6, Equation 3.7 with A = 0.5 and vf_{max} = 0.906. Tow density ρ_t and specific heat Cp_t were not required in these steady-state simulations. Values of kt_a and kt_t are presented in Table 3.3.

$$k_{t,a} = v_{f,t} \cdot k_{f,a} + (1 - v_{f,t}) \cdot k_r \tag{3.4}$$

$$k_{t,t} = k_r \left[\frac{1 + A \cdot B \cdot v_{f,t}}{1 - B \cdot \phi \cdot v_{f,t}} \right] \tag{3.5}$$

$$B = \frac{(k_{f,t}/k_r) - 1}{(k_{f,t}/k_r) + A} \tag{3.6}$$

$$\phi = 1 + \left[\frac{1 - v_{f,t}}{v_{f,max}^2} \right] .v_{f,t} \tag{3.7}$$

Tow axial and transverse Young's moduli Et_a and Et_t were calculated for each unit

Table 3.3: Tow properties for cell models

cell model	Kt_a (m^2)	Kt_t(m^2)	kt_a (W/mK)	kt_t (W/mK)	Et_a (GPa)	Et_t (GPa)
1A,2A	30.3	38.8	6.76	0.626	200.9	23.1
1B,2B	54.9	88.4	6.46	0.579	192	19.8
1C,2C	17.1	15.4	7.01	0.673	208.5	26.8
1D,2D	34.2	46.3	6.7	0.617	199.2	22.4
1E,2E	6.59	1.85	7.35	0.747	218.7	34.5
1F,2F	30.3	38.8	6.76	0.626	200.9	23.1
1G,2G	2.44	0	7.63	0.818	227	44.6
1H,2H	17.1	15.4	7.01	0.673	208.5	26.9
1I,2I	163	327	5.81	0.495	172.6	15.2
1J,2J	237	494	5.55	0.468	165	13.9
1K,2K	116	223	6.02	0.52	179	16.5
1L,2L	175	355	5.76	0.489	171.1	14.9
1M,2M	70.5	122	6.32	0.559	187.8	18.6
1N,2N	163	327	5.81	0.495	172.6	15.2
1O,2O	45.9	69.6	6.55	0.593	194.8	20.8
1P,2P	116	223	6.02	0.52	179	16.5
1Z,2Z	109	207	6.07	0.525	180.2	16.7

Kt_a= Axial tow permeability (10-15 m^2)
Kt_t= Transverse tow permeability (10-16 m^2)
kt_a= Axial tow conductivity
kt_t= Transverse tow conductivity
Et_a= Axial tow modulus
Et_t= Transverse tow modulus

cell from the fibre axial modulus Ef_a and resin modulus E_r using the rule of mixtures by volume shown in Equation 3.8 and Tsai's micromechanical model [96] appearing in Equation 3.9. Values of Et_a and Et_t are presented in Table 3.3. Other structural properties of the tows were calculated using established models from reference [96]; individual values are not reported.

$$E_{t,a} = v_{f,t} \cdot E_{f,a} + (1 - v_{f,t}) \cdot E_r \tag{3.8}$$

$$E_{t,t} = \frac{E_{f,a} \cdot E_r}{v_{f,t} \cdot E_r + (1 - v_{f,t}) \cdot E_{f,a}} \tag{3.9}$$

3.6 Simulations

Tows in models of unidirectional $[0°]_m$ composites (17 models: 1A-1P, 1Z) extend along x only while tows in the first and second reinforcement layers of bidirectional $[0°/90°]_m$ composites (lower and upper z respectively, 17 models: 2A-2P, 2Z) extend along x and y respectively. Simulations performed are: in-plane, steady-state saturated laminar flow along x and y for $[0°]_m$ laminates (1A-1P, 1Z, 34 simulations); in-plane, steady-state saturated laminar flow along x for $[0°/90°]_m$ laminates (2A-2P, 2Z, 17 simulations); through-thickness steady-state conductive heat transfer along z for $[0°]_m$ and $[0°/90°]_m$ composites (1A-1P, 1Z, 2A-2P, 2Z, 34 simulations); static elastic loading along x and y for $[0°]_m$ composites (1A-1P, 1Z, 34 simulations); and static elastic loading along x for $[0°/90°]_m$ composites (2A-2P, 2Z, 17 simulations).

Predicted properties are in-plane permeabilities of reinforcements Kr_x and Kr_y, through-thickness thermal conductivity of composites kc_z, and in-plane Young's moduli of composites Ec_x and Ec_y. Full-factorial Taguchi simulation plans were used in all cases as detailed above. Figure 3.2 shows the evolution of the cell height (th + gv , models 1A-1P, 1Z or 2 (th + gv), models 2A-2P, 2Z) and tow fibre volume fraction vf_t and their relation with input parameters tw (tow width), gv (vertical inter-tow gap), gh (horizontal inter-tow gap) and n (tow section hyperellipse power).

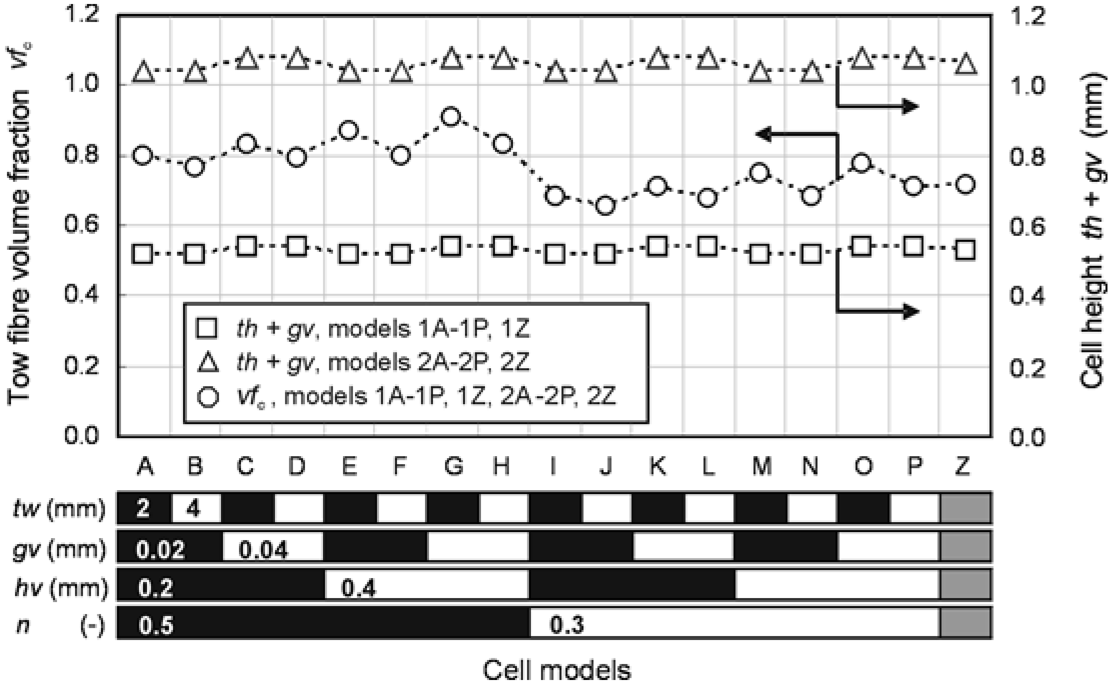

Figure 3.2: Geometric parameters $th + gv$ (models 1A-1P, 1Z) or 2 $(th + gv)$ (models 2A-2P, 2Z) and vf_t

All geometric models were created using TexGen v2 [92] and meshed using Gambit™ 2.2.30 with 100 000 to 500 000 4-noded tetrahedral elements. Different meshes were created from the same geometric models for flow, heat transfer and static loading to better suit boundary conditions and symmetry. Faces normal to axes x, y and z were labeled *xmin*, *xmax*, *ymin*, *ymax*, *zmin* and *zmax*. Convergence was verified using model 1A in all cases.

Results of contrast analysis generated from Taguchi plans appear in Table 3.4 for all predicted properties. Significant parameters are listed in each case and their effect is quantified.

3.6.1 Resin flow simulations

Steady-state simulations of laminar saturated in-plane flow of resin through reinforcements were conducted using Fluent™ 6.2.16. Typical flow domains for materials 1 and 2 appear in Figure 3.3. Pressures of 10 Pa and 0 Pa were imposed on inlet face *xmin* (or *ymin*) and outlet face *xmax* (or *ymax*). Other faces were set as walls; these were located in zones of very slow flow hence cell permeability was unaffected by these walls.

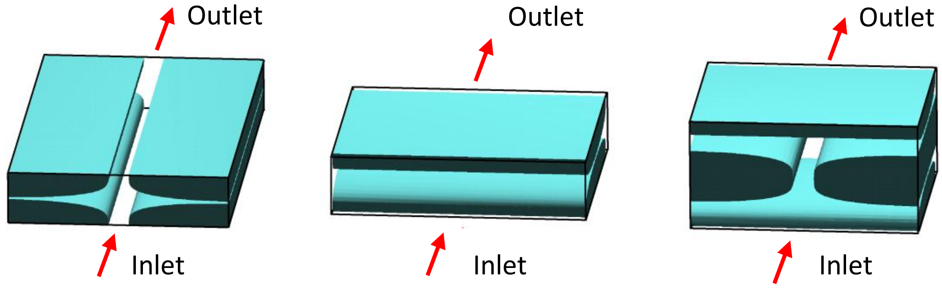

Figure 3.3: Typical flow domains; a) material 1, flow along x; b) material 1, flow along y; c) material 2

Uniform pressure distributions and velocity fields developed along the flow direction in all cases simulated in this work. Darcy's law was used for calculating reinforcement permeability Kr_x or Kr_y along x or y as shown in (3.10) from the imposed pressure gradient $\Delta P/\Delta x$ or $\Delta P/\Delta y$ and total mass flow rate converted to seepage velocity u_x or u_y . Resin viscosity μ and density ρ_s are specified in Table 3.2.

$$u_x = -\frac{Kr_x}{\mu} \cdot \frac{\Delta P}{\Delta x} \quad ; \quad u_y = -\frac{Kr_y}{\mu} \cdot \frac{\Delta P}{\Delta y} \tag{3.10}$$

A typical flow field appears in Figure 3.4 for flow along axis x through model 1C. Flow simulation results appear in Figure 3.5. These results clearly show that permeability is strongly influenced by the reinforcement configuration, in cases where the fibre volume fraction vf_c is kept constant.

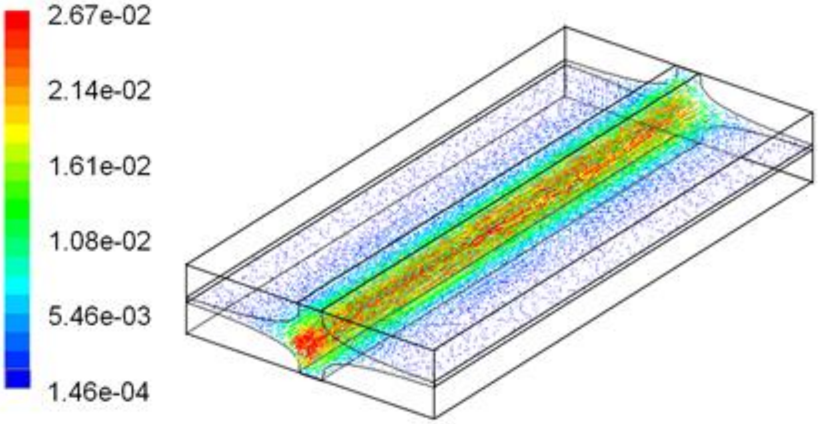

Figure 3.4: Flow field: velocity vectors collared by amplitude (m/s), cell model 1C, flow along x

This finding can be related to the large variability that is typically observed for permeability measurement performed on reinforcements. It is also informative to compare variability in the above results with that arising from different nesting patterns for a fabric of constant configuration and vf_c [131], and from varying gaps in fabrics where tows are not perfectly straight [125], again for a constant vf_c. Finally, narrow inter-tow gaps lead to predicted permeability values that are in line with reported experimental values, indicating the critical importance of accurate geometrical modelling to flow simulations.

Figure 3.5 also shows a factor of approximately 10 between Kc_x and Kc_y for material 1 as seen in reported experimental results. Trends in Kc_x ($= Kc_y$) for $[0°/90°]_m$ material 2 closely follow those of Kc_x for $[0°]_m$ material 1 as expected. Analysis of contrasts for Kc_x, $[0°]_m$ material 1, Table 3.4, indicates that horizontal gap gh has the strongest positive effect (increases Kc_x). Amplitudes of the positive effect of tow section power n – resulting in smaller tow sections –, negative effect of tow width tw and positive effect of vertical gap gv are less than half the amplitude of the effect of gh. All of these effects clearly indicate that inter-tow channels in the horizontal plane control flow in

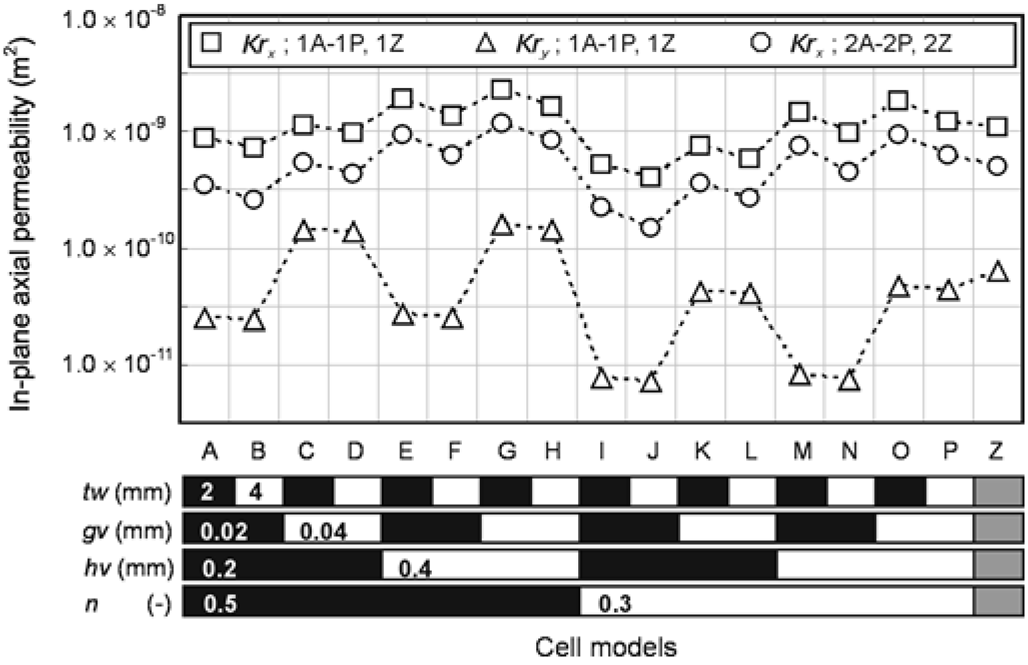

Figure 3.5: Flow simulation results

this case. Analysis of contrasts for Kc_y, $[0°]_m$ material 1 indicates that both *gv* and *n* have strong positive effects whilst other parameters are not significant. Pressure loss mostly occurs in gaps between vertical apexes of tows; the geometry of these gaps controls transverse permeability Kc_y for material 1. It can be concluded that flow along and across tows in $[0°]_m$ materials is controlled by inter-tow gaps, with horizontal and vertical inter-tow gaps dominating flow along and across tows respectively. Analysis of contrasts obtained with Kc_x for $[0°/90°]_m$ material 2 shows trends very similar to those observed with Kc_x for $[0°]_m$ material 1. This was expected as Kc_x values for material 1 are larger than those of Kc_y for the same material, resin flowing though the path of least resistance.

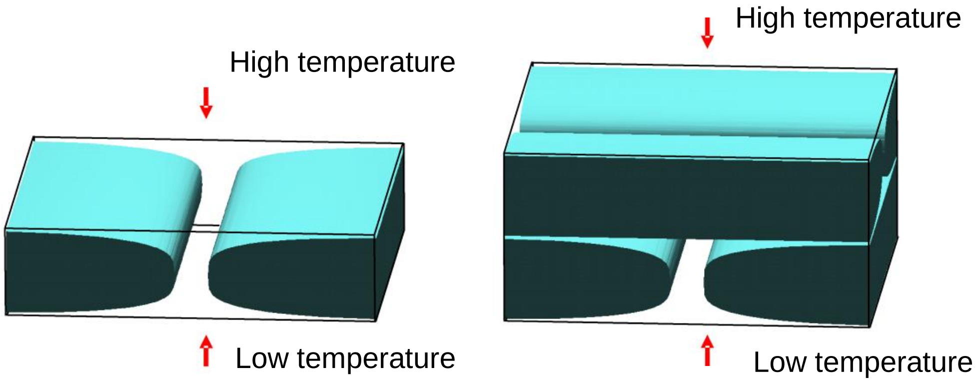

Figure 3.6: Typical heat transfer domains: material 1, material 2

3.6.2 Heat transfer simulations

Steady-state simulations of through-thickness heat conduction through composites were conducted using Fluent^{TM} 6.2.16. Typical heat transfer domains appear in Figure 3.6. Constant temperatures were imposed on lower and upper faces *zmin* and *zmax*. Other boundary faces were set as adiabatic walls. Symmetrical temperature and heat flux fields developed in all cases. Fourier's law was used in calculating composite conductivity kc_z along z, stated as Equation 3.11 from imposed temperature gradient $\Delta T/\Delta z$ and the area-weighted surface heat flux q_z on faces *zmin* and *zmax*.

$$q_z" = -kc_z \frac{\Delta T}{\Delta z} \tag{3.11}$$

The temperature field for case 2A appears in Figure 3.7. Heat transfer simulation results appear in Figure 3.8. Reinforcement configuration has limited effect on through-thickness conductivity for a constant fibre volume fraction vf_c in the composite. Whilst published measurements are few this can be correlated with the limited variability observed experimentally for this property, and explain that published predictions of kc_z seem equally successful whether based on complex or simplified geometric models [11, 26, 35, 76].

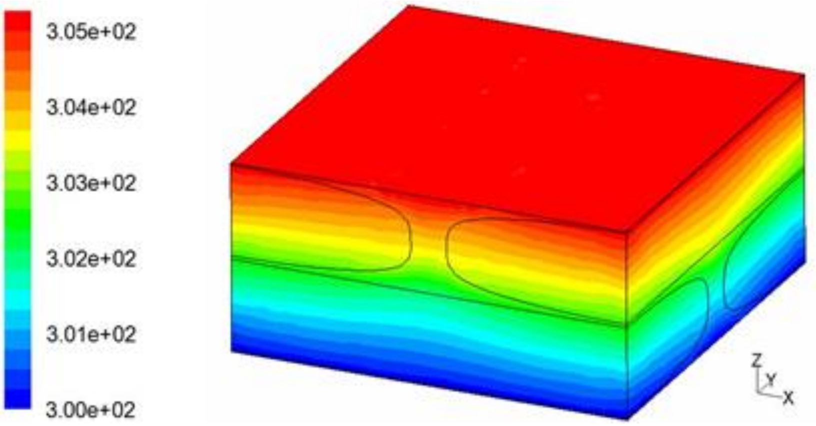

Figure 3.7: Temperature field (K), cell model 2A

Model geometry is less critical for conductivity than it is for permeability. Figure 3.8 also shows that values of kc_z are virtually identical for $[0°]_m$ material 1 and $[0°/90°]_m$ material 2. Tow configuration has a much greater influence than laminating sequence; having 2 superimposed $[0°/90°]_m$ layers in material 2 as opposed to parallel tows in $[0°]_m$ material 1 had virtually no effect on kc_z , as expected.

Analyses of contrasts for kc_z in $[0°]_m$ material 1 and $[0°/90°]_m$ material 2, Table 3.4, lead to nearly identical results. Some effects are counterintuitive: kc_z increases most when hyperellipse section power n goes from 0.3 to 0.5 corresponding to smaller sections of conductive tow embedded in a larger volume of less conductive matrix. However, at a constant composite fibre volume fraction vf_c, tows of smaller section have higher tow fibre volume fractions vf_t resulting in larger transverse tow conductivity kt_t and through thickness composite conductivity kc_z. Amplitudes of the negative effect of vertical gap gv, negative effect of tow width tw and positive effect of horizontal gap gh – through its relation to vf_t – are less than a third of the amplitude of the effect of n.

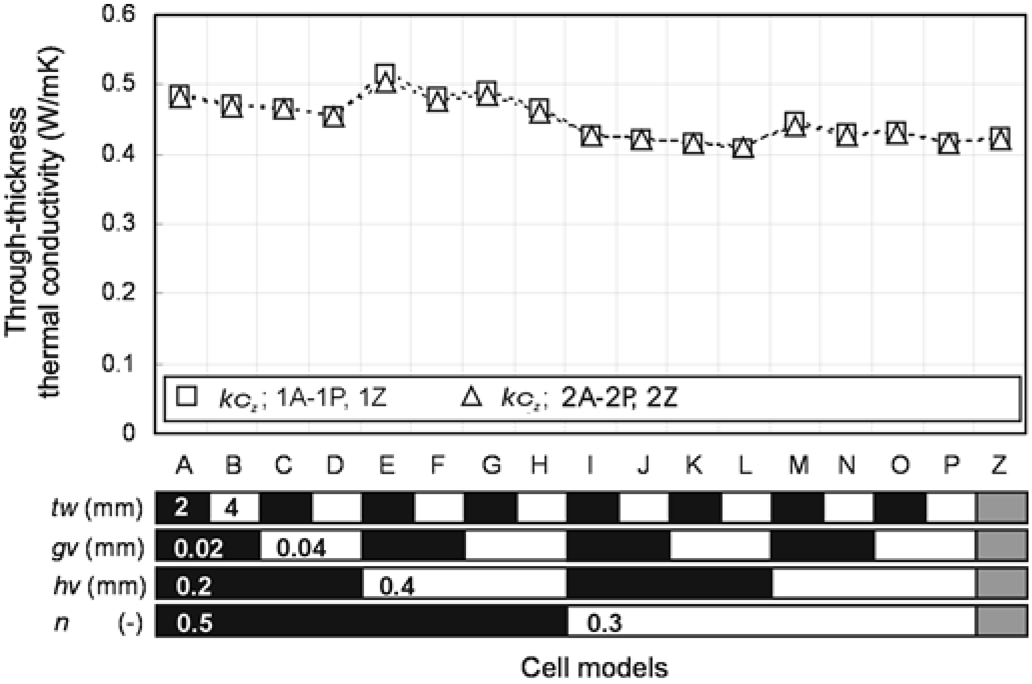

Figure 3.8: Heat transfer simulation results

3.6.3 Static loading simulations

Static elastic in-plane loading simulations of materials 1 and 2 were conducted using Abaqus^{TM} 6.7-1. Static loading domains are identical to heat transfer domains, Figure 3.6. A tensile stress of 10 MPa was imposed along axis x (or y) on faces x_{min} and x_{max} (or y_{min} and y_{min}). Displacements of all nodes on each boundary face along the face normal were forced equal, hence boundary faces remained straight upon loading. Symmetrical stress and strain fields developed in all cases. Hooke's law was used in calculating composite Young's moduli Ec_x or Ec_y along x or y as stated in Equation 3.12, Equation 3.13 and Equation 3.14 from imposed stress σc_x or σc_y and axial strains εc_x or εc_y .

$$Ec_x = \frac{\sigma c_x}{\varepsilon c_x} \tag{3.12}$$

$$Ec_y = \frac{\sigma c_y}{\varepsilon c_y} \tag{3.13}$$

$$\varepsilon c_x, \varepsilon c_y = \frac{\delta L}{L_o} \tag{3.14}$$

The stress field for case 1B loaded along x appears in Figure 3.9. Static loading simulation results appear in Figure 3.10. The reinforcement configuration has virtually no effect on in-plane Young's moduli. Only Ec_y for $[0°]_m$ material 1 varied slightly with section power n and tow width tw through their effect on vf_t and its relation to Et_t. This expected conclusion for constant fibre volume fraction vf_c composites can be correlated to the low variability levels typically observed on Young's moduli in testing, which are usually much lower than variability levels associated with strength. All values were in line with expectations and predictions of simple micromechanical models for homogeneous composites. In view of the limited effect of parameters, analyses of contrasts were not conducted for static loading simulations.

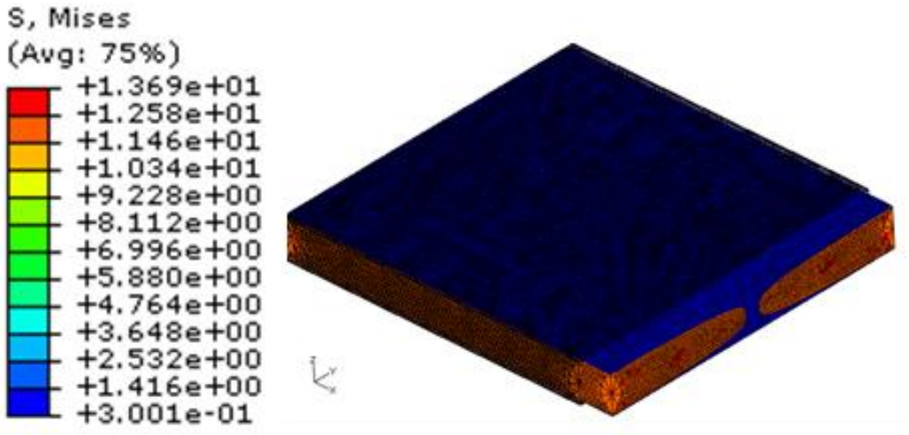

Figure 3.9: Von Mises stress field (MPa), cell model 1B, stress along x

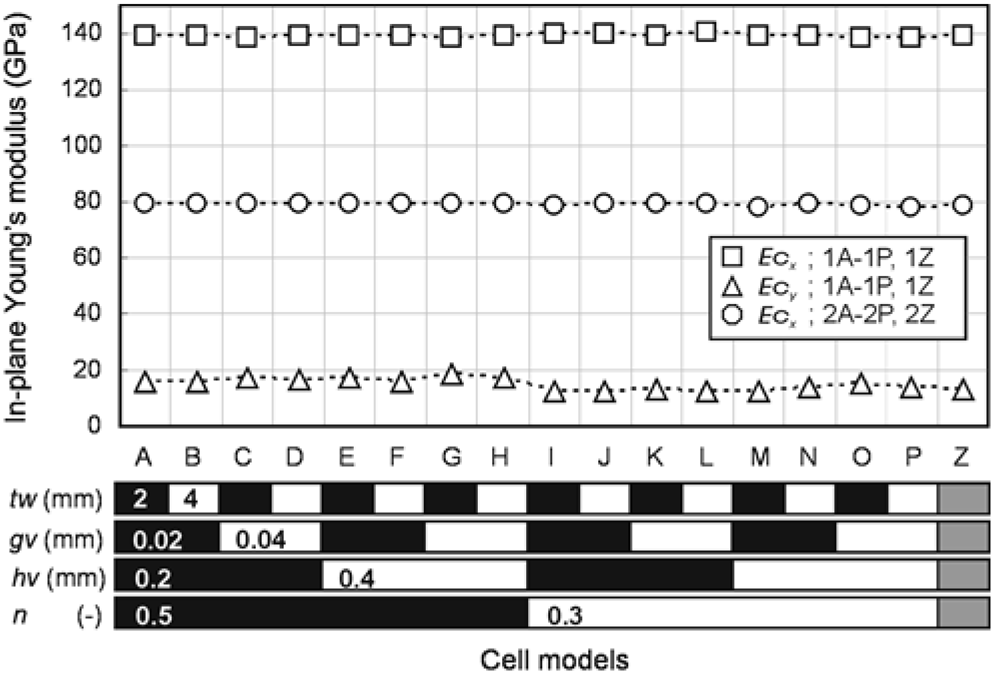

Figure 3.10: Static loading simulation results

3.7 Experiments

Flow, heat transfer and static loading experiments were conducted on carbon fibre reinforcements and on composites made from unidirectional non-crimp fabric style 1152 from Fabric Development Inc. The 366.7 g/m^2 reinforcement available in 7.5 cm wide ribbon is made of 34 parallel T300-12K carbon warp tows held by light glass weft threads. The widths of tows and of horizontal inter-tow gaps created by the weft threads are approximately 2 mm and 0.2 mm respectively. Room-temperature epoxy resin Mia-poxy 100 with hardener 95 at 100:24 ratio by mass was used in flow tests and for making the composites. Viscosity of the mixed resin was 800 cP at 25°C. Cure and post-cure were conducted under press at controlled thickness.

Permeability measurements were conducted in a 74 mm by 300 mm cavity with constant thickness of 1.52 mm under an imposed pressure difference of 1 bar, Figure 3.11.

The purpose-built, non-adjustable cavity had a width slightly lower than that of the fabric hence race-tracking was avoided. Permeability was measured for $[0°]_4$, $[90°]_4$ and $[0°/90°]_s$ 4-layer preforms with $vf_c = 55$ %. Each measurement was repeated 3 times. Values of permeability along the flow direction were derived from Darcy's law as $Kc_x = 7.2 \times 10^{-10}$ m^2 $\pm$ 1.1×10^{-10} m^2, $Kc_y = 6.5 \times 10^{-11}$ m^2 $\pm$ 1.2×10^{-11} m^2 and $Kc_x = 4.1 \times 10^{-10}$ m^2 $\pm$ 9.4×10^{-11} m^2 respectively where the variability number is the standard deviation. The amplitudes of measured values generally correspond to those obtained from simulations. Kc_y is significantly lower than Kc_x for the unidirectional case, and Kc_x for the $[0°/90°]_s$ preform is only slightly lower than Kc_x for the $[0°]_4$ preform. Variability is relatively large as expected.

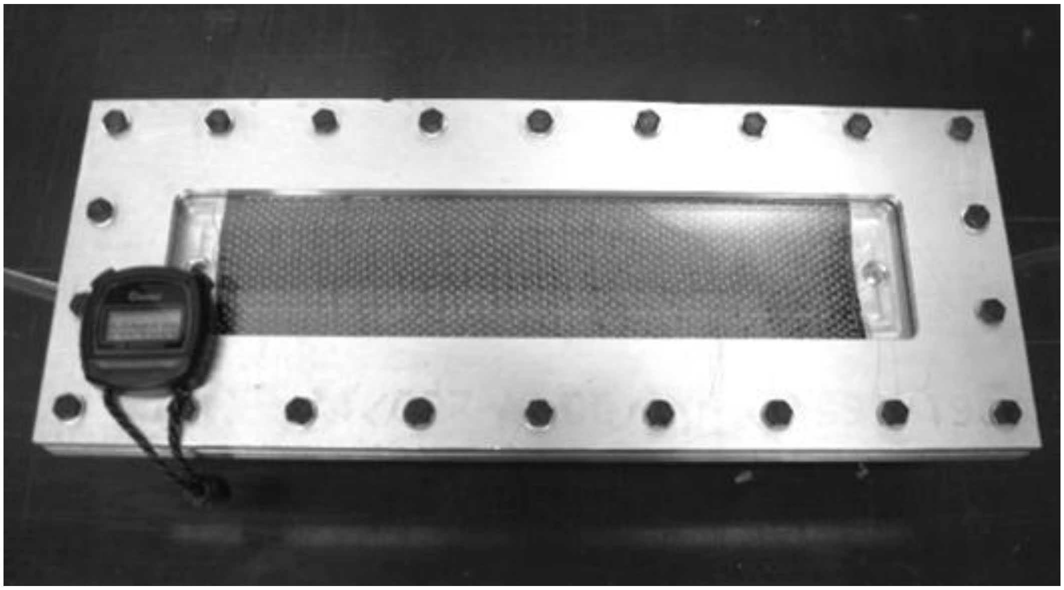

Figure 3.11: Permeability measurement apparatus

Through-thickness thermal conductivity measurements were conducted on 3 plates using the Hukseflux THASYS apparatus available at the Institute for Aerospace Research, National Research Council of Canada (Ottawa), Figure 3.12. Laminating sequences and thicknesses were $[0°]_6$ at 2.29 mm for 2 plates and $[0°/90°]_s$ at 1.52 mm for 1 plate.

All plates had a vf_c of 55%. A total of 23 measurements were conducted. The measured through-thickness thermal conductivities kc_z derived from Fourier's law were 0.450 W/mK ± 0.001 W/mK, 0.458 W/mK ± 0.002 W/mK and 0.451 W/mK ± 0.001 W/mK where the variability number is the standard deviation. It was clearly apparent that the laminating sequence had no discernable effect on kc_z as expected. Accurate values could be obtained as the thermal properties of Hexcel T300 carbon fibres are well reported in the literature. Variability was very low, especially when compared with variability levels seen with permeability.

Figure 3.12: Hukseflux THASYS transverse permeability measurement apparatus and samples

Tensile testing was conducted using an Instron 4482 universal testing frame with samples loaded at 1 mm/min. Samples were not loaded to failure. Laminating sequences and thicknesses were $[0°]_6$ at 2.29 mm, $[90°]_6$ at 2.29 mm and $[0°/90°]_s$ at 1.52 mm. The evaluation of variability offered little interest hence one plate was tested in each case. For the 3 plates a vf_c of 55% was used. Values of Young's modulus along the sample length were derived from Hooke's law as Ec_x = 131.8 GPa, Ec_y = 8.5 GPa and Ec_z =

72.0 GPa respectively. The measured values are generally in line with those obtained from simulations.

3.8 Discussion

The geometric models used in the simulations presented here are idealized: tows are straight, and in each model the tow sections and inter-tow gaps are constant. Furthermore, tows in adjacent layers are perfectly superimposed. Examples of variability for comparable models were provided by Lomov et al [27, 75] and Long et al. [131]. The levels of variability observed in this chapter, for different configurations, may be tempered by the fact that in reality variability is present within a given reinforcement, though it is limited in the case of those used in the aerospace sector. Still, it is clear that variability on permeability data will be significantly larger than it is for other properties.

Inter-tow channel size largely determines preform permeability. It also determines the relation between the general flow front and the inner impregnation of tows (macro/micro flow) during filling. This relation was not investigated as all flow simulations were conducted for saturated domains; however, it could be studied systematically in a similar way. The effect of geometry in transverse flow through unidirectional preforms may be magnified as small gaps result from the assumed perfect alignment of tows; conversely, vertical gap sizes equivalent to 3 to 5 fibre diameters are representative of reality. Therefore, it is reasonable to assume that whilst the amplitudes of permeability Kc_y in unidirectional preforms are adequate, variability might be somewhat overestimated. The former assumption is well supported by experimental results. Tow permeability is largely irrelevant in saturated flow.

Variation in through-thickness conductivity kc_z was limited even for different stacking sequences. From a modelling perspective the effect of imperfect tow superimposition would be interesting to assess, though simulation results indicate that this is likely to be minor. Observed effects of vf_t and vf_c for the realistic situation of a composite of constant vf_c produced from reinforcements of constant surface density ρ_s were not intuitive, showing the value of unit cell modelling.

As expected, static loading simulations led to negligible variability in stiffness. However, one can safely state that analysis of failure would lead to a different conclusion. Unit cell modelling of carbon fibre reinforcements makes possible the quantification of effects that cannot be readily tested. It also enables quantifying the relation between the reinforcement configuration and selected physical properties pertaining to processing and performance of the composite materials, the expected variability for these physical properties. Crucially, it also enables the designer to assess which element of the reinforcement configuration must be controlled to a high level of repeatability in order to ensure reproducible manufacturing and performance of the composite parts. Simulation results were well corroborated by experiments in all cases.

3.9 Conclusion

Meso-scale simulations of the in-plane permeability, thermal through-thickness conductivity and in-plane stiffness of unidirectional and bidirectional carbon fibre reinforcements and composites were presented and validated. The effect of reinforcement configuration was quantified systematically and assigned to specific geometric parameters. Variability was quantified for each property at a constant composite fibre volume fraction vf_c. It was observed that variability differs strongly between properties; the behaviour can be related to variability levels seen in experimental measurements.

Table 3.4: Significant parameters and contrast values ć

#	Parameter	Contrast value
	Kr_x Permeability along tows, [0°] material 1	
1	gh Horizontal inter-tow gap	ć = + 8.38×10^{-10} m^2
2	n Hyperellipse tow section power	ć = + 3.92×10^{-10} m^2
3	tw Tow width	ć = - 3.58×10^{-10} m^2
4	gv Vertical inter-tow gap	ć = + 2.66×10^{-10} m^2
	Kr_y Permeability across tows, [0°] material 1	
1	gv Vertical inter-tow gap	ć = + 7.84×10^{-11} m^2
2	n Hyperellipse tow section power	ć = + 6.04×10^{-11} m^2
	Kr_x Permeability along axis x, [0°/90°] material 2	
1	gh Horizontal inter-tow gap	ć = + 4.70×10^{-10} m^2
2	tw Tow width	ć = - 2.05×10^{-10} m^2
3	gv Vertical inter-tow gap	ć = + 1.87×10^{-10} m^2
4	n Hyperellipse tow section power	ć = + 1.76×10^{-10} m^2
	kc_z Through-thickness conductivity, [0°] material 1	
1	n Hyperellipse tow section power	ć = + 0.0547 W/mK
2	gv Vertical inter-tow gap	ć = - 0.0170 W/mK
3	tw Tow width	ć = - 0.0164 W/mK
4	gh Horizontal inter-tow gap	ć = + 0.0163 W/mK
	kc_z Through-thickness conductivity, [0°/90°] material 2	
1	n Hyperellipse tow section power	ć = + 0.0509 W/mK
2	tw Tow width	ć = - 0.0147 W/mK
3	gv Vertical inter-tow gap	ć = - 0.0129 W/mK
4	gh Horizontal inter-tow gap	ć = + 0.0112 W/mK

Chapter 4

Particle-based modelling of the compaction of fibre yarns and woven textiles

4.1 Preamble

Chapter 4 contains results obtained from particle-based modelling of textiles subjected to compaction normal to their plane. An introduction to particle-based modelling, as explored in chapter 2, was included again for publication purposes. Compaction simulations were executed on aligned fibres and also on single layer and double-layer plain woven textiles. Selected experimental validation work was performed on woven textiles, and compared well with simulations. Parameters investigated in this work were the effect of different contact and lateral yarn compaction models, domain size and relative positioning of textile layers.

Models aimed at assessing the behaiviour of yarns when loaded in compaction normal to their axis were Hertz' contact model along with Gutowski's compaction model. Suitability of using these models was studied and validated with different materials including copper fibres as a higher modulus material and Nylon 6/6 fibres as a low modulus material. This work introduces realistic geometric modelling of textile reinforcements done in parallel with modelling of their mechanical behaviour, during compaction. Other elements of mechanical behaviour are investigated in following chapters. Results reported in this chapter were accepted in final form for publication in a peer reviewed journal paper [104].

4.2 Abstract

This paper proposes a particle-based modelling method for predicting the constitutive behaviour of textiles when subjected to various compressive loading conditions. The method, which is demonstrated for stacked layers of plain woven textiles, utilizes discrete mechanics as an alternative to traditional continuum mechanics. Fibres are modelled as a series of conjoined points, and their configurations are determined mechanistically using a modified Metropolis algorithm and inter-particle strain energy terms. The implementation presented in this paper enables intricate geometric modelling of textiles at the microscopic, mesoscopic and macroscopic scales. It also enables extensive mechanical modelling of the textiles, from first principles, as they are loaded upon manufacturing of typical technical textile structures. While this paper focuses on the compaction behaviour of weaves, the modelling method is readily adaptable to the analysis of shear, bending, buckling, punching, relaxation and other loading scenarios applied on a wide array of textiles of different types. These scenarios will be described in forthcoming publications.

Comparative data from in silico and in situ testing shows excellent agreement. Results demonstrate an improvement in simulation accuracy over comparable, prior modelling

techniques. The method presented here successfully predicts the actual behaviour of yarns, single layer and double-layer textile stacks in compaction.

4.3 Introduction

Technical textiles and structures such as components for artificial organs, load-bearing elements in architectural tensile surface structures, preforms used as reinforcements for high-performance polymer composites, and others are subjected to various shaping and forming operations at the manufacturing stage, and to a large array of load cases in service. The constitutive mechanical behaviour of such textiles is intimately linked to their construction and internal configuration [85, 90], which in turn have a strong influence on other physical properties such as the thermal conductivity, permeability to fluids, and others [101]. The geometrical configuration of textiles is altered by normal compaction pressure (P), affecting operations such as coating and calendering for example. Textile thickness is reduced; furthermore, the configuration of yarns in the textile is altered. Elastic and plastic deformations are imparted to the yarns leading to yarn flattening, shifting within textile layers, and nesting at higher fibre volume fractions (v_f). These factors result in very complex textile geometry at the scale of the yarn and repeating unit cell. Predetermination of stress-induced geometric changes during manufacturing or service is crucial to understanding processing behaviour and predicting mechanical performance; relatively small changes in textile geometry can have major effect on physical properties. Anticipating such changes also is useful in documenting which aspects of textile geometry and configuration must be controlled to ensure reproducible physical properties.

Recent geometric and constitutive models were proposed for heterogeneous fibre assemblies featuring yarns and defined textile architectures. Wang and Sun [127] modelled individual yarns as a series of rigid elements joined by frictionless pins acting as ball-joints, to simulate yarn paths in simple twisted yarn assemblies and 3D braids. The model enabled quantitative analysis on the distribution of yarn orientations and fibre volume fraction v_f in such textiles; v_f within yarns and the behaviour of individual fibres were not considered. Simulations were restricted to small numbers of yarns due to computational restrictions.

Zhou et al. [134] employed a finite-element method using stiffness matrices and boundary conditions defined for multi-chain digital elements, to predict yarn deformations based on the displacements of joints defined in the simulated yarns. The technique was limited to small numbers of digital chains within each yarn. Deformations of yarn cross-sections and paths as well as fluctuations in v_f were available as output of simulations of the braiding process.

Sun and Sun [118] used a similar method for investigating the microstructure and mechanical properties of 3D braided rectangular preforms, and compared simulation results with those obtained from topological models featuring yarn interaction, and from experimental trials. Discrepancies were observed for tensile and shear stiffness, between experimental results and simulations.

Miao et al. [74] presented algorithms for reducing computational demand while increasing simulation accuracy through targeted use of a coarser digital element mesh. Two critical issues were addressed in overcoming limitations of the digital element approach. Firstly, the original shape of a yarn and its influence on the final geometry was investigated and the authors found a negligible effect. Secondly, accuracy associated with the number of digital elements in a yarn was explored and minimal effect was observed when compared with experimental results. As with other studies cited above, computational demand was a difficulty and simulations were limited to small numbers of elements in the systems modelled.

Zhou et al. [133] investigated the effect of compression under a vacuum bag on fabric geometry, using another digital element approach. Fibres within yarns were represented using digital elements woven into a textile, and the vacuum bag was modelled as a fish-net type structure. In this work a smoothing method was used for obtaining a solid model of yarns from fibre distributions. Experimental results showed good agreement with a number of simulations.

Maze et al. [72] simulated the geometry and compaction of highly porous stacks of continuous thermoplastic fibres, aiming at modelling the thermal calendaring of non-woven. Following on the work of Niskanen and Alava [78], fibres with square sections represented as series of cubes were laid along axes x and y only, in varying proportions. Fibre sections remained unchanged upon compaction. Non-elongating fibres separated by statistically set transverse gaps were precluded from moving in the x-y plane upon compaction, which is appropriate in the context of thermal calendaring where fibres may fuse together as opposed to sliding past one another upon compaction. Initial v_f values were well below 10%, and the fibre stacks featured no structure at the mesoscopic scale, in the sense that fibres were not grouped explicitly into yarns as they are in woven fabrics. The purely geometric compaction algorithm simulated fibre bending through a unified parameter. The authors report v_f values up to 50% upon compaction, resulting from fibre bending.

While useful in specific applications, the above approaches suffer from limitations. Most importantly these methods lead to good agreement with experimental results, but under strictly controlled conditions or for materials that are distinctly different from those studied here. Furthermore, they are limited to a few selected applications and are applied to specific cases with precise initial conditions.

The approach described in this paper aims at overcoming limitations of the prior methods and at improving computer-based simulation of the geometry and constitutive behaviour of textile structures, by integrating particle displacements and strain energies in modelling interactions between system components (fibres), subcomponents (fibre particles) and the external environment (typically a plate).

Deformation of the fibres results from external, imposed boundary motions as well as from internal, fibre-to-fibre contacts. Strains in fibres result from relative displacements of individual fibre particles in the three-dimensional space. Strain energy in fibres results from physical strains which cause deviations away from a state of lowest energy in the textile. Displacements, strains and energy may change in a system as a result of a boundary motion, in response to the application or removal of pressure, or during a relaxation phase resulting from the stabilisation or removal of a displacement or pressure.

Particle-based modelling provides an accurate and general numerical tool for simulating the large-strain constitutive behaviour of non-homogeneous or structured textiles, by accounting for the detailed geometric configuration at fibre scale. In this work, particle-based modelling simulations of fibre assemblies were used for locating fibre positions and quantifying fibre interactions that minimize the total strain energy stored in the textile during compaction. The program used for modelling fibre interactions during compaction uses several simulation steps wherein each step comprises an iterative series of calculations modelling the fibre assembly as it is taken from an arbitrarily chosen initial state to a state wherein the fibres contain minimum strain energy. Specific details about the algorithm and the manner in which strain energies are calculated appear in following sections. Briefly, each calculation is based on a modified Metropolis algorithm adapted to 1) specific interaction functions [72], and 2) a specific acceptance function [78]. Compaction displacements impose evolving boundary conditions for a set of iterative calculations determining the textile geometry at each step. In addition to the determination of fibre position shifting, the simulations produce information pertaining to changes in yarn shapes, contact configurations and forces [73, 128].

Additionally, a parallel can be drawn between the iterative process and the time-dependent relaxation behaviour of textiles. That is, the same modelling method and framework can also be used for predicting fibre relaxation behaviour at the cessation of compaction either from removal of pressure, steady-state application of pressure or constant platen spacing. Modelling the time dependence of particles or fibre interaction is thus an integral part of the method with only one time-scaling parameter being required between the number of iterations and relaxation time. This aspect of the constitutive behaviour will be explored in a forthcoming paper.

4.4 Modelling methodology

Fibres are represented by a series of discrete spherical particles with diameters equal to the fibre diameter. The relative positions of individual particles in a series collectively describe the fibre geometry. By tracking the response or displacements of individual particles interacting with neighbouring particles, the overall behaviour of the system is modelled. Particle-based modelling differs from traditional continuum mechanics; it enables more thorough expression of the geometry of discontinuous assemblies making a textile, especially when subjected to large strains. Changes in strain energy in individual and interacting fibres are determined in predicting and validating particle displacements as textiles are compacted.

4.4.1 Modelling method

A modified Metropolis algorithm [72] with Boolean function [78] was used for enabling accurate discrete particle modelling of the geometry of textiles. The modified Metropolis algorithm iterates particle positions towards configurations of lower strain energy, ultimately defining the geometry of the textile under constant boundary conditions. Iterations on particle positions are performed within a physical subspace [-a, a] with a step size limitation and uniformly distributed random walk, for a number of particles that is sufficient for intricate representation of geometrical features. Within each compaction step and under constant boundary conditions, tentative configuration changes are attempted iteratively by adding a small displacement of random amplitude to the x, y and z coordinate of a randomly chosen particle. This results in a strain energy differential between configurations before and after the displacement. If the differential is negative and strain energy is reduced in response to the displacement of the single particle, the new configuration is validated and becomes the initial state for the next iteration, still under the same boundary conditions. Conversely if the strain energy remains constant or increases, the new configuration may still be accepted if the result satisfies statistical arguments using predefined probabilities [99] based on a Boolean decision function. The number of iterations required for the system to reach a stable state of lower strain energy depends on several factors and is usually estimated empirically. Afterwards, boundary conditions are changed to reflect on-going compaction and the iterative procedure is repeated.

4.4.2 Strain energy terms

Compaction of the textile as described above induces interaction forces between the particles, producing stresses and strains within the fibres. Strain energy results from i) relative displacement between particles within a single fibre (intra-fibre strain energy), and ii) fibre deformations resulting specifically from interactions between neighbouring fibres in a yarn (inter-fibre strain energy).

Intra-fibre strain energy

For each fibre, particle displacement leads to changes in the fibre's strain energy which can be associated to axial tension, axial compression or bending stresses; fibre torsion is disregarded and radial fibre compression is discussed in the next section. For each fibre segment, strain energy in axial tension or compression is a function of Young's modulus E, fibre cross-section A, and actual and initial distances between 2 particles L_{mn} and L, Figure 4.1. In Equation 4.1, values of E and A are embedded into axial stiffness K_{mn}.

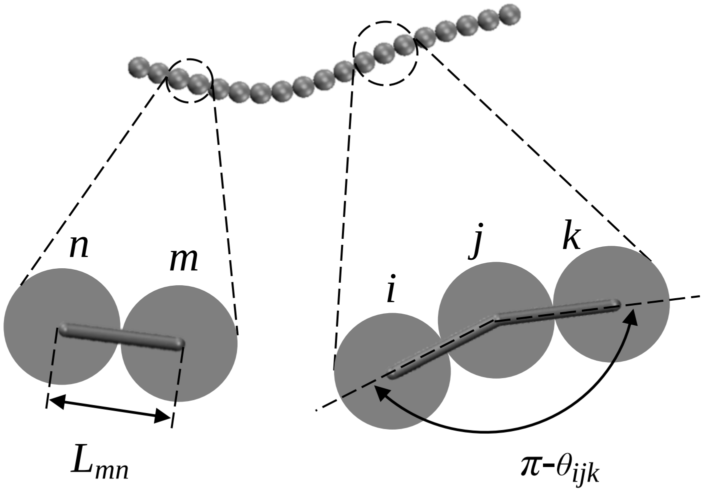

Figure 4.1: Tension/compression axial strain energy between two particles (right) and bending strain energy between three particles (left)

$$U_a = -0.5K_{mn} \cdot (L_{mn} - L)^2 \tag{4.1}$$

where $K_{mn} = AE/L$

Bending strain energy is calculated using angle θ_{ijk} defined between particles i and k framing particle j as illustrated in Figure 4.1; strain energy is calculated for both halves of segments ij and jk adjacent to particle j. The strain energy stored in a fibre characterized by Young's modulus E, second moment of area I for circular fibres and total length between 3 particles $2L$ when subjected to pure bending is defined in Equation 4.2.

$$U_B = \frac{EI}{2L} \cdot (\pi - \theta)^2 \tag{4.2}$$

where $L = (L_{ij} + L_{jk})/2$

It should be noted that the above equation calculates bending strain energy in 2 neighbouring half-segments. In the implementation, when particle j is moved the angle θ_{ijk} changes, as do angles θ_{hij} and θ_{jkl}. The change in bending energy over all half-segments involved is calculated along with other energy terms, and then the energy differential is evaluated.

Inter-fibre strain energy: Hertz' model

Contact forces between two elastic bodies with curved surfaces may be calculated using the Hertzian theory [100] where E^* is the representative modulus of the two contacting bodies with modulus E and Poisson's ratio υ, as defined by Hertz:

$$E^* = \frac{E}{2 \times (1 - \upsilon)^2} \tag{4.3}$$

and h is the penetration distance for two fibres of radius r, Figure 4.2. For fibres having the same radius, the contact distance is:

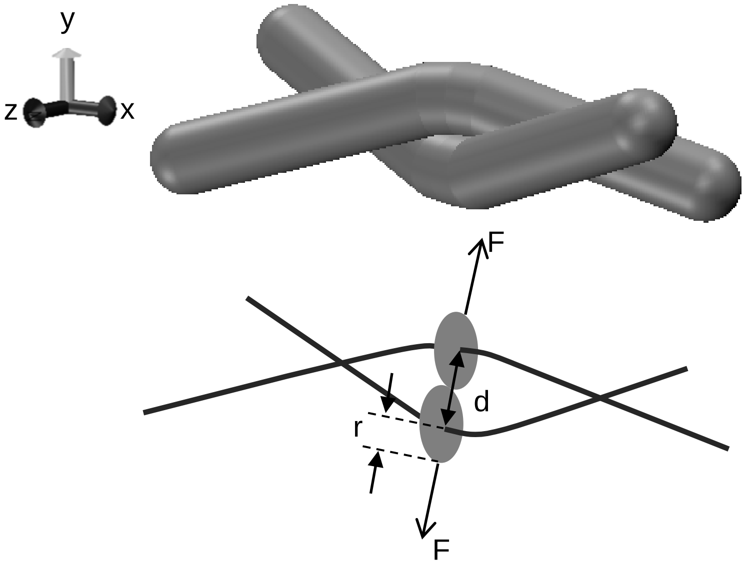

Figure 4.2: Contact between the curved surfaces of two fibres

$$\begin{aligned} h &= 2r - d \qquad && (\text{if } \; d \leq 2r) \\ h &= 0 \qquad && (\text{if } \; d > 2r) \end{aligned} \tag{4.4}$$

Hertz' contact force F_H and strain energy U_H for the elastic radial compression is given as [89]:

$$F_H = \frac{4}{3}.E^* r^{0.5} h^{1.5} \tag{4.5}$$

$$U_H = \int \frac{4}{3} E^* r^{0.5} h^{1.5} \cdot dh = \frac{8}{15} E^* r^{0.5} h^{2.5} \tag{4.6}$$

Inter-fibre strain energy: Gutowski's model

Contact forces between curvilinear fibres within a fibre assembly such as a yarn may also be calculated using Gutowski's compaction model [47]. Gutowski's compaction model states that instead of being perfectly straight individual fibres within yarns are wavy. A fibre sub-domain with radius r, projected length L, modulus E and second moment of area I submitted to 3-point bending as a result of inter-fibre contact force F is illustrated in Figure 4.3. The relation between vertical deflection δ and the contact force F at the centre of the fibre is:

$$\delta = \frac{FL^3}{192EI} \tag{4.7}$$

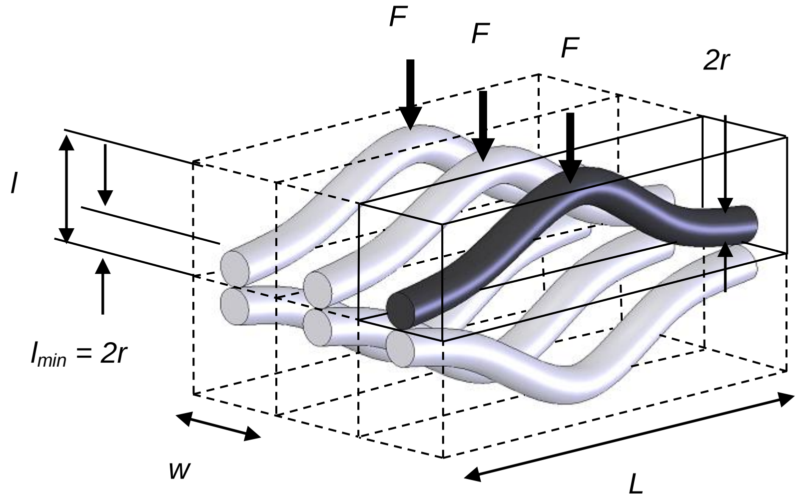

Figure 4.3: Fibre segments and encompassing prisms in Gutowski's model

Projected length L and deflection δ are related to other dimensions as follows:

$$\begin{aligned} L &= \beta(l - l_{min}) \\ \delta &= (l_o - l) \end{aligned} \tag{4.8}$$

where l, l_{min} and l_o are the actual, minimal and initial height of a rectangular cuboid encompassing the fibre and β is a parameter either evaluated by microscopy or fitted to experimental results. It is assumed that l_{min} is equal to $2r$. The width w of the cuboid is assumed to stay equal to its height at all times during compaction. The model relating the compaction pressure P_G calculated from the above to v_f is:

$$P_G = \frac{F}{Lw} = \frac{3E\pi}{\beta^4} \cdot \frac{\left[\sqrt{\dfrac{v_f}{v_o}} - 1\right]}{\left[\sqrt{\dfrac{v_a}{v_f}} - 1\right]^4} \tag{4.9}$$

where v_a and v_o represent the initial and maximum values of v_f ; whilst in its basic form Gutowski's model would not allow values of v_f higher than $\pi/4$, parameters v_a and v_o are used as fitted parameters. From Gutowski's model the strain energy is calculated by integrating force over distance for the displaced particle interacting with surrounding fibres; for a displaced particle separated by distance l_{ij} with $l_{min} < l_{ij} < l_o$, strain energy is calculated as:

$$U_G = \int F_{ij} \cdot dx = \int \frac{192EI}{\beta^3} \cdot \frac{(l_o - l_{ij})}{(l_{ij} - l_{min})^3} \cdot dl_{ij} \tag{4.10}$$

where l_o is the initial distance between particle centres and l_{min} is the fibre diameter. Again, tentative positions are maintained if U_G is reduced. Gutowski's model is equivalent to the beam bending equation, with reducing span; it has been used successfully in many occurrences [19, 39, 83].

Calculation of compaction pressure P and fibre volume fraction v_f

Compaction is simulated by progressively reducing the domain height. Fibres located near the upper boundary are displaced accordingly, total strain energy is minimized iteratively, and P is recalculated at each step by summing vertical components of forces applying on the horizontal boundary.

Values of v_f are obtained in two ways in this work. v_f calculation method 1 proceeds by identifying fibres crossing a rectangular plane and adding individual cross-section areas, accounting for any angle between the normal to the plane and the local fibre direction. Plane height corresponds to domain height and plane width is, at most, the minimum width that encompasses all fibres. The sum of section areas is then divided by the plane area. v_f calculation method 2 proceeds by calculating the volume of all fibres whilst neglecting compaction of individual fibres as per Hertz' model, and dividing by the volume of the smallest rectangular cuboid encompassing all fibres.

4.5 Simulations and validation experiments

Three series of simulations of increasing complexity were performed; only the latter two were validated by experimental results as this was not relevant for the first series.

Series 1 features 2 cases where two superimposed fibres are compacted between two platens. Lateral fibre displacements are restricted. Interaction forces between the two fibres are modelled using either the Hertz' contact function (series 1.1) or the Hertz' contact function and Gutowski's function combined (series 1.2). The purpose of series 1 is to verify that the modelling environment replicates the basic functions accurately, and show the difference in behaviour for the 2 functions.

Series 2 features 3 cases where yarn compaction is studied. The purpose is to assess the deformation of compacted yarns, especially lateral displacement as well as yarn widening and flattening. The statistical nature of the simulations is investigated by conducting groups of identical simulations for each case. Yarn compaction is studied for a single yarn with restrictions on lateral fibre displacement (series 2.1), a single yarn with no restrictions on lateral fibre displacement (series 2.2) and 2 superimposed yarns laid perpendicularly (series 2.3). Fibre diameters were measured using a micrometer; 50 samples were used. Diameter of Nylon 6/6 and copper fibres were 299 ± 1 μm and 297 ± 2 μm respectively. Tensile tests were performed using an Instron 4482 universal testing frame equipped with a 1 kN load cell; 10 samples with gauge length of approximately

100 mm were used. Young's moduli of Nylon 6/6 and copper fibres were 1.05 ± 0.02 GPa and 117 ± 3 GPa. Compaction tests were performed using the same Instron frame and cell. Aligned copper and Nylon 6/6 fibres were compacted between a lower rectangular cavity measuring 2.5 mm by 40 mm and flat cover, enabling compaction of aligned fibres in a laterally constrained domain corresponding to series 2.1, Figure 4.4 .

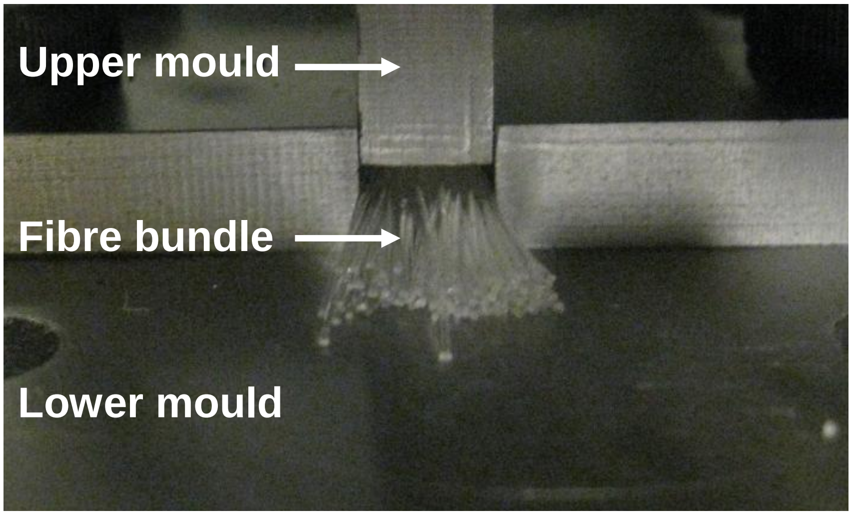

Figure 4.4: Compaction rig for single yarn with restrictions on lateral fibre displacement

It should be noted that whilst use of copper fibres in textile applications is limited, the fibres were used in this work for the following reasons: i) use of Gutowski's model is validated for fibres with significantly different stiffness, and likely different waviness; ii) copper and Nylon 6/6 fibres used in this work have diameters that are both similar and sufficiently large for enabling modelling of each fibre individually; iii) copper modulus is closer to that of high-stiffness structural fibres, which are a primary target in the development of the model; iv) copper textiles are used as lightning protection devices in polymer composite structures, in line with the author's background.

Series 3 features 2 cases where the compaction of a single layer of plain weave textile is studied. The purpose is to look at yarn deformation and reorganisation within a textile, and at the joint effect of boundary conditions and domain size. Again the statistical nature of the simulations is investigated. Single layer compaction is studied for a single unit cell within an extended textile domain (series 3.1) and the full domain (series 3.2). Validation was conducted by manufacturing 30 textile samples measuring 100 mm × 100 mm, Figure 4.5, and testing using the aforementioned Instron frame and cell. Yarns in each sample contained 30 monofilament Nylon 6/6 fibres, with 5 mm yarn spacing in both directions. Other characteristics of the fibres and textile samples appear in Table 4.1.

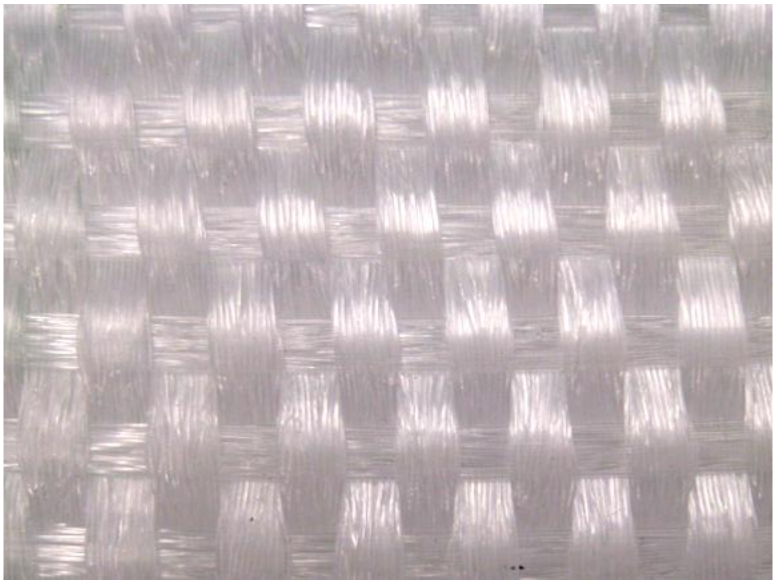

Figure 4.5: Manufactured textile with Nylon 6/6

Table 4.1: Characteristics of fibres and textiles

Properties		**Number of samples**
Fibre diameter ($2r$)	0.296 ± 0.001 mm	50
Fibre density	1.172 ± 0.001 g/cm^3	20
Initial v_f of preform	25 ± 3.1 %	10
Surface density of preform	0.117 ± 0.001 g/cm^2	10
Number of fibres in yarn	30	20

Two parallel 40mm × 40mm platens were carefully mounted and aligned in the frame, ensuring uniform compaction, Figure 4.6. Stiffness of the platens and frame were measured and any platen assembly deformation was removed from the raw compaction data. First, 10 different tests were conducted on single-layer samples, with 5 consecutive compaction cycles performed on 1 of these 10 samples. In half of these tests the sample was aligned at 45° from platen edges to verify any orientation effect. Then, 10 different tests were conducted on superimposed, double-layer samples. In 5 of these latter tests, yarns in both textile layers were superimposed as far as practically possible; in the 5 other tests, yarns in both textile layers were staggered as far as practically possible. In all cases, a compaction speed of 0.5 mm/min was used.

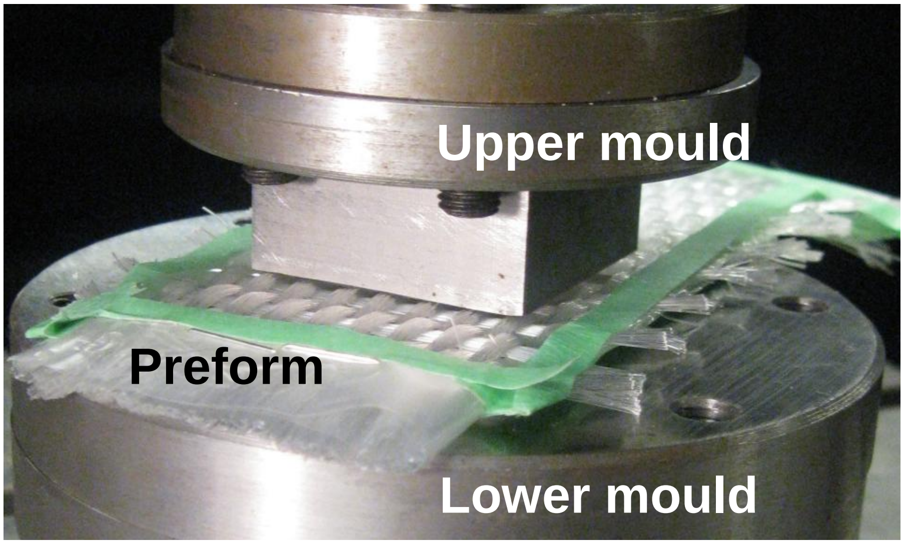

Figure 4.6: Compaction rig with a single layer textile

4.5.1 Series 1: fibre compaction

This section features series 1.1 and 1.2. Two parallel and superimposed Nylon 6/6 fibres with 300 μm diameter and 1 GPa Young's modulus were compacted between platens. Lateral displacements were precluded through rigid side domain boundaries with domain width equal to fibre diameter. Series 1.1 used Hertz' contact function whilst series 1.2 included both Hertz' and Gutowski's functions.

Simulation results for series 1.1 and 1.2 appear in Figure 4.7, along with predictions from Hertz' equation only and Gutowski's equation only. Data points identified as calculation results in Figure 4.7 were obtained from equations 5 and 6; in the case of Gutowski's model, parameters $\beta = 200$, $v_o = 0.25$ and $v_a = 0.80$ were selected as first estimates from past experience, as these curves aimed at validating implementation in the simulation software and were not to be fitted to experimental results.

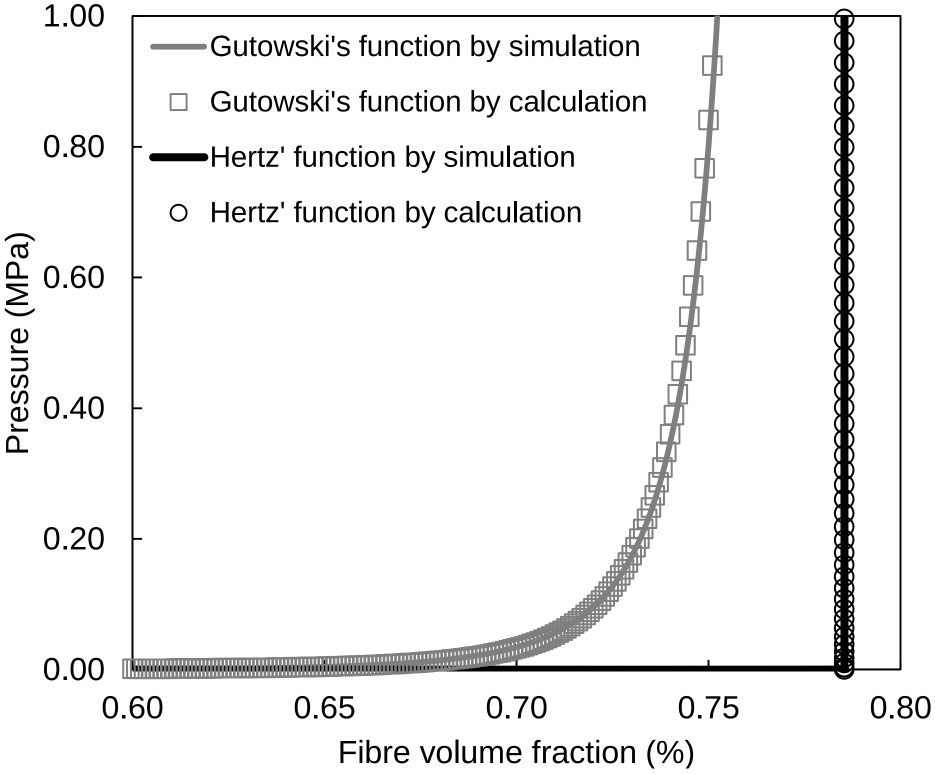

Figure 4.7: Results of the compaction of two superimposed fibres with lateral constrains (series 1)

For series 1.1 contacts between parallel fibres and a rapid build-up in pressure corresponding to deformation of actual fibre cross-sections start at a $v_f = \pi/4$ as expected for square fibre packing. For series 1.2, P increases more gradually with v_f with non-zero values seen at lower v_f as suggested in several prior studies [19, 47]. Higher values of pressure are achieved at v_f values lower than $\pi/4$, hence Gutowski's function takes clear precedence over Hertz' in predicting the compaction behaviour at these relatively low pressures, where radial compaction of the fibres will be negligible. Significant changes in pressure start at around 65% v_f ; 1 MPa is reached at approximately 73% v_f .

4.5.2 Series 2: yarn compaction

This section features series 2.1, 2.2 and 2.3.

For series 2.1, simulations were performed where various single yarns made of 30 fibres of copper and Nylon 6/6 were compacted between two parallel platens. Lateral boundaries were present, forbidding lateral displacement of fibres beyond the initial yarn width, Figure 4.8. Strain energy terms arising from axial tension/compression, bending and lateral compaction were present. Firstly, copper yarns were simulated where yarn compaction was modelled using either Hertz' or Hertz' and Gutowski's functions.

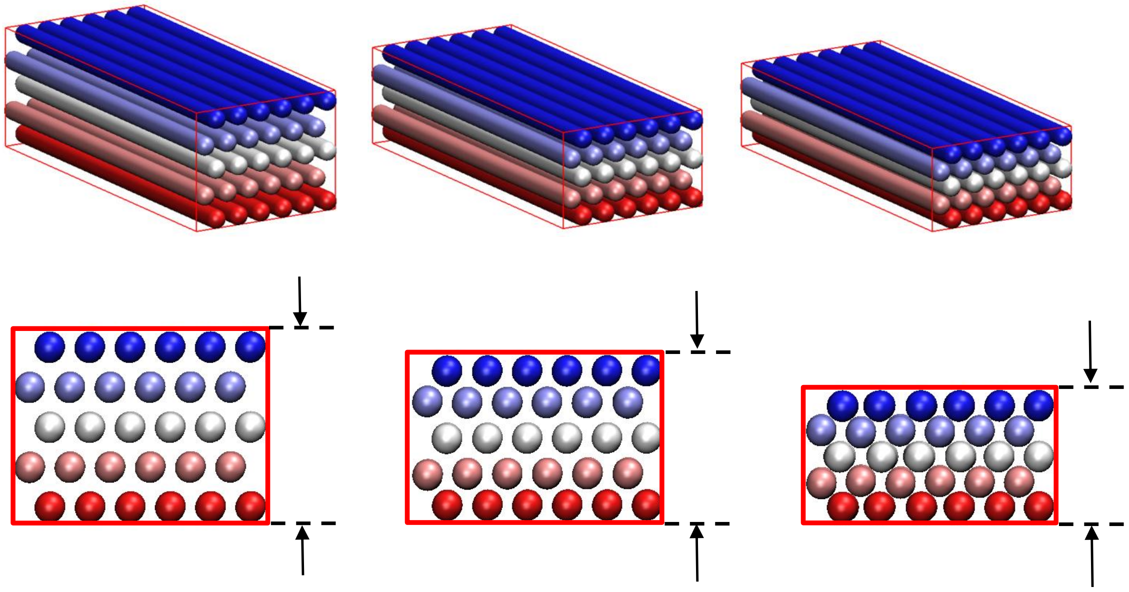

Figure 4.8: Single yarn compaction with restrictions on lateral fibre displacement (series 2.1)

Comparison with experimental results led to including Gutowski's function for modelling compaction as discussed below. Secondly, Nylon 6/6 yarns were simulated where yarn compaction was modelled using Hertz' and Gutowski's functions. Comparison with experimental results validated that choice as discussed below. Two Nylon 6/6 fibre lengths were simulated to assess the effect of this parameter. The numbers of fibres in yarns and of particles in fibres were selected from early trials, with a view of obtaining yarns exhibiting progressive compaction behaviour within acceptable simulation run times. The numbers compare favourably with those used in published work [39, 47].

Yarns made of 30 copper fibres with 300 μm diameter and laid in hexagonal arrangements were simulated, first using Hertz' function and then using both Hertz' and Gutowski's functions for modelling compaction. Copper fibre modulus was set at 117 GPa. Simulations were performed with 100 000 iterations per compaction step; values of the compaction step and maximum particle displacement were both 0.001 μm when using Hertz' function, or 0.1 μm when using Hertz' and Gutowski's functions. Initial distance between platens was 1.2 mm when using Hertz' function, or 1.9 mm when using Hertz' and Gutowski's functions. Gutowski parameters were $\beta = 450$, $v_o = 0.42$ and $v_a = 0.80$ for copper fibres. 5 identical simulations were repeated for each of these series, featuring fibres made of 20 particles corresponding to a length of 6 mm.

In simulations of copper fibres where only Hertz' function was employed, P was null up to a v_f of 0.718 and rose rapidly afterwards. This value differs from $\pi/4$ seen in series 1.1 because of the hexagonal fibre packing and domain shape; as the lateral boundaries preclude lateral fibre motion, the value of v_f at which P increases depends on the dimensions of the domain. More generally, simulation results do not correlate the trend seen with experimental results, Figure 4.9.

Simulations of copper fibres where Gutowski's function was employed lead to a com-

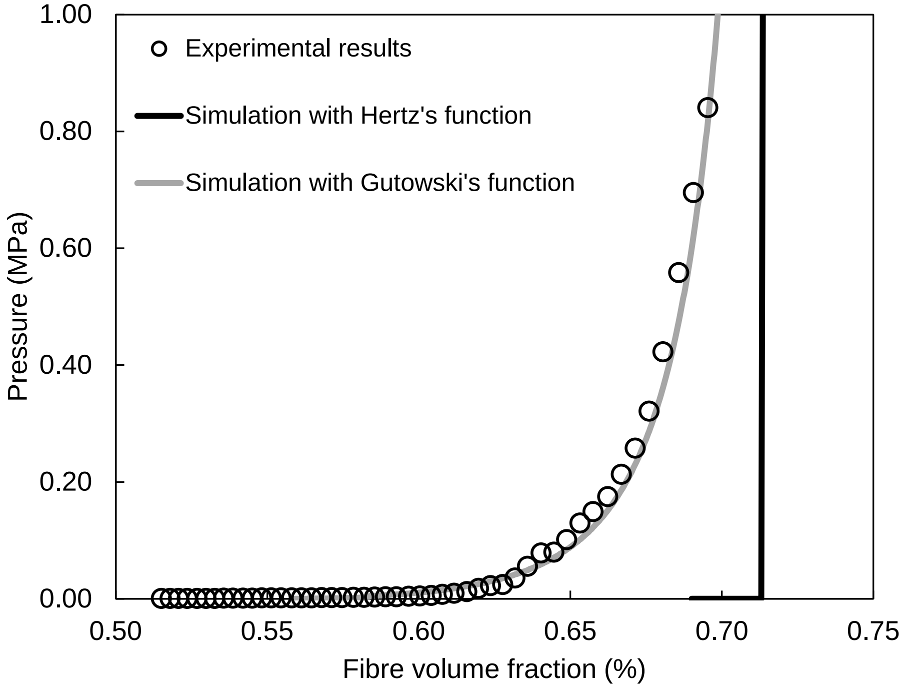

Figure 4.9: Results of single copper yarn compaction with lateral restrictions (series 2.1)

paction behaviour matching experimental results much more closely upon selecting appropriate parameter values. Hertz' function assumes perfectly straight fibres; experimental evidence shows that real fibres do not conform to this idealised geometry. In view of these results, yarns made of 30 Nylon 6/6 fibres with 300 μm diameter and laid in hexagonal arrangements were simulated. Fibres were made of either 20 or 40 particles corresponding to lengths of 6 and 12 mm respectively. The number of iterations, compaction step, maximum particle displacement and initial distance between platens were unchanged. Gutowski parameters were $\beta = 200$, $v_o = 0.28$ and $v_a = 0.79$ for Nylon 6/6 fibres. 5 simulations with identical initial states were performed for each fibre length. Simulation results for Nylon 6/6 were validated experimentally. As shown in Figure 4.10, simulations replicated experimental results very well especially at higher pressures, and no discernible effect of length could be identified.

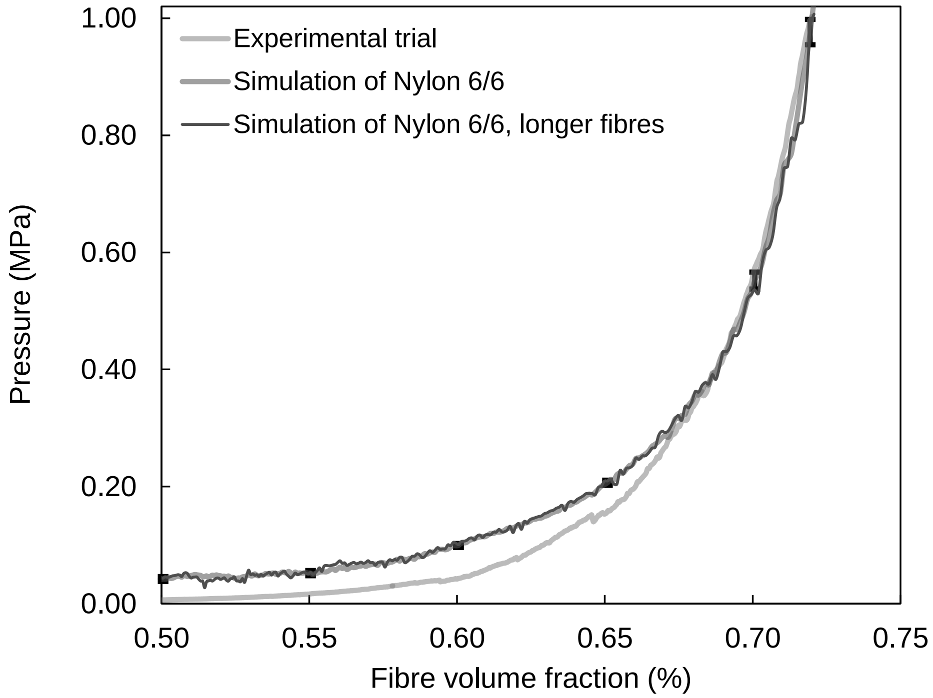

Figure 4.10: Results of single Nylon 6/6 yarn compaction with lateral restrictions (series 2.1)

In series 2.2, simulations were performed where a single yarn made of 34 Nylon 6/6 fibres was compacted between two parallel platens. The higher number of fibres was used in creating a representative, generic yarn cross-section. No lateral boundaries were present thereby allowing lateral displacement and rearrangement of fibres during compaction, leading to lateral expansion of the yarn beyond its initial width, Figure 4.11. Strain energy terms arising from axial tension/compression, bending and lateral compaction were present. The latter was simulated using both Hertz' and Gutowski's functions with the same parameters as above; the modulus, number of iterations, compaction step and maximum particle displacement were unchanged. Initial distance between platens was higher at 2.3 mm to ensure null forces between fibres at the onset of simulations. 10 simulations with identical initial states were repeated for this series.

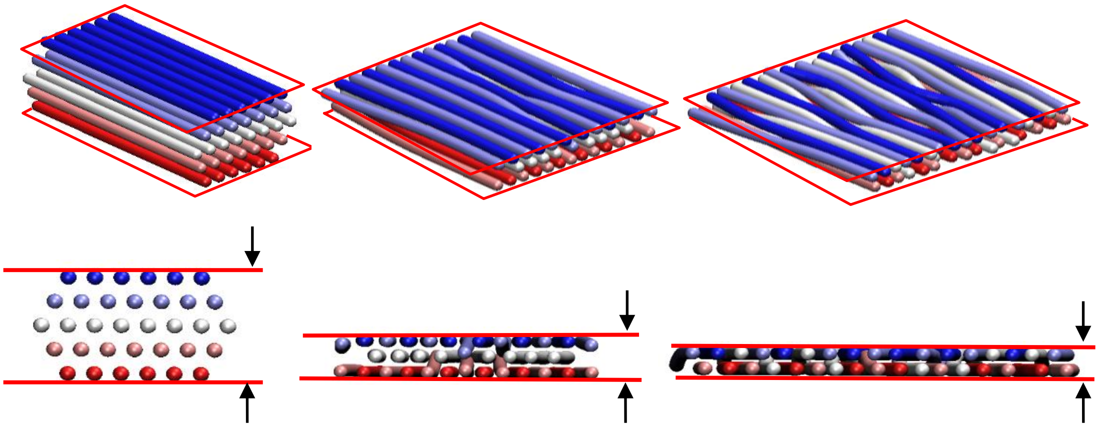

Figure 4.11: Single yarn compaction without restrictions on lateral fibre displacement (series 2.2)

Although particle selection and displacements were random, the resulting compaction behaviour was very similar for 8 simulations with a thickness at 1 MPa corresponding to approximately 2 fibre diameters, Figure 4.12. In these simulations, misalignment of fibres during compaction produced some fibre entanglement which limited further compaction. Small variations in results for these 8 simulations may be further reduced by using increased numbers of particles and fibres. However, it must be noted that 1 simulation featured no entanglement, leading to a completely flattened yarn with a final thickness close to 300 μm and limited pressure build-up beforehand. Furthermore, 1 other simulation lead to 3 fibres being entangled with a final thickness of the order of 900 μm. Such behaviour is to be expected in statistical modelling, and its relative importance reduces as more fibres, longer fibres, more yarns and more realistic boundary conditions are introduced.

It is worth observing the evolution of v_f for series 2.2 where the domain is devoid of lateral boundaries and fibres are not confined to a fixed volume. Figure 4.13 shows values of v_f calculated using method 1 detailed above, over a series of different cross-section

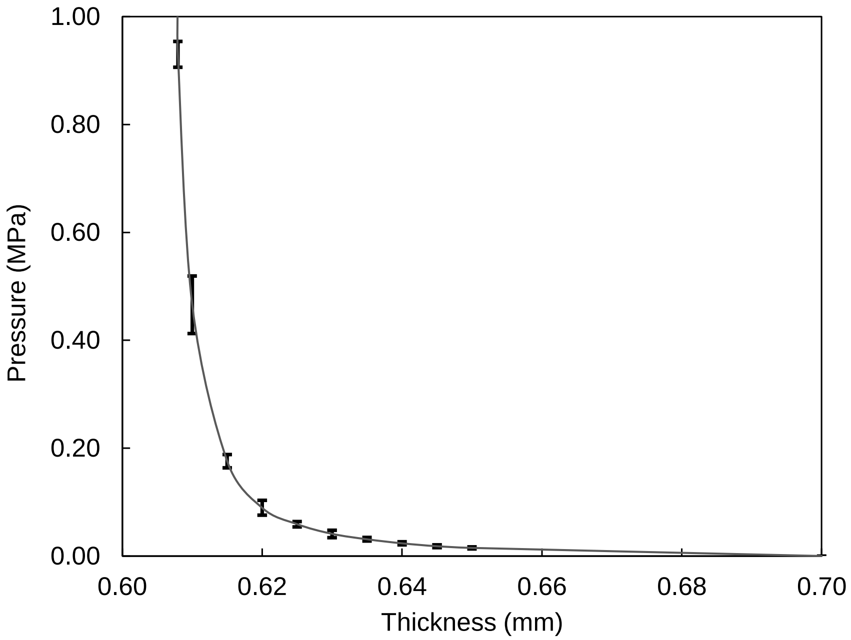

Figure 4.12: Results of 5 compaction trials for yarn without lateral restrictions (series 2.2)

planes normal to axis x. For each reinforcement thickness, 500 cross-section planes were used, with height and width corresponding to domain height and half-domain width, respectively. Whilst v_f is essentially constant between thicknesses 1.00 mm and 0.62 mm, inter-fibre distance stays mostly constant whilst yarn width increases resulting in an increase in compaction force. At lower thicknesses inter-fibre distances reduce, increasing the pressure markedly. Figure 4.14 shows v_f variation within a yarn at thickness = 0.63 mm; v_f fluctuations are well contained around an average value.

In series 2.3, simulations were performed where 2 superimposed perpendicular yarns each made of 34 Nylon 6/6 were compacted between two parallel platens, Figure 4.15. No lateral boundaries were present. The strain energy terms, Gutowski's parameters, modulus, number of iterations, compaction step and maximum particle displacements were unchanged. Initial distance between platens was 5.0 mm. 5 simulations with identical

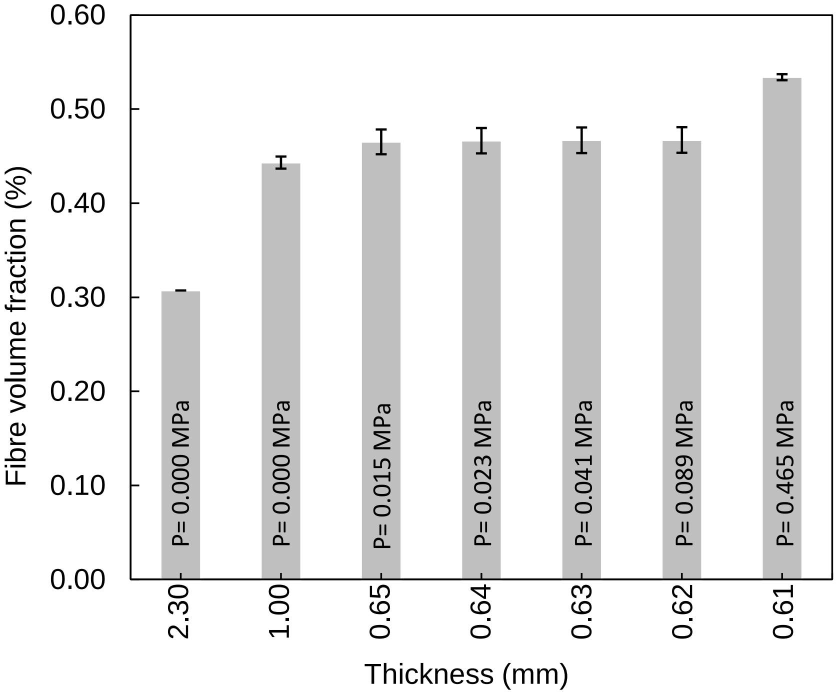

Figure 4.13: Values of v_f over different cross-section planes normal to axis x (series 2.2)

initial states were repeated for this case.

Due to the yarns being perpendicular, fibres in the crossover zone cannot interpenetrate hence they create effective boundaries to relative vertical displacement. In the simulations, compaction proceeded until yarns reached a thickness approximately equivalent to 2 fibres for each yarn, with orthogonalily effectively maintained and no possibility of further compaction at relatively low pressures. Local deformations were observed where yarn compaction was more extensive at the crossover, demonstrating that the simulation environment can predict local deformation which is prevalent in actual cases. No curves of P as a function of v_f are presented because of the domain shape; however, good consistency was seen for the 5 simulations performed.

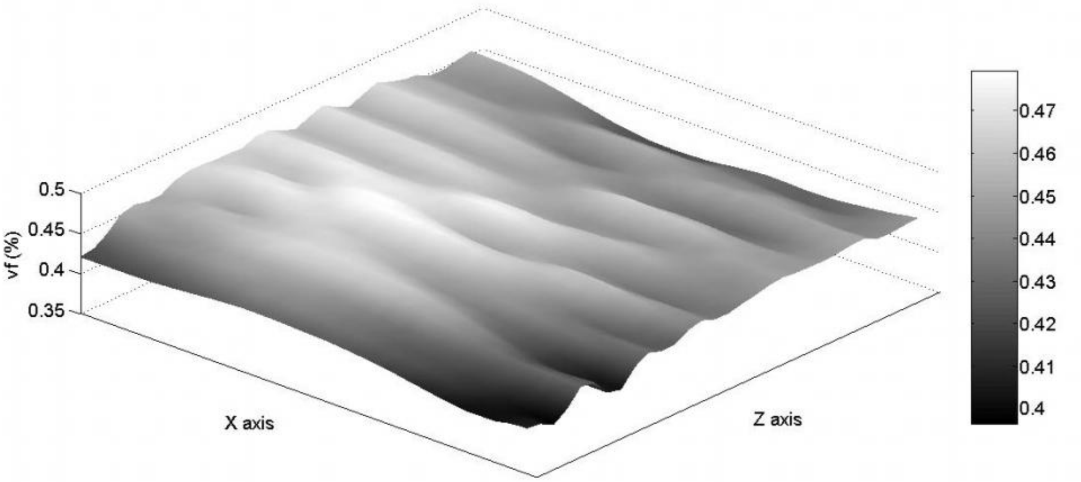

Figure 4.14: v_f variation within a yarn at thickness = 0.63 mm (series 2.2)

4.5.3 Series 3: textile compaction

This section features series 3.1 and 3.2.

In series 3.1, simulations were performed where single unit cells of plain woven textile made of 30 Nylon 6/6 fibres were compacted between two parallel platens as shown in Figure 4.16. Unit cells featured 2 yarns in each direction and 4 crossovers. Simulations were performed both with and without lateral boundaries along the x and z axes. Series 3.2 featured larger textile domains with 4 yarns in each direction and 16 crossovers; no lateral boundaries were used.

Simulations of smaller domains in series 3.1 aimed at reducing run times. Parameter values for series 3.1 were unchanged from those used in series 2.3. Values of P and v_f were calculated over a smaller volume measuring 5 mm along axes x and z and extending over the domain thickness as shown in Figure 4.16.

For series 3.1 with lateral boundaries, the side walls restrict the flattening of yarns along their limited length and induce some lateral bending. For series 3.1 without lateral boundaries, individual fibres can escape laterally. In both cases the compaction behaviour

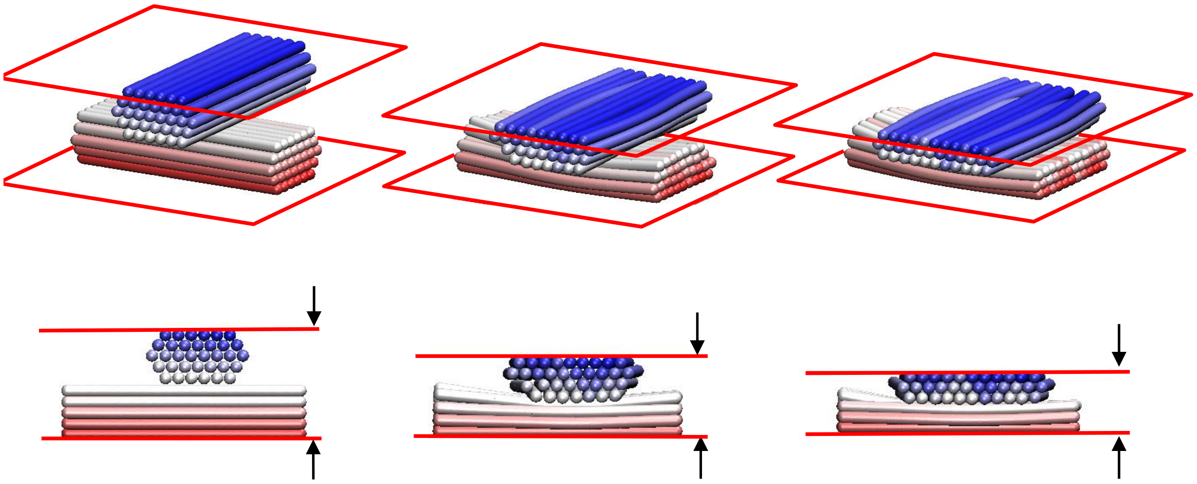

Figure 4.15: Compaction of crossed yarns without restrictions on lateral fibre displacement (series 2.3)

remains generally realistic in the sense that it corresponds to experimental results; for the textile simulated and tested pressure generally increased from a v_f value of 0.36. However, unacceptable fluctuations in the P-v_f curves are present, Figure 4.17; domains simulated are limited in extent, hence displacements and interactions of individual fibres remain visible in the overall compaction curve. Figure 4.18 shows extreme fibre deformations for both scenarios.

In series 3.2, single-layer and double-layer stacks of textiles featuring multiple plain woven unit cells were simulated. All parameters were identical to those used in series 3.1. Values of P and v_f were calculated over larger domains, Figure 4.19. Results shown in Figure 4.20 for the single-layer case matched experimental results well and fluctuations were much reduced, showing the beneficial effect of the larger simulation domain. Following this, double-layer stacks of the same textile were also simulated, firstly with perfectly aligned yarns and secondly with yarns that were perfectly staggered in both directions. The aim of these latter simulations was to investigate the ability of

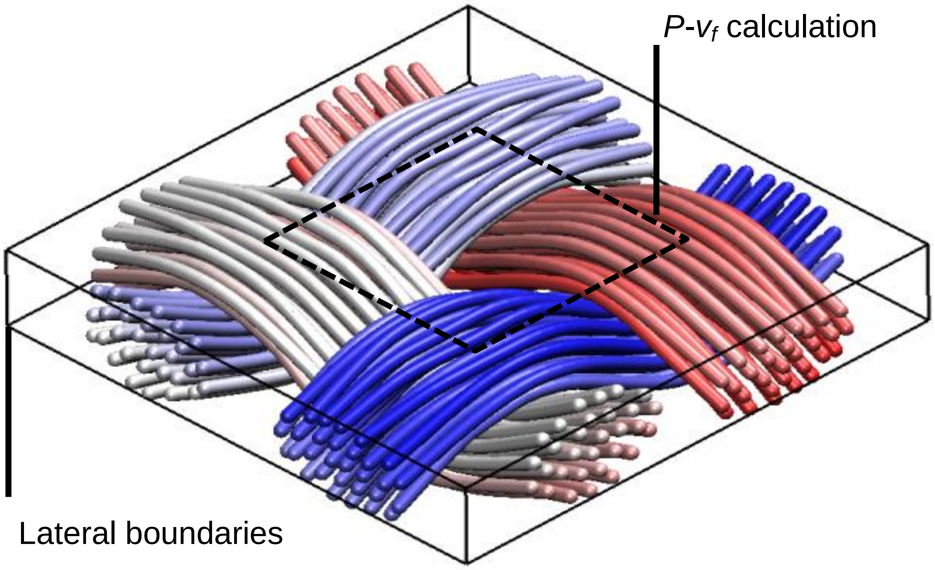

Figure 4.16: Single unit cell of plain woven textile (series 3.1)

the particle-based modelling method at replicating nesting. Figure 4.21 shows initial configurations for the two cases. In the latter case, a higher v_f results at lower P due to the shifted layers; also, a more equally distributed v_f is observed in the perfectly staggered preform, Figure 4.22.

4.6 Conclusion

A particle-based modelling method enabling the accurate modelling of the geometry and constitutive behaviour of textile assemblies was developed. Simulation results were validated experimentally for yarns, single-layer textiles and multi-layer textiles. Numerous cases and parameters were investigated including fibre length, fibre properties, restrictions and boundary conditions as well as domain size. Validation work shows that the particle-based modelling method replicates reality very well, and for the specific case of compaction it also shows the need for including Gutowski's function along with Hertz'

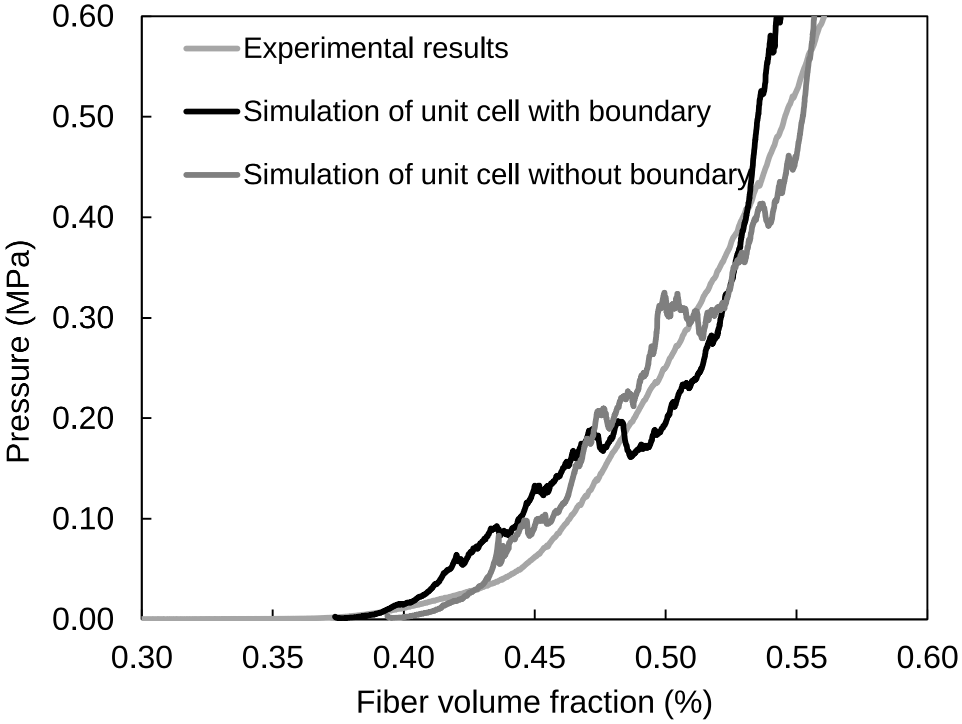

Figure 4.17: P as a function of v_f in a single unit cell of plain woven textile (series 3.1)

function. The modelling enables very thorough understanding of the behaviour of the textile and the deformation that it undergoes as it is loaded.

Real textiles may contain several thousand yarns, with each yarn containing thousands of fibres. In this paper, relatively large but nevertheless restricted numbers of fibres were used for demonstrating the concept and capabilities of the method. The software developed can be used for modelling a vast array of different textile structure subjected to varied, complex loading cases. An algorithm enabling the representation of much larger numbers of physical fibres within yarns from the use of a limited number of particle-based fibres in the models is being developed and will be presented in forthcoming publications.

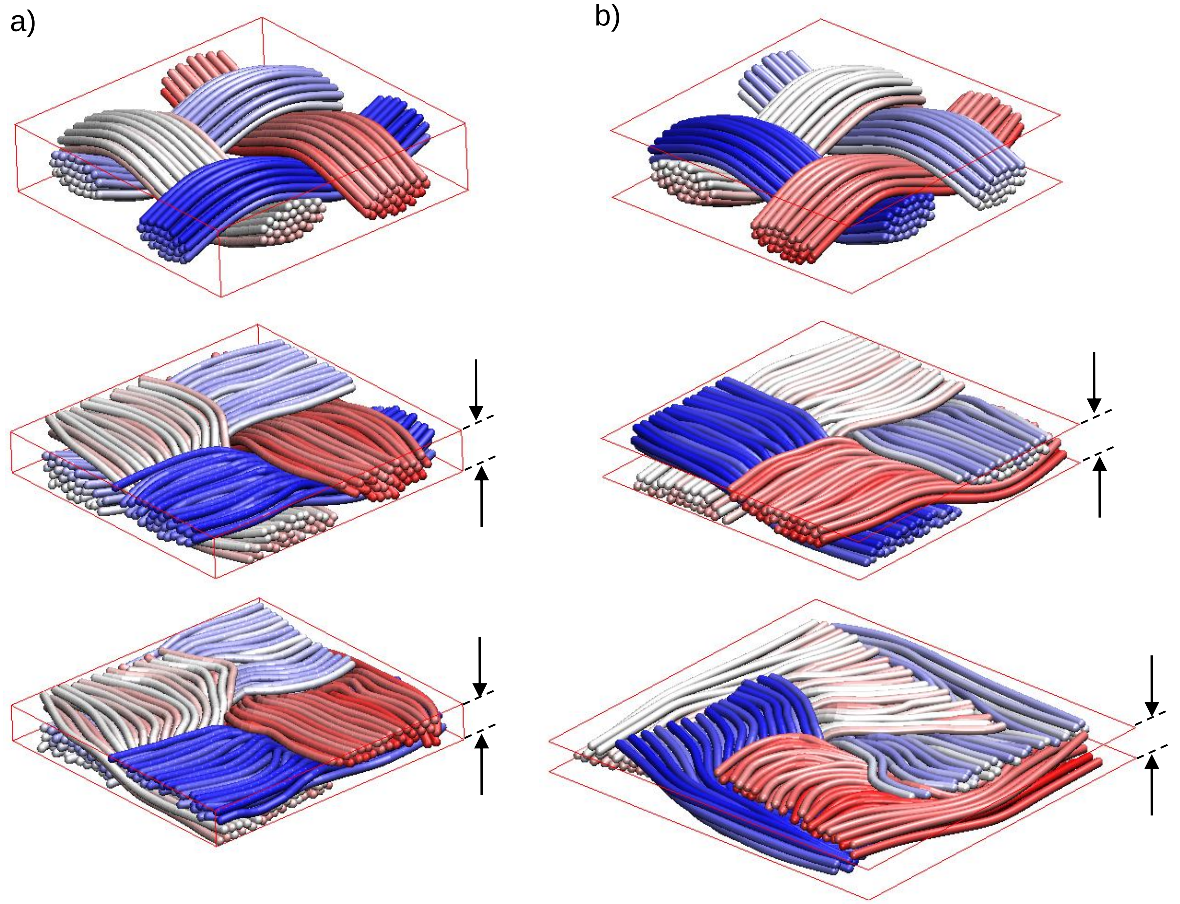

Figure 4.18: Extreme fibre deformations for both scenarios of: a) with lateral boundaries, b) without lateral boundaries (series 3.1)

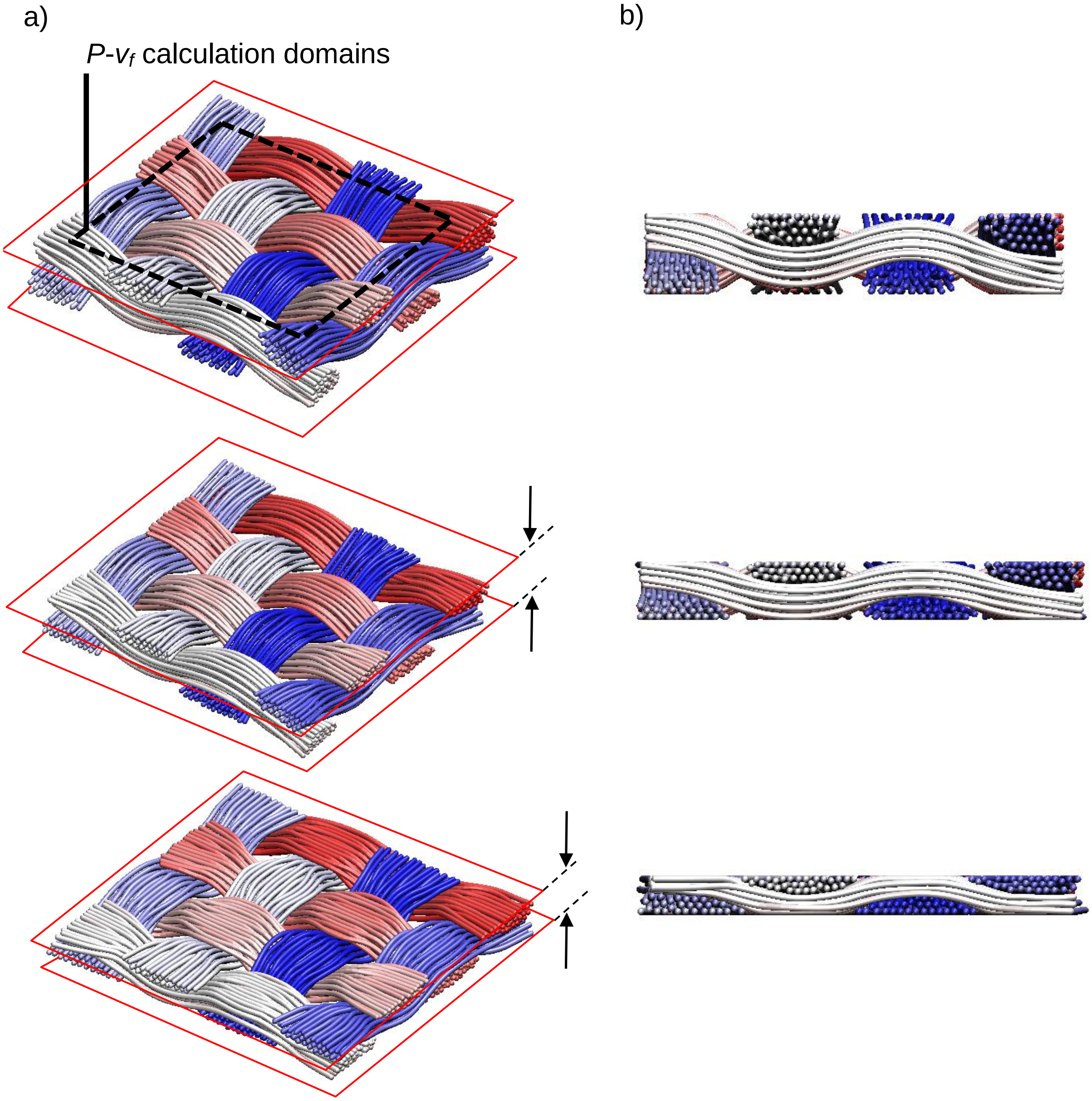

Figure 4.19: Simulations of single-layer with multiple unit cells in plain woven textile: a)3D view, b) 2D view (series 3.2)

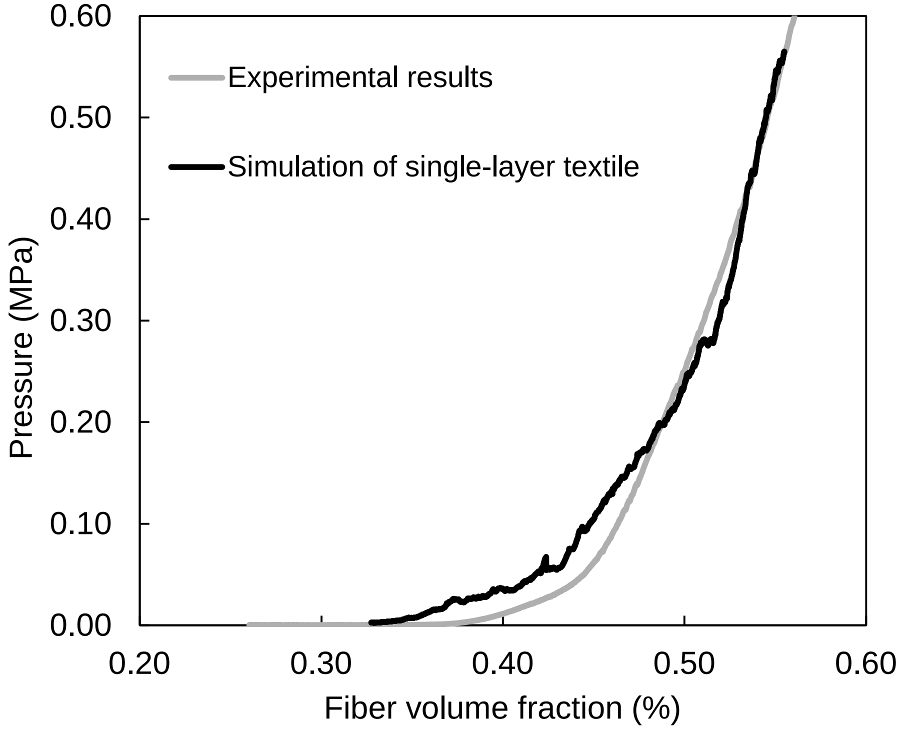

Figure 4.20: P as a function of v_f in a single layer plain woven textile (series 3.2)

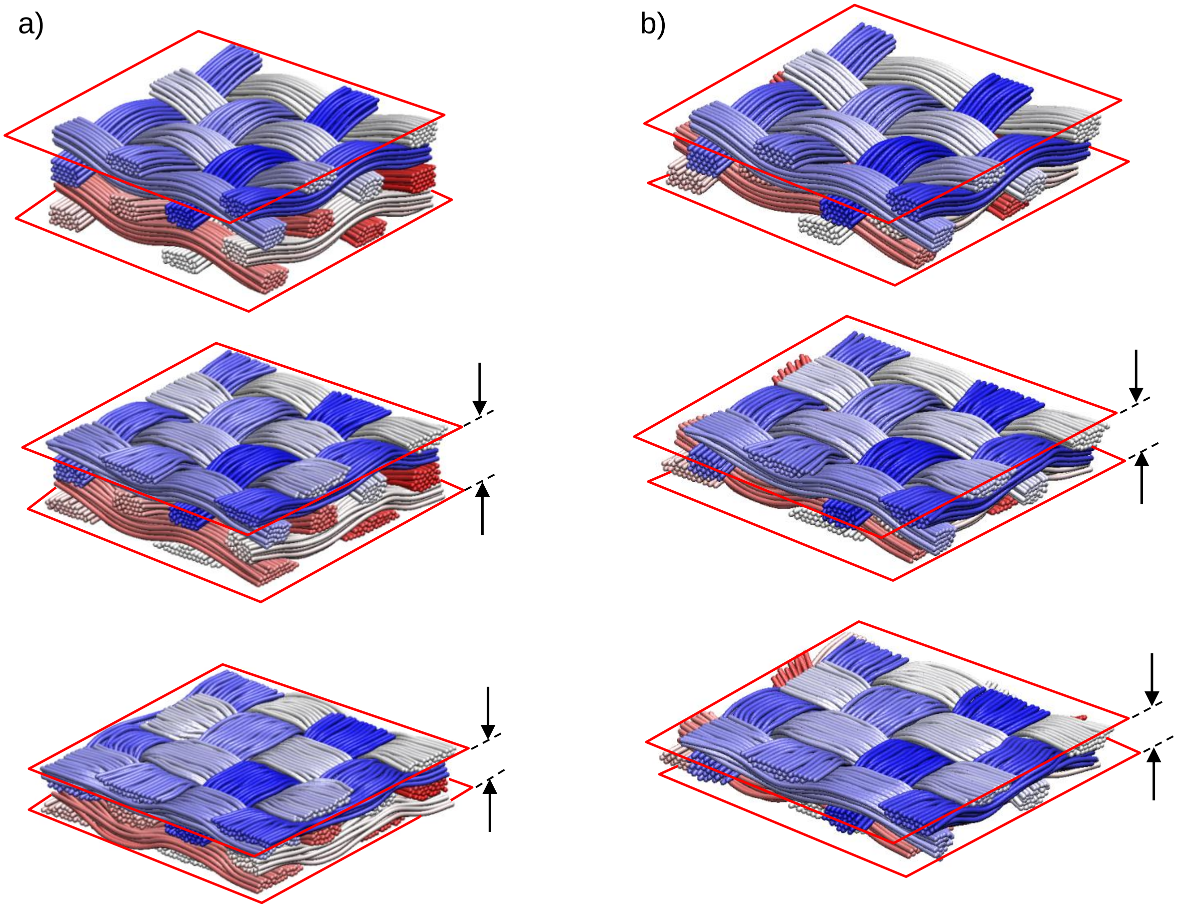

Figure 4.21: Simulations of double-layer plain woven textile with multiple unit cells: a)perfectly aligned yarns, b) perfectly staggered yarns

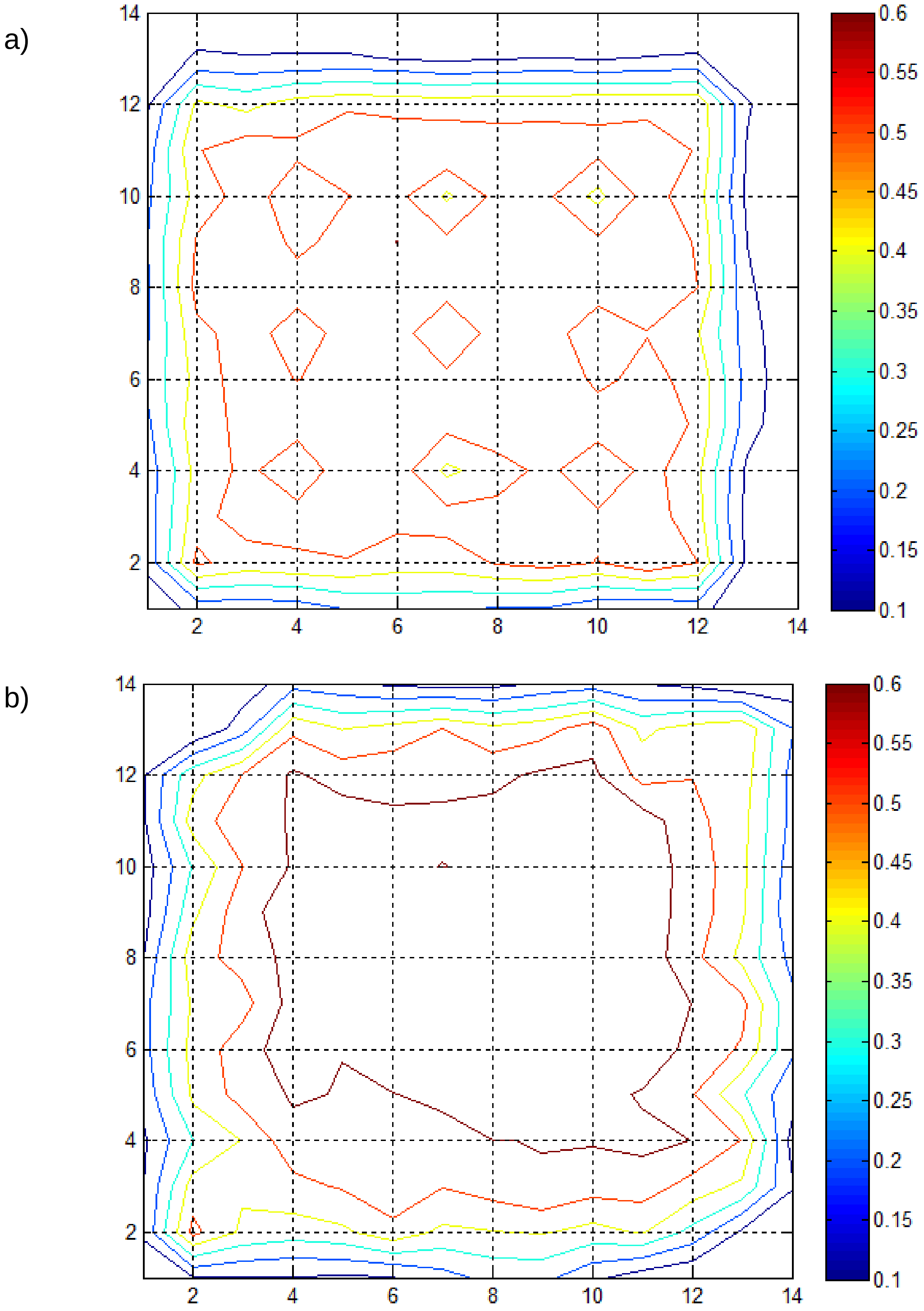

Figure 4.22: Fibre volume fraction of double-layer textile: a) perfectly aligned yarns, b) perfectly staggered yarns

Chapter 5

Particle-based modelling of relaxation and reconfiguration in woven textiles

5.1 Preamble

This chapter describes time-dependent relaxation and reconfiguration of woven textiles during and after compaction using the particle-based modelling method. Time-dependent relaxation simulations were performed on single plain woven textile reinforcements. Selected experimental trials conducted with different compaction rates and iteration numbers were performed for woven textiles and compared with simulations. The particle-based modelling method enables modelling of both compaction and relaxation in the same simulations and environment. The same parameters investigated in previously reported compaction modelling work were also used in this study, such as contact model parameters, step sizes in random walks and iteration procedures. The time-dependent relaxation behaviour of textile reinforcements can be related to iteration numbers during and after compaction within the particle-based modelling framework. This leads to a credible explanation of the time-dependent behaviour of textile reinforcements. This study and chapter contents will be submitted for publication in a peer-reviewed journal [103].

5.2 Abstract

This paper demonstrates the capability of particle-based modelling towards replicating the time-dependent relaxation and reconfiguration of woven textiles subjected to compaction loading normal to their plane. The capability, which is demonstrated for single and double-layer of plain weave textiles, is intrinsic to the particle-based method which utilizes discrete mechanics as an alternative to traditional continuum mechanics. The method is unique in the fact that in contrary to work previously reported in the literature, it can model the compaction and the relaxation seamlessly, in the same simulations.

Fibres are modelled as a series of conjoined points and their configurations are determined from first principles using a modified Metropolis algorithm and inter-particle strain energy terms. Whilst this paper focuses on the relaxation and reconfiguration behaviour of weaves, the modelling method is readily adaptable to the analysis of compaction [104], shear [102], bending, punching and other loading scenarios, for a wide array of textiles of different types. In order to characterize the relaxation behaviour of textiles, a series of simulations featuring different compaction rates as well as different target fibre volume fractions (v_f) or pressures were performed. From these simulations, compaction and relaxation curves were constructed with v_f and t as the independent variables. A relation between compaction pressure and compaction rate was also drawn.

Comparative data from simulations and different analytical models are investigated. Results demonstrate convincingly the new mechanistic approach to simulating of stress

relaxation. The method presented in this paper predicts successfully the actual behaviour of a single layer of textile undergoing stress relaxation, for different compaction rates. Whilst the compaction behaviour is obtained by quantifying loads obtained after a number of iterations for each set of boundary conditions, the relaxation and reorganization behaviour is informed from results obtained upon iterating, whereby iterations are effectively assimilated to time.

5.3 Introduction

The loading of textile reinforcements normal to their plane can be separated for analysis into three distinct phases, namely compaction, relaxation and load removal, Figure 5.1. In the first phase, the distance between loading platens (h_p) is reduced and textile reinforcements are compacted, resulting in increases in both fibre volume fraction (v_f) and pressure (P) recorded on the platens.

In the second phase, platen distance is held constant and consequently v_f remains unchanged, but P decreases as a result of rearrangement of fibres occurring over time. The reduction of P recorded on the platens is termed relaxation. The amount of relaxation is influenced by fibre and textile properties and by processing parameters. Fibre and textile properties include fibre modulus, friction properties and the architecture of the textile reinforcement. Processing parameters include the rate of compaction during the compaction phase, maximum P and v_f at onset of relaxation, and relaxation time. Accordingly, compaction and relaxation are not two separate incidences but rather they are interrelated within composites manufacturing process. Unified modelling of compaction and relaxation either in parallel where relaxation occurs during compaction, or in series where relaxation occurs after compaction is a worthwhile approach but it is hardly discussed in concrete, physically meaningful terms; this forms the main focus of this paper.

In the third phase, platen distance (h_p) returns to its initial value and the textile reinforcement is unloaded, resulting in decreases in both v_f and P recorded on the platens. In most manufacturing operations all three phases are performed and so the study of each phase is important.

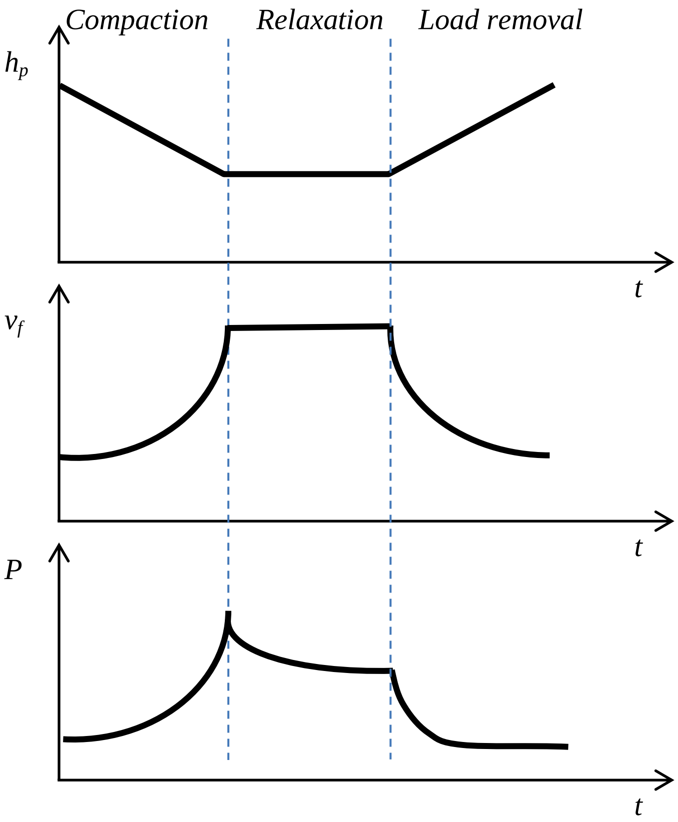

Figure 5.1: Evolution of h_p, v_f and P during 3 phases of textile processing

The constitutive mechanical behaviour of technical textiles is intimately linked to the textile architecture and fibre configuration, which refers to the level of alignment of fibres within yarns and so to the position of fibres with respect to each other [46,121]. Architecture and configuration of the textile have a strong influence on its physical properties in the original and deformed states, such as the permeability to fluid, thermal conductivity and others [101]. The geometrical configuration of the textile is altered by normal compaction pressure (P) and by the rate of compaction. Recoverable and non-recoverable deformations are imparted to the yarns leading to changes in fibre configuration, yarn shape and average thickness of textile layers. Any change of configuration within a textile produced by stresses imparted upon manufacturing operations or in service is crucial to understanding the processing behaviour and predicting the mechanical performance of the textile. Predicting such changes is also useful in documenting which aspects of textile geometry and configuration must be controlled to ensure reproducible physical properties in the textile. The compaction and relaxation of textiles were studied extensively during the last decades but there remains a lack in terms of modelling these two phenomena simultaneously following a unified mechanistic approach.

N. Pearce and J. Summerscales [81] conducted compaction experiments on plain woven glass fibre reinforcements. Tests were conducted on 1 to 5 layers of fabric to maximum target pressures of 100, 200 or 300 kPa at a compaction rate of 0.05 mm/min. Once samples were compacted to the target pressure, compaction platens were held for 5 minutes inducing relaxation, and then released. Samples were compacted to the target pressure 10 times successively in each test. Compaction and relaxation data were fitted to power laws. The authors observed that relaxation occurred under even the lowest selected compaction rate, and that relaxation was linearly proportional to the fibre volume fraction increase. Relaxation increased with target pressure and with the addition of fabric layers. The authors stated that higher volume fractions may be achieved by allowing relaxation to occur prior to applying maximum mould closing force.

Y. Luo and I. Verpoest [71] studied the compaction and relaxation behaviour of Multimat®, a glass reinforcement consisting of a layer of weft knit fabric sandwiched between two layers of random mat fabric, and compared with woven, mat and knit fabrics. The knit and the mat layers in Multimat® are stitched together. 1 and 2 layers of Multimat® fabric were compacted along with 2 and 4 layers of mat and woven fabrics and 1 layer of knit fabric. Compaction pressure ranged from 10 to 700 kPa with a compaction rate of 0.5 mm/min. All reinforcements were compacted in discrete steps to a certain thickness and left to relax for 5 minutes, after which time a further compaction step was applied and so forth up to the target pressure. Relaxation was explained in terms of fabric stiffness and volumetric dissipation energy. Volumetric energy was obtained from the area under the curve of compaction load as a function of thickness, and volumetric dissipation energy was defined as the difference between energy values before and after relaxation. Significant relaxation was observed for the Multimat®, mat and woven fabrics as a result of high stiffness or high volumetric dissipation energy. Relaxation was negligible for the knit fabric because of low stiffness and low volumetric dissipation energy.

S. Bickerton and M.J. Buntain [10] studied the compaction and relaxation behaviour of continuous glass filament mat (CFM) and chopped strand glass mat (CSM) in the dry and wet. Compaction tests were performed at 25 mm/min for dry fabrics and 8 mm/min for wet fabrics. Two compaction scenarios were followed, labelled as the static scenario and the dynamic scenario. In the static scenario reinforcements were compressed in steps to progressively higher v_f up to 0.50, stress being allowed to relax for 10 minutes in each step. In the dynamic scenario reinforcements were compacted to a target v_f in a single, continuous step after which compaction platens were held to enable relaxation. A single elastic model in the form of a 4^{th} order polynomial did not lead to good agreement to experimental results. An extension to the single elastic model was proposed in the absence of a comprehensive time-dependent model. This proposed extension, called the mixed elastic model, represented experimental data well for dry and saturated reinforcements subjected to static or dynamic loading.

P. A. Kelly et al. [51] performed two series of tests and compared results with predictions from their nonlinear relaxation model. Test samples consisted of eight layers of glass fibre continuous filament mat (CFM). In a first test series, samples were compacted to a v_f of 0.35 at rates of 0.035, 0.5, 2, 5 and 100 mm/min. In a second test series, samples were compacted at rate of 2 mm/min to v_f of 0.25 and 0.45. In both series, after undergoing compaction the samples were held at a constant target fibre volume fraction for $5\,T$ seconds to allow relaxation, where T is the time taken for compaction. Tests conducted at compaction rates of 0.035 and 100 mm/min constituted two extremes where in the first one most relaxation happens during compaction and in the latter one relaxation occurs essentially after compaction. These two extreme cases were performed to assess feasible and practical compaction rates. The model developed by the authors was based on a linear generalized Maxwell model featuring a free spring element and multiple Maxwell units. Six different fitting parameters were fed to the model as input. Modelling did not consider the number of layers or any nesting explicitly. Experimental results for dry and saturated textiles could be replicated by the model presented, to some extent. Phenomena governing compaction and relaxation differ and so the model with set parameters could be applied to either compaction or relaxation.

G. Francucci et al. [32] studied the behaviour of a plain weave fabric made of jute subjected to compaction and relaxation. Stacks of six layers with stacking sequence $0°/90°$ were compacted at rates of 0.5, 5 and 50 mm/min to v_f of 0.35, 0.45 and 0.55, dry and saturated with a mix of water and glycerine. After compaction the samples were held at their final thickness for 10 minutes to study their relaxation behaviour. Tests were repeated three times. The dependency of maximum compaction pressure, permanent deformation and stress relaxation on the fibre volume fraction and compaction rate was investigated. Faster compaction led to higher compaction pressure at a given v_f and to more stress relaxation. As the fibre volume fraction recorded at a given compaction pressure decreased under different compaction rates, stress relaxation increased.

Y. R. Kim et al. [53] studied the compaction and relaxation behaviour of cloth, mat and unidirectional glass and carbon fabrics, dry and lubricated. Compaction rates were set to 0.5, 2.0 and 5.0 mm/min and maximum compaction pressure was 8.6 MPa. Samples consisted of stacks of 20 and 40 layers; pressure was recorded as a function of fibre volume fraction and time. The authors stated that the relaxation behaviour was dependent on textile structure, compaction rate and fibre volume fraction. Lower compaction rates provided more time for the reconfiguration of fibres, resulting in more relaxation. Furthermore, with an increase in compaction rate to a set target pressure, relaxation was increased. Relaxation was less prevalent in textiles characterized by better fibre alignment; random mats and plain weaves showed more relaxation than unidirectional fabrics. Relaxation data for these fabrics was fitted very faithfully using a 5 element Maxwell-Wiechert rheological model [2]. Dryness increased fibre misalignments, contact points and resistance to movement; this resulted in lower fibre volume fractions at a given pressure for the dry fabrics.

R. A. Saunders [105] performed compaction tests on dry and resin impregnated plain woven glass fabrics. Stacks were laid along alternating 0°/90° and ±45° orientation in 5, 10 and 20 layers. Compaction rates were set at 0.05, 0.10, 0.50 and 1.00 mm/min with a maximum target pressure of 1768 kPa. A power law relationship expressing compaction pressure as a function of fibre volume fraction was applied successfully, with different parameters used for different numbers of textile layers. Compaction rates within the range 0.05 to 1.00 mm/min yielded no significant differences in compaction pressure for dry fabrics. Changes in the compaction rate affected the compaction curves of resin impregnated preforms, which behaved in a time-dependent manner. Compaction rate was also an important parameter influencing relaxation. The authors studied the microstructure of resin cured samples and characterized the average distance between layers, crimp amplitude and wavelength of yarns as well as the area and other geometrical parameters of yarn cross-sections, at different compression pressures and rates. With a reduction of compaction rate, pressure on the resin impregnated reinforcement was transferred to the fibres and the compaction curve moved towards that of the dry reinforcement. It was also seen that nesting was present even at very low pressures which could affect relaxation, and that individual yarn amplitude and height decreased due to compaction.

R.A. Saunders et al. [106] studied the time-dependent compaction behaviour of a resin impregnated plain woven glass fabric under different compaction rates. Assemblies of 20 fabric layers were saturated with non-curing polyester resin and compacted using two rates of 0.05 and 1.0 mm/min, to a maximum pressure of 840 kPa. Compaction hysteresis and relaxation tests were also performed. Results showed that power-law relations are appropriate for modelling the loading curve for dry compaction. Compaction hysteresis and pressure relaxation tests showed time-dependant behaviour for dry and wet textiles. Finally, additional tests revealed that the relaxation time was longer on the first cycle of dry compaction compared with further cycles.

F. Robitaille and R. Gauvin [90] presented a review of published experimental data related to the compaction and relaxation of random mats and woven reinforcements. The number of textile layers, number of compaction cycles, compaction speed, presence of a lubricant, temperature, stacking sequence, level of fibre alignment and level of initial compaction pressure were discussed. Compaction and relaxation data for 3, 6 and 12 layers of glass woven reinforcement compacted at rates of 2 and 5 mm/min over 1 to 7 cycles, both dry and saturated, were used. Relaxation from different maximum pressures was studied. The authors showed comparisons between experimental curves and identified general trends for compaction and relaxation results. Less relaxation was observed at higher initial compaction pressure levels, and more relaxation was observed after higher compaction rates. The authors reported more relaxation as the number of layers increased for both random mats and woven materials.

M. Nziengui et al. [79] studied the time-dependent behaviour of textiles during liquid composite moulding. 10, 15 and 20 layers of dry and glycerine-saturated mat were compacted at rates of 1.5, 2.0, 2.5 and 3.0 mm/min. Experimental trials also compared 10 layers of twill, plain woven and unidirectional textiles compacted at 3 mm/min. Finally, results obtained with 20 layers of mat were compared with Zener, Burger and Maxwell rheological models. In the case of the mat reinforcement, increases in the number of layers lead to an increase in relaxation. The authors observed that higher compaction rates led to shorter relaxation times, whilst relaxation increased at higher compaction rates. They also observed less resistance to deformation during compaction of wet reinforcements compared to dry stacks, leading to lower pressures at a given v_f under higher compaction rates. Rheological models, particularly the Maxwell model, showed good agreement with experimental results.

F. Robitaille and R. Gauvin [91] investigated the compaction and relaxation behaviour of three H_2O-saturated woven reinforcements; a bidirectional twill woven, a bidirectional plain weave and a non-crimp stitched glass. Successive loading cycles were applied to the reinforcements. Each cycle featured three sequential steps: compaction, relaxation and retrieval of the load. Processing parameters investigated were the number of layers, holding time, compaction rate and number of cycles. The latter two parameters showed the most pronounced effects on the compaction and relaxation behaviour. This emphasized the role of reorganization of the fibre network in defining the mechanical properties of the reinforcements. Effects of the reorganization of fibres on successive compaction cycles were observed. Also, relaxation decreased as the number of layers rose for both random mats and woven materials.

D. Sajn et al. [97] investigated the effect of fabric elasticity on stress relaxation. Different proportions of Lycra® were added in yarns leading to different levels of elasticity in fabrics. Results of experimental trials were compared to different mechanical models sourced from the literature. Relaxation models were fitted to experimental relaxation curves for 1 hour and 24 hour relaxation times. Six twill weave fabrics made of wool and Lycra® yarns, with different values of thickness, mass and yarn density were used. Fabrics were compacted to a maximum pressure of 1 MPa, maintained under the same strain and let to relax. A single Maxwell model did not show agreement with experimental data. 3 Kelvin models connected in series and a general 3 component Maxwell model with a parallel non-linear spring best fitted experimental data. Relaxation occurred mainly in the first 15 minutes, with 15.6% to 21.5% decreases from maximum pressures observed for all fabrics. After 15 more minutes relaxation decreased only by additional 2.0%. Relaxation was most pronounced with highest Lycra® amounts. A higher number of components within the Maxwell model led to better fit to relaxation data.

S. Lee et al. [60] studied the relaxation behaviour of dry reinforcement textiles for the resin transfer moulding process. 5 different textiles were used, namely a glass random mat, glass woven, aramid woven, carbon woven and hybrid aramid/glass woven. Compaction was carried out up to a force of 20 kN for 5, 10 and 20 layers of textile at a rate of 1 mm/min. The compaction platens were held stationary for 5 min to induce relaxation. Hysteresis curves were obtained from experimental trials conducted on the plain woven fabric. Time-dependent behaviour and significant stress relaxation occurred non-linearly. A Maxwell model was used for modelling the time-dependent behaviour of the textile stacks. Results were compared to those of experiments and FEA simulations. Discrepancies between values obtained from models, FEA simulations and experimental trials were linked to geometrical approximations and nesting effects.

A. Somashekar et al. [116] modelled the relaxation behaviour of glass fibre reinforcements subjected to constant compaction strain using a generalized 5 component Maxwell model. Stacks of 6, 8 and 10 layers of biaxial stitched fabric, chopped strand mat, continuous filament mat and plain weave fabric were tested at compaction rates of 2 and 5 mm/min to target maximum fibre volume fractions ranging from 0.28 to 0.65. Different relaxation times were observed for the different reinforcements, ranging between 600 min and 1620 min depending on fabric architecture. The 5 components Maxwell model consisted of 2 parallel Maxwell models in parallel with a spring. It was shown that this model could predict the relaxation of the reinforcements, without accounting for the effects of the compaction rate, number of layers and dry or wet state of the reinforcements.

J. Echaabi et al. [31] studied the compaction and relaxation of textiles during liquid composite moulding. 20 layers of random mat and twill reinforcement textiles were compacted at a rate of 3 mm/min to 45% and 55% target maximum fibre volume fractions, in dry and saturated states. The relaxation behaviour of the textiles was compared with Zener, Burger and Maxwell rheological models. The Maxwell model showed good agreement with compaction and relaxation experiments. Relaxation time decreased in the saturated state and increased with the fibre volume fraction.

S. Aranda et al. [4] investigated the effect of temperature on the compaction and relaxation of 8 layers of non-crimp carbon fibre reinforcement (+45°/0°/-45°). A compaction rate of 0.5 mm/min was applied up to a maximum pressure of 200 kPa. When the maximum pressure was reached, the platens were held steady and pressure was recorded as a function of time. A 24% reduction in pressure was observed after 10 min under constant v_f for the textile at room temperature; this increased to 28% at 60 C° and 37% at 120 C°.

The above results and trends arise from experimental trials and/or rheological models, and they suffer from limitations in applicability and generalization due to the large number of fitting parameters that they entail. However, they can be very useful in specific applications. Most importantly, the references cited above focus on compaction and on relaxation individually, and they are limited to specific cases. The particle-based modelling method proposed here aims at overcoming the limitations of rheological modelling by predicting the actual geometry of textile structures, as well as their constitutive behaviour based on the representation of actual physical phenomena.

Particle-based modelling provides a general numerical tool for simulating the large-strain constitutive behaviour of non-homogeneous or structured textiles upon loading and in time. Minimizing the total strain energy stored in the textile under set boundary conditions lies at the core of the method. Details of algorithms used for the calculation of strain energy terms appear in previous paper [104] and they are revisited briefly in the following section. As discussed above, the textile reinforcement architecture, fibre properties, compaction rate, pressure at the onset of relaxation and relaxation time have major effects on the relaxation of textiles during and after compaction. In this paper, these processing parameters are investigated through simulations validated by experimental trials, using the particle-based modelling method.

In modelling the relaxation, a parallel is established between the number of iterations and time. The iterative process and the time-dependent relaxation behaviour of textiles show very similar behaviour. This feature is used in predicting fibre relaxation, both during and after compaction either at set pressure, steady-state v_f or constant platen spacing.

5.4 Modelling method

Fibres in a textile are represented as series of discrete spherical particles with diameters equal to the fibre diameter. Tracking the individual particles as loads or displacements are imposed enables the representation of the geometry and behaviour of the yarns and textile. The modified Metropolis algorithm [73] iterates particle positions towards a configuration of lower strain energy, ultimately defining the geometry of the textile, under constant boundary conditions. Iterations of particle positions are performed within a predefined physical subspace limitation and uniformly distributed random walk. In each iteration, by adding a small displacement of random amplitude to the coordinate of a randomly chosen particle the strain energy of the system is changed. If the strain energy differential before and after iteration is negative and strain energy is reduced, the new configuration becomes the initial state for the next iteration. Conversely if the strain energy remains constant or increases, the new configuration is rejected and the iterative procedure is repeated from the initial configuration. The number of iterations required for the system to reach a stable state of lower strain energy depends on several factors.

Afterwards, boundary conditions are changed to reflect on-going processing; distance between platens may be reduced for compaction, held steady for relaxation or increased for load removal. The iterative procedure is repeated in the defined boundaries. Given the nature of the modelling method, the number of iterations required for reaching a stable state follows trends that are comparable but differ in amplitude for each textile that is investigated within this paper.

5.4.1 Strain energy terms

Any relative displacement between particles that results from either changes in boundaries or iteration under stable boundaries, produces strains and stresses within the fibres represented by these particles. Changes in strain energy result from i) relative displacement between particles within a single fibre leading to changes in intra-fibre strain energy, and ii) fibre deformations resulting specifically from interactions between neighbouring fibres, leading to changes in inter-fibre strain energy.

For each fibre, particle displacement leads to changes in the fibre's strain energy which can be associated with axial tension, axial compression or bending stresses; fibre torsion is neglected. For each fibre segment, strain energy in axial tension or compression is a function of the fibre's Young's modulus E and cross-section A. Bending strain energy is calculated using angle θ_{ijk} defined between particles i and k framing particle j; the change in bending energy for the total length of both segments involved is calculated along with other energy terms, and then the energy differential is evaluated.

Contact forces between curvilinear fibres within a fibre assembly such as a yarn may be calculated using Gutowski's compaction model [19]. Selection of this function was investigated previously and discussed at length [104]; it was shown to be suitable for particle-based modelling of textiles. Gutowski's compaction model states that instead of being perfectly straight individual fibres within yarns are wavy. β is a fitting parameter in Gutowski's function either evaluated by microscopy or fitted to experimental results. It is assumed that l_{min}, the minimum distance between two particles, is equal to $2r$.

From Gutowski's model the strain energy is calculated by integrating force over distance for the displaced particle interacting with surrounding fibres; for a particle separated by distance l_{ij} with $l_{min} < l_{ij} < l_o$, strain energy is calculated as:

$$U_G = \int F_{ij} \cdot dx = \int \frac{192EI}{\beta^3} \cdot \frac{(l_o - l_{ij})}{(l_{ij} - l_{min})^3} \cdot dl_{ij} \tag{5.1}$$

where l_o is the initial distance between particle centres. Gutowski's model is equivalent to the beam bending equation with reducing span; it has been used successfully [19,39,104] in many occurrences.

5.5 Simulations and validation experiments

In this work, 6 series of experiments A-1 to A-5 were performed with the aim of identifying the parameters affecting P, v_f and relaxation time for compaction followed by relaxation. The experimental series also aimed at assessing the effect of the compaction rate on pressure and fibre volume fraction at the onset and during relaxation.

6 series of simulations B-1 to B-6 were also performed with the aim of replicating some of the effects and trends observed in the aforementioned experiments. Compaction rates and relaxation times were related to the number of iteration cycles. Images extracted from a simulation of the compaction of a single layer plain woven textile are shown in Figure 5.2.

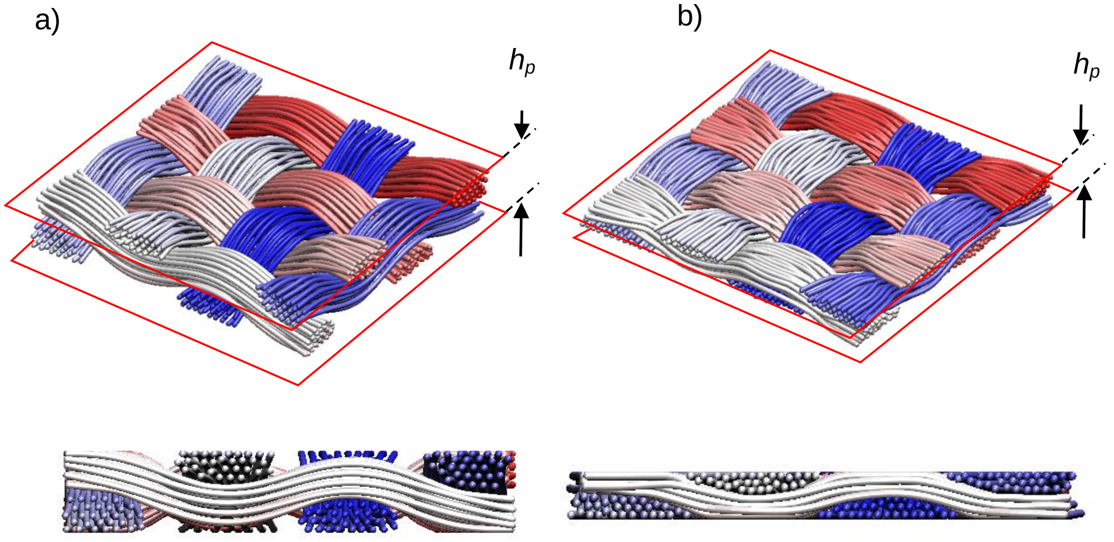

Figure 5.2: Simulation of single-layer of plain woven textile featuring multiple unit cells: a) before compaction, b) after compaction, at the onset of relaxation

Table 5.1: Characteristics of fibres and textiles

Properties		**Number of samples**
Fibre diameter ($2r$)	0.296 ± 0.001 mm	50
Fibre density	1.172 ± 0.001 g/cm^3	20
Initial v_f of preform	25 ± 3.1 %	10
Surface density of preform	0.117 ± 0.001 g/cm^2	10

Experimental trials were conducting using a plain woven textile made of yarns containing 30 monofilament Nylon 6/6 fibres, with 5 mm yarn spacing in both directions. Diameter of the Nylon 6/6 fibres was measured at 296 ± 1 μm using a micrometre. An Instron 4482 universal testing frame equipped with a 1 kN load cell was used for compaction and relaxation experiments. Young's modulus of Nylon 6/6 fibres was measured at 1.05 ± 0.02 GPa. Characteristics of the fibres and textile samples appear in Table 5.1.

Textile samples were compacted between two parallel platens mounted and aligned in the Instron frame, ensuring uniform compaction, Figure 5.3. Upper platen dimensions were measured at 40 mm × 40 mm. The effect of any platen and frame assembly deformation was measured by conducting dry compaction runs performed with no textile sample placed between the platens, and removed from the raw compaction data in tests where textiles were compacted. Tests were conducted on single and double layer samples. Samples were aligned at 45° from platen edges to reduce any orientation edge effect. Compaction rates of 2.0, 1.0 and 0.5 mm/min were used.

In simulations, virtual samples were compacted and then held to constant thickness reached at a designated target maximum pressure level, to enable relaxation. Textiles featuring yarns made of 30 virtual Nylon 6/6 fibres with 300 μm diameter were simulated, with yarns virtually woven into a plain weave textile. Fibres featured 60 particles along their length. The numbers of iterations were unchanged in each step but changed for different compaction rates. Compaction steps were set to 0.1 μm and pressure was

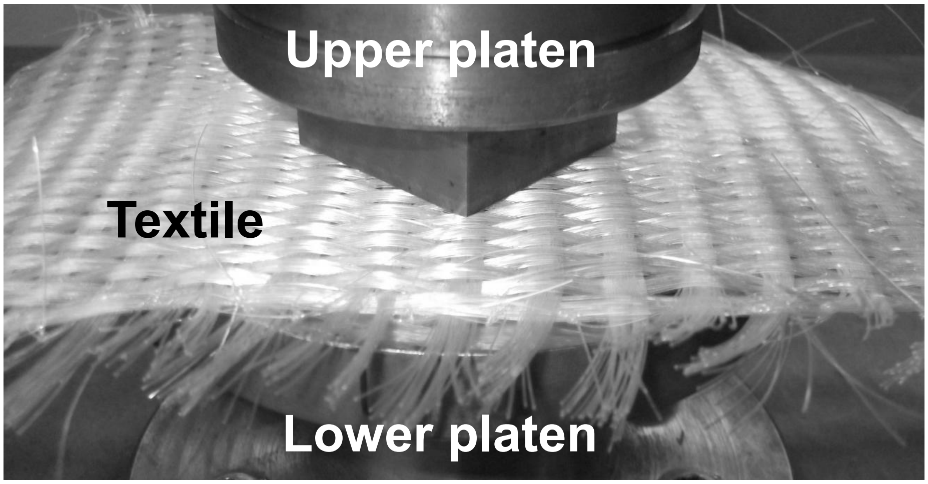

Figure 5.3: Compaction/relaxation platens with single layer textile

recorded as a function of h at each 100 steps. Maximum particle displacement or random walk step was set to 1.0 μm. Gutowski's parameters were β= 200, v_o = 0.28 and v_a = 0.79 for Nylon 6/6 fibres as identified in previous work [104].

5.5.1 Experimental trails

6 experimental series A-1 to A-6 were performed.

Experimental series A-1 featured 5 distinct trials with compaction followed by relaxation of textile samples. Compaction rate was 1.0 mm/min and pressure on compaction platens was recorded as function of time. Textile samples were compacted and then held to a maximum v_f of 0.5 in series A-1 to allow for relaxation to occur, Figure 5.4. All 5 tests were similar and showed typical compaction and relaxation behaviour with minor scatter. After the compaction stage, textile relaxed through a reduction in pressure amounting to 0.05 MPa which is approximately 10% of the maximum target pressure, after 360 seconds of relaxation time. From the same series pressure as a function of v_f is presented for one trial, Figure 5.5.

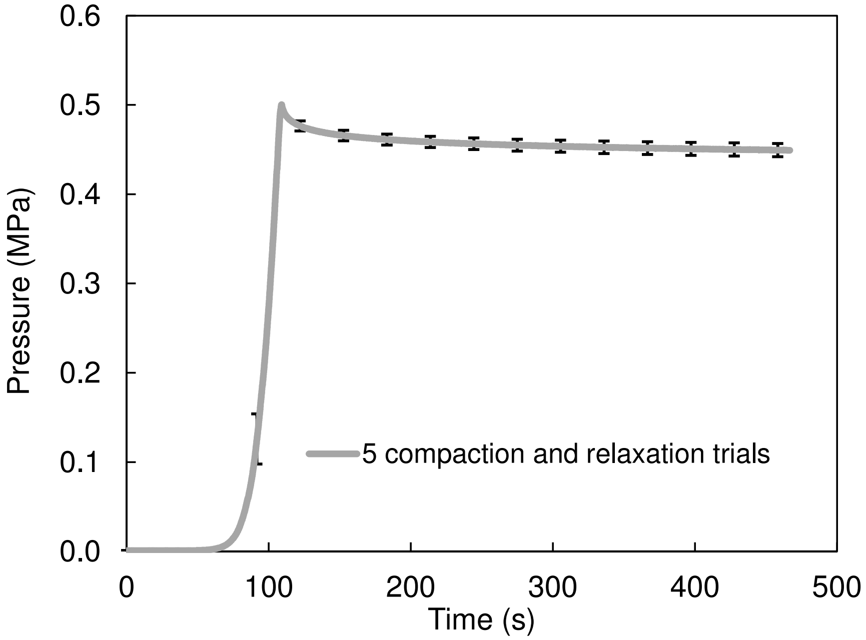

Figure 5.4: Compaction and relaxation of single layer plain woven textile samples (series A-1)

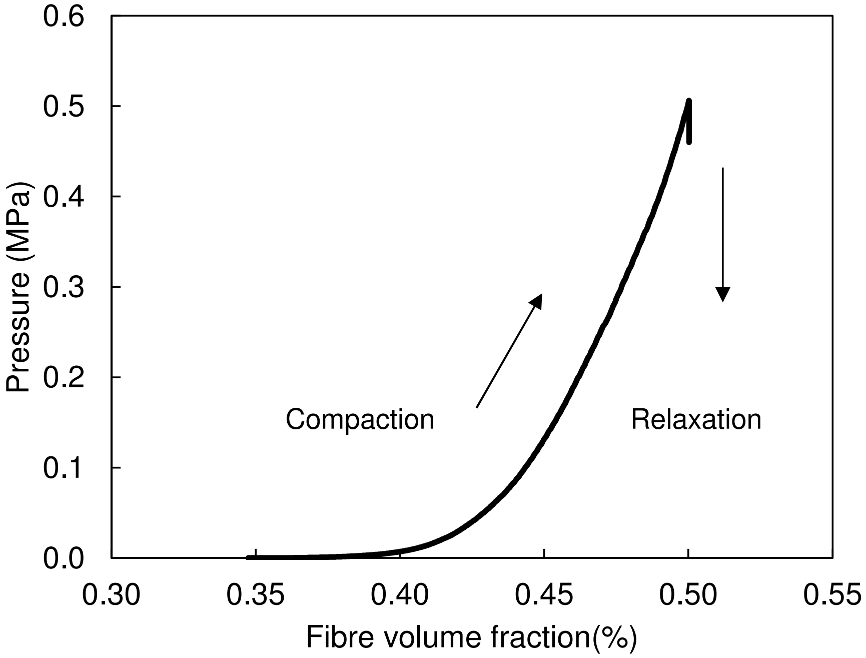

Figure 5.5: P as a function of v_f during compaction and relaxation of a single layer plain woven textile sample (series A-1)

Experimental series A-2 featured 3 cases where compaction rates were 2.0, 1.0 and 0.5 mm/min for cases A-2.1, A-2.2 and A-2.3 respectively, Figure 5.6. Maximum target pressure was set to 0.45 ± 0.001 MPa. Textile samples were compacted to the maximum pressure and then held to the thickness reached at that pressure to enable relaxation, Figure 5.6. At higher compaction rates the slope of the curve of pressure as a function of time increased. Relaxation periods were kept constant at 360 seconds for all 3 cases regardless of the compaction rate.

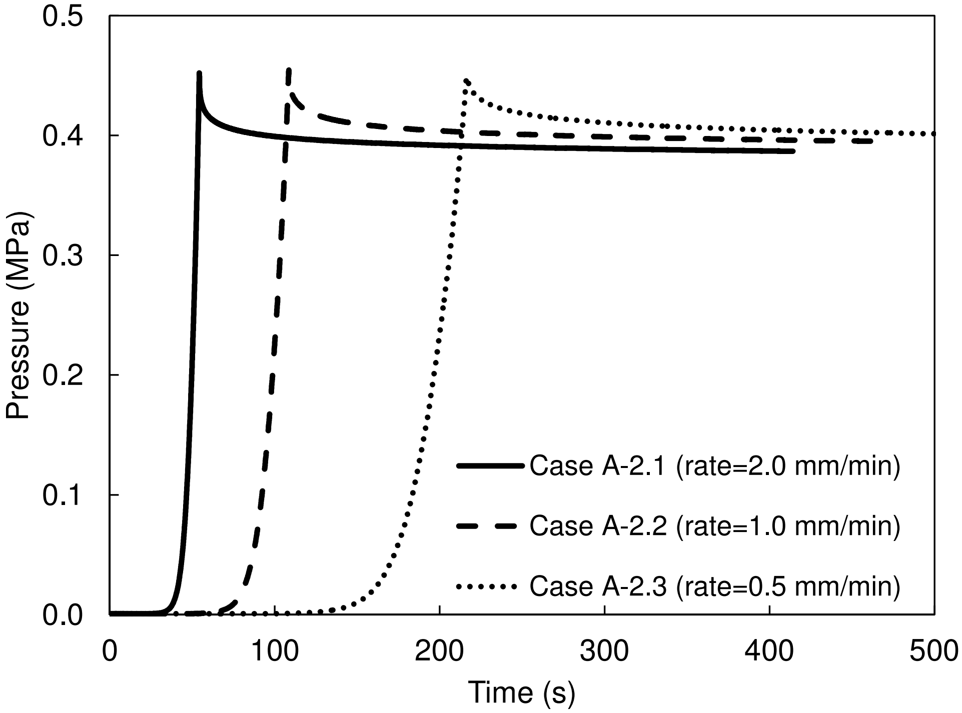

Figure 5.6: Compaction and relaxation of single layer plain woven textiles at different compaction rates, target pressure P=0.45 MPa (series A-2)

Fibre volume fractions results where single layer plain woven textiles were compacted at different rates to the same target pressure show differences in v_f although the maximum pressures reached in the compaction phase were the same, Figure 5.7. This may be caused by more relaxation and fibre network reorganization getting sufficient time to occur at lower compaction rates during the compaction phase.

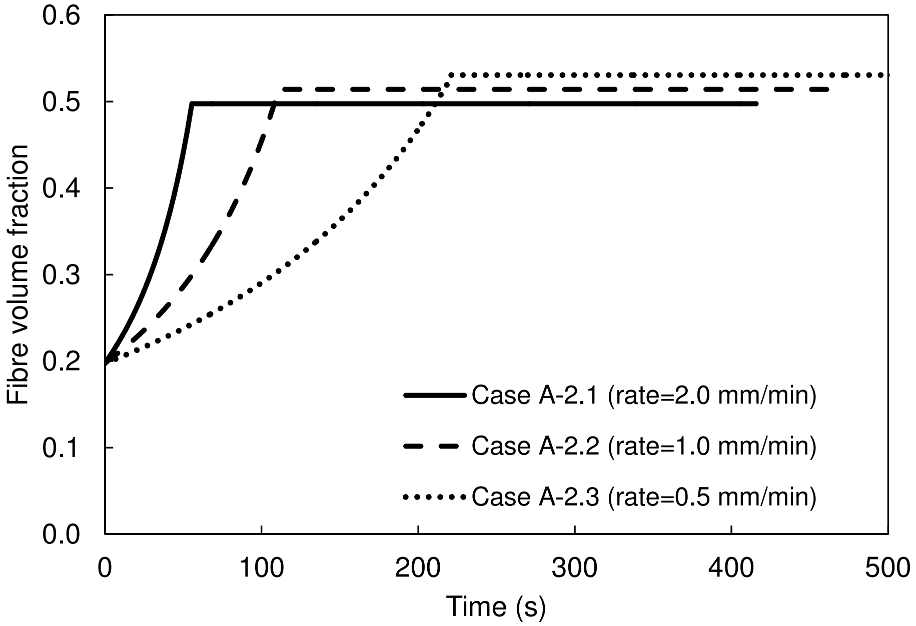

Figure 5.7: v_f as a function of time for single layer plain woven textiles subjected to different compaction rates with target pressure P=0.45 MPa (series A-2)

Quantification of relaxation was performed by calculating the difference between the maximum pressure at the onset of relaxation and the pressure after relaxation occurred over a set time. More relaxation was observed with higher compaction rates. As mentioned above, at the lower compaction rates most relaxation occurred during the compaction phase and as a result, relaxation occurring afterwards is less, Figure 5.8.

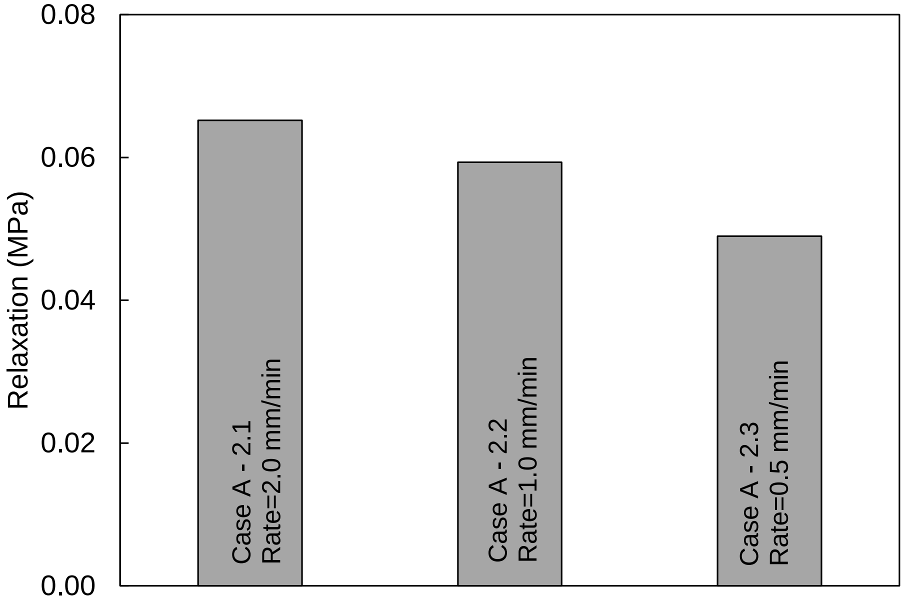

Figure 5.8: Relaxation of single layer plain woven textiles subjected to different compaction rates (series A-2)

Experimental series A-3 featured 3 cases where compaction rates were 2.0, 1.0 and 0.5 mm/min for cases A-3.1, A-3.2 and A-3.3 respectively. Maximum target v_f was limited to 0.53. Textile samples were compacted and then held to the target maximum v_f to allow relaxation to occur, Figure 5.9. At higher compaction rates, higher pressures were observed at a given v_f. A very interesting similarity was observed between the 3 relaxation curves, despite the different compaction rates. Where compaction rate was higher, say in case A-3.1, more relaxation occurred during the relaxation phase as a result of limited relaxation taking place during the compaction phase. However, it is worth noting that in all 3 cases, the textiles relaxed to the same final pressure level in the same allowed relaxation time.

Fibre volume fraction results for textiles samples subjected to different compaction rates towards a target v_f reach the same v_f from different onset pressures, Figure 5.10, as expected.

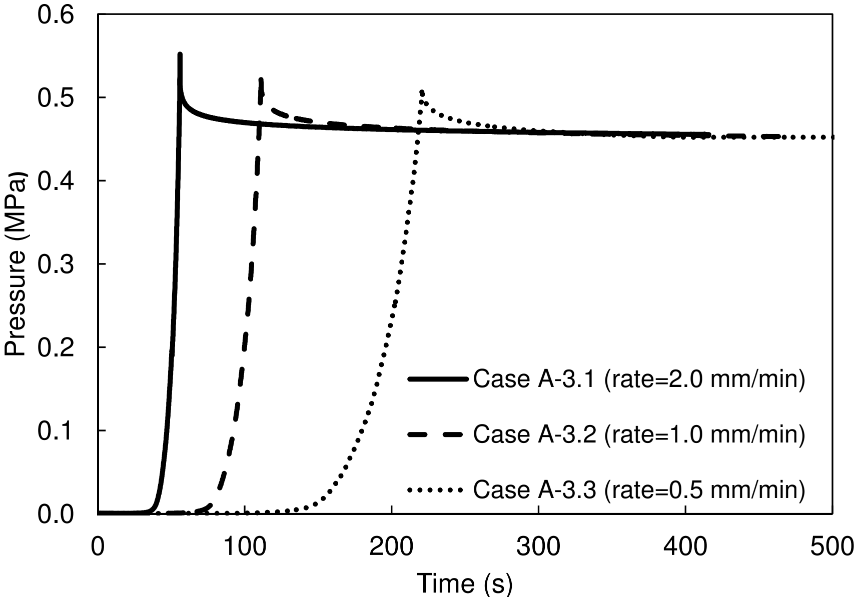

Figure 5.9: Compaction and relaxation of single layer plain woven textiles at different compaction rates, target v_f=0.53 (series A-3)

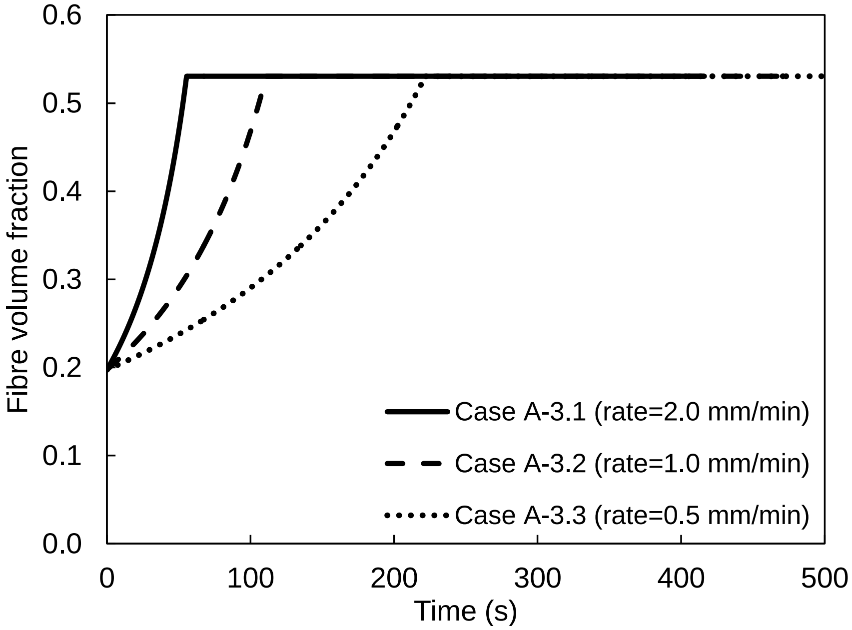

Figure 5.10: v_f as a function of time for single layer plain woven textiles subjected to different compaction rates with target v_f=0.53 (series A-3)

Quantification of relaxation was done using the same procedure described above, Figure 5.11. More relaxation was observed at higher compaction rates; as mentioned above, with higher rates of compaction most relaxation occurred after the compaction phase, and as a result relaxation after the compaction phase shows higher values.

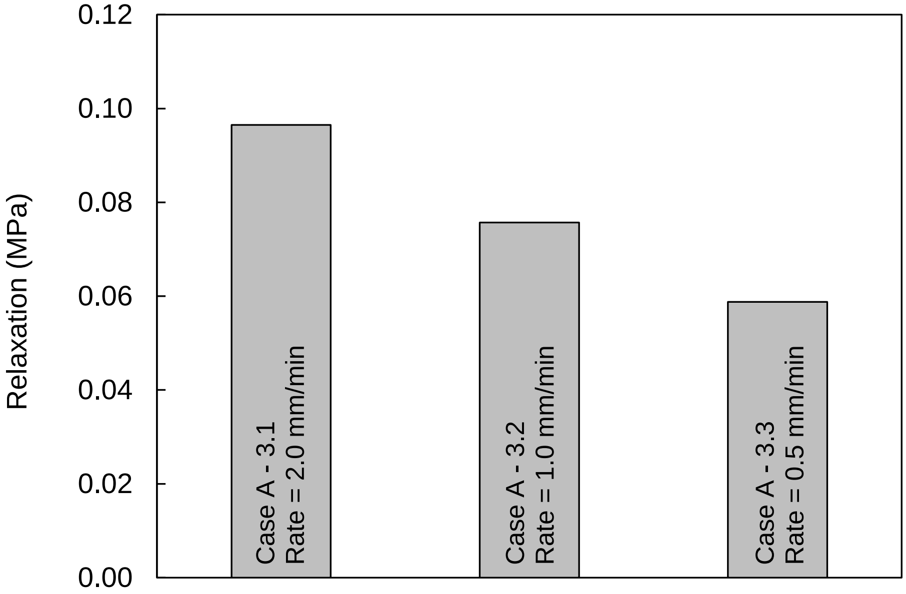

Figure 5.11: Relaxation of single layer plain woven textiles subjected to different compaction rates (series A-3)

Experimental series A-4 featured 3 cases with compaction rate set at 1.0 mm/min in all cases. Maximum target pressures were set to 0.40, 0.50 and 0.60 MPa for cases A-4.1, A-4.2 and A-4.3 respectively. Textile samples were compacted and then held at the thickness reached at maximum target pressures, to allow relaxation, Figure 5.12.

Quantification of relaxation is reported in Figure 5.13. More relaxation was observed for higher maximum target compaction pressures, for the same compaction rate. very interestingly, relaxation was essentially constant in terms of proportions, standing between 12% to 13% of the target pressures.

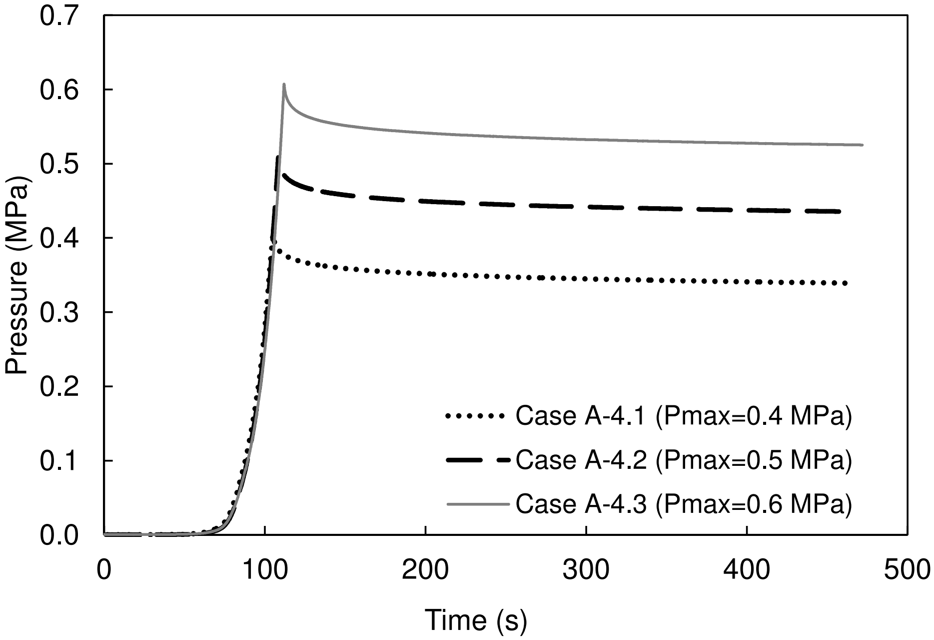

Figure 5.12: Compaction and relaxation of single layer plain woven textiles at one compaction rate for different target P (series A-4)

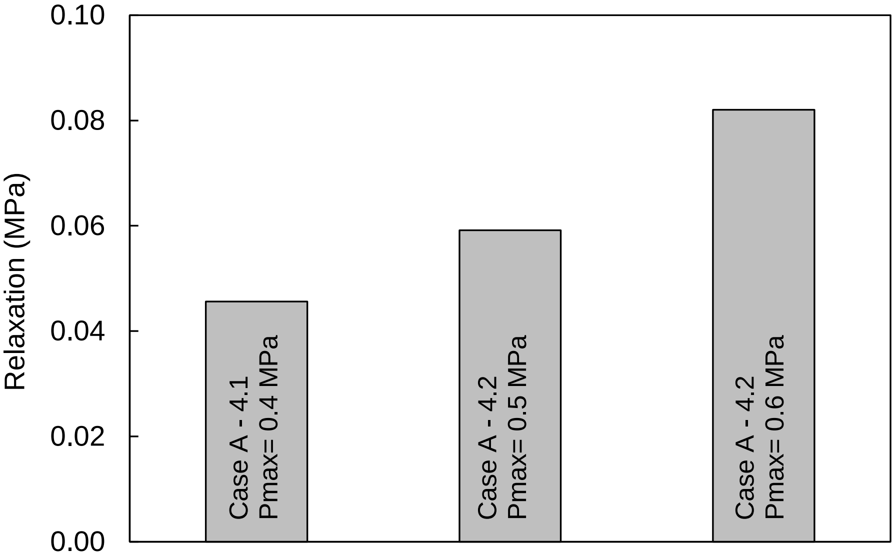

Figure 5.13: Relaxation of single layer plain woven textiles subjected to the same compaction rate, for different target P (series A-4)

Experimental series A-5 featured one case with compaction rate set to 1.0 mm/min. Maximum target pressure was limited to 0.55 MPa. The textile sample was compacted and then load was removed to investigate the complete loading cycle as well as any non-linear behaviour.

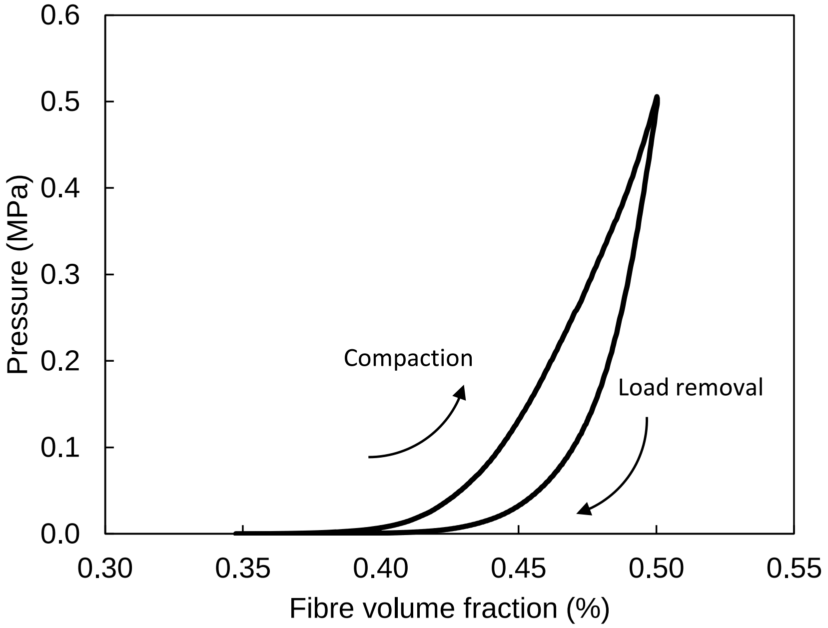

Figure 5.14: Compaction and load removal of single layer plain woven textile (series A-5)

Compaction and load removal done on a textile enables reorganization of the fibres and yarns within the textile. To investigate this matter more closely, the topography of the surface of the sample before and after loading was obtained as presented in Figure 5.15.

The surface topography of a layer of textile before compaction was recorded using a 3D KEYENCE microscope VHX-2000. Coordinates normal to the textile plane could be obtained using 300× magnification. The same textile sample was positioned within the compaction set-up and compacted to a pressure of 0.6 MPa, once. After compaction, the textile was secured and positioned again under the microscope. The same topography measurement method, and then again after subjecting the sample to a further 100 compaction cycles, was applied. Results show clearly that the non-compacted textile features more surface irregularity and roughness from a configuration where the fibre network has not undergone reorganization, compared to the compacted textile layer which has a smoother top surface. Clearly a higher v_f values may be achieved using pre-compaction prior to any PCM manufacturing process. On the other hand, tomography showed that for this particular case, compacting for 1 cycle or 100 cycles did not change the topography of the textile surface significantly.

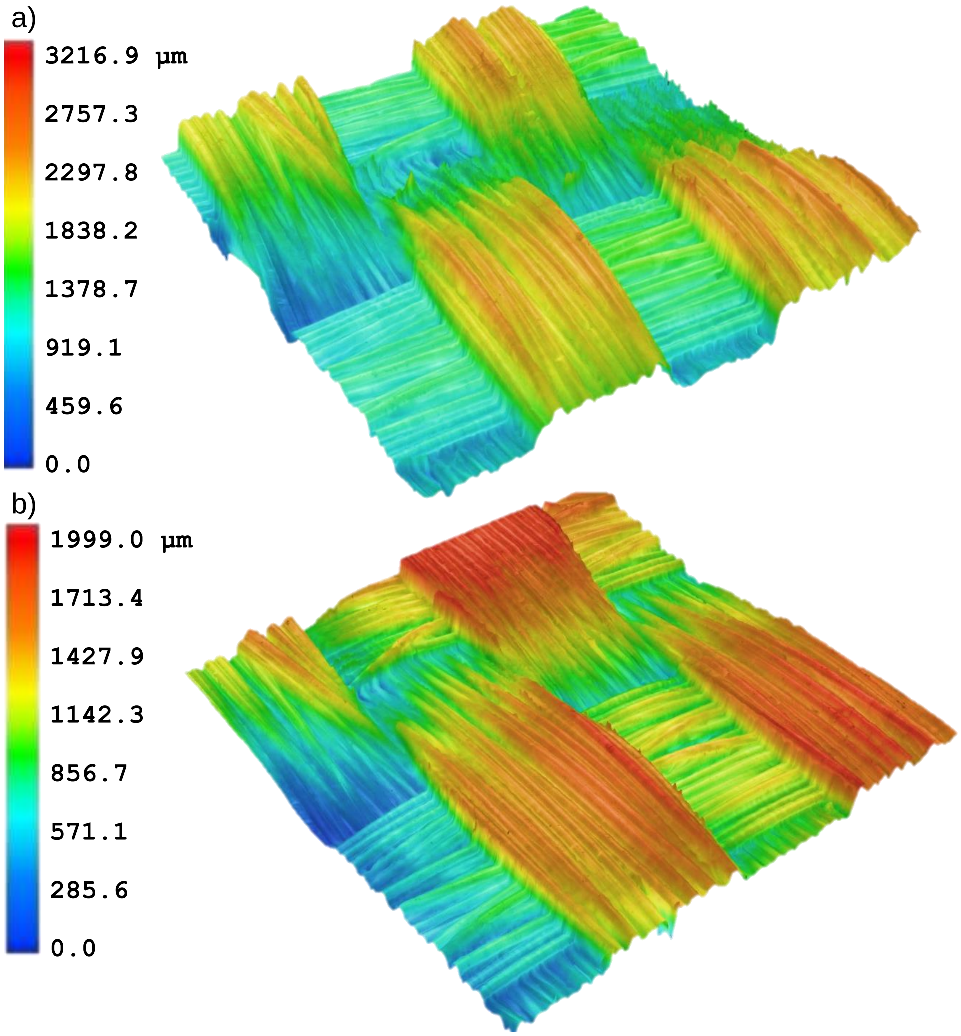

Figure 5.15: Topography of textile surface: a) before compaction, b) after 100 cycles of compaction and load removal

5.5.2 Simulation trials

6 simulation series were performed in attempting to replicate the findings obtained through physical testing.

Simulation series B-1 featured the compaction of 3 virtual samples where the numbers of iterations between each compaction step were 2×10^7, 5×10^7 and 10×10^7 for cases B-1.1, B-1.2 and B-1.3 respectively. Maximum target pressure was set to 0.50 MPa. Due to procedure by which compaction is effected, with displacement being the controlled variable, maximum pressures feature some minor fluctuations from case to case. These series were performed so as to identify the number of iterations that would best replicate experimental compaction results reported previously, Figure 5.16. In this way, a first correlation between time and numbers of iterations is established. It is worth notifying that the curve fit is generally excellent over the whole curve, and so this correlation can credibly be deemed as valid for the whole simulation.

This series of simulations enabled the identification of an appropriate number of iterations to be performed at each step. Setting the number of iterations to 5×10^7 (Case B-1.2) between each compaction step of 1.0 μm offered the best match with experimental trials at a compaction rate of 1 mm/min. When the number of iteration was lower than 5×10^7 (Case B-1.1), compaction pressure built up at lower fibre volume fractions which is expected from the experimental trials as a similar trend was observed experimentally with higher compaction rates. Conversely, a higher number of iterations (Case B-1.3) led to compaction pressure values that were lower at the same v_f, which was also expected from comparable experimental compaction results obtained at lower compaction rates.

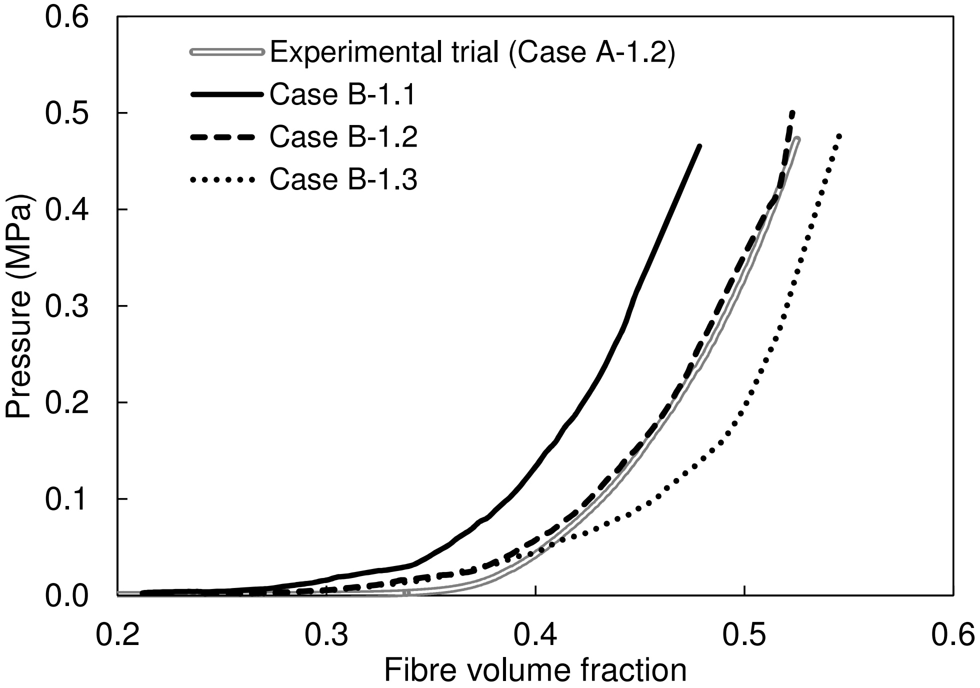

Figure 5.16: Compaction of a virtual single layer plain woven textile using different iteration numbers, and experimental trial (series B-1 vs. A-1)

In case B-1.2 the textile was allowed to iterate at constant height for a much higher number of iteration cycles after the compaction phase. This enabled relaxation occurrence, demonstrating the capability of the proposed simulation method to replicate relaxation as an intrinsic feature, Figure 5.17. This figure demonstrates that pressure increased mostly linearly up to v_f of 0.37, and beyond that pressure increased in a non-linear manner. From a v_f of approximately 0.5 pressure increased mostly linearly again as a function of v_f.

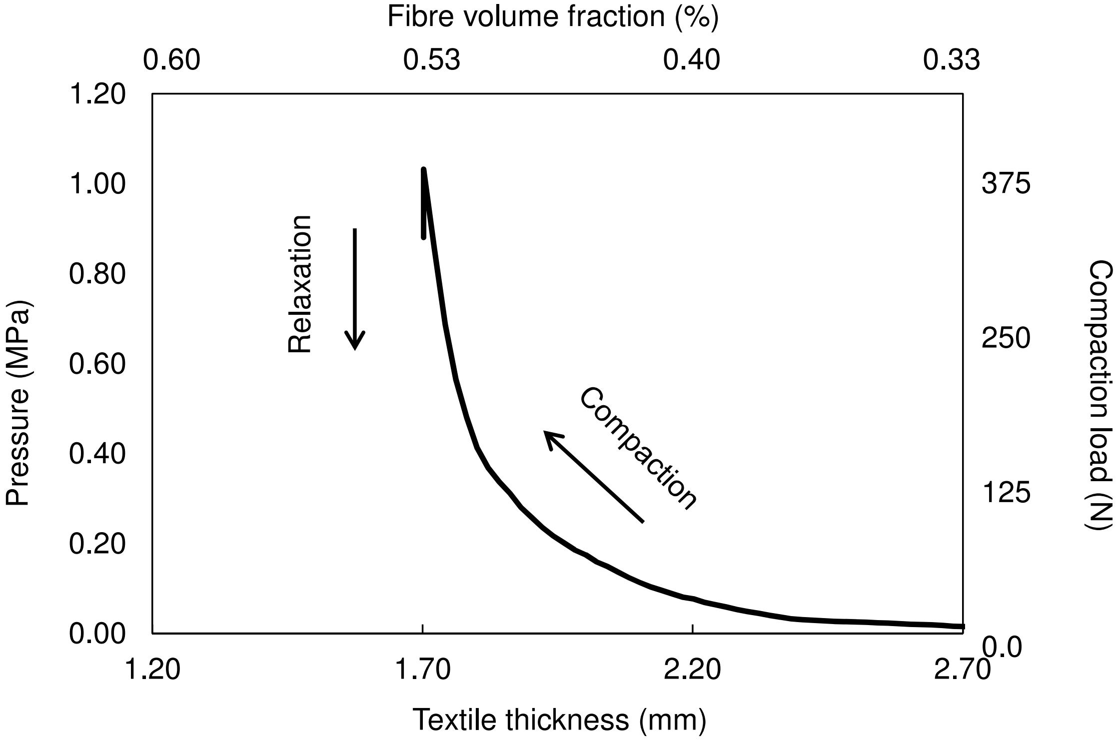

Figure 5.17: Compaction and relaxation of virtual single layer plain woven textile (series B-1.2)

Simulation series B-2 featured a single case where the number of iterations between each compaction step was set to 2×10^7, similar to case B-1.1 during its compaction phase, Figure 5.18. The virtual sample was compacted, with relaxation started at 0.20, 0.40, 0.6, 0.8, 1.0 MPa in cases B-2.1 to B-2.5, respectively, Figure 5.19. This series of simulations were performed to quantify the effect of initial pressure on subsequent relaxation.

More relaxation was observed at higher maximum compaction pressures. Relaxation taking place from higher pressures also required more time to reach stable pressure levels. This may be caused by the fact that less relaxation takes place during the compaction phase in such cases. Relaxation from the highest pressure of 1.0 MPa was very large, suggesting an unrealistic number of iterations for this virtual sample in high pressures.

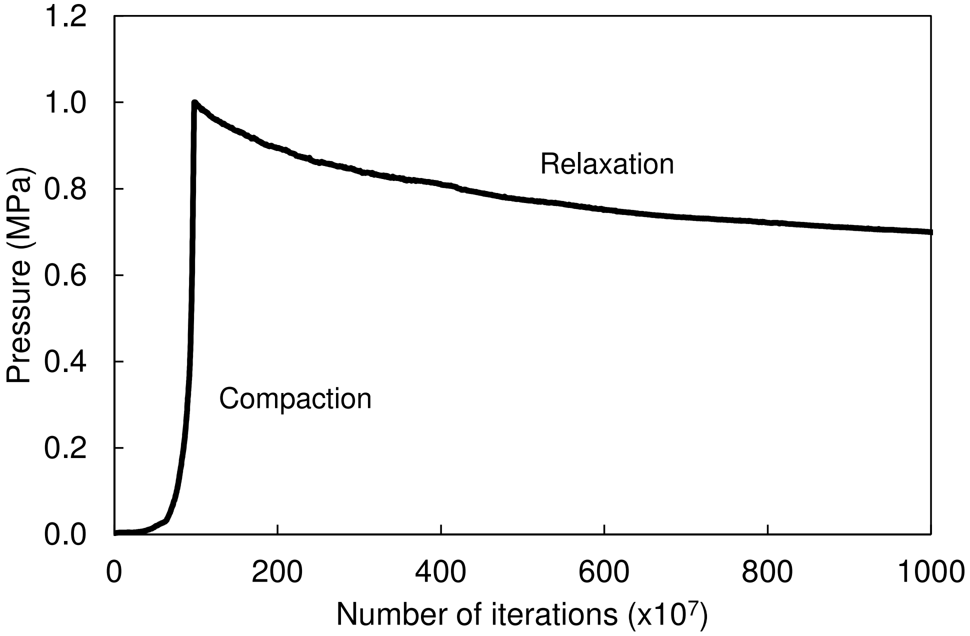

Figure 5.18: Compaction and relaxation of virtual single layer plain woven textile (series B-2.5)

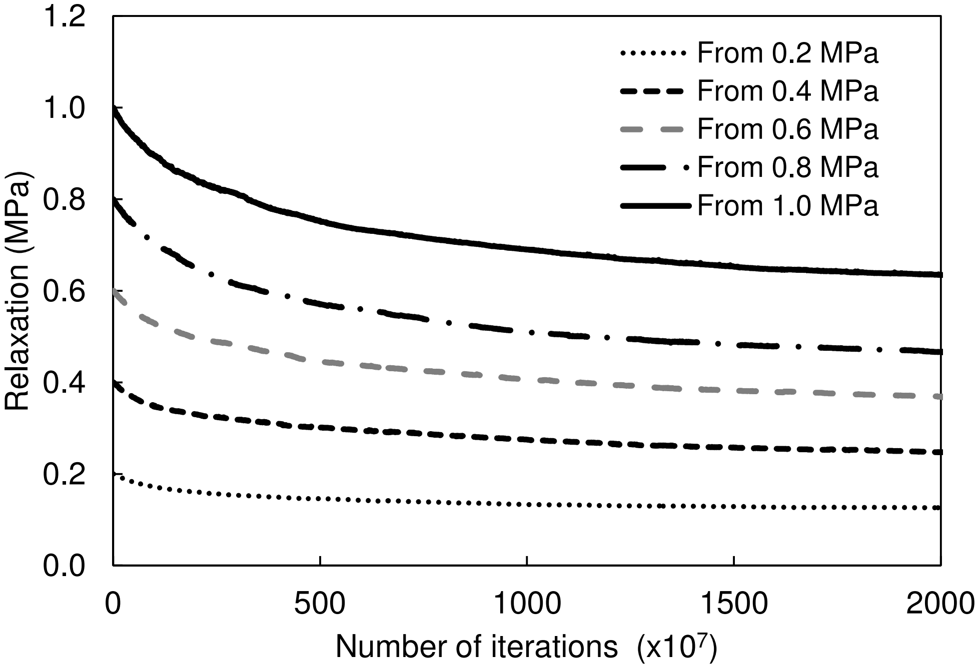

Figure 5.19: Relaxation of virtual single layer plain woven textile from various onset pressure P (series B-1.1)

Simulation series B-3 features 3 cases where the number of iterations between each compaction step were 2×10^7, 5×10^7 and 10×10^7 for cases B-3.1, B-3.2 and B-3.3 respectively. The maximum pressure was set to 0.5 MPa. Virtual samples were compacted and then held to the constant thickness reached at maximum pressure, enabling relaxation.

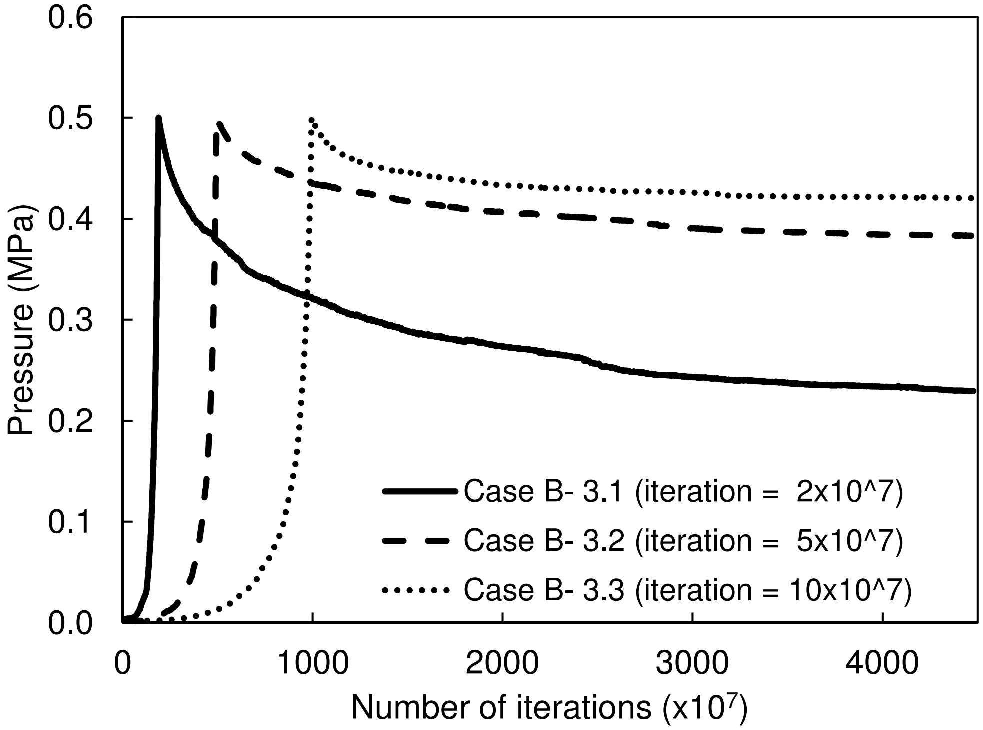

Figure 5.20: Compaction and relaxation of virtual single layer plain woven textiles subjected to different number of iterations with the same target P=0.5 MPa (series B-3)

Small numbers of iterations corresponding to very fast compaction (case B-3.1) include large relaxation levels about 50% after the compaction phase, as a consequence of pressure build-up at low v_f during the compaction phase. Therefore, higher numbers of iterations are probably more advisable. This paralleled what was seen in experimental trials; less relaxation during compaction leads to more relaxation after the compaction phase when using higher compaction rates.

As seen in Figure 5.21, relaxation experienced by the virtual textiles was reduced with an increase of iteration numbers. It is interesting, even for experimental trials that the effect of the compaction rate features a plateau in terms of number of iterations, beyond which relaxation is essentially constant.

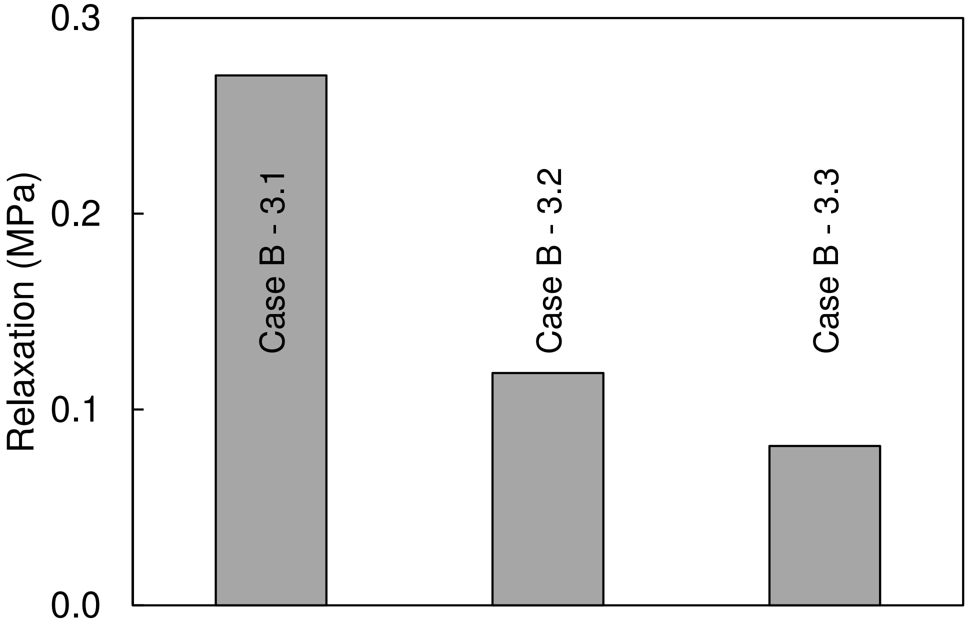

Figure 5.21: Relaxation of virtual single layer plain woven textiles subjected to different numbers of iterations (series B-3)

Fibre volume fraction results where virtual single layer plain woven textiles were compacted using different numbers of iterations toward the same target pressure showed differences in v_f although the maximum pressures reached in the compaction phase were the same, Figure 5.22. Higher v_f may be caused by more relaxation and fibre network reorganization at higher numbers of iterations, comparable to experimental trials using lesser compaction rates.

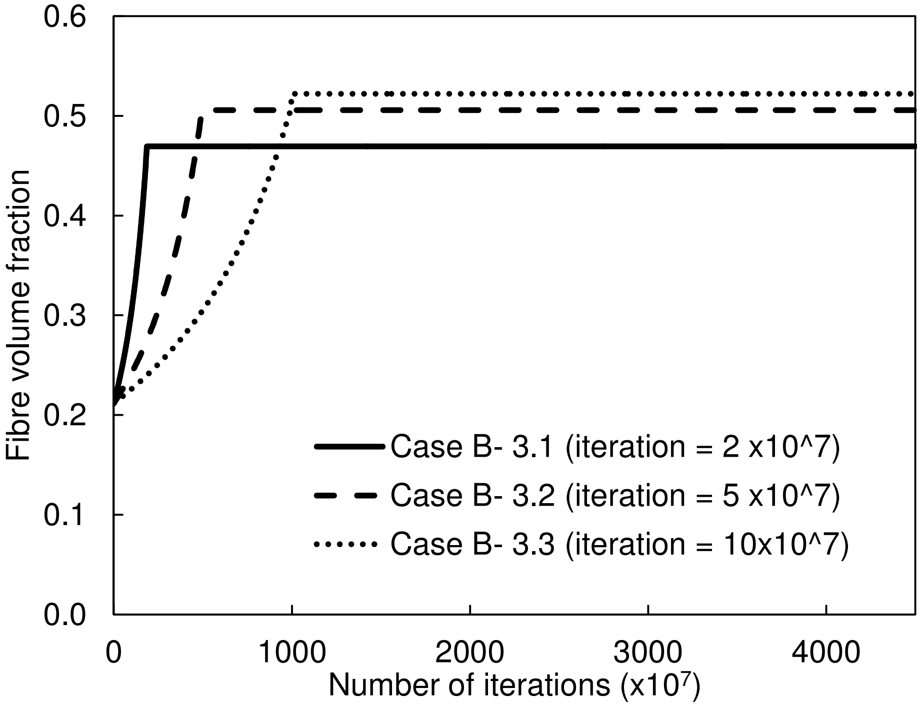

Figure 5.22: v_f as a function of the number of iterations for virtual single layer plain woven textiles subjected to different iteration number for target P=0.5 MPa (series B-3)

Simulation series B-4 featured 3 cases similar to series B-3 where iteration numbers between each compaction step were set to 2×10^7, 5×10^7 and 10×10^7 for cases B-4.1, B-4.2 and B-4.3 respectively. The maximum target v_f was set to 0.50. Virtual samples were compacted and then held to the constant thickness reached at the maximum v_f, enabling relaxation.

Small numbers of iteration or very fast compaction rates resulted in a large pressure peak in early stages of the compaction phase corresponding to low levels of v_f. This was paralleled with observations in the experiment trails with fast compaction rates. Regardless of this large pressure peak, relaxation after the compaction phase for case B-4.1 continued beyond the set simulation period. This case may reach a stable pressure condition after a longer time, which was not practical in these simulations. In spite of differences in initial pressures at on onset of relaxation phase for cases B-4.2 and B-4.3, stable pressures were reached after a short iterative period, in both cases.

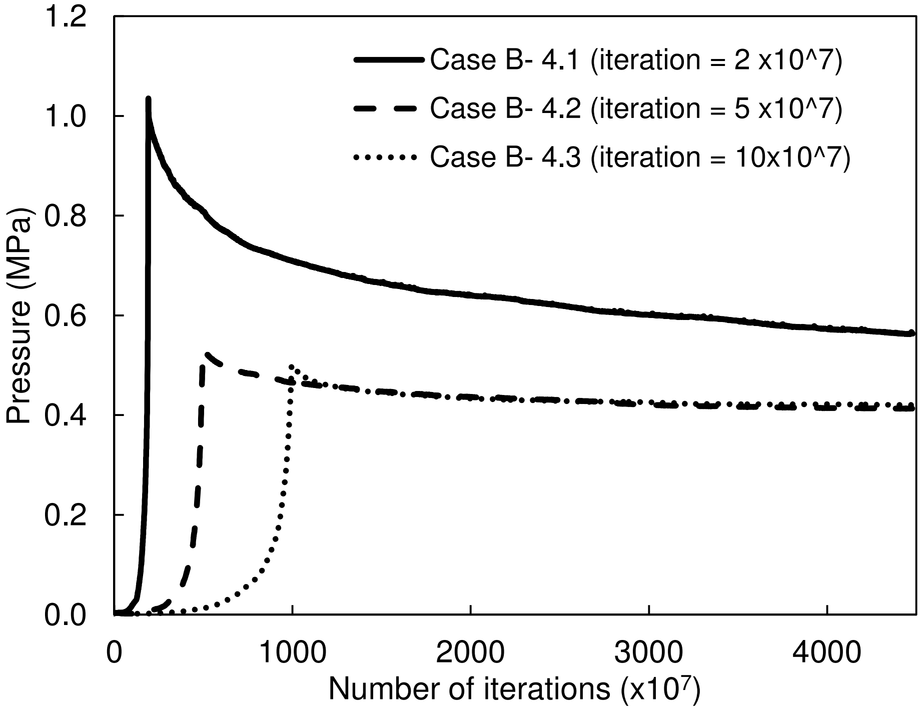

Figure 5.23: Compaction and relaxation of virtual single layer plain woven textile subjected to different iteration numbers for target v_f=0.5 (series B-4)

As seen in Figure 5.24, the amount of relaxation experienced by the virtual textiles was reduced with an increase in iteration numbers. Relaxation levels in cases B-4.2 and B-4.3 were commensurate with those observed in experimental trials. Case B-4.1 showed more relaxation as previously discussed.

Fibre volume fraction results where virtual single layer plain woven textiles were compacted subjected to different iteration numbers to the same target v_f are presented in Figure 5.25.

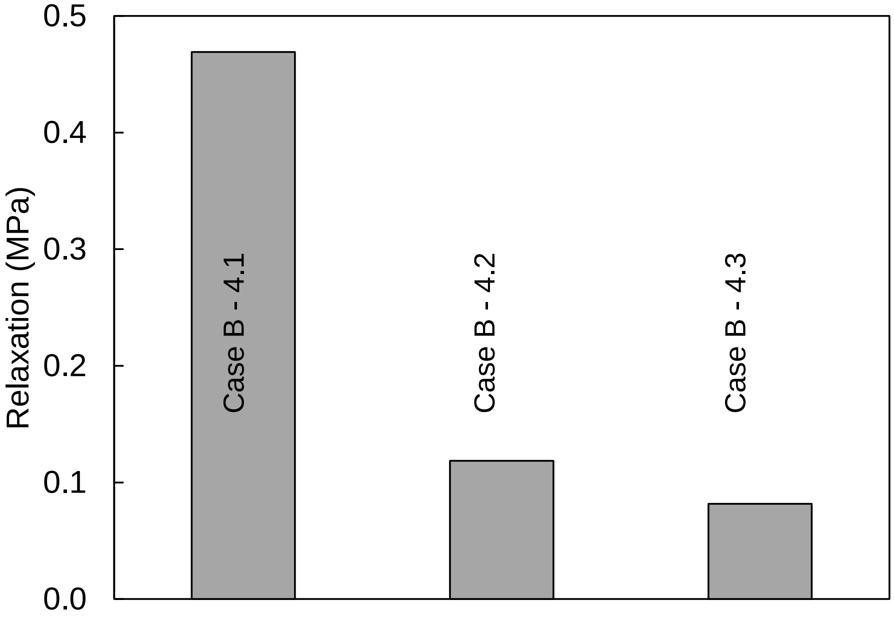

Figure 5.24: Relaxation of virtual single layer plain woven textiles for various numbers of iterations and target v_f (series B-4)

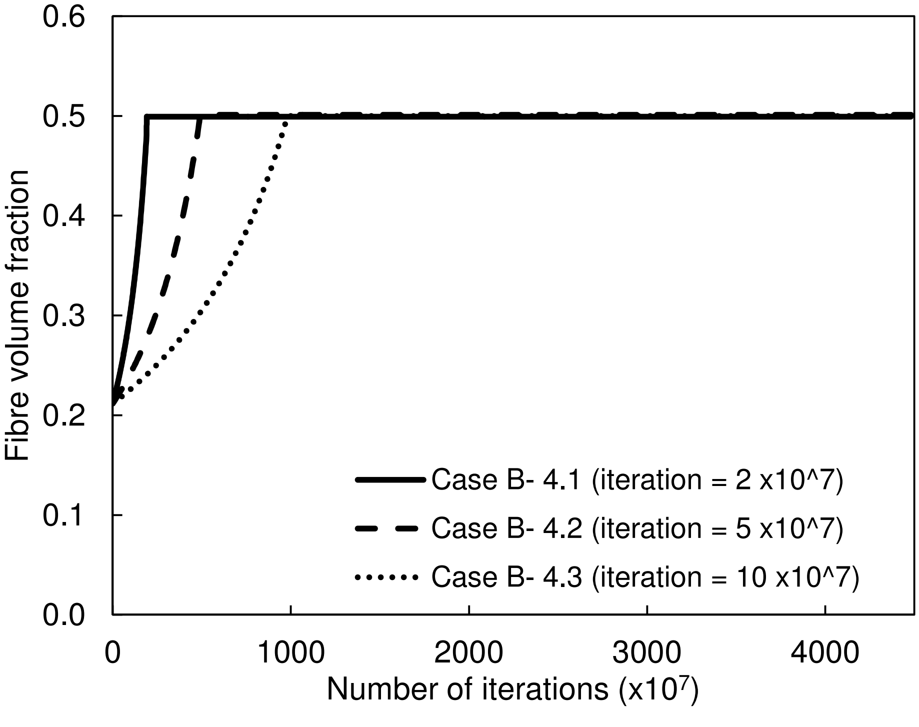

Figure 5.25: v_f as a function of number of iterations for virtual single layer plain woven textiles subjected to different iteration number for target v_f (series B-4)

Simulation series B-5 featured a single case with the number of iterations set to 5×10^7. Maximum pressure was limited to 1.10 MPa. The virtual textile sample was compacted and then load was removed to simulate a complete loading cycle similar to experimental trials, Figure 5.26.

This simulation series presents the linear and non-linear behaviours upon loading and load removal for the textile simulate using the particle-based modelling method, similar to those observed in experimental trials. Also, clearly the results show that after load removal, reorganization of fibres within yarns lowers the pressures that may be achieved at higher v_f, similarly to experimental trials.

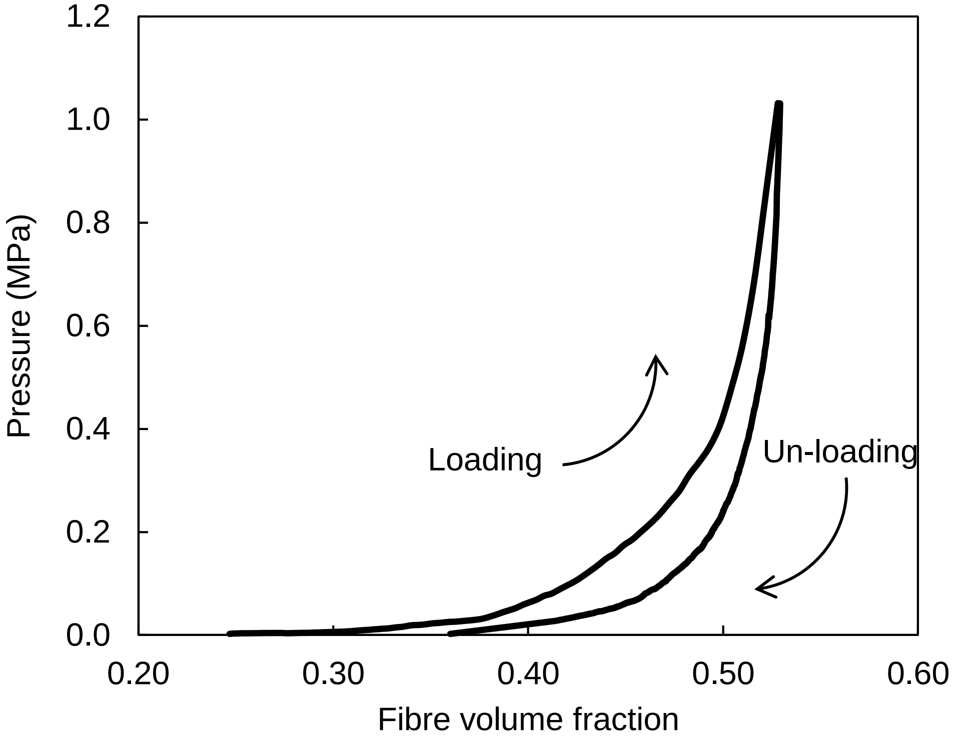

Figure 5.26: Compaction and load removal of virtual single layer plain woven textile (series B-5)

Simulation series B-6 featured two cases where the number of iterations was set to 10×10^7. Maximum pressures were targeted to 0.50 MPa. This series included double-layer stacks of textiles with perfectly aligned yarns and with yarns that were perfectly staggered in both directions. Samples were compacted then allowed to relax. During the compaction phase of the double-layer stack of textile with perfectly aligned yarns, pressure increased from lower fibre volume fractions compared with the stack featuring yarns that were perfectly staggered, Figure 5.26.

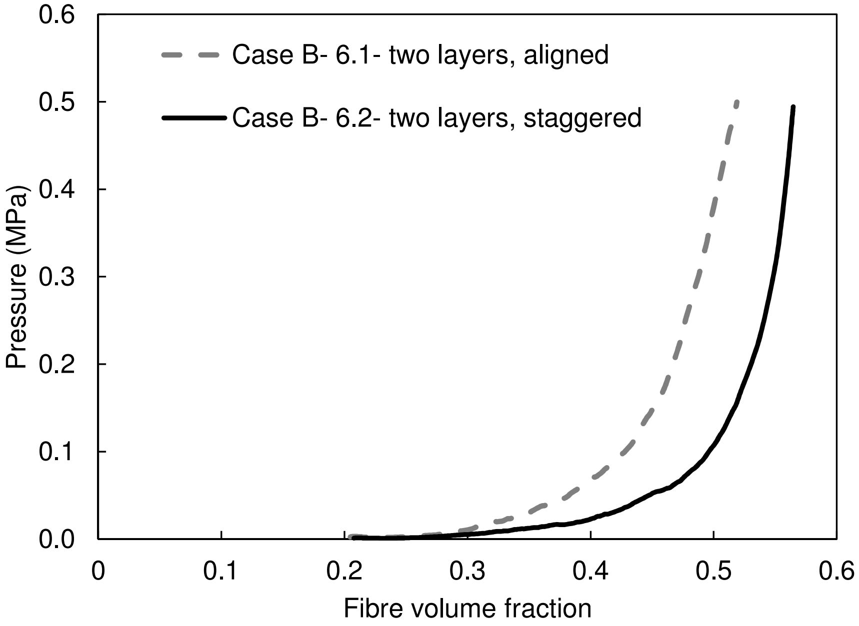

Figure 5.27: P as a function of v_f in a double-layer aligned and staggered plain woven textile in compaction phase

Figure 5.28 shows isometric views of initial and compacted configurations for the two cases. Also, yarn cross-section in the centre of the layers are presented for both cases. From these geometric representations obtained from the particle-based modelling method it is seen that, in case B-6.1 yarns were flattened on top of each other unlike in case B-6.2 where yarns were moved along with changing cross-section shapes. This clearly replicates the nesting behaviour of layers as expected and investigated earlier [101]. This figure also shows isometric views of initial configurations for the two cases. In the latter case, a higher P appear at lower v_f due to the staggered layers.

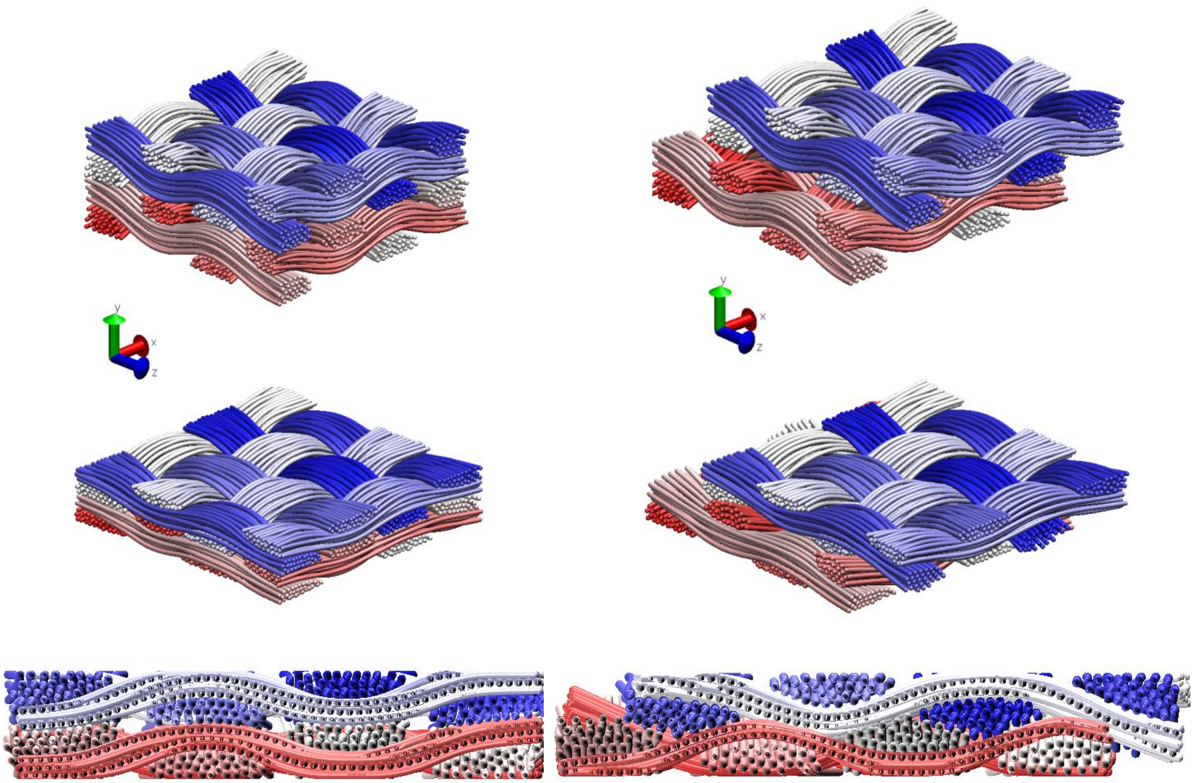

Figure 5.28: Geometric representation of compaction and relaxation of virtual double-layer plain woven textiles subjected to different layering for target P=0.5 MPa (series B-6)

After the compaction phase in both B-6 cases, virtual samples were held to the constant thickness reached at maximum target pressure, enabling relaxation, Figure 5.29. More relaxation resulted in case B-6.1. This paralleled with what was expected in physical reality, as shifting yarns and filling inter yarn gaps during compaction resulted in late pressure build-up. Nesting can be compared to relaxation taking place during the compaction phase for case B-6.2, and this leads to lower relaxation taking place after the compaction phase. Relaxation in case B-6.1 continued beyond the set simulation time and suggested yarns flattening as well as yarns shifting into the gaps between layers.

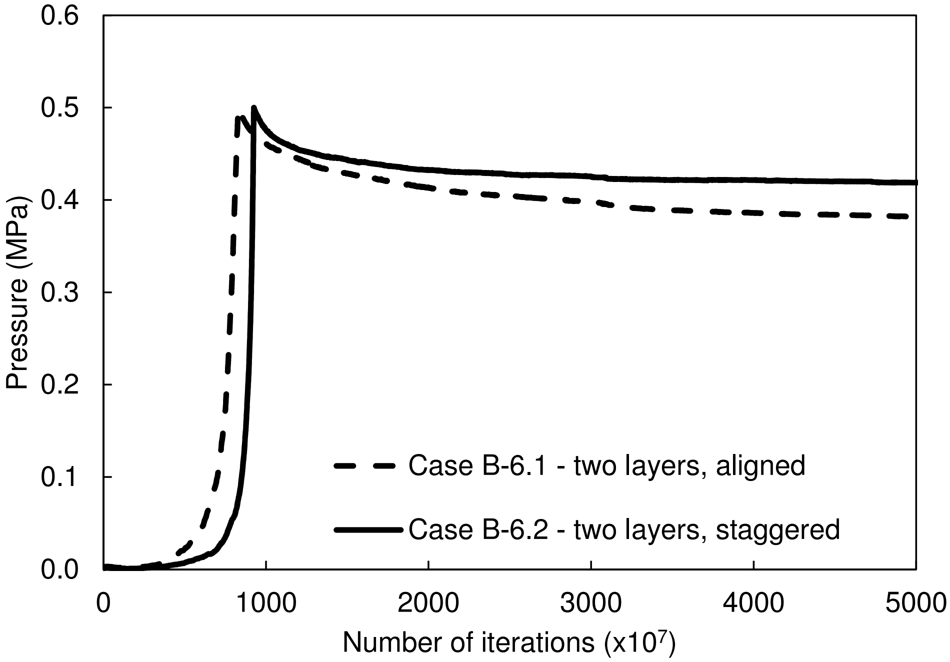

Figure 5.29: Compaction and relaxation of virtual double layer plain woven textiles subjected to different stacking for target P=0.5 MPa (series B-6)

5.6 Conclusion

Using the particle-based method for modelling the relaxation behaviour of technical textiles was investigated. Simulation results were validated experimentally in many cases. Validation work showed that the particle-based modelling method replicates the relaxation behaviour of textiles very well. Modelling enables the prediction of the relaxation behaviour of textiles during and after compaction phase.

The particle-based modelling method developed can be used for relaxation modelling of different textile structures and numbers of layers. The procedure for enabling the representation of time-dependent behaviour of textiles by drawing a parallel with the number of iterations was introduced.

Chapter 6

Particle-based modelling of in-plane shear of textiles

6.1 Preamble

Chapter 6 contains the results obtained from particle-based modelling of woven textiles subjected to in-plane shear. In-plane shear simulations of woven textiles were performed on a plain woven textile, following compaction and relaxation covered in prior chapters. Selected simulations performed on virtual woven textiles were validated with experimental trials. Parameters used in previous chapters were used, again, such as the same yarn contact models and same Nylon 6/6 within yarns. New boundary conditions were introduced replicating shear the frame rig, along with other parameters such as the shear force and locking angles used in defining the in-plane shear behaviour of textile reinforcements. Two different algorithms were introduced and assessed, for modelling friction, resulting in the choice of a less computationally demanding procedure in simulations. work presented in this chapter was submitted for publication in a peer-reviewed journal [102].

6.2 Abstract

Prediction of the geometry and constitutive behaviour of textiles subjected to in-plane shear loading using a particle-based modelling method is investigated in this chapter. Plain weave textiles featuring fibres represented as a series of conjoined particles are modelled using discrete mechanics as an alternative to traditional continuum mechanics. The configurations of individual fibres are obtained from first principles, minimising strain energy terms via a modified Metropolis algorithm.

In previous work [104], modelling of both the geometry and constitutive behaviour of textiles at the microscopic, mesoscopic and macroscopic scales using a particle-based method was reported and the compaction behaviour of woven textiles was predicted with good levels of accuracy. In this work, the particle-based approach enables prediction of in-plane shear behaviour of the textiles from first principles during loading as it would occur in technical textile structures. Other elements of constitutive behaviour such as bending and buckling and punching may be predicted for different types of textile using this method. Such scenarios will be reported in forthcoming publications.

In order to characterize the in-plane shear behaviour of woven textiles, a series of simulations replicating articulated frame in-plane shear tests were performed. The effects of different boundary conditions at fibre ends upon application of a displacement field to the particles, and iterations of the positions toward lower strain energy levels, are reported. From these simulations, load-displacement curves were constructed; furthermore displacement fields, locking angles and shear stresses were identified. Results of simulations and experiments performed on woven textiles subjected to in-plane shear showed good agreement as well as improvement in simulation accuracy over other modelling techniques.

6.3 Introduction

Textiles are subjected to different load cases upon service, resulting in deformations which may include in-plane shear, bending, in-plane tension and out-of-plane compression. Deformations, displacements and the resulting textile configuration may be defined at the mesoscopic and macroscopic scales.

In-plane shear is the dominant deformation mode that occurs upon wrinkle-free draping of textiles on surfaces featuring double curvatures. Conversely, in-plane shear is not prevalent when draping textiles over surfaces which exhibit single curvature; over such surfaces the textile will bend so as to conform to the supporting surface [62, 70].

In-plane shear of woven textiles is characterised by the relative rotation of warp and weft yarns at crossovers. A woven textile is illustrated in Figure 6.1, both in the undeformed state and as it might appear after in-plane shear.

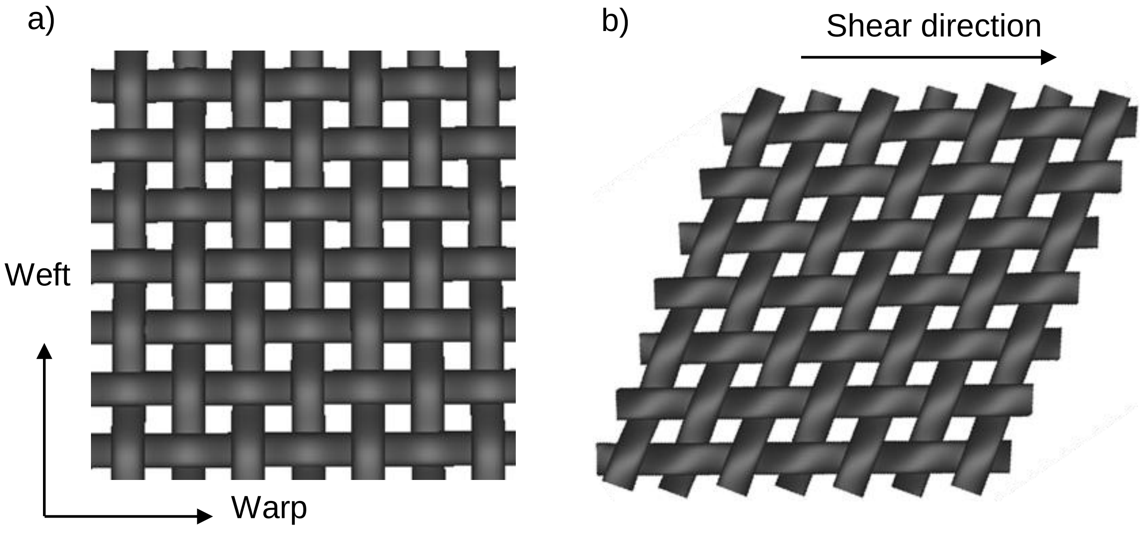

Figure 6.1: Textiles: a) undeformed, b) after in-plane shear

The constitutive behaviour of a textile subjected to in-plane shear can be quantified experimentally through articulated frame testing or bias-extension testing [20]. The articulated frame test apparatus consists of four links of equal length connected by low friction pivots so as to form a square that will be deformed into a rhombus as the test proceeds and two opposing pivots are pulled away from each other. A textile sample is mounted between grips on each link. Extension of the frame imparts shear to the textile as detailed in section 6.4 of this chapter. The bias-extension test probes the in-plane shear behaviour of a textile sample subjected to axial extension with yarns initially aligned at 45° from the extension axis. Realignment of yarns in the sample is observed upon extension, with pure shear imparted over the central section of the sample only [16].

In-plane shear characteristics of woven textiles and a comparison of articulated frame and bias-extension testing were reported by Harrison et al. [43]. A normalization procedure for bias-extension results was developed for enabling direct comparison of results obtained from both methods. Analysis of experimental results obtained from each method indicated that deformations induced upon articulated frame testing are more consistent and better related to the sample boundary conditions than their counterpart induced upon bias-extension testing. In so doing, the importance of boundary conditions at frame edges and bias-extension testing grips during tests was emphasised.

Sharma et al. [110] investigated the in-plane shear behaviour of dry woven textiles upon draping. Deformations were measured from images collected in articulated frame tests. The authors noted that the increase in shear force is associated with an increase in friction forces at yarn cross-overs resulting from reduced yarn crimp.

The maximum in-plane shear angle of a textile is defined as the in-plane shear deformation angle that the textile can withstand before wrinkles appear and major out-of-plane deformations occur over its surface. The angle defined between the warp and weft yarns that characterises the onset of wrinkling is termed the locking angle. In cases where the warp and weft yarns are initially perpendicular, the locking angle and the maximum in-plane shear angle are numerically similar; both are function of textile architecture and material properties [14,18]. Generally the angle can be detected by visual inspection [115]. Alternatively, it may be identified on a curve of the shear force as a function of the shear angle as the intersection of the tangent to the curve at its steepest slope and the horizontal axis [5]. In a plain weave textile the ratio of the yarn width to yarn spacing largely contributes to determining the locking angle between warp and weft yarns [87].

Harrison et al. [1] used biaxial bias-extension testing to investigate coupling between in-plane shear and tension, and textile wrinkling. Biaxial bias-extension testing was proven as an accurate method of characterising wrinkling and in-plane shear for woven textiles. This technique uses a straightforward experimental set-up and analysis procedures based on readily available image analysis software.

Boisse et al. [14] studied the occurrence of wrinkling upon textile forming. The authors noted that wrinkles affected the bending stiffness adversely. A simplified formulation of virtual internal work involving tension, in-plane shear and bending moments was applied to woven repeating unit cell (RUC) for simulating the onset of wrinkling. It was found that the bending stiffness largely determined wrinkle occurrence and geometry.

In further work, Boisse et al. [15] conducted finite element simulations of woven unit cells subjected to in-plane shear. The study was carried out using an explicit dynamic approach based on a simplified dynamic equation which accounted for tension and in-plane shear strain energy terms. Simulation results were compared to those of articulated frame experiments. The authors concluded that in-plane shear stiffness has a major effect on the appearance of wrinkles and on the value of the locking angle. During simulation it was assumed that in-plane shear and bending stiffness were independent of in-plane tension. The proposed finite element analysis did not consider the effect of yarn twist on bending stiffness.

Potluri et al. [84] reported an improved method for measuring the shear properties of textiles using a wide strip bias-extension test and compared this to conventional narrow strip bias-extension testing. Results of the proposed method were in close agreement with those obtained from the Kawabata Evaluation System (KES). Yarn deformations were measured and confirmed through two independent techniques, namely optical scanning and a strain-freezing technique. The authors stated that yarn deformations included upon bias-extension differ from those normally expected in pure shear. It was observed that yarn thickness increased initially, whilst after the locking angle was reached the yarn thickness started to decrease with individual yarn width remaining constant.

Lomov and Verpoest [69] studied the in-plane shear behaviour of plain, twill and 5-harness satin glass textiles using finite element analysis (FEA) models incorporating friction, compression and bending of the yarns. The models used non-linear tension, bending and compaction properties of the yarns, a coefficient of friction at yarn crossovers and the fabric weave structure as input data; all quantities were measured. The authors observed that pretension of textile samples in the picture frame was a major contributor to result variability. Furthermore, it was observed that shear-tension coupling had a strong influence on geometric configuration during draping simulations. The authors noted that the entire shear behaviour is of significance to the response of textiles to draping, rather than the single value of the locking angle.

Badel et al. [6] aimed at quantifying changes to textile permeability resulting from draping the textile over a curved surface. The authors simulated the in-plane shear behaviour of a RUC of plain woven textile using FEA. A feature specific to the simulations was the use of periodic boundary condition in large deformations. Also, although yarns were modelled as continuous entities their fibrous, orthotropic nature was taken into account through a fitting parameter introduced in material properties. Simulation results were in good agreement with the experimental shear curves.

Willems et al. [130] used digital image correlation techniques to assess macro scale deformations in different glass and carbon textiles subjected to shear testing, with three different sample in-plane preloads. The effects of material, textile architecture and preloads on shear behaviour were discussed. It was demonstrated that the author's correlation technique can characterize textile deformation well. Also, the influence of sample configuration and pretension on the shear behaviour was highlighted. Substantial increase in shear force was recorded with a rise in sample tension. Also, inconsistencies in data were detected upon articulated picture frame testing resulting from minimal yarns misalignments.

Lomov et al. [65] used an optical extensometer in improving the accuracy of strain measurements during textile deformation at the microscopic and mesoscopic scales. The approach permitted the measurement of the deformed shape of draped textiles in three dimensions, and of local shear angles. The data was used in validating drape models and predicting the performance of consolidated composite parts using FEA. The authors stated that the proposed optical full-field strain techniques is a preferred technique for ensuring that deformation measurements performed during tensile or in-plane shear tests of textiles are of high accuracy, with possible limitations for textiles with uneven or rough surfaces.

Launay et al. [58] proposed an experimental device for measuring the warp and weft tensions in woven textiles undergoing an articulated frame test. Reduction of tensions decreased the values of shear load measured during articulated frame tests significantly. In finite element simulations performed by the authors it was assumed that in-plane shear strain energy is independent of initial yarn tension; however, the authors demonstrated the effect of initial tension on shear force experimentally. Initial tension was identified as a significant parameter in wrinkle formation during processing.

Cao et al. [20] presented a comprehensive study on experimental methods and benchmark results for characterizing in-plane shear in woven textiles. Advantages and limitations of existing experimental and associated modelling approaches were discussed. In-plane shear testing of textiles using articulated frame and bias-extension setups were conducted for both balanced and unbalanced fabrics, and compared. The authors' work constitutes a benchmark toward the understanding of strengths and limitations of experimental and modelling approaches.

Finally, as noted by Vanclooster et al. [123] determining the mechanical properties and deformation behaviour of textiles subjected to in-plane shear or undergoing draping requires substantial skill and is time consuming; the associated high costs justify the development of advanced predictive techniques.

The particle-based modelling method proposed in this paper enables accurate intricate modelling of the geometry and mechanical behaviour of textiles subjected to in-plane shear at the microscopic, mesoscopic and macroscopic scale. Particle-based modelling constitutes a powerful whilst general numerical tool for simulating the large-strain constitutive behaviour of non-homogeneous or structured textiles, by accounting for the detailed geometric configuration at fibre scale during deformation as shown in the following sections.

6.4 Modelling methodology

In keeping with the modelling methodology reported previously [104], individual fibres making up textile domains submitted to in-plane shear are represented by series of discrete spherical particles with diameters equal to the nominal fibre diameter. Positions of the particles describe the geometry of fibres within yarns. Changes in strain energy resulting from displacements of individual particles as well as from interactions with neighbouring particles enable the modelling of the overall behaviour of the textile when subjected to large in-plane shear strains.

6.4.1 Modelling method

As a simulation of textile in-plane shear proceeds, individual particles are displaced randomly under fixed boundary conditions in an iterative procedure until a stable state of minimum strain energy in the system is reached. As particles move whilst boundary conditions remain unchanged, the configuration of fibres evolves. Once a stable state is reached, boundary conditions are altered corresponding to shear strain imposed on the textile, and the individual positions are iterated again under altered but fixed boundary conditions, randomly, towards a new state of minimum strain energy. The non-conservative behaviour associated with friction, which was demonstrated to play an important role in defining the in-plane shear behaviour as discussed above, is modelled through the inclusion of a threshold of acceptance applied on new particle configurations reflecting energy loss as discussed later in this section.

In this implementation, a modified Metropolis algorithm manages iterations of particle positions which collectively are referred to as configurations and define the textile geometry. Iterations of particle positions are done over physical subspace [a, a] using a set limitation on the step size and a uniformly distributed random walk. A random number generator is used in this implementation for generating values over the range (0, 1) that are statistically independent, with a distribution that is uniform over an extended period of time. Within each iterative procedure performed under constant boundary conditions representing the articulated frame, the configuration is changed by adding a small random displacement to the x, y or z coordinate of a randomly chosen particle. This results in a change in strain energy between two given configurations defined before and after the iterative step.

A practical aspect of this computational method is the time required for iterating enough particle positions, in models that feature sufficient numbers of particles to make them appropriately detailed and useful reliably, leading to a configuration of minimum strain energy stored in the textile. The time required for the system to reach a stable, low level of energy depends on several factors including the number of particles, initial fibre volume fraction and friction within particles assemblies; this time is usually estimated from experience.

The total strain energy stored in the particle assembly will progressively diminish towards equilibrium. After computing the change in energy resulting from the displacement of a single particle, the result is assessed. If strain energy in the whole system was reduced the new configuration is accepted and used as the initial state for the next step. If strain energy was not reduced acceptance may still result from statistical arguments based on a predefined probability [100]; alternatively the change may be rejected. In both cases the new configuration becomes the initial state for the next iteration. Following convergence, boundary conditions are changed to reflect ongoing shear, and the iterative procedure is repeated.

An important physical parameter in the system is friction, which partially restricts fibres from slipping relatively to each other. Whilst conservative strain energy terms associated with elastic loading may be calculated for a given static configuration, non-conservative friction losses occur only as the fibre assembly goes from one configuration to another. Friction also contributes to hysteretic losses observed experimentally in deformed textiles, most notably for in-plane shear.

Two approaches to managing friction may be considered in particle-based modelling. In a direct approach, normal forces between pairs of contacting fibres are determined at every contact point. Displacements at all contact points in the fibre assembly are also calculated. Knowing these forces and displacements, a total energy loss associated with fibre friction between two configurations is obtained. This energy term is subtracted from appropriate strain energy terms defined from previously mentioned elastic strains. This direct approach requires highly computationally intensive work due to number of contact points involved. Also, a proper value of the coefficient of friction must be introduced from trials, and the determination of this is not trivial.

The alternative indirect approach proceeds as follows. In the absence of friction, contacting fibres slip freely relative to each other and resulting configurations are dictated only by the ensuing reduction in total elastic strain energy stored in the assembly at a given fibre volume fraction, as discussed above. In the presence of friction, fibre slippage is impeded and as a result, additional energy must be expensed for evolving towards configurations corresponding to the same fibre volume fraction as for a system devoid of friction. This is integrated in the algorithm by altering the strain energy threshold conducting to a tentative configuration being accepted upon iteration. When no friction is present, upon iteration generally any tentative configuration that reduces the elastic strain energy stored in the textile is accepted as the new configuration on an ongoing basis. On the other hand, when friction is present, evolution from one configuration to another requires that some of the initial elastic strain energy must be expensed through friction. The energy balance will only remain favourable if final configurations with lower strain energy levels are accepted.

This approch, this is implemented through a percentage applied on the strain energy in the initial state, which remains constant through the entire simulation. As a result, at lower fibre volume fractions when fewer contacts are present, friction generally does not have a major effect. However, with increases in fibre volume fraction and number of contacts, strain energy differences resulting from small displacement have a significant effect as expected for friction.

6.4.2 Yarn configurations and tension upon in-plane shear of textiles

During in-plane shear of a textile the area covered by the textile is reduced leading to an increase in v_f under constant thickness. Inter-yarn spacings defined perpendicularly between neighbouring warp yarns and between neighbouring weft yarns respectively both decrease, eventually leading to lateral compaction of the yarns, Figure 6.2.

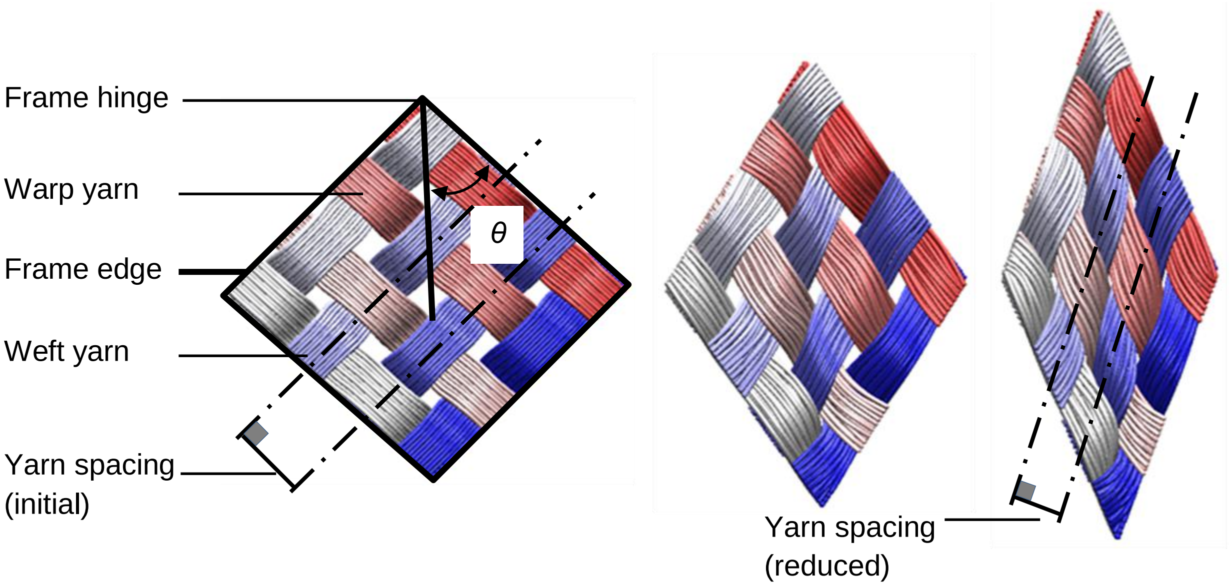

Figure 6.2: Simulation of 16 crossovers of plane woven textile undergoing in-plane shear in articulated frame configuration

Shear can also increase yarn crimp as yarns get thicker with less inter-yarn space available for yarns weaving back and forth between either surfaces of the textile. Finally, as crossovers are no longer defined by yarns crossing at 90°, yarn sections effectively rotate around yarn axes. All these effects can lead to tensioning of the yarns and of the fibres within them. The critical question of clamping and boundary conditions is closely related to yarn and fibre tensioning; this is revisited in section 6.5.2 further in this chapter. Finally, increased yarn and fibre tension results in increased friction at yarn crossovers, which is neither elastic nor conservative.

6.4.3 Strain energy terms

Imposing in-plane shear strain to a textile as described above prompts changes in yarn configuration leading to particle displacements, and to fibre strains and stresses. Intra-fibre and inter-fibre strain energies refer to strain energy terms defined for a single fibre and from interactions between neighbouring fibres respectively.

Changes in axial tension, axial compression and/or bending stresses within a fibre change its strain energy. Strain energy term U_A arising from axial tension/compression is a function of fibre material's Young's modulus E, fibre cross-section area A, and distances between 2 particles l_{ab} and l under and without loading respectively, Equation 6.1, Figure 6.3. Bending strain energy U_B is calculated from the angle ψ defined between three successive particles with second moment of area I for circular fibres, Equation 6.2, assuming an initially straight fibre as represented by angle π.

$$U_a = \frac{AE}{2L} \cdot (l_{ab} - l)^2 \tag{6.1}$$

$$U_B = \frac{EI}{l_{ab} + l_{bc}} \cdot (\pi - \psi)^2 \tag{6.2}$$

Contact forces between curvilinear fibres within a yarn may be calculated using Hertz'

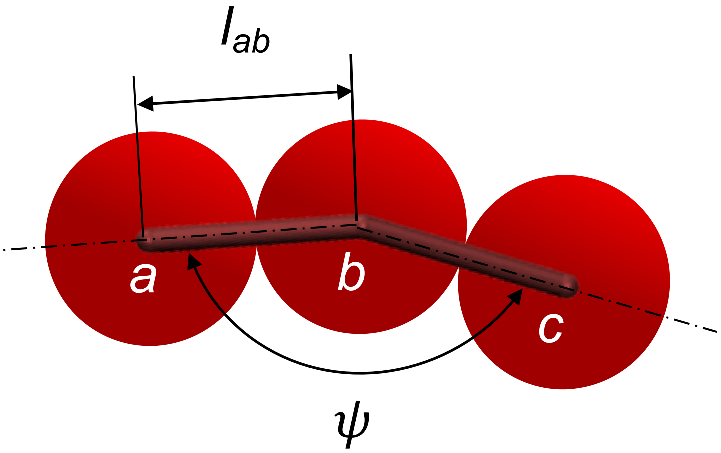

Figure 6.3: Distance and angle between neighbouring particles within a fibre, enabling calculation of axial and bending strain energy terms

contact model [83] and/or Gutowski's compaction model [99]. In Gutowski's compaction model the fibres within yarns are wavy instead of being perfectly straight, Figure 6.4. The suitability of jointly using both Hertz' fibre compaction model and Gutowski's compaction model for fibre assemblies as done here was validated by the authors in a previous work [104].

The strain energy resulting from inter-fibre contacts and yarn compaction described by Gutowski's model is calculated from the contact forces between neighbouring fibres F_{ij}, integrating these forces over the particle's displacement:

$$U_G = \int F_{ij} \cdot dx = \int \frac{192EI}{\beta^3} \cdot \frac{(l_o - l_{ij})}{(l_{ij} - l_{min})^3} \cdot dl_{ij} \tag{6.3}$$

In Gutowski's model, particles other than immediate neighbours in the same fibre are separated by distance l_{ij}, with $l_{min} < l_{ij} < l_o$ where l_o is the initial distance between particle centres and l_{min} is the fibre diameter. β is a fitting parameter either evaluated by microscopy or fitted to experimental results. Gutowski's model is equivalent to the beam bending equation with reducing span; it has been used successfully in many

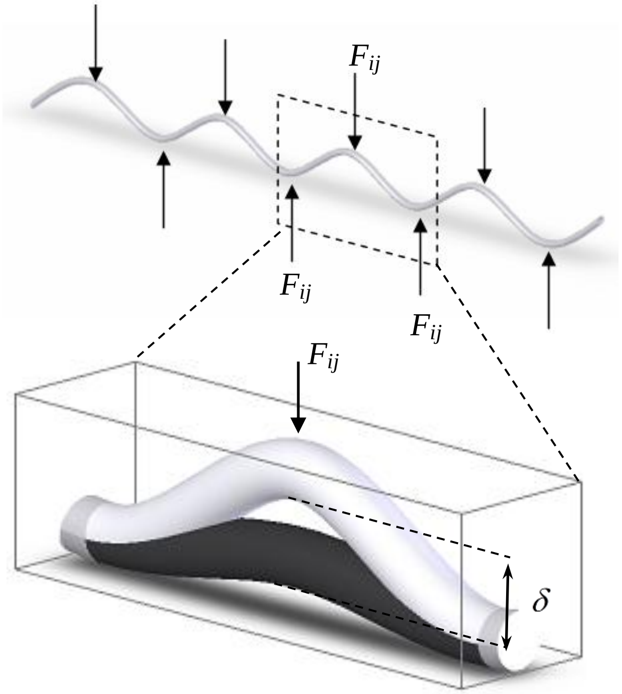

Figure 6.4: Schematic representation of fibres and their deflection in Gutowski's compaction model

occurrences [19, 39, 83, 99] and validated in [104] for the system discussed here.

6.5 In-plane shear simulation methodology

In-plane shear simulations that replicated the articulated frame test method based on the algorithm described previously were performed. Ends of each individual fibre were positioned within planes representing the edges of the frame. In all simulations, all fibres in the balanced fabrics had the same initial free length between edges. In-plane shear was induced by progressively reducing angle 2θ defined between the two upper edges of the articulated frame, Figure 6.2, with the shear angle α defined as:

$$\alpha = \varphi - 2\theta \tag{6.4}$$

and angle φ being the angle between the initial warp and weft directions, which is usually 90°.

Edge and fibre ends were displaced in discreet steps, between which the total strain energy was minimized iteratively. The total shear force was recalculated at each step for the stabilised system by summing the edge-wise components of forces computed directly from strains generated in individual fibres on the frame edges, as detailed in the following section 6.5.1.

Two different methods were investigated for imposing initial displacements to the particles upon changes in boundary conditions during the simulated articulated frame tests. In the first method, particles located on the boundaries were displaced whilst other particles were left unmoved initially, to be displaced only through the iterative procedure, Figure 6.5a. Whilst this method is consistent with edge displacements in an articulated frame test, it imposes large displacements to a very small number of particles leading to high and localised strains in fibres. As a consequence, in the iterative procedure a large number of particles must undergo large displacements and within a reasonable computational time, most particles get limited chance to be displaced toward a minimum strain energy configuration.

In a second method which was used in simulations reported in this chapter, a full displacement field is imposed to all particles within the boundaries as shown in Figure 6.5b. The particles are displaced as a function of their positions relative to the centre of the domain and iterations towards lower strain energies are executed afterwards. This method is significantly more effective in terms of computational time even with larger numbers of particles present within the boundaries.

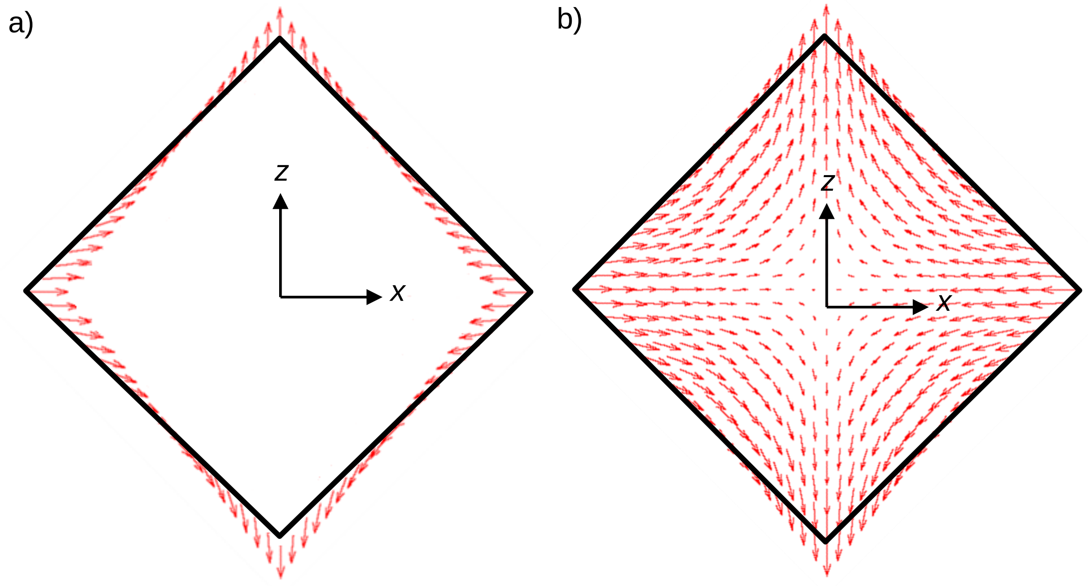

Figure 6.5: Imposed displacements applied to: a) boundary particles, b) all particles

6.5.1 Shear angle and shear forces

The shear angle α is a macroscopic measure of shear defined at the scale of the sample, corresponding to the departure from an initial 90° angle defined between the two upper edges of the articulated shear frame. It can also be viewed as the departure from 90° between the nominal warp and weft orientations. The angle α is initially 0° and increases upon shearing. Values of α during a test are determined from the vertical displacement of the top hinge, Equation 6.5, where d is the hinge displacement from its initial position and L_{frame} is the length of shear frame edges, Figure 6.6.

$$\alpha = 90^\circ - 2\cos^{-1}\left(\frac{\sqrt{2}L_{frame} + d}{2L_{frame}}\right) \tag{6.5}$$

Upon testing, the force F_s required for shearing the fabric can be calculated from the measured pulling force F as follows:

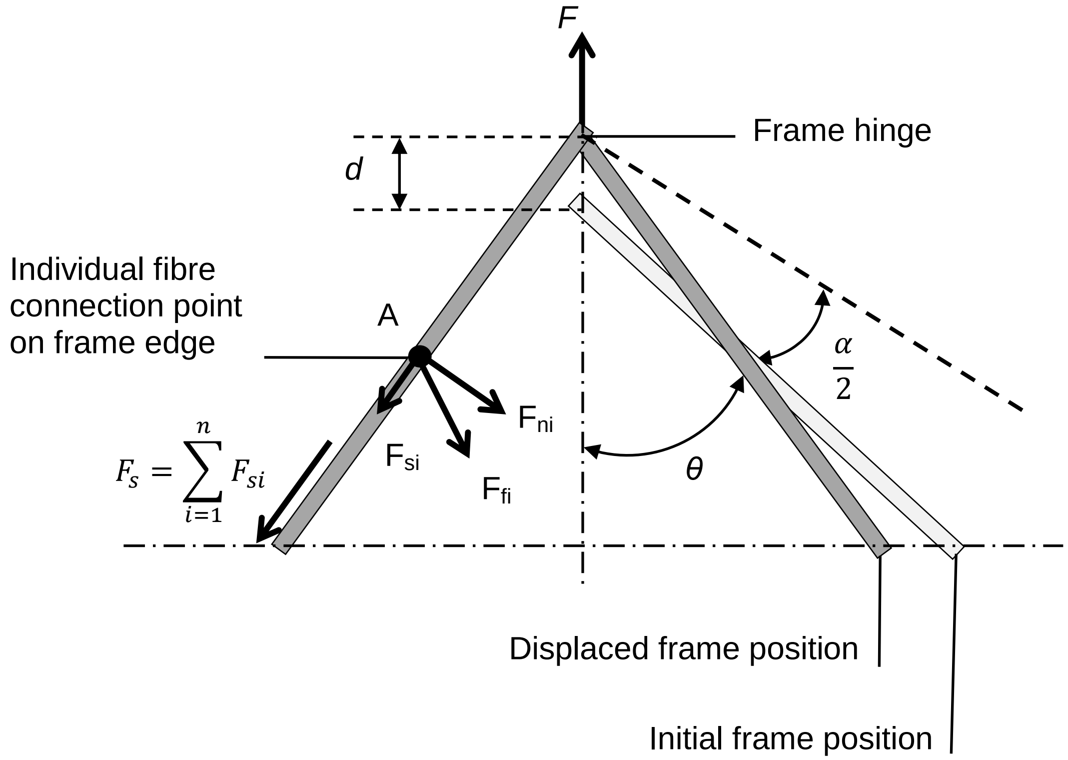

Figure 6.6: Shear angle and shear forces

$$F_s = -\frac{F}{2\cos\theta} \tag{6.6}$$

In simulations the shear force F_s was calculated from the summation of edge-wise projections F_{si} of individual fibre tension forces F_{fi} acting on the frame edges, for all fibres; in Figure 6.6 fibre force F_{fi} acting on the frame edge at point A is expressed as its normal component F_{ni} and edge-wise component F_{si}. Within simulations, confirmation may be obtained by calculating the pulling force F from the summation of the vertical components of all fibre forces F_{fi}. Validation against experimental results is then done through values of F_s.

6.5.2 Boundary conditions

Four different sets of boundary conditions may be imposed for attaching fibres to the frame edges during in-plane shear simulations. All four condition sets were implemented and evaluated for a plain weave unit cell. The four condition sets are labelled as: a) fixed segments, b) fixed pivots, c)pivots unlimited in edge plane and d)pivots limited in edge plane. The four sets of boundary conditions shown in Figure 6.7 are described below.

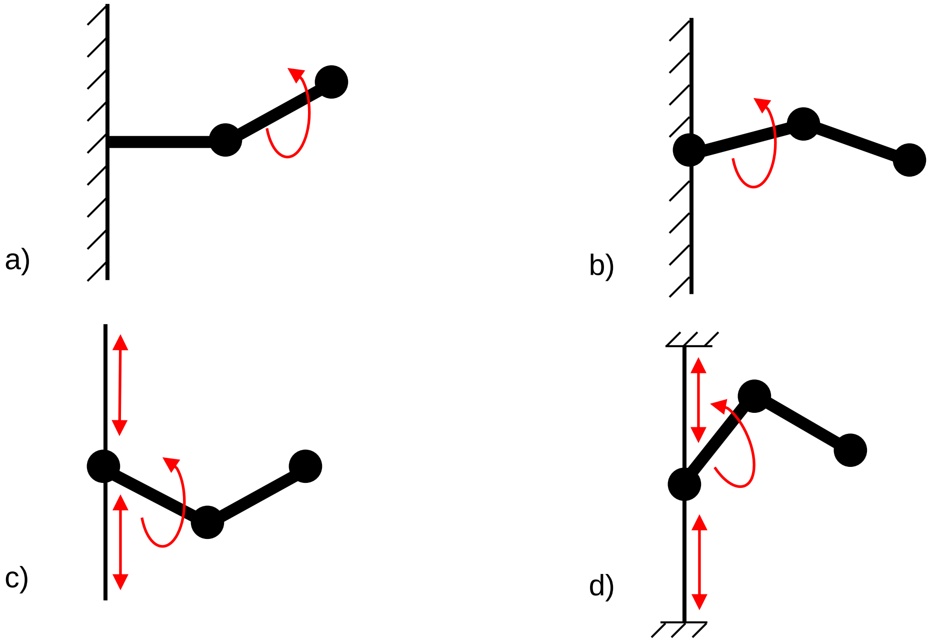

Figure 6.7: Four different boundary conditions: a) fixed segments, b) fixed pivots, c) pivots unlimited in edge plane, d) pivots limited in edge plane

The fixed segment condition (a) corresponds to fibres built into the frame edges, with all displacements and rotations restricted. Whilst this boundary condition will correspond to experimental reality in idealized cases where fibres are clamped perfectly into the testing frame, it induces difficulties especially for smaller domains as bending stiffness forces the fibres to extend normal to the frame edges during shearing, effectively leading to parasitic fibre extension. In experimental trials this problem is alleviated by using larger samples but in any case it will have an unwelcome influence on results.

The fixed pivot condition (b) aims at correcting the above situation by attaching fibres to the frame edges through pivots. The fibre ends can rotate but any displacement in or out of the plane of the frame edges is precluded. In doing so, fibre ends may form an angle with frame edges just like warp and weft yarns form an angle at crossovers during a test, leading to in-plane shear that is more uniform over the surface of the fabric. For small shear angles and yarns where fibres are not in very close proximity this works reasonably well, but when shear angles increase and fibres come close to each other, eventually contacting, the fibres are compressed laterally and very high parasitic forces ensue. This also has a very large effect on fibre strain, Figure 6.8.

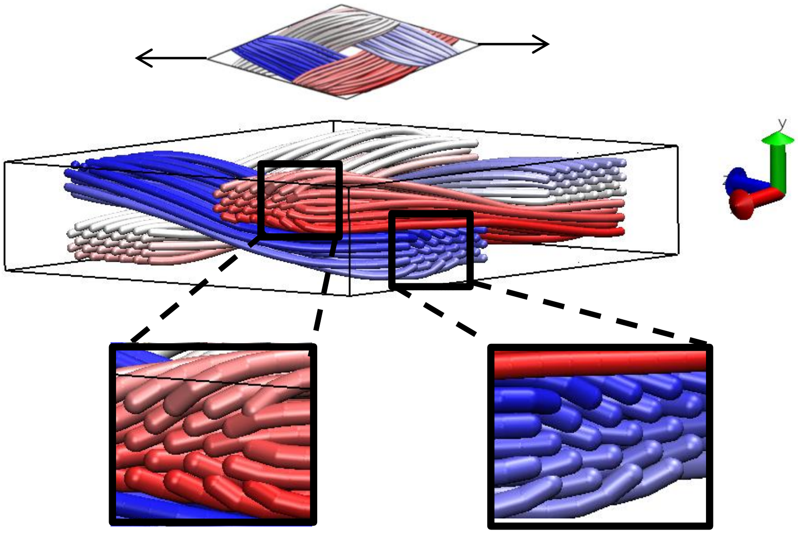

Figure 6.8: Simulation of unit cell with fixed pivots boundary condition; top view unit cell on shear, 3D view and problematic zones

The pivots unlimited in edge plane condition (c) aims at correcting both situations described above by attaching fibres to the frame edges through pivots that can rotate freely and may be displaced in the plane of frame edges, without any restrictions. Like condition (b), this works well at small shear angles but as the shear angle increases, the free movement of the pivots leads to unit cells that are distorted and not sheared to the extent intended. Negligible or no shear force is recorded, Figure 6.9.

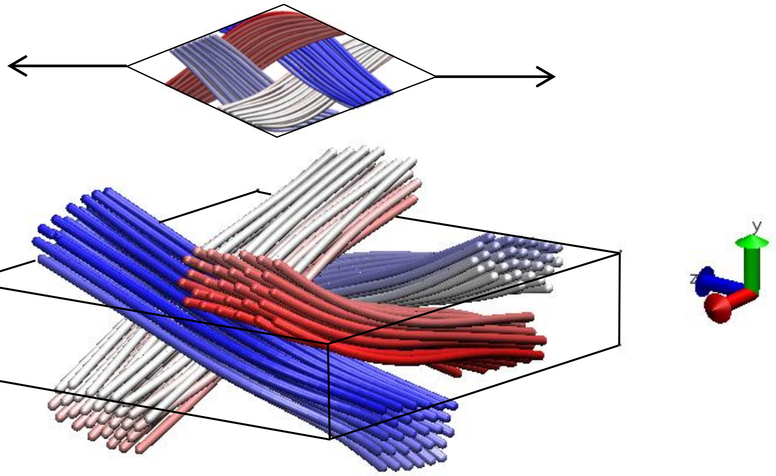

Figure 6.9: Simulation of unit cell with pivots unlimited in edge plane boundary condition; top view unit cell on shear, 3D view and problematic zones

The pivot limited in edge plane boundary condition (d) represents fibres attached to the frame edges through pivots that can rotate freely and may be displaced in the plane of frame edges, within the initial area defining the associated edge plane. The height and width of all boundary areas corresponds to the initial dimensions of the edge planes, and they remain unchanged during a simulation. Simply put, fibre ends can move in the domain boundaries, or edge planes, as needed for reaching lower states of strain energy; given that domain boundaries extend exactly along the centreline of yarns or exactly at mid-distance between yarns, they are effectively constrained by neighbouring fibres and yarns, as happens in experimental reality.

6.6 Articulated frame in-plane shear testing

The accuracy of particle-based simulations of the in-plane shearing of woven textiles was benchmarked by producing and physically testing a series of textile samples. Samples were manufactured from yarn featuring 30 monofilament Nylon 6/6 fibres with Young's modulus measured at 1.05 ± 0.02 GPa. The characteristics of the fibres and textiles appear in Table 6.1.

Table 6.1: Characteristics of fibres and textiles

Properties		**Number of samples**
Fibre diameter ($2r$)	0.296 ± 0.001 mm	50
Fibre density	1.172 ± 0.001 g/cm^3	20
Initial v_f of preform	25 ± 3.1 %	10
Surface density of preform	0.117 ± 0.001 g/cm^2	10

An articulated frame used for in-plane shear characterisation is shown in Figure 6.10. The frame featured four aluminium edges connected together by four ball bearing pivots. The upper and lower pivots were connected to an Instron 4482 universal testing frame with pin-type load cell mounts. Displacement speed was set to 1 mm/min and the load cell had a capacity of 1 kN. As the traverse of the universal testing frame pulled the upper and lower pivots away from each other at a constant rate, the angle between the two upper edges of the articulated frame 2θ decreased at the hinge, and the textile sample was sheared.

In order to minimize the effect of clamping whereby yarns may be construed as more or less effectively built in the frame edges with rotation mostly prevented at fibre level, and also to avoid any possible interaction of the textile piece with the pivots, the four corners of larger square pieces of textile were cut off prior to shearing so as to generate a cross-shaped sample. It should be noted that aforementioned issues with yarn bending near the frame edges as a result of attachment largely corresponding to built-in conditions

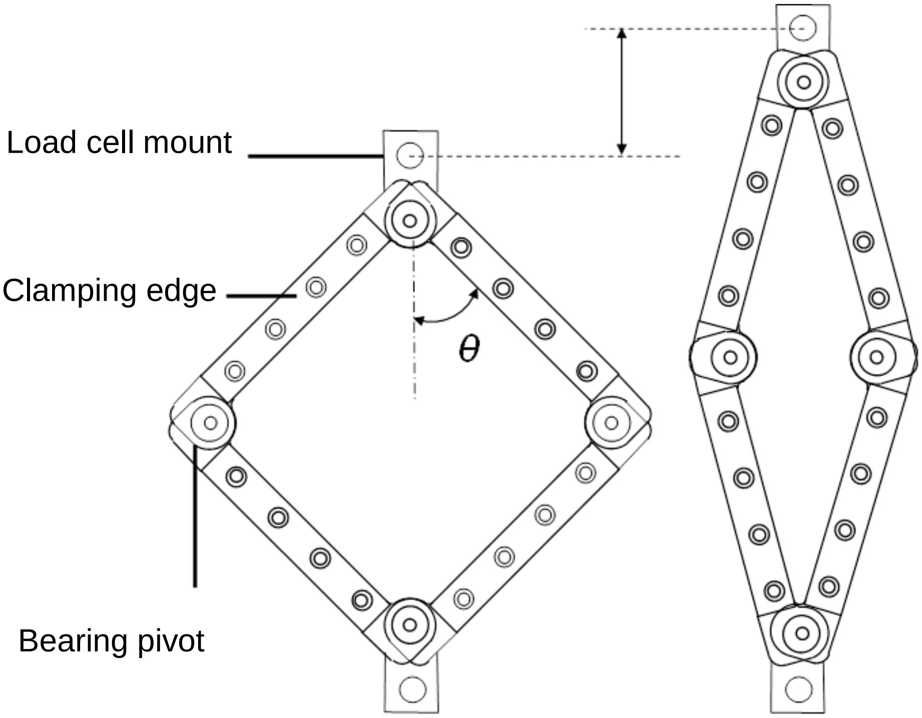

Figure 6.10: Initial and deformed configurations of articulated frame

in the experimental set-up, which are typically alleviated by using cross-shaped samples, were resolved in simulations through the careful selection of boundary conditions as discussed in section 6.5.2.

The load-displacement behaviour of the empty frame devoid of any textile sample was measured. Recorded forces were deducted from forces measured during regular in-plane shear tests, cancelling any contributions of the frame to the load. Textile samples were mounted in the frame, Figure 6.11, and 5 repeats of each in-plane shear test were performed, Figure 6.12. All tests were carried out to a shear angle of 52°, at which point wrinkles appeared on the surface of samples. It should be noted that since wrinkling starts very progressively, it is difficult to identify a unique point separating un-wrinkled and wrinkled states. The initiation of wrinkling is approximated by visual inspection from the side direction if the central region of the sample.

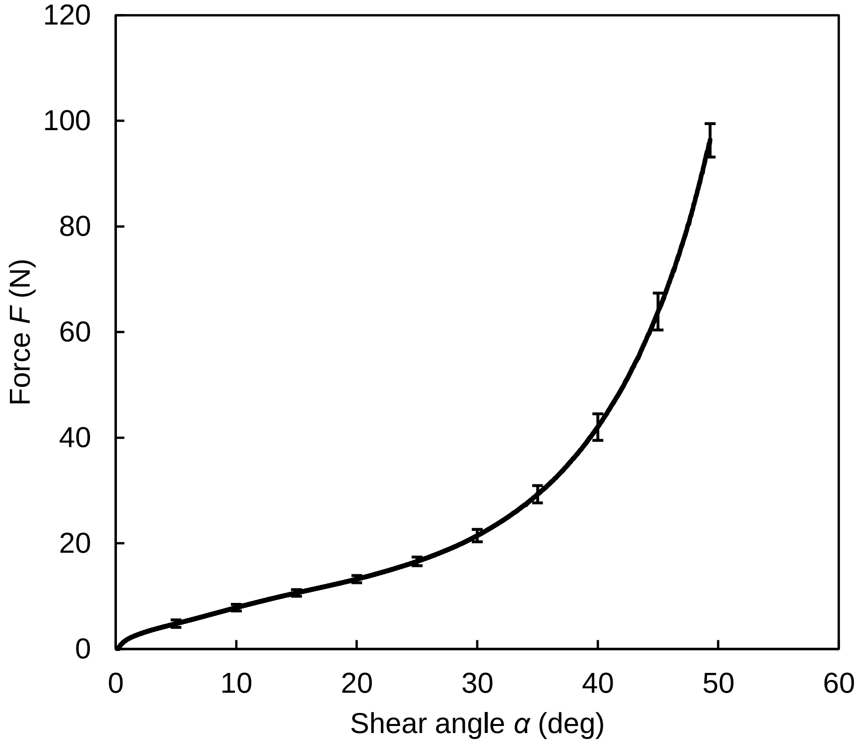

Figure 6.11: Force F as function of shear angle α from experimental trials

In-plane shear testing of the aforementioned Nylon 6/6 textile samples showed a mostly linear increase in shear force F until approximately 32°. Past that angle, shear force increased following a generally exponential trend.

All results were normalized to obtain normalised shear force F_N and enable comparison with results available from literature, Figure 6.13. Shear force data were normalized to the side length of the textile samples in simulations and in experiments; in simulations this length is L_{frame} whilst in experiments in corresponds to the length of any side of the sample's central square zone. Normalization is typically performed in analysing in-plane shear results due to the use of various frame sizes used by different researchers [20].

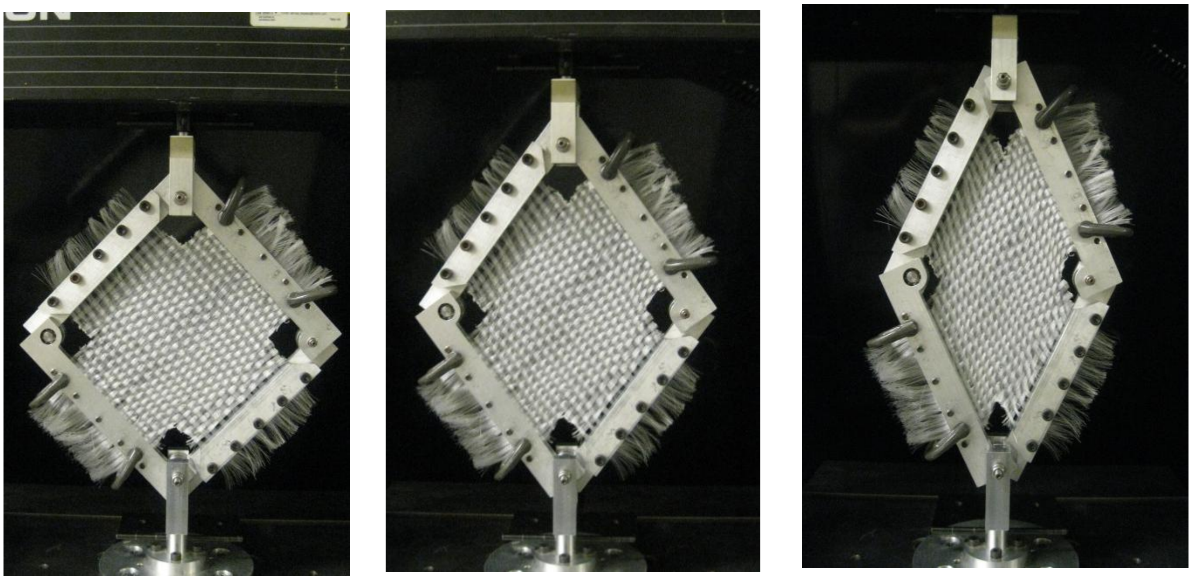

Figure 6.12: Nylon 6/6 textile sample undergoing in-plane shear test in articulated frame

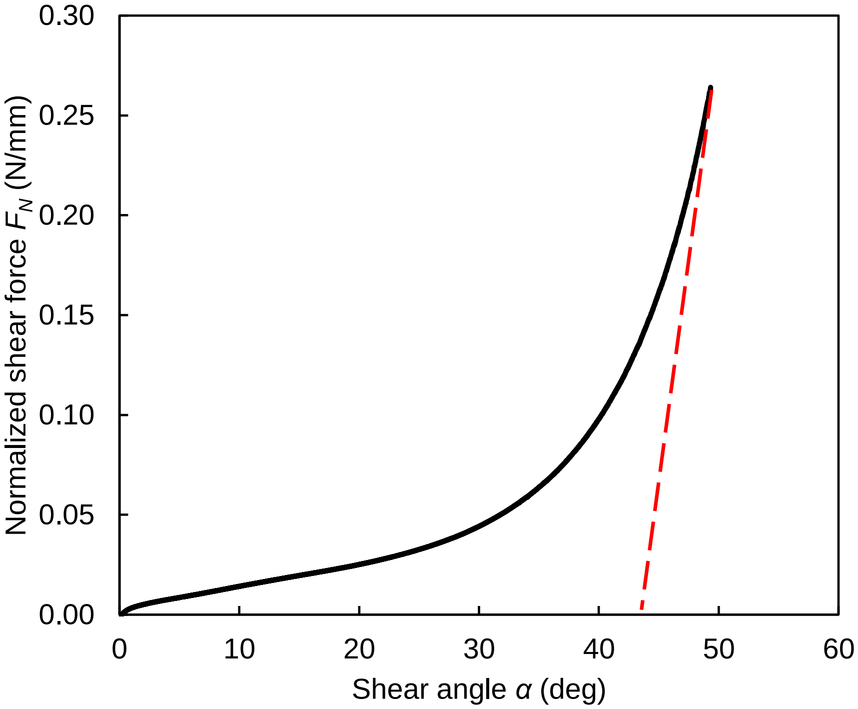

Figure 6.13: Normalized shear force F_N as a function of shear angle α obtained from experimental trials

6.7 Simulations of in-plane shear: mechanical behaviour

Particle-based simulations of in-plane shear of woven textiles were performed, replicating the articulated frame test in various conditions. Larger plain woven textile domains were modelled initially in simulations that featured 4 yarns in both the weft and warp directions leading to 16 crossovers; but mostly, equivalent unit cell domains of the same textile featuring 2 yarns in both the weft and warp directions were modelled in further simulations. Both domains are illustrated in Figure 6.14. The boundaries of the larger domain run along planes defined at mid-distance between yarns, so that these planes do not cut through yarns along the yarn paths. On the contrary, boundaries of the smaller domain run along planes that include the yarn paths, effectively sectioning the yarns in a symmetrical manner. In all cases, every yarn featured nominally 30 Nylon 6/6 fibres with 300 μm diameter and 1 GPa Young's modulus. Half-yarns modelled in the smaller unit cell domain actually featured 15 fibres made of the same material. Gutowski parameters were $\beta = 200$, $v_o = 0.28$ and $v_a = 0.79$ for Nylon 6/6 fibres as determined in previous work [104]. Lengths of virtual shear frame edges L_{frame} were 17.150 mm and 4.550 mm for the larger and smaller domains respectively as described above. Numbers of iterations under constant boundary conditions were 2×10^6 and 5×10^5 for the larger and smaller domains respectively, and simulated domains were extended by 0.1 mm at each step in both cases. In all simulations the pivot limited in edge plane boundary condition (d) was used as described in section 6.5.2.

This section probes the mechanical behaviour of simulated woven textiles undergoing in-plane shear. Specifically, simulations 1A and 1B probe the effect of domain size as discussed above. Simulations 2A, 2B, and 2C probe the effect of fibre tension. Simu-

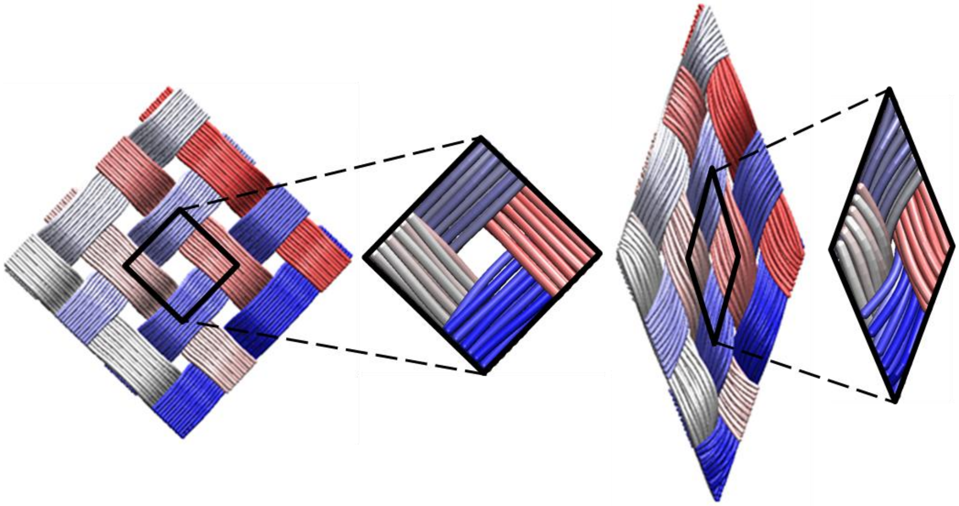

Figure 6.14: Larger and smaller domains used towards virtual in-plane shear simulations 1A and 1B

lations 3A, 3B and 3C probe the effect of friction. Finally, simulations 4A, 4B and 4C probe the effect of bending stiffness.

6.7.1 Effect of domain size: simulations 1A and 1B

Simulations 1A and 1B aimed at comparing results obtained with the larger and smaller domains as described above. Results for normalized in-plane shear force as a function of shear angle replicated those from experimental trials very faithfully as shown in Figure 6.15. The outcome of these simulations and experiments lead to further simulations being conducted using smaller domains featuring fewer fibres, requiring less computational resources. In-plane shear simulations for the smaller domain were repeated five times with the same parameters and negligible variability was observed as shown in Figure 6.15.

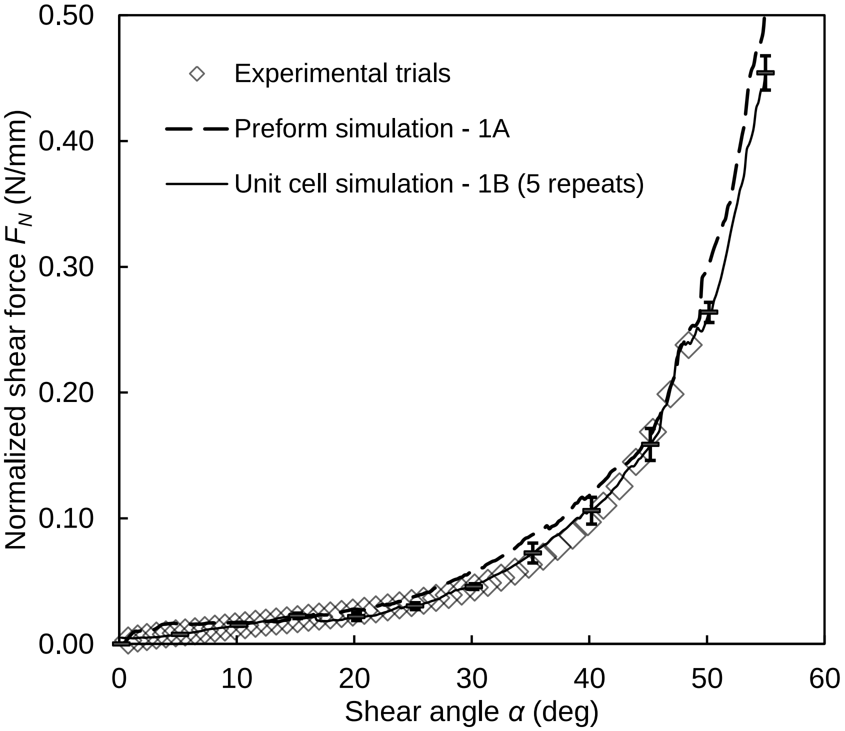

Figure 6.15: Normalized shear force F_N as function of shear angle α for simulations 1A and 1B and experimental trials

6.7.2 Effect of fibre tension: simulations 2A, 2B and 2C

Simulations 2A, 2B and 2C aimed at quantifying the effect of tensioning the fibres prior to in-plane shear. Three different unit cell models featuring different initial levels of fibre tension but otherwise identical positions of fibre ends on the virtual frame edges, boundary conditions and parameters were studied. Fibre tension was induced as follows. All 3 cases started with the same initial geometry defined by particle positions; particle spacing in this initial, unique configuration was typically 330 μm. The 3 cases were differentiated by modifying equilibrium distance l as defined in Equation 6.1; values of l in simulations 2A, 2B and 2C were 330 μm, 320 μm and 310 μm respectively. Prior to shearing, the above domains were subjected to 5×10^5 iteration cycles leading to tension building in the fibres, until stable strain energy levels were reach with tensioned fibres; in-plane shear was imposed afterwards.

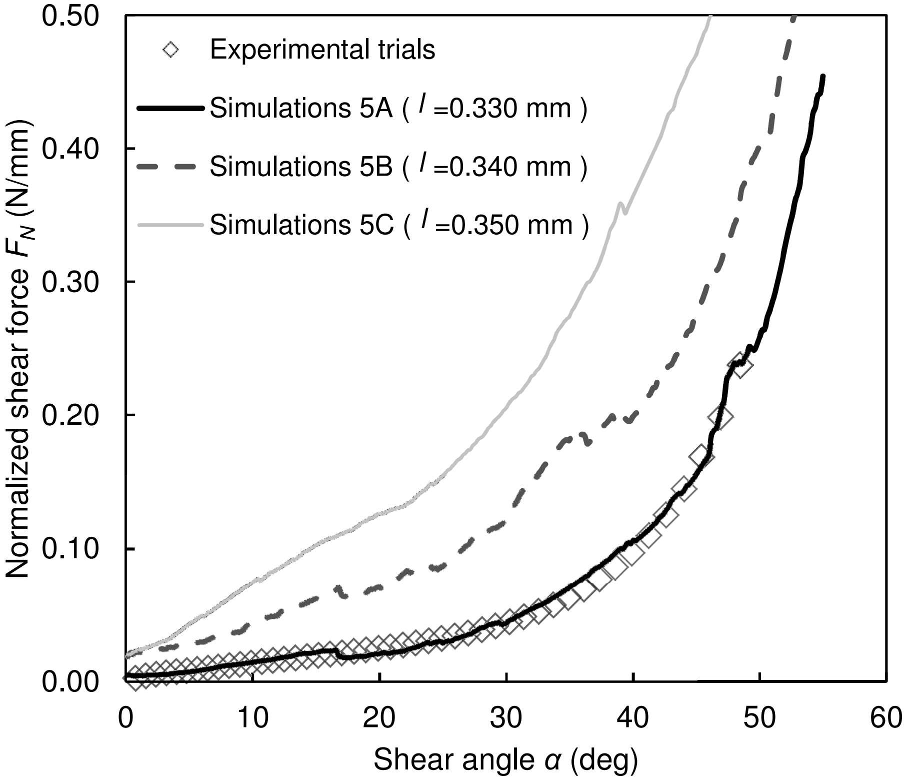

Figure 6.16: Effect of initial fibre tension on in-plane shear simulation results for simulations 2A, 2B and 2C, compared with experimental results

The normalised shear force F_N as a function of shear angle α increased substantially with an increase in fibre tension, Figure 6.16. Previous research work [69] has shown that pretension of the textile sample in an articulated frame had a similar, major effect on shear force, which was confirmed here. Particle-based modelling enabled the quantification of this effect.

6.7.3 Effect of fibre friction: simulations 3A, 3B and 3C

Simulations 3A, 3B and 3C aimed at quantifying the independent effect of friction during in-plane shear. Three unit cell models characterised by different values of the friction parameter *FP* introduced in section 6.4.1 but otherwise identical were studied. Values of *FP* in simulations 3A, 3B and 3C were 0.000, 0.001 and 0.005 respectively; all other parameters were unchanged.

A major effect on the normalised shear force *FN* results as a function of shear angle α was observed as shown in Figure 6.17. An increase in *FP* led to a significant increase of the shear force for a given value of the shear angle α, replicating expected trends. Again, particle-based modelling enabled the prediction of the phenomenon.

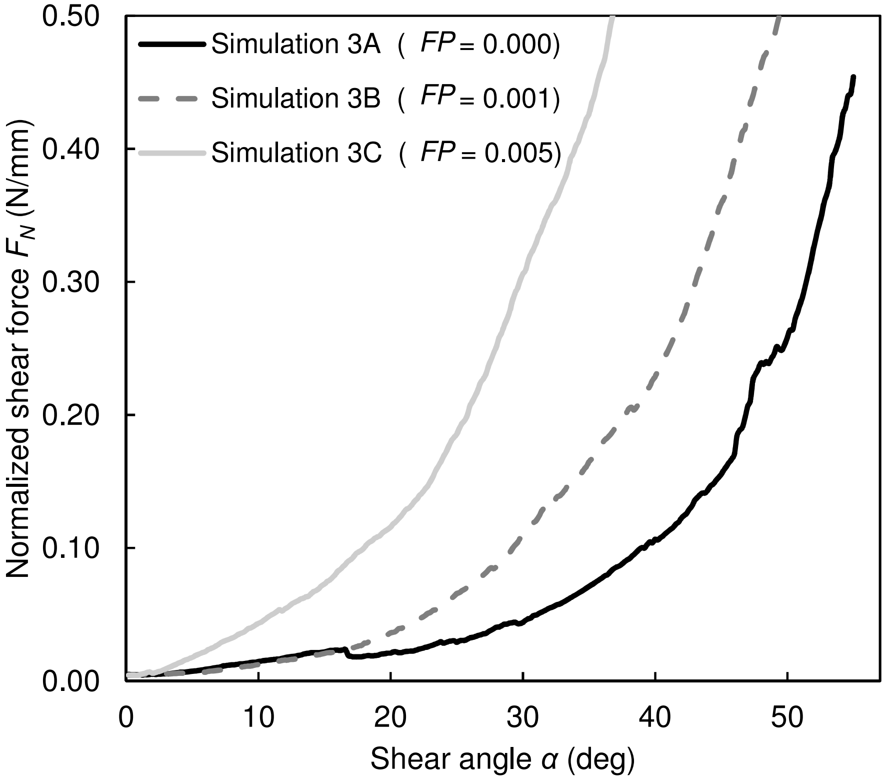

Figure 6.17: Effect of friction parameter *FP* on in-plane shear simulation results for simulations 3A, 3B and 3C

6.7.4 Effect of bending stiffness: simulations 4A, 4B and 4C

Simulations 4A, 4B and 4C aimed at quantifying the independent effect of bending stiffness, under the following rationale. Literature suggests that bending stiffness affects in-plane shear properties of textiles [14,15], essentially based on the fact that a yarn taken as a whole typically has a higher stiffness than the added stiffness of the fibres making up this yarn. The hypothesis is that yarn bending stiffness lies somewhere between the algebraic addition of individual fibre stiffness terms and the stiffness that would be obtained by considering that the dry yarn bends as a solid unit, as a beam would. Under particle-based modelling this issue was apprehended by introducing a bending stiffness parameter *BP* multiplying the bending energy term *UB* as defined in Equation 6.2.

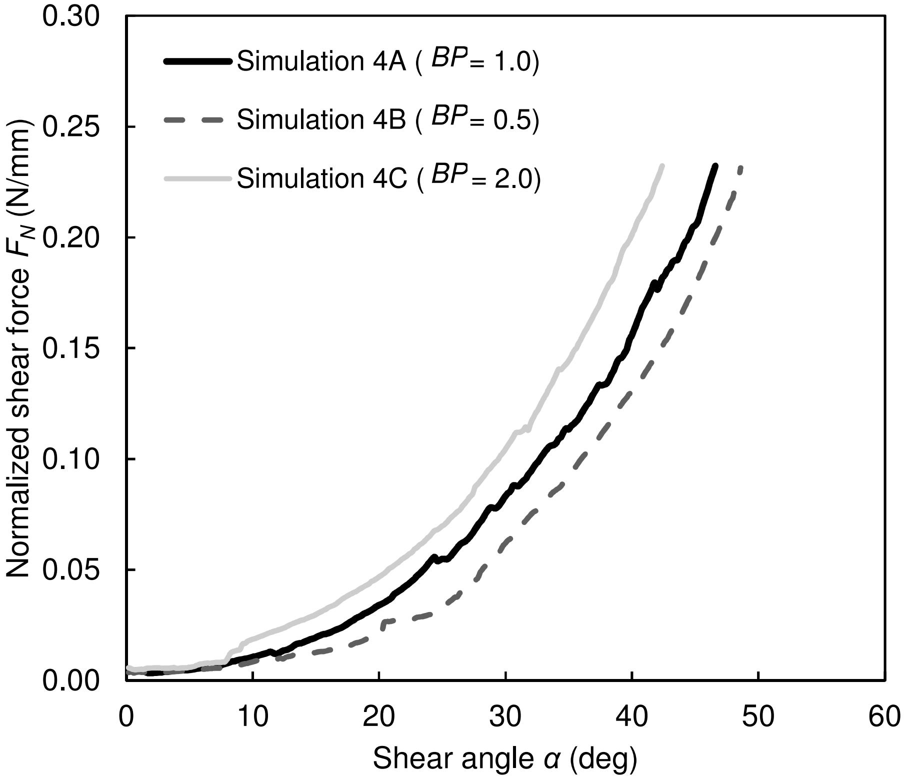

Figure 6.18: Effect of bending stiffness parameter *BP* on in-plane shear simulation results for simulations 4A, 4B and 4C

An effect on the normalised shear force F_N was observed as shown in Figure 6.18. An increase in BP led to an increase in shear force, despite the relatively minor contribution of fibre bending to the total strain energy of the system.

6.8 Simulation of in-plane shear: evolution of geometry

Particle-based simulations of in-plane shear of woven textiles undergoing articulated frame tests showed clear effects on the geometry of textiles and yarns, which are discussed in this section. Selected parameters quantifying the geometry of plain woven textile domains were recorded during simulations, and their evolution was probed. Parameters shown in Figure 6.19 are the textile thickness, yarn centre spacing, inter-yarn gap, and yarn section dimensions. It should be noted that in the balanced textiles simulated, width and thickness of yarns extending along the warp and weft are expected to be generally similar along with inter-yarn gap and yarn centre spacing; inter-yarn gap and yarn section dimensions are reported for different planes within the unit cell domain. Results were extracted from simulations 1A and 1B first presented in section 6.7.1.

Figure 6.20 shows the evolution of yarn centre spacing obtained from simulations 1A and 1B along with analytical values ($L_{frame} \cdot sin\alpha$) which, in macroscopic terms, correspond to the spacing defined as the distance perpendicular to the centrelines of 2 neighbouring yarns. Simulation results presented in the figure were obtained by identifying the highest particles in two parallel yarns and calculating the horizontal distance between these particles defined in a plane that is perpendicular to the relevant frame edge, for yarns extending in a single direction and for the 2 central yarns only in the case of simulation 1A. For the 5 simulations 1B it was found that yarn centre spacing

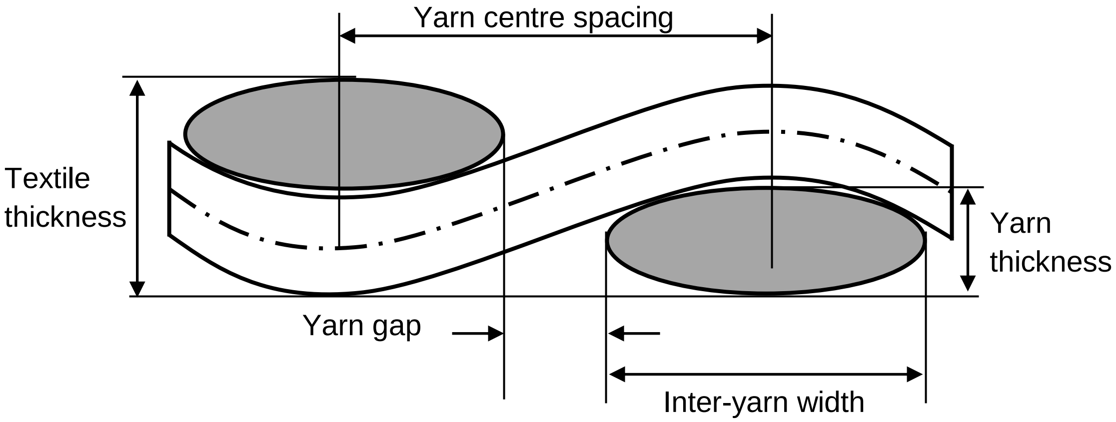

Figure 6.19: Parameters quantifying the cross-section of a unit cell in sheared fixture

curves superimposed. Figure 6.22 shows that yarn spacing data obtained from simulations 1B evolved smoothly. Data from simulation 1A showed limited fluctuations around the same trend, with discrete steps on the curve corresponding to the relevant particles being associated with different fibres at different values of angle α. Both cases replicated the analytical trend very faithfully. These results can be related to the increase in shear force in general terms and provide further evidence of the suitability of the smaller domain as used in simulations 1B for predicting in-plane shear behaviour accurately.

Textile thickness was probed as it is an important parameter to processing and performance of technical textiles. Thickness was defined as the vertical distance between the lowest and highest particles found within a domain as it is sheared. Figure 6.21 shows that the unrestricted thickness of the textile in simulations 1B increased under in-plane shear, in a manner consistent with generally reported behaviour. For the simulated textile, thickness starts increasing mostly around a shear angle α of 15°, with a generally linear trend beyond that value. Figure 6.21 also shows the simulated yarn centre spacing for the same simulation as reported in Figure 6.20 for comparison purposes. The decrease in spacing leads to reorganisation of the fibres within yarns and translates into an increase in thickness.

Figure 6.22 shows yarn centre spacing and yarn gap evaluated in 2 different planes as shown in Figure 6.23. At the onset of shearing the reduction in yarn centre spacing is mostly compensated by a reduction in yarn gap; effectively, yarns are getting closer without major changes to their widths. However, for shear angle values α beyond 30°, always in the context of the parameters used for simulations 1B, the reduction in yarn centre spacing accelerates whilst the reduction in yarn gaps progressively slows down. Hence at this stage of shearing yarn widths must decrease. As seen in Figure 6.24, the decrease in yarn centre spacing is also compensated through an increase in yarn thickness. Figure 6.24 also shows that for all practical purposes yarn gaps become null around $\alpha = 43°$, which was previously identified as the value of the locking angle in Figure 6.13. Finally, it is observed that the evolution of inter-yarn gap does not vary significantly for the 2 planes probed.

Quantification of the effect of in-plane shear on yarn width and thickness is shown in Figure 6.24. The curves show that increases in yarn thickness and decreases in yarn width become more prominent around the locking angle, which is consistent with other trends discussed above. Most of the trends which were simulated in this work were observed experimentally as reported in other research work, notably [84].

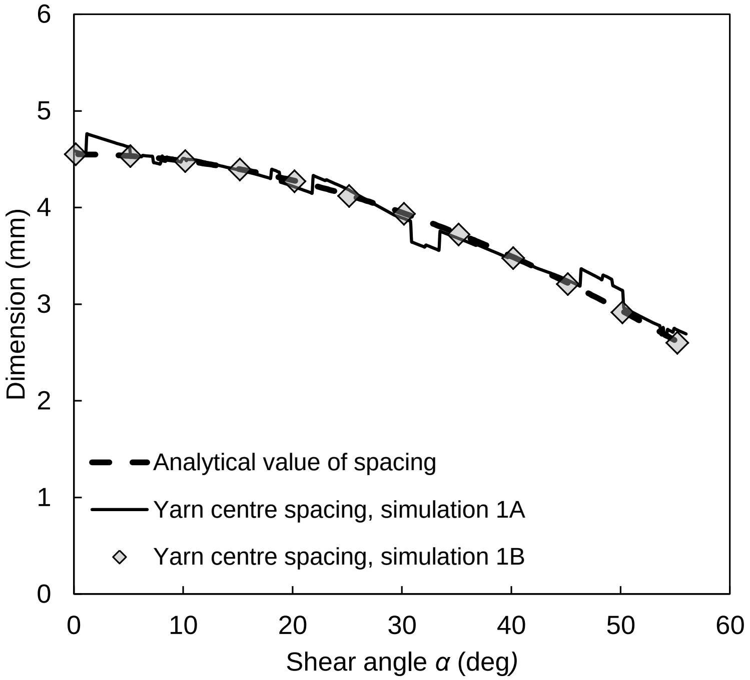

Figure 6.20: Yarn centre spacing as a function of shear angle α, for simulations 1A and 1B

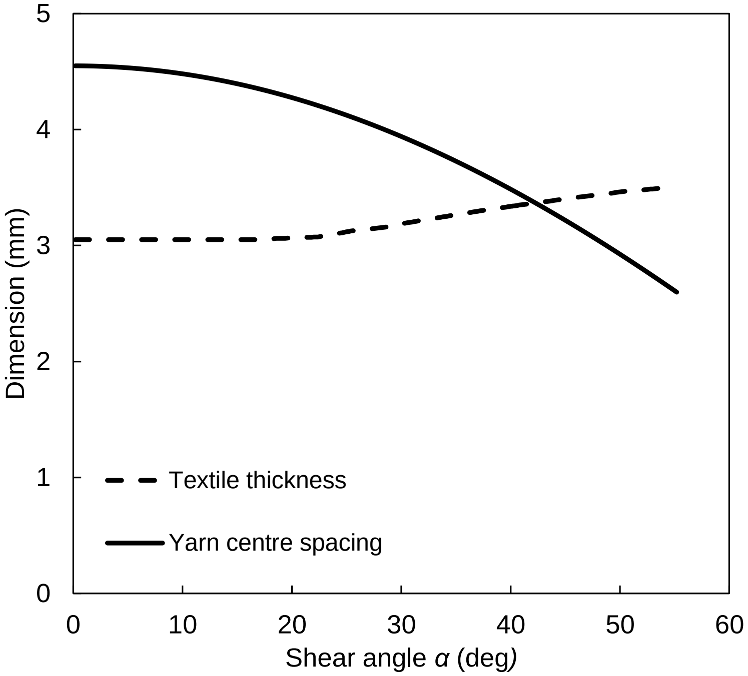

Figure 6.21: Textile thickness and yarn centre spacing as a function of shear angle α, for simulation 1B

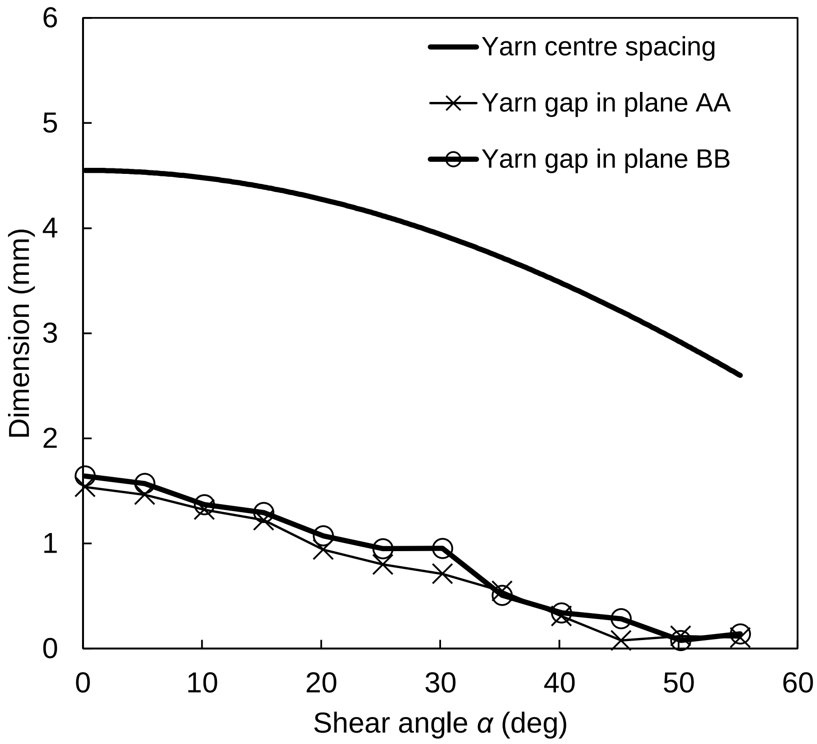

Figure 6.22: Yarn centre spacing and inter-yarn gaps as a function of shear angle α, for simulation 1B

6.9 Conclusion

A particle-based modelling method was used for modelling in-plane shear in woven textiles. Simulation results were validated experimentally for a unit cell of a single-layer plain woven textile and for a larger domain of the same textile. Several cases were investigated to enable comparisons with further experimental results available in the published literature including the probing of fibre tension, fibre friction and the effect of yarn bending stiffness on the in-plane shear behaviour. Validation work shows that the particle-based modelling method reproduces experimental data reality and trends reported in literature very well. A new algorithm for modelling friction led to results being obtained from a less computationally demanding procedure. Changes in the width and thickness of yarns upon shearing could be related with the locking angle.

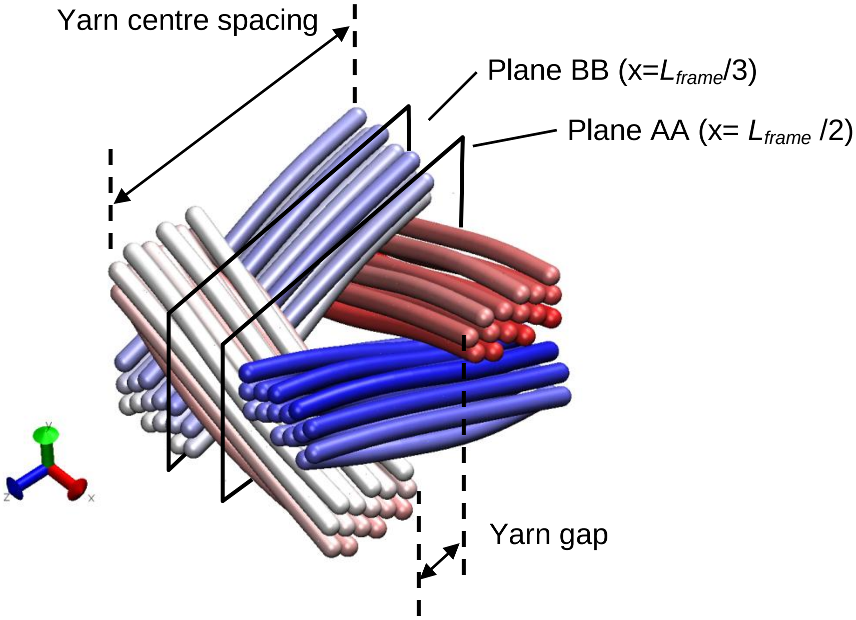

Figure 6.23: Yarn centre spacing and yarn gaps of plane AA and BB for simulation 1B

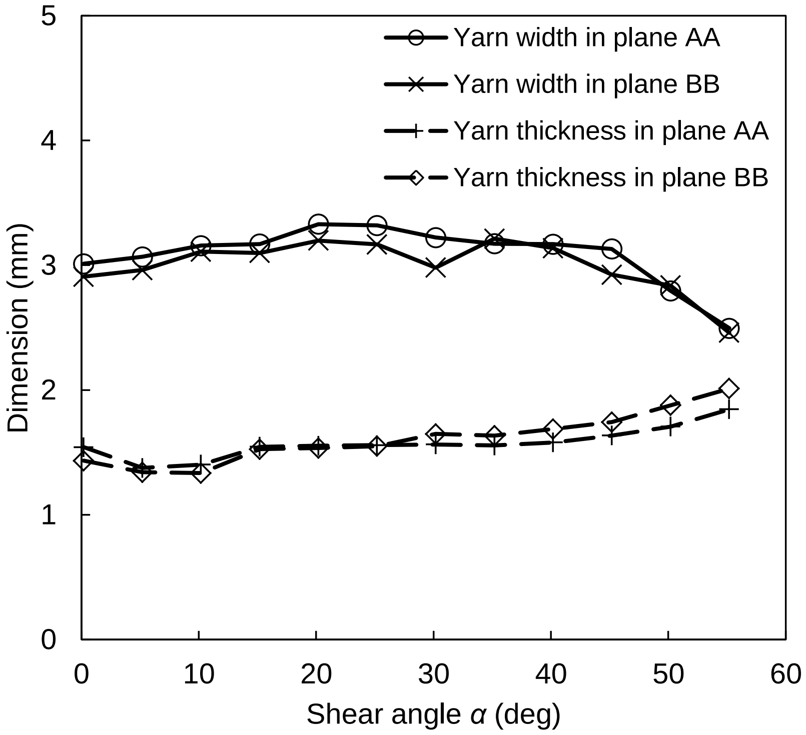

Figure 6.24: Yarn width and thickness as a function of shear angle α on in-plane shear for simulation 1B

Chapter 7

Discussion and Conclusion

7.1 Introduction

This chapter discusses further developments in the form of a proposed expansion algorithm and of additional modelling work aimed at more complex textile manufacturing and assembly operations. The expansion algorithm (EA) constitutes the link which enables the particle-based modelling method developed in this thesis to apply to composites manufacturing, where textile reinforcements feature glass or carbon yarns within large numbers of fibres, say 3 to 12 thousand or more. Brief examples of application to advanced textile manufacturing operations are presented as early work, to show the ability of the particle-based modelling method to document industrial problems. Both the algorithm and additional modelling work are proposed in the context of applying this thesis work to modelling the engineering of advanced preforms for polymer composite manufacturing. The chapter concludes by revisiting the most important findings reached in this thesis; recommendations for future work are made.

7.2 Expansion algorithm

Applying the particle-based modelling method described herein to textile reinforcements where yarns feature thousands of fibres was investigated, leading to the development of the expansion algorithm described herein. Through the expansion algorithm, one may generate curves representing the constitutive behaviour of such reinforcements using simulations featuring less fibres in an otherwise unchanged domain. Each fibre modelled for usage in the context of the expansion algorithm represents a number of actual physical fibres with different dimensions and properties; the constitutive behaviour of these larger fibres is adapted so as to replicate the behaviour of a number of actual fibres. The larger modelled fibres are labelled as EA-fibres. EA-fibres have a circular cross-section, the diameter of which is larger than that of the individual, physical fibres that each EA-fibre represents. Material properties are altered appropriately as highlighted below. Other elements of the simulations remain essentially unchanged.

7.2.1 Intra-fibre strain energy terms for *EA*-fibres

The two major components of intra-fibre strain energy in EA-fibres are the axial tension/compression term and the bending term, as discussed for physical fibres in previous chapters. Fundamentally, the expansion algorithm aims at replacing n real, smaller physical fibres of radius r with N EA-fibres of larger radius R, where both the total volume of fibre material and volume of the domain remain the same. Both fibre assemblies should have the same axial and bending stiffnesses at the same fibre volume fraction, hence the aim is to store the same amount of strain energy for the same elongation and curvature, respectively. If this is achieved, it is foreseen that friction can be processed as described in previous chapters, without change. The expression for axial tensile/compressive elastic strain energy, Equation 7.1, is unchanged:

$$U_a = \frac{E \cdot A_{EA}}{2L} \cdot \Delta^2 \tag{7.1}$$

The adjusted diameter of the *EA*-fibre is used in the equation, hence elongating one *EA*-fibre by a given length is equivalent to elongating n/N physical, smaller fibres by the same length.

In an *EA*-fibre, strain energy in axial tension/compression U_a is a function of Young's modulus E, which is not changed when going from physical to *EA*-fibres. Strain energy is also relates to the distance between particles which will be larger than for physical fibres in typical models. However, in computation the value of L may or may not be changed compared to values characterising actual fibres; this value can be determined independently of the diameter without bringing specific computational difficulties or issues. Finally, given the fact that the fibre volume fraction, and so the volume of material, are made to stay the same when N larger fibres of radius R are replacing n smaller physical fibres of radius r, the total cross-section of all fibres must stay the same and so:

$$\begin{aligned} v_{f_{EA}} &= v_{f_r} \\ N \cdot R^2 &= n \cdot r^2 \end{aligned} \tag{7.2}$$

The strain energy stored in an *EA*-fibre subjected to pure bending is defined by the equivalent Young's modulus E, second moment of inertia I and segment length L, Equation 7.3:

$$U_{ij} = \frac{E \cdot I}{2L} \cdot {\theta_{ijk}}^2 \tag{7.3}$$

where θ_{ijk} is the bending angle as discussed in previous chapters.

Bending of each physical and *EA*-fibre is reasonably assumed to take place independently around their individual neutral axes, and so I_{EA} is affected only by the diameter increase. Therefore, I_{EA} will be altered for *EA*-fibre diameter in the expansion algorithm. As stated above, when replacing a large number of physical fibres by a smaller number of *EA*-fibres within a physical domain of identical dimensions, It desired to maintain a constant value for v_f.

Meanwhile, for both cases of simulation with physical fibres and *EA*-fibres the following equation needs to be satisfied, on the grounds that bending one *EA*-fibre around a given radius should require the same amount of strain energy as bending n/N physical fibres having the same length L and made of the same material, around the same bending radius. If the moments of inertia in bending of the physical and *EA*-fibres are labelled as I_r and I_{AE} respectively, then:

$$\begin{cases} I_{EA} = \sum I_r \\ \dfrac{\pi R^4}{4} = \dfrac{n}{N} \cdot \dfrac{\pi r^4}{4} \\ \dfrac{R^4}{r^4} = \dfrac{n}{N} \end{cases} \tag{7.4}$$

Here a difficulty arises; as stated before, to maintain v_f constant one must have:

$$\frac{R^2}{r^2} = \frac{n}{N} \tag{7.5}$$

which is obviously incompatible with the above equation. The solution adopted consists in using a different value of Young's modulus for *EA*-fibres that is specific to the strain energy bending term only and is not used in the axial tension/compression term.

The increase in total bending stiffness when going from n fibres of readies r to N fibres of radius R is effectively too large by a factor of:

$$\frac{R^2}{r^2} = \frac{n}{N} \tag{7.6}$$

and so the solution consists in dividing the Young's modulus E_m by n/N in the bending strain energy equation only. As such the following equation is applied:

$$U_{ij} = \frac{E_m \cdot I_{EA}}{2L} \cdot \theta^2 \tag{7.7}$$

with

$$E_m = E \cdot N/n \tag{7.8}$$

Reducing the modulus by n/N will lead to the same bending strain energy being imparted as if bending the same mass of physical fibres extending over the same length. This will be discussed through an example in forthcoming sections.

7.2.2 Inter-fibre strain energy terms for *EA*-fibres

The expansion algorithm makes it possible to use less, larger fibres for predicting the mechanical behaviour of textiles featuring large numbers of smaller fibres, such as textile reinforcement used in manufacturing composites. Textiles modelled using the expansion algorithm feature *EA*-fibres, the centrelines of which are further apart than those of the more numerous physical fibres that they aim to represent within the same domain. Hence, pressures generated must stay the same as if using the actual number of physical fibres at a given v_f.

The following discussion concerns the case of an assembly of parallel fibres being compacted; aiming at discussing early developments towards the expansion algorithm. Pressure say on the top surface of a domain results from individual fibres contacting this surface, resulting in contact forces. As the domain is compacted and fibres reorganize, it can be shown that the relation between representative numbers of columns and rows of parallel fibres in the domain is independent of fibre diameter, a most useful characteristic in the present case as it enables direct scaling independently of v_f; this is demonstrated through an example in the following pages.

Put more simply, if it is reasonably assumed that the average distance between 2 fibre centrelines is independent of direction, then reducing the number of fibres from n physical fibres to N EA-fibres does not change the way in which the proportion of fibres contacting say the top surface of the domain to the total number of fibres in the domain evolves as compaction proceeds. Whilst the argument has yet to be formalised and generalised, it is used here on basis of discussing. As a result early development as stated above, forces between individual pairs of fibres must be increased as they are less numerous, both to compensate higher distances in Gutowski's model and the smaller number of fibres contacting say the top surface and contributing to pressure. This will be done by altering Gutowski's model as shown below.

As Gutowski's model uses the distance between the centrelines of two neighbouring fibres as its main input parameter, a relation between this distance, the number of fibres in a domain, and the domain size must be established towards the aforementioned objective. Again, the simpler development proposed here is based on parallel fibres; it is worth noting that it will still be widely applicable to more complex cases, especially in the context of the expansion algorithm, as fundamentally it applies to yarn as opposed to textiles.

The relation is established by reasonably assuming, as a starting point, that parallel fibres will align in a triangular or hexagonal configuration as this maximises the distance between neighbouring fibres at a given v_f, hence minimising any strain energy term associated with lateral compaction of the yarn. Whilst insightful geometric arguments can be made and demonstrated about boundary conditions leading to networks of parallel fibres that are more stable for constant v_f and domain size. If the domains are relatively wider, for larger numbers of fibres the effect of boundary conditions becomes negligible and the number of triangles in the fibre network tends toward the double of the number of fibres. So, given a domain size and a number of fibres the dimensions of the triangular defining the network of parallel fibres that will lead to a state of smaller strain energy can be obtained, and so the distance between 2 neighbouring fibres can be calculated directly. The ratio of the distance fo v_f stays constant for different numbers of fibres hence here again, direct scaling may be applied. Distances are multiplied by a factor γ in Gutowski's model, and so multiplying forces by γ^2 constitutes the needed scaling.

As explained in prior chapters, Gutowski's equation is:

$$F_G = \frac{192EI}{\beta^3} \cdot \frac{(l_o - l_{ij})}{(l_{ij} - l_{min})^3} \tag{7.9}$$

In Equation 7.9 above, the only parameter that changes for a network of EA-fibres is inter-fibre distances, and I which can be processed as explained above for bending. As a result, if all dimensions are multiplied by γ equal to reduction factor n/N, Equation 7.9 will be modified for EA-fibres:

$$F_G = \frac{192EI}{\beta^3} \cdot \frac{\gamma \cdot (l_o - l_{ij})}{\gamma^3 \cdot (l_{ij} - l_{min})^3} \tag{7.10}$$

and then one shall increase the force generated within EI-fibres by γ^2 to obtain same forces generated as with the actual number of physical fibres. Reducing the number of fibres does not change the way in which the proportion of fibres contacting the top surface to the total number of fibres in the assembly evolves as compaction proceeds.

7.3 Demonstration

The expansion algorithm is demonstrated through two scenarios that are developed and compared. These scenarios were established for the compaction of textiles but shall be extended to other mechanical loadings cases in future development work. In the first scenario, 1000 parallel physical fibres contained in a domain measuring 10 mm by 10 mm are compacted to a final height of 5 mm. In the second scenario, the same domain measuring 10 mm by 10 mm, contains 100 parallel *EA*-fibres which are compacted to the same final height of 5 mm, Figure 7.1. Domain width stays constant in both cases, for the minimum strain energy to be stored in all cases, it is assumed fibres aligned in hexagonal/triangle arrangements. In Figure 7.1 the numbers given on the top and on the left of domains are representative of numbers of columns and lines of fibres respectively, assuming equal average distances in the horizontal and vertical directions.

As mentioned above,decreasing the number of fibres from the first scenario to the second does not change the way in which the proportion of fibres contacting the top surface to the total number of fibres changes as compaction proceeds. In the first scenario, approximately 32 fibres should be contacting the top surface at the onset of compaction and this number would increase to approximately 45 after compaction. In the second scenario, approximately 10 fibres should be contacting the top compaction platen at the onset of compaction and this number would increase to approximately 14 after compaction, if one reasonably assumes that minimum strain energy is sustained throughout the compaction. Ratios of the number of fibres in contact with the top platen and v_f in both scenarios are constant. Results for both scenarios are summarized in Table 7.1.

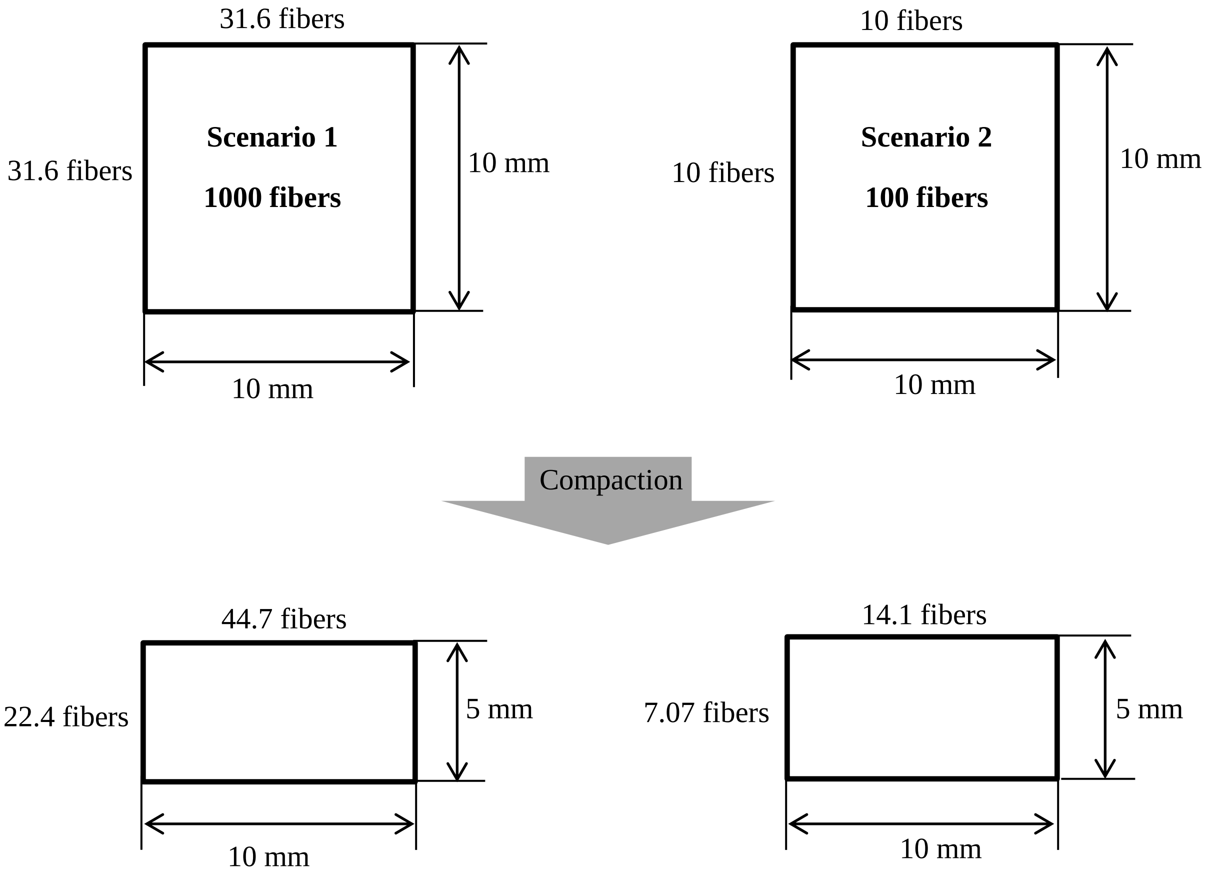

Figure 7.1: Schematic for two scenarios

Table 7.1: Results of two scenarios

Properties	**Scenario 1** Actual fibres	**Scenario 2** EA-fibres
v_f at start of compaction	0.30	0.30
v_f at end of compaction	0.60	0.60
Number of triangles	2000	200
Fibre radius (r)	0.0309 mm	0.0977 mm
Total cross-section of fibres (A)	30 mm^2	30 mm^2
Fibres distance before compaction (l)	0.1414 mm	0.4472 mm
Fibres distance after compaction (l)	0.1 mm	0.3162 mm
Moment of inertia of single fibre (I)	7.16×10^{-7}mm^4	7.16×10^{-5}mm^4
Moment of inertia of total domain (I)	0.7162 mm^4	7.1620 mm^4
Strain energy by tension/compression	$\frac{E \cdot A}{2L} \cdot \varDelta^2$	$\frac{E \cdot A_{EA}}{2L} \cdot \varDelta^2$
Strain energy by bending	$\frac{E \cdot I}{2L} \cdot \theta^2$	$\frac{(0.1E) \cdot I_{EA}}{2L} \cdot \theta^2$
Inter fibre force by Gutowski's model	$\frac{192EI}{\beta^3} \cdot \frac{(l_o - l_{ij})}{(l_{ij} - l_{min})^3}$	$\frac{192EI_{EA}}{\beta^3} \cdot \frac{(l_o - l_{ij})}{\gamma^2(l_{ij} - l_{min})^3}$

7.4 Modelling of manufacturing operations

Technical textiles undergo a diverse range of manufacturing operations tied to their end-use. Early modelling works for such manufacturing operations is presented and discussed briefly in this section. Manufacturing operations may be listed as bending, punching, stitching or forming for example. Such operations were not modelled for querying the mechanical properties of textiles as in previous chapters, but rather the simulations were developed to present forward-looking capabilities of the particle-based modelling method which is the subject of this thesis.

7.4.1 Textile bending

Bending simulations were performed using single unit cells and single layers plain woven textiles featuring multiple unit cells. Both virtual samples were made of yarns featuring 30 Nylon 6/6 fibres. Unit cells featured 2 yarns in each direction and 4 crossovers. The larger textile domains included 4 yarns in each direction and 16 crossovers. Simulations were performed where virtual samples were placed between two rigid half-platens connected through a linear pivot, on each side of the samples. Both pivot lines for both platens were parallel. Lateral boundaries were imposed to maintain sample dimensions along that direction. Selected deformation states appear in Figure 7.2 for both cases.

Matters of specific interest in these cases include friction and relative displacements of fibres and yarns in and near the corner, any fibre buckling occurring at the inner side of the corner, and also the possibility of shifting between yarns either side of the corner and the possible influence of nesting in multi-layers. All these matters will warrant further investigation, which will be made possible by the proposed modelling method and software.

A similar procedure was used for simulating the manufacturing of a 3D profile, corre-

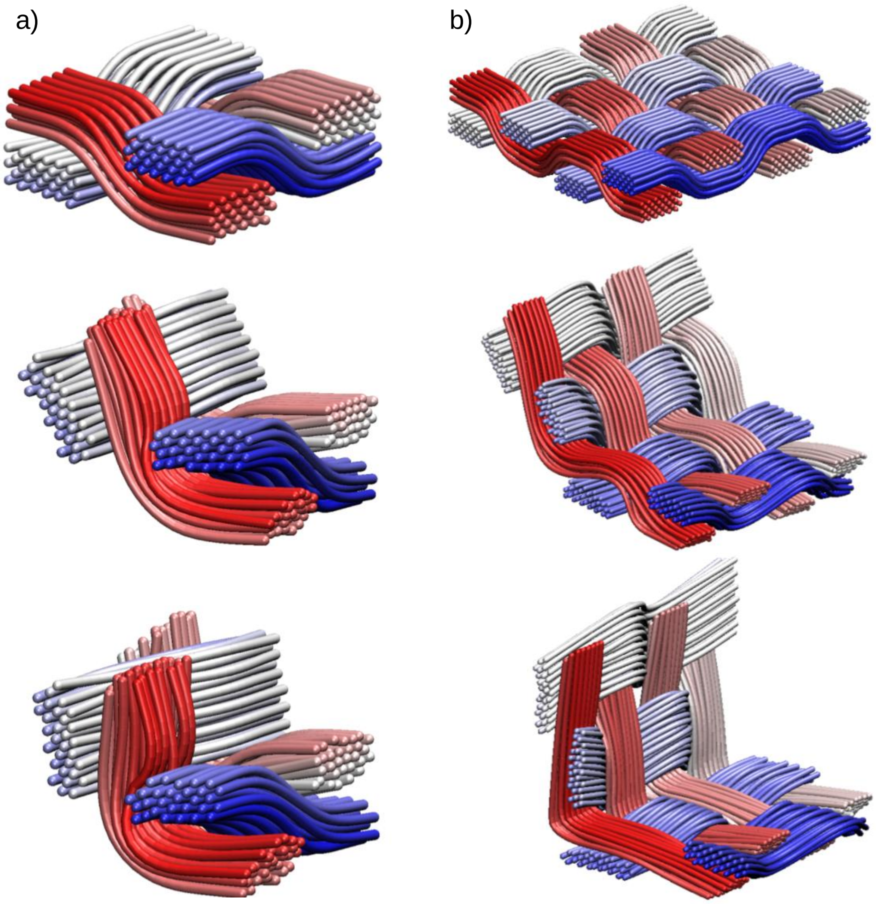

Figure 7.2: Selected deformation states in simulations of bending for: a) a single unit cell, b) plain woven textile

sponding say to an integrated T-section in an advanced textile structure. Notably, both the bending of top two textile layers and the compaction of all layers could be performed concurrently, achieving a 3D profile with higher v_f as would be obtained in the actual process, Figure 7.3. This T-section profile may be assembled further by stitching the different layers, so as to keep the integrity of the profile after mechanical loading.

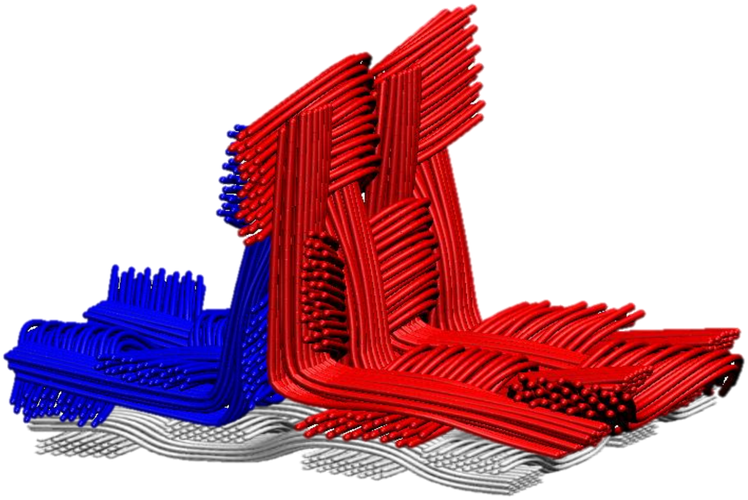

Figure 7.3: T-section profile undergoing concurrent bending and compaction

7.4.2 Textile punching for assembly through stitching

After forming stacks of textiles into a desired shape and form, it may be required to maintain this shape hence enabling its handling for further processes such as matrix injection, coating, calendering, etc. Maintaining the shape may achieved through the application of liquid or mechanical binders. Mechanical binding may also be preformed through different approaches for instance tufting and stitching. Such mechanical binding processes require that a needle passes completely through the textile stack. Passing needles of possibly different sizes and orientations through a textile stack is named punching, and it is very rarely discussed in scientific terms in the open literature.

A series of early punching simulations were performed over small domains to study and replicate the punching of textiles in different conditions. First, punching was performed on a single layer of plain woven textile with a frictionless needle penetrating perpendicular to the textile plane, Figure 7.4. The tip of the needle featured a 15° angle. Interaction between fibres and needle, as well as the blunt tip angle pushed some fibres laterally and caused defects in the textile. Punching was performed at the cross-over of two yarns to best demonstrate the ability of simulating the process. Other cases of punching were also performed on compacted and sheared single layers, and on double-layers textiles, Figure 7.5.

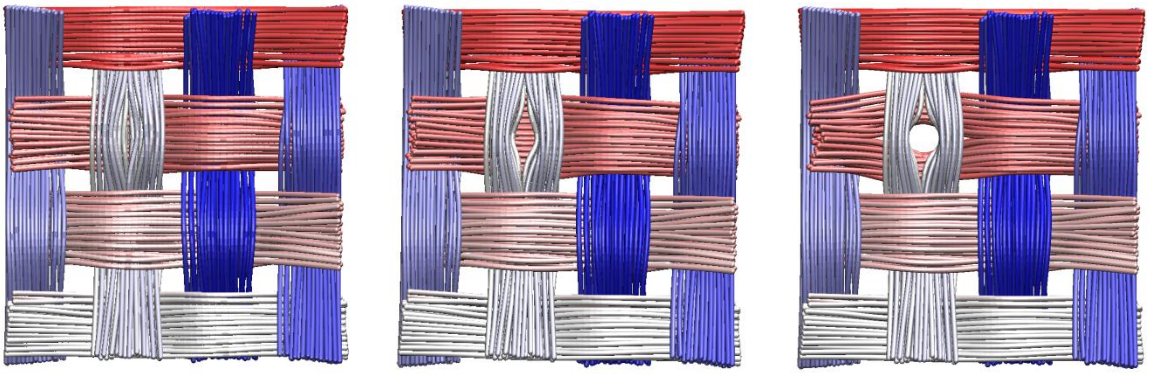

Figure 7.4: Process of punching through a virtual textile

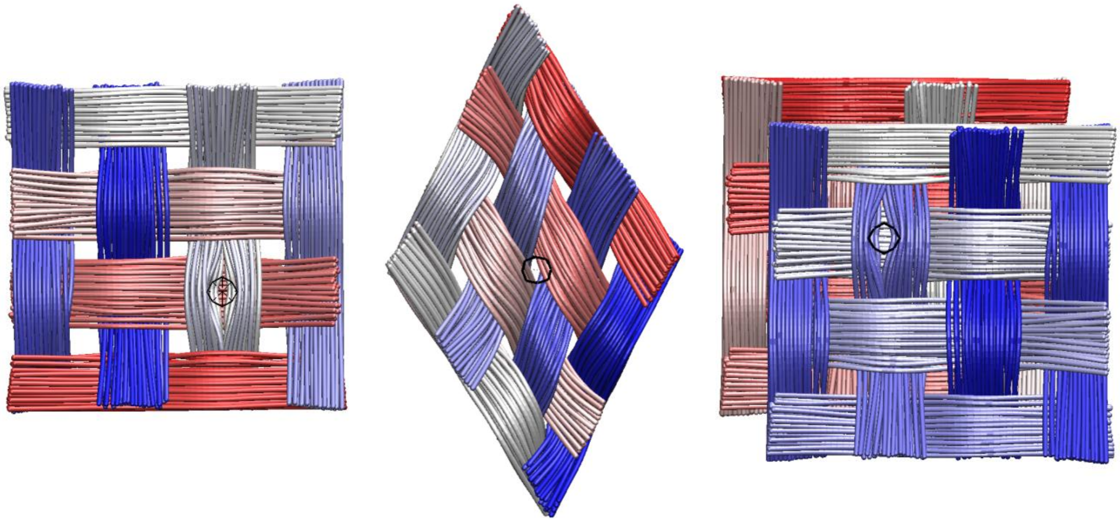

Figure 7.5: Punching performed for different cases of compacted and sheared single layers, and a double-layer textile

The most advanced, current stitching techniques performed on textile assemblies require access only to one side of the textile stack, with penetration by the needles occurring at different angles to the plane of the textile. In this last simulation, the textile was punched at angle of 60° to its plane, to illustrate further capabilities of the modelling method and software, Figure 7.6.

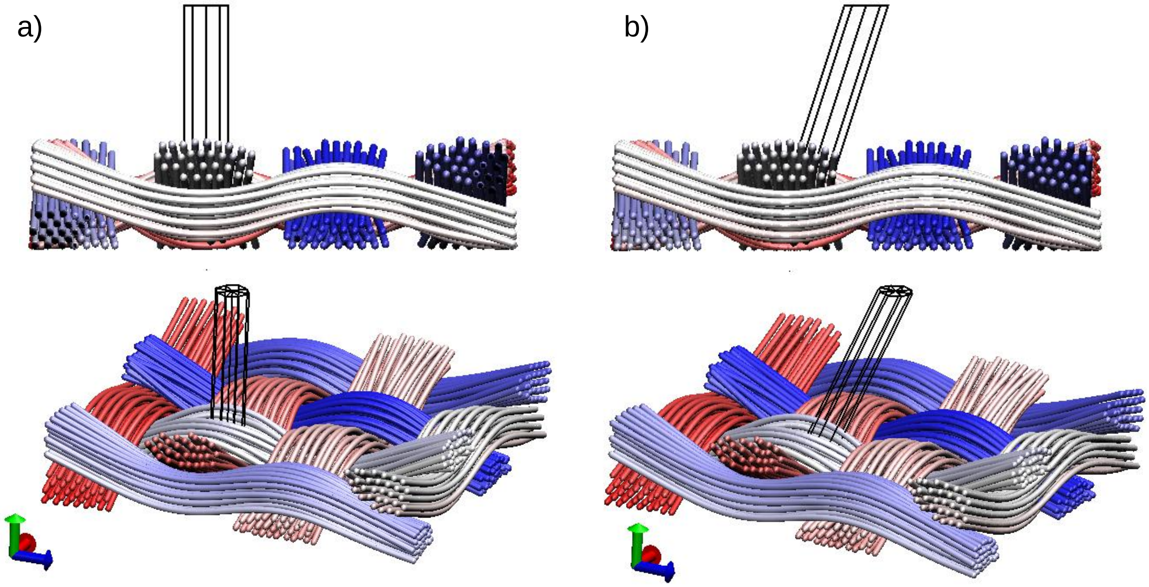

Figure 7.6: Punching virtual textile at 90° and 60° from its plane

The above simulations show, in a succinct manner, the potential of the simulation method and software in replicating the physical behaviour of textiles subjected to a very large array of loading scenarios, potentially leading to the identification and quantification of problematic ones such as, say, bending around tight corners; such scenarios will be studied as future work.

7.5 Discussion

The objective of this thesis was to provide and to validate realistic, unified geometric and mechanical modelling methods for technical textiles and reinforcements. This aim was achieved in this thesis, supported by validation through experimental trials.

7.5.1 Geometric modelling

The particle-based modelling method was developed for representing the geometry of technical textiles in microscopic and mesoscopic scales, say at fibre and yarn levels. The method was used in locating fibre positions which minimize the total strain energy stored in a textile assembly. Any mechanical loading displaces particles which make up the fibres, from their original positions to new positions, resulting in changes in the geometry of the technical textile. By using the Metropolis algorithm, a very well established procedure, along with a set of rules, new fibre configurations could be derived. The main driver of this procedure consists in reaching a minimum state of strain energy in the system. A substantial iterative process takes place during simulations to reach this state of minimum strain energy. The particle-based modelling method was implemented in a multi-module software, and different cases of textiles were created. Yarn and textile models were also used for defining geometries used afterwards in mechanical modelling of the constitutive behaviour.

7.5.2 Mechanical modelling

The particle-based modelling method was also developed with the aim of predicting the constitutive behaviour of textile assemblies. Models of yarns, single-layer textiles and multi-layer textiles subjected to various loading scenarios were simulated. The main components of strain energy in the system were grouped as intra-fibre and inter-fibre energy terms. Inter-fibre energy terms were described using Gutowski's model along with Hertz' function, for stresses in contacting solids. Simulation results for compaction, relaxation and in-plane shear of textiles were validated experimentally. The particle-based modelling method replicated reality faithfully. An extension algorithm is in development, enabling the particle based modelling method to be used for technical textiles containing yarns featuring high numbers of fibres.

In the course of in-plane shear of textiles, the effects of fibre tension, fibre friction and yarn bending stiffness on the in-plane shear behaviour were quantified. Friction between fibres was simulated using a direct and an indirect method. In the direct approach, normal forces between pairs of contacting fibres and displacements at all contact points were used in determining total energy loss associated with fibre friction during a change of configuration. This direct approach required an accurate value of the coefficient of friction and intensive computational resources. In the indirect approach, in the presence of friction fibre slippage is impeded and as a result, additional energy must be expensed for evolving towards configurations corresponding to the same fibre volume fraction as for a system devoid of friction. As a result, the strain energy threshold conducting to a tentative configuration being accepted upon iteration and the ensuing evolution between configurations involves that some of the initial elastic strain energy must be expensed through overcoming friction. The indirect method led to results being obtained using a less computationally demanding procedure, and it was used throughout the thesis.

In the last chapter of this thesis, the modelling of manufacturing processes for technical textiles is introduced in a qualitative manner. This subject shall be investigated in a systematic way as future work, but work has already identified interesting points for the particle-based modelling method that bring it to real, practical and complex applications.

7.6 Conclusion

The following conclusions were reached through this thesis work:

- The effects of geometry on the in-plane permeability of dry reinforcements, through-thickness thermal conductivity of composites and in-plane moduli of composite were investigated.

- Geometric modelling of technical textiles of any architecture, properties and fibre and yarn characteristics was conducted at the microscopic and mesoscopic scales.
- Technical textile geometries were represented prior to, during and after mechanical loading, and investigated for their quantitative characteristics.
- The particle-based modelling method for the constitutive behaviour of fibre yarns and woven textiles subjected to compaction loading was introduced.
- Pressure as a function of fibre volume fraction of yarns, single layers and double layers of textiles subjected to compaction and relaxation was predicted. Local fibre volume fractions defined using the particle-based modelling method are more accurate due to scale at which modelling is done.
- Relaxation of the fibre network during and after compaction was modelled and a parallel between the number of iterations, compaction rate and relaxation time was provided. The 3D surface geometry of a plain weave textile showed similar reorganization of fibres and occurrence of relaxation in the textile, as predicted by simulations.
- In-plane shear using the articulated frame test procedure was modelled using the particle-based modelling method. The shear angle and locking angle were presented as a function of shear force. Simulations and experiments showed an improvement in simulation accuracy over other modelling techniques.
- An expansion algorithm (EA) was introduced as early work towards modelling textiles made of yarns featuring very large numbers of fibres. This algorithm is under development, aiming primarily towards textile reinforcements used in PMC manufacturing.

- Advanced manufacturing processes of textile bending and punching were modelled using the particle-based modelling method, and showed very promising results.

7.7 Future work

The following points pertaining to geometric modelling may be explored in further research:

- Geometric models presented here are limited to 2D woven textiles, and future exploration of 3D textiles may show more complete capabilities of the particle-based modelling method as well as predict behaviour for materials before they are physically made.
- Providing interfaces for geometric models to be used in commercial software, to validate and use the results of particle-based modelling may hold much potential.
- Micrography and μCT observation shall be used to further characterise textiles utilized in geometric modelling validation.
- Further simulation and experimental validation work is warranted, extending the results of the investigation conducted in this thesis to larger scales and a wider array of textile architectures.

The following points pertaining to mechanical modelling may be explored in further research:

- Samples in this thesis were limited to two layers of woven textile; simulation of the compaction and relaxation for stacks featuring many nested layers and orientations would provide additional insightful results from the particle-based modelling method.

- The simulation procedure was improved in terms of the application of displacements on particles upon changes in boundary conditions; this led to simulations being completed much quicker, and will be employed systematically for further simulations from now on.

- Friction is a critically important issue in mechanical modelling, especially for in-plane shear. Two methods were provided and represented the validation trials well, but this subject warrants more exploration and the creation of a database for friction for different materials.

- During the compaction and relaxation of textile reinforcements, one cycle of compaction followed by relaxation was performed throughout this thesis. Although this showed a good match with experimental results, trials featuring many cycles are needed for investigating the cyclic loading of textiles.

- The modelling of manufacturing processes showed much promise, but it is at early stages of development. Various stitching tensions and patterns are critically important to advanced preforms, and constitute one major priority for future work.

Bibliography

[1] F. Abdiwi, P. Harrison, Z. Guo, P. Potluri, and W. R. Yu. Measuring the shear-tension coupling of engineering fabrics. *AIP Conference Proceedings*, 1353(1):889–894, 2011.

[2] J. J. Aklonis and W. J. MacKnight. *Introduction to polymer viscoelasticity.* A Wiley - Interscience publication. Wiley, 1983.

[3] S. L Anderson, D. R. Cox, and L. D. Hardy. Some rheological properties of twistless combed wool slivers. *Journal of the Textile Institute Transactions*, 43(8):T362–T379, 1952.

[4] S. Aranda, F. Klunker, and G. Ziegmann. Compaction response of fibre reinforcements depending on processing temperature. In *ICCM 17, Edinburgh, Great Britain*, Jan 2009.

[5] P. Badel, S. Gauthier, E. Vidal-Salle, and P. Boisse. Rate constitutive equations for computational analyses of textile composite reinforcement mechanical behaviour during forming. *Composites Part A-applied Science and Manufacturing*, 40:997–1007, 2009.

[6] P. Badel, E. Vidal-Sallé, and Ph. Boisse. Computational determination of in-plane shear mechanical behaviour of textile composite reinforcements. *Computational Materials Science*, 40:439–448, 2007.

[7] P. N. Balaguru, United States. Federal Highway Administration, Rhode Island. Dept. of Transportation. Bureau of Research, and Rutgers University. *Construction of fiber reinforced polymer (FRP) jackets for the protection of pier caps.* Rutgers University, 2005.

[8] G. L. Batch and C. W. Macosko. A model for two-stage fiber deformation in composite processing. In *20th International SAMPE Technical Conference*, 1988.

[9] E. B. Belov, S. V. Lomov, I. Verpoest, T. Peters, D. Roose, R. S. Parnas, K. Hoes, and H. Sol. Modelling of permeability of textile reinforcements: lattice Boltzmann method. *Composites Science and Technology*, 64:1069–1080, 2004.

[10] S. Bickerton and M. J. Buntain. Modeling forces generated within rigid liquid composite molding tools. Part B: Numerical analysis. *Composites Part A-applied Science and Manufacturing*, 38:1742–1754, 2007.

[11] D. Bigaud, J.-M. Goyhénèche, and P. Hamelin. A global-local non-linear modelling of effective thermal conductivity tensor of textile-reinforced composites. *Composites Part A-applied Science and Manufacturing*, 32:1443–1453, 2001.

[12] A. E. Bogdanovich. Multi-scale modeling, stress and failure analyses of 3-D woven composites. *Journal of Materials Science*, 41:6547–6590, 2006.

[13] P. Boisse, N. Hamila, F. Helenon, B. Hagege, and J. Cao. Different approaches for woven composite reinforcement forming simulation. *International Journal of Material Forming*, 1:21–29, 2008.

[14] P. Boisse, N. Hamila, E. Vidal-Sallé, and F. Dumont. Simulation of wrinkling during textile composite reinforcement forming. Influence of tensile, in-plane shear and bending stiffnesses. *Composites Science and Technology*, 71:683–692, 2011.

[15] Ph. Boisse, B.Zouari, and J. Daniel. Importance of in-plane shear rigidity in finite element analyses of woven fabric composite preforming. *Composites Part A-applied Science and Manufacturing*, 37:2201–2212, 2006.

[16] P. Buckenham. Bias-extension measurements on woven fabrics. *Journal of The Textile Institute*, 88:33–40, 1997.

[17] A. R. Bunsell and J. Renard. *Fundamentals of Fibre Reinforced Composite Materials*. Series in Material Science and Engineering. Taylor & Francis, 2010.

[18] N. Burnford. *Development of drape simulation software and the optimisation of variable-length textiles*. PhD thesis, University of Ottawa, 2011.

[19] Z. Cai and T. G. Gutowski. The 3-D deformation behavior of a lubricated fiber bundle. *Journal of Composite Materials*, 26:1207–1237, 1992.

[20] J. Cao, R. Akkerman, P. Boisse, J. Chen, H. S. Cheng, E. F. de Graaf, J. L. Gorczyca, P. Harrison, G. Hivet, J. Launay, W. Lee, L. Liu, S. V. Lomov, A. Long, E. de Luycker, F. Morestin, J. Padvoiskis, X. Q. Peng, J. Sherwood, Tz. Stoilova, X. M. Tao, I. Verpoest, A. Willems, J. Wiggers, T. X. Yu, and B. Zhu. Characterization of mechanical behavior of woven fabrics: Experimental methods and benchmark results. *Composites Part A-applied Science and Manufacturing*, 39:1037–1053, 2008.

[21] G. A. Carnaby, E. J. Wood, L. F. Story, Wool Research Organisation of New Zealand, and England). New Zealand Section Textile Institute (Manchester.

The application of mathematics and physics in the wool industry: proceedings of an advenced workshop held at Lincoln College, Canterbury, New Zealand on 9-12 February 1988. Wool Research Organisation of New Zealand special publications. WRONZ, 1988.

[22] A. Charmetant, E. Vidal-Sallé, and P. Boisse. Hyperelastic modelling for mesoscopic analyses of composite reinforcements. *Composites Science and Technology*, 71:1623–1631, 2011.

[23] J. Crookston and F. Robitaille. A systematic study of the mechanical properties of textile composite unit cells based on geometric modelling. In *Composite Materials (ICCM-14), San Diego*, 2003.

[24] J. I. Curiskis and G. A. Carnaby. Continuum mechanics of the fiber bundle. *Textile Research Journal*, 55:334–344, 1985.

[25] M. Cybulska, T. Florczak, and T. Lodz. 3-d graphics in textile designing. In *In AUTEX, 2006 World Textile Conference*, June 2006.

[26] A. Dasgupta, R. K. Agarwal, and S. M. Bhandarkar. Three-dimensional modeling of woven-fabric composites for effective thermo-mechanical and thermal properties. *Composites Science and Technology*, 56:209–223, 1996.

[27] F. Desplentere, S. V. Lomov, D. L. Woerdeman, I. Verpoest, M. Wevers, and A. Bogdanovich. Micro-CT characterization of variability in 3D textile architecture. *Composites Science and Technology*, 65:1920–1930, 2005.

[28] R. G. Djaja, P. J. Moss, A. J. Carr, G. A. Carnaby, and D. H. Lee. Finite element modeling of an oriented assembly of continuous fibers. *Textile Research Journal*, 62(8):445–457, 1992.

[29] R.G. Djaja and Wool Research Organisation of New Zealand. *Tangent compliance matrix for an oriented assembly of continuous fibres*. Wool Research Organisation of New Zealand communications. Canesis Network Limited, 1989.

[30] S. Dowdy, S. Wearden, and D. Chilko. *Statistics for Research*. Wiley Series in Probability and Statistics. Wiley, 2011.

[31] J. Echaabi, M. B. Nziengui, and M. Hattabi. Compressibility and relaxation models for fibrous reinforcements in liquid composites moulding. *International Journal of Material Forming*, 1:851–854, 2008.

[32] G. Francucci, E. S. Rodriguez, and A. Vazquez. Experimental study of the compaction response of jute fabrics in liquid composite molding processes. *Journal of Composite Materials*, 46:155–167, 2012.

[33] B. R. Gebart. Permeability of unidirectional reinforcements for RTM. *Journal of Composite Materials*, 26:1100–1133, 1992.

[34] J.E. Gentle. *Random Number Generation and Monte Carlo Methods*. Statistics and Computing. Springer, 2003.

[35] Y. Gowayed and J. Hwang. Thermal conductivity of composite materials made from plain weaves and 3-D weaves. *Composites Engineering*, 5:1177–1186, 1995.

[36] P. Grosberg. The strength of twistless slivers. *Journal of the Textile Institute Transactions*, 54(6):T223–T233, 1963.

[37] P. Grosberg and P. A. Smith. The strngth of slivers of relatively low twist. *Journal of the Textile Institute Transactions*, 57(1):T15–T23, 1966.

[38] T. G. Gutowski, Z. Cai, S. Bauer, D. Boucher, J. Kingery, and S. Wineman. Consolidation experiments for laminate composites. *Journal of Composite Materials*, 21:650–669, 1987.

[39] T. G. Gutowski, T. Morigaki, and Z. Cai. The consolidation of laminate composites. *Journal of Composite Materials*, 21:172–188, 1987.

[40] Lee D. H., Carnaby G. A., Carr A. J., and Moss P. A review of current micromechanical model of the unit fibrous cell. *WRONZ Communication*, 1990.

[41] Lee D. H., Carnaby G. A., and Tandon S. K. An energy analysis of the compression of a random fibre assembly. In *Proceedings of the 8th Textile Research Conference, Christchurch, New Zealand*, 1990.

[42] N. Hamila and Ph. Boisse. A mesomacro three node finite element for draping of textile composite preforms. *Applied Composite Materials*, 14:235–250, 2007.

[43] P. Harrison, M. J. Clifford, and A. C. Long. Shear characterisation of viscous woven textile composites: a comparison between picture frame and bias extension experiments. *Composites Science and Technology*, 64:1453–1465, 2004.

[44] J. Hearle. Techtext cad. `http://www.tensiontech.com/software/techtext_cad.html`. Accessed December 20, 2012.

[45] J. Hofstee and F. van Keulen. 3-D geometric modeling of a draped woven fabric. *Composite Structures*, 54:179–195, 2001.

[46] D. Hull and T.W. Clyne. *An Introduction to Composite Materials*. Cambridge Solid State Science Series. Cambridge University Press, 1996.

[47] K. L. Johnson. *Contact mechanics*. Cambridge University Press, 1987.

[48] O. Kallmes and H. Corte. The structure of paper, i. the statistical geometry of an ideal two dimensional fiber network. *Tappi J*, 43(9):737–752, 1960.

[49] V. M. Karbhari and P. Simacek. Notes on the modeling of preform compaction: Ii- effect of sizing on bundle level micromechanics. *Journal of Reinforced Plastics and Composites*, 15(8):837–861, 1996.

[50] S. Kawabata and M. Niwa. Fabric performance in clothing and clothing manufacture. *Journal of the Textile Institute*, 80(1):19–50, 1989.

[51] P. A. Kelly, R. Umer, and S. Bickerton. Viscoelastic response of dry and wet fibrous materials during infusion processes. *Composites Part A-applied Science and Manufacturing*, 37:868–873, 2006.

[52] A. Kemp. An extension of peirce's cloth geometry to the treatment of non-circular threads. *Journal of the Textile Institute Transactions*, 49(1):T44–T48, 1958.

[53] Y. R. Kim, S. P. McCarthy, and J. P. Fanucci. Compressibility and relaxation of fiber reinforcements during composite processing. *Polymer Composites*, 12:13–19, 1991.

[54] D.E. Knuth. *The Art of Computer Programming: Fundamental algorithms. Vol. 1.* Addison-Wesley, 2012.

[55] T. Komori and M. Itoh. A new approach to the theory of the compression of fiber assemblies. *Textile Research Journal*, 61(7):420–428, 1991.

[56] T. Komori and M. Itoh. Theory of the general deformation of fiber assemblies. *Textile Research Journal*, 61(10):588–594, 1991.

[57] T. Komori and K. Makishima. Numbers of fiber-to-fiber contacts in general fiber assemblies. *Textile Research Journal*, 47(1):13–17, 1977.

[58] J. Launay, G. Hivet, A. V. Duong, and Ph. Boisse. Experimental analysis of the influence of tensions on in plane shear behaviour of woven composite reinforcements. *Composites Science and Technology*, 68:506–515, 2008.

[59] D. H. Lee and J. K. Lee. Initial compressional behaviour of fibre assembly. *Objective Measurement: Applications to Product Design and Process Control (S. Kawabata, R. Postle, and M. Niwa (Eds.))*, pages 613–622, 1985.

[60] S. H. Lee, J. H. Han, S. Y. Kim, J. R. Youn, and Y. S. Song. Compression and relaxation behavior of dry fiber preforms for resin transfer molding. *Journal of Composite Materials*, 44:1801–1820, 2010.

[61] ScotCad Textiles Limited. Scotweave. `http://www.scotweave.com/`. Accessed December 20, 2012.

[62] H. Lin, M. J. Clifford, A. C. Long, and M. Sherburn. Finite element modelling of fabric shear. *Modelling and Simulation in Materials Science and Engineering*, 17, 2009.

[63] H. Y. Lin and A. Newton. Computer representation of woven fabric by using b-splines. *Journal of the Textile Institute*, 90(1):59–72, 1999.

[64] S. V. Lomov, E. B. Belov, T. Bischoff, S. B. Ghosh, T. Truong Chi, and I. Verpoest. Carbon composites based on multiaxial multiply stitched preforms. Part 1. Geometry of the preform. *Composites Part A-applied Science and Manufacturing*, 33:1171–1183, 2002.

[65] S. V. Lomov, Ph. Boisse, E. Deluycker, F. Morestin, K. Vanclooster, D. Vandepitte, I. Verpoest, and A. Willems. Full-field strain measurements in textile deformability studies. *Composites Part A-applied Science and Manufacturing*, 39:1232–1244, 2008.

[66] S. V. Lomov, A. V. Gusakov, G. Huysmans, A. Prodromou, and I. Verpoest. Textile geometry preprocessor for meso-mechanical models of woven composites. *Composites Science and Technology*, 60:2083–2095, 2000.

[67] S. V. Lomov, G. Huysmans, Y. Luo, R. S. Parnas, A. Prodromou, I. Verpoest, and F. R. Phelan. Textile composites: modelling strategies. *Composites Part A-applied Science and Manufacturing*, 32:1379–1394, 2001.

[68] S. V. Lomov and I. Verpoest. Modelling of the internal structure and deformability of textile reinforcements: WiseTex software. *Proc. of 10th European Conf. Composite Materials (ECCM-10), Brugge, Belgium, June*, pages 3–7, 2002.

[69] S. V. Lomov and I. Verpoest. Model of shear of woven fabric and parametric description of shear resistance of glass woven reinforcements. *Composites Science and Technology*, 66:919–933, 2006.

[70] A. C. Long, B. J. Souter, F. Robitaille, and C. D. Rudd. Effects of fibre architecture on reinforcement fabric deformation. *Plastics Rubber and Composites*, 31:87–97, 2002.

[71] Y. Luo and I. Verpoest. Compressibility and relaxation of a new sandwich textile preform for liquid composite molding. *Polymer Composites*, 20:179–191, 1999.

[72] B. Maze, H. V. Tafreshi, and B. Pourdeyhimi. Geometrical modeling of fibrous materials under compression. *Journal of Applied Physics*, 102, 2007.

[73] N. Metropolis, A. W. Rosenbluth, M. N. Rosenbluth, A. H. Teller, and E. Teller. Equation of state calculations by fast computing machines. *The Journal of Chemical Physics*, 21(6):1087–1092, 1953.

[74] Y. Miao, E. Zhou, Y. Wang, and B. A. Cheeseman. Mechanics of textile composites: Micro-geometry. *Composites Science and Technology*, 68(78):1671 – 1678, 2008.

[75] D. S. Mikhaluk, T. C. Truong, A. I. Borovkov, S. V. Lomov, and I. Verpoest. Experimental observations and finite element modelling of damage initiation and evolution in carbon/epoxy non-crimp fabric composites. *Engineering Fracture Mechanics*, 75:2751–2766, 2008.

[76] Q. Ning and T. Chou. A closed-form solution of the transverse effective thermal conductivity of woven fabric composites. *Journal of Composite Materials*, 29:2280–2294, 1995.

[77] Q. G. Ning and T. W. Chou. A general analytical model for predicting the transverse effective thermal conductivities of woven fabric composites. *Composites Part A: Applied Science and Manufacturing (Incorporating Composites and Composites Manufacturing)*, 29(3):315–322, 1998.

[78] K. J. Niskanen and M. J. Alava. Planar random networks with flexible fibers. *Physical Review Letters*, 73:3475–3478, 1994.

[79] M. B. Nziengui, M. Hattabi, and J. Echaabi. Viscoelastic analysis of fibrous reinforcments in liquid composite moulding processes. In *In 9th International Conference on Flow Processes in Composite Materials, Montreal*, 2008.

[80] N. Pan and G. A. Carnaby. Theory of the shear deformation of fibrous assemblies. *Textile Research Journal*, 59(5):285–292, 1989.

[81] N. Pearce and J. Summerscales. The compressibility of a reinforcement fabric. *Composites Manufacturing*, 6:15–21, 1995.

[82] F. T. Peirce. The geometry of cloth structure. *Journal of the Textile Institute Transactions*, 28(3):T45–T96, 1937.

[83] V. L. Popov. *Contact mechanics and friction: physical principles and applications*. Springer, 2010.

[84] P. Potluri, D. A. Perez Ciurezu, and R. B. Ramgulam. Measurement of meso-scale shear deformations for modelling textile composites. *Composites Part A-applied Science and Manufacturing*, 37:303–314, 2006.

[85] P. Potluri, I. Parlak, R. Ramgulam, and T. V. Sagar. Analysis of tow deformations in textile preforms subjected to forming forces. *Composites Science and Technology*, 66:297–305, 2006.

[86] P. Potluri, A. Rawal, M. Rivaldi, and I. Porat. Geometrical modelling and control of a triaxial braiding machine for producing 3d preforms. *Composites Part A: Applied Science and Manufacturing*, 34(6):481 – 492, 2003. ¡ce:title¿ICMAC 2001 - International Conference for Manufacturing of Advanced Composites¡/ce:title¿.

[87] A. G. Prodromou and J. Chen. On the relationship between shear angle and wrinkling of textile composite preforms. *Composites Part A-applied Science and Manufacturing*, 28:491–503, 1997.

[88] T.J. Reinhart and ASM International. Handbook Committee. *Engineered materials handbook: composites*. Engineered Materials Handbook. ASM International, 1987.

[89] C. Robert and G. Casella. *Monte Carlo statistical methods*. Springer Texts in Statistics. Springer, 2004.

[90] F. Robitaille and R. Gauvin. Compaction of textile reinforcements for composites manufacturing. I: Review of experimental results. *Polymer Composites*, 19:198–216, 1998.

[91] F. Robitaille and R. Gauvin. Compaction of textile reinforcements for composites manufacturing. II: Compaction and relaxation of dry and H_2O-saturated woven reinforcements. *Polymer Composites*, 19:543–557, 1998.

[92] F. Robitaille, A. C. Long, and C. D. Rudd. Geometric modelling of textiles for prediction of composite processing and performance characteristics. *Plastics Rubber and Composites*, 31:66–75, 2002.

[93] C. D. Rudd, A. C. Long, K. N. Kendall, and C. Mangin. *Liquid moulding technologies: resin transfer moulding, structural reaction injection moulding and related processing techniques.* Woodhead Publishing Limited, 1997.

[94] C. D. Rudd, M. J. Owen, and V. Middleton. Mechanical properties of weft knit glass fibre/polyester laminates. *Composites Science and Technology*, 39(3):"261 – 277, 1990.

[95] P.J. Russell, S.L. Wolfe, P.E. Hertz, and C. Starr. *Biology: The Dynamic Science.* Number v. 2. Cengage Learning, 2007.

[96] D. Raizenne S. Hind, F. Robitaille. Parametric unit cell modelling of the effective transverse thermal conductivity of carbon plain weave composites. In *TexComp-8, Nottingham*, 2006.

[97] D. Sajn, J. Gersak, and R. Flajs. Prediction of stress relaxation of fabrics with increased elasticity. *Textile Research Journal*, 76(10):742–750, 2006.

[98] R. Samadi. *Compaction, flow and mechanical properties in lap joints for large multilayer VARTM preforms*. PhD thesis, University of Ottawa, 2007.

[99] R. Samadi and F. Robitaille. Compaction of aligned fibre assemblies using particulate methods. In *In 9th International Conference on Flow Processes in Composite Materials, Montreal*, 2008.

[100] R. Samadi and F. Robitaille. Particulate methods for the mechanics of dry textile. In *In International Conference on Textile Composites(TEXCOMP08), Newark*, 2008.

[101] R. Samadi and F. Robitaille. Concurrent simulation of permeability, thermal conductivity and modulus for carbon fibre reinforcements and composites. *International Review of Mechanical Engineering*, 61:29–38, 2011.

[102] R. Samadi and F. Robitaille. Particle-based modelling of in-plane shear in textiles. *Textile Research Journal*, Manuscript ID:TRJ-13-0079: Submitted, 2013.

[103] R. Samadi and F. Robitaille. Particle-based modelling of stress relaxation in textiles. *Textile Research Journal*, Manuscript ID: To be submited, 2013.

[104] R. Samadi and F. Robitaille. Particle-based modelling of the compaction of fibre yarns and woven textiles. *Textile Research Journal*, Manuscript ID:TRJ-12-0391.R1: Accepted for publication in final form, 2013.

[105] R. A. Saunders, C. Lekakou, and M. G. Bader. Compression and microstructure of fibre plain woven cloths in the processing of polymer composites. *Composites Part A-applied Science and Manufacturing*, 29:443–454, 1998.

[106] R. A. Saunders, C. Lekakou, and M. G. Bader. Compression in the processing of polymer composites 2. Modelling of the viscoelastic compression of resin-

impregnated fibre networks. *Composites Science and Technology*, 59:1483–1494, 1999.

[107] J. S. U. Schell, M. Renggli, G. H. van Lenthe, R. Müller, and P. Ermanni. Micro-computed tomography determination of glass fibre reinforced polymer mesostructure. *Composites Science and Technology*, 66:2016–2022, 2006.

[108] K. Searles, G. Odegard, and M. Kumosa. Micro- and mesomechanics of 8-harness satin woven fabric composites: I evaluation of elastic behavior. *Composites Part A: Applied Science and Manufacturing*, 32(11):1627 – 1655, 2001.

[109] W. J. Shanahan and J. W. S. Hearle. An energy method for calculations in fabric mechanics part ii: examples of application of the method to woven fabrics. *Journal of the Textile Institute*, 69(4):92–100, 1978.

[110] S. B. Sharma, M. P. F. Sutcliffe, and S. H. Chang. Characterisation of material properties for draping of dry woven composite material. *Composites Part A-applied Science and Manufacturing*, 34:1167–1175, 2003.

[111] M. Sherburn. Texgen. `http://texgen.sourceforge.net/index.php/Main_Page`. Accessed December 20, 2012.

[112] M. Sherburn. *Geometric and mechanical modeling of textiles.* PhD thesis, University of Nottingham, 2007.

[113] M. Sherburn, F. Robitaille, A. Long, and C. Rudd. Geometric pre-processor for the calculation of physical properties of textiles. In *Proceedings of the Industrial Simulation Conference, Malaga, Spain*, pages 479–486, 2004.

[114] P. Simacek and V. M. Karbhari. Notes on the modeling of preform compaction: I- micromechanics at the fiber bundle level. *Journal of Reinforced Plastics and Composites*, 15(1):86–122, 1996.

[115] P. Smith, C. D. Rudd, and A. C. Long. The effect of shear deformation on the processing and mechanical properties of aligned reinforcements. *Composites Science and Technology*, 57:327–344, 1997.

[116] A. A. Somashekar, S. Bickerton, and D. Bhattacharyya. Modelling the viscoelastic stress relaxation of glass fibre reinforcements under constant compaction strain during composites manufacturing. *Composites Part A: Applied Science and Manufacturing*, 43(7):1044–1052, 2012. cited By (since 1996) 0.

[117] A. E. Stearn. The effect of anisotropy in the randomness of fibre orientation on fibre-to-fibre contacts. *J. Text. Inst*, 62(7):353–360, 1971.

[118] X. Sun and Ch. Sun. Mechanical properties of three-dimensional braided composites. *Composite Structures*, 65(34):485 – 492, 2004.

[119] D. S. Taylor. The determination of contacts between the constituents of fibre assemblies. *J. Textile Inst*, 47:T141–T153, 1956.

[120] L. Tong and A.P. Mouritz. *3D Fibre Reinforced Polymer Composites.* Elsevier Science, 2002.

[121] S.W. Tsai and H.T. Hahn. *Introduction to composite materials.* Technomic Publishing Company, 1980.

[122] C. M. van Wyk. Note on the compressibility of wool. *Journal of The Textile Institute Transactions*, 37, 1946.

[123] K. Vanclooster, S. V. Lomov, and I. Verpoest. Experimental validation of forming simulations of fabric reinforced polymers using an unsymmetrical mould configuration. *Composites Part A-applied Science and Manufacturing*, 40:530–539, 2009.

[124] B. Verleye, R. Croce, M. Griebel, M. Klitz, S. V. Lomov, I. Verpoest, and D. Roose. Finite difference computation of the permeability of textile reinforcements with a fast stokes solver and new validation examples. *AIP Conference Proceedings*, 907:945–950, 2007.

[125] B. Verleye, M. Klitz, R. Croce, D. Roose, S.V. Lomov, and I. Verpoest. *Computation of permeability of textile with experimental validation for monofilament and non crimp fabrics*, volume 55 of *Studies in Computational Intelligence*. Springer Berlin Heidelberg, 2007.

[126] I. Verpoest and S. V. Lomov. Virtual textile composites software WiseTex: Integration with micro-mechanical, permeability and structural analysis. *Composites Science and Technology*, 65:2563–2574, 2005.

[127] Y. Wang and X. Sun. Digital-element simulation of textile processes. *Composites Science and Technology*, 61(2):311 – 319, 2001.

[128] Wikipedia. Boolean function, 2004. [Online; Accessed December 20, 2012].

[129] Wikipedia. Random walk, 2007. [Online; Accessed December 20, 2012].

[130] A. Willems, S. V. Lomov, I. Verpoest, and D. Vandepitte. Drape-ability characterization of textile composite reinforcements using digital image correlation. *Optics and Lasers in Engineering*, 47:343–351, 2009.

[131] C. C. Wong, A. C. Long, M. Sherburn, F. Robitaille, P. Harrison, and C. D. Rudd. Comparisons of novel and efficient approaches for permeability prediction based

on the fabric architecture. *Composites Part A-applied Science and Manufacturing*, 37:847–857, 2006.

[132] R. Wright, N. Haemel, G.M. Sellers, and B. Lipchak. *OpenGL SuperBible: Comprehensive Tutorial and Reference*. OpenGL. Pearson Education, 2010.

[133] E. Zhou, D. Mollenhauer, and E. Iarve. Micro-geometric modeling of textile preforms with vacuum bag compression:an application of multi-chain digital element technique. In *AIAA, Schaumburg,IL*, 2006.

[134] G. Zhou, X. Sun, and Y. Wang. Multi-chain digital element analysis in textile mechanics. *Composites Science and Technology*, 64(2):239 – 244, 2004.

Appendix A

Appendix A: Flowchart

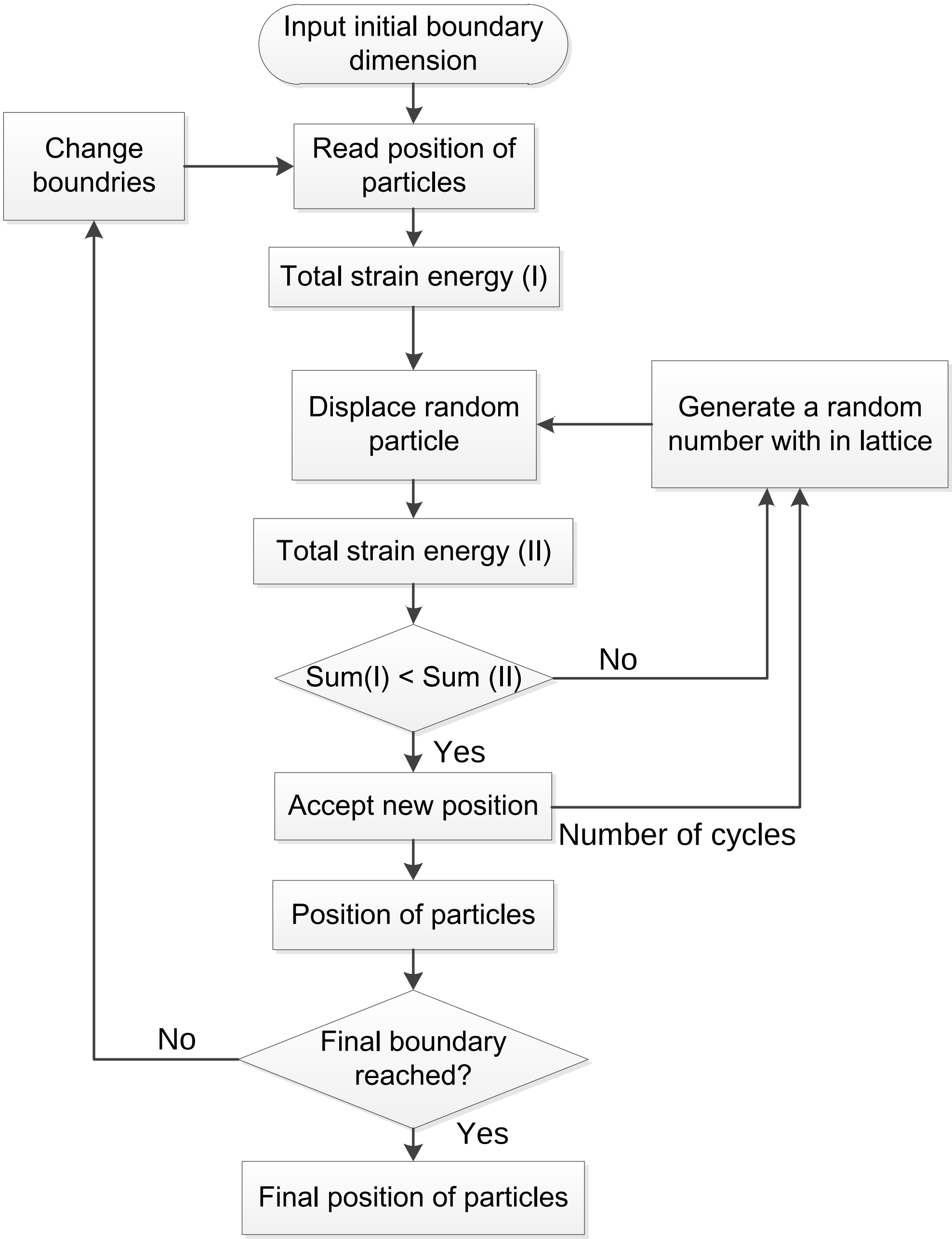

Figure A.1: Flow chart of particle-based modelling method